OPTIMIZATION OF ENZYMATIC HYDROLYSIS CONDITIONS FOR ANTIMICROBIAL ACTIVITY AGAINST *Pantoea* Spp. CAUSING RICE LEAF BLIGHT

Siti Norazura Jamal[1ab*], Dhilia Udie Lamasudin[2b], Belal J. Muhialdin[3c], Noor Baity Saidi[4b], Lai Kok Song[5d] and Mohd Termizi Yusof[6e]

Abstract: The Central Composite Design (CCD) within the Response Surface Methodology (RSM) was applied to optimize the enzymatic hydrolysis process. This process used Alcalase® to hydrolyze *Bactronophorus thoracites* protein with the goal of maximizing its antimicrobial effects. Four distinct parameters were identified as independent variables: pH (A: 8.5–10.5), temperature (B: 45–65 °C), hydrolysis time (C: 120–360 min), and enzyme-to-substrate ratio (D: 1.45%–2.65% w/v). Meanwhile, the antimicrobial activity was chosen as the response variable, specifically against *Pantoea ananatis* (Y_1) and *Pantoea stewartii* (Y_2). According to the findings, the constructed quadratic polynomial model showed a significant correlation with the experimental data, as evidenced by the coefficient of determination (R^2) values for antimicrobial activity: Y_1 being 0.9893 ($p < 0.0001$) and Y_2 at 0.9848 ($p < 0.0001$). Optimal antimicrobial activity for *Bactronophorus thoracites* protein hydrolysates (BTPH) was recorded at 46.748% against *P. ananatis* and 40.768% against *P. stewartii*. This result was observed under the optimal conditions of pH 9.5, temperature 55ºC, hydrolysis duration of 240 minutes, and 2.05% w/v enzyme-to-substrate ratio. There was a notable alignment between the actual and predicted values from our models, with the Residual Standard Error (RSE) values falling under 5%. Furthermore, the established Minimum Inhibitory Concentration (MIC) was 250µg/mL, and the Minimum Bactericidal Concentration (MBC) was 500µg/mL for both *P. ananatis* and *P. stewartii*. In conclusion, the findings suggest that the refined BTPH has great promise as an effective bioactive component for agricultural use.

Keywords: Alcalase®, Antimicrobial, Response Surface Methodology (RSM), Rice pathogens, Shipworms.

1. Introduction

Leaf blight, a disease caused by *Pantoea* bacteria, is a significant issue in many rice-growing countries, causing substantial economic losses (Chukwu et al., 2019). The disease can cause up to 70% yield reduction in some regions. The disease was first linked to *Pantoea agglomerans* in Venezuela in 2002 (González et al., 2015), and later found in India in 2008 and Korea in 2009 (Lee et al., 2010; Mondal et al., 2011). Recent Malaysian outbreaks were attributed to *P. stewartii*, *P. ananatis*, and *P. dispersa* (Azizi et al., 2019a, b; Toh et al., 2019), with *P. stewartii* and *P. ananatis* suggested as the primary agents (Azizi et al., 2019a, b). The symptoms include water-soaked lesions evolving into brown leaf stripes, and in severe cases, yellowing or burning patterns along leaf borders.

Although numerous strategies for managing leaf blight in rice have been published, the precise procedure for controlling *Pantoea* spp. has not been determined. For instance, *Xanthomonas oryzae* leaf blight can be controlled by spraying agrochemical chemicals on the diseased plants (Khan et al., 2012). Even though agrochemical chemicals are beneficial from a crop production perspective, excessive use might have significant environmental implications and acute toxicity issues due to their bio-magnification and persistency, resulting in rapid pathogen resistance towards the chemical (Sharma et al., 2000; Sundin & Wang 2018; Valarmathi, 2020). Therefore, the world needs novel active biomolecules to fight the emerging and re-emerging plant pathogens (Hamed et al., 2018).

The extraction process plays a crucial role in the identification of bioactive components when producing bioactive compounds from natural sources. Protein hydrolysis is an extraction process

Authors information:

[a]Faculty of Applied Sciences, Universiti Teknologi MARA, Kampus Kuala Pilah, Pekan Parit Tinggi, 72000 Kuala Pilah, Negeri Sembilan, Malaysia. E-mail: norazura6775@uitm.edu.my[1]

[b]Department of Cell and Molecular Biology, Faculty of Biotechnology and Biomolecular Sciences, Universiti Putra Malaysia, 43400, Serdang, Selangor, Malaysia. E-mail: norazura6775@uitm.edu.my[1]; dhilia@upm.edu.my[2]; norbaity@upm.edu.my[4]

[c]Department of Food Science and Nutrition, University of Minnesota, 1334 Eckles Ave, Saint Paul, MN 55108, USA. E-mail: mulah001@umn.edu[3]

[d]Health Sciences Division, Abu Dhabi Women's College, Higher Colleges of Technology, 41012, Abu Dhabi, UAE. E-mail: laikoksong@gmail.com[5]

[e]Department of Microbiology, Faculty of Biotechnology and Biomolecular Sciences, Universiti Putra Malaysia, 43400, Serdang, Selangor, Malaysia. E-mail: mohdtermizi@upm.edu.my[6]

*Corresponding Author: norazura6775@uitm.edu.my

that uses an enzyme in an acidic or alkaline setting to dismantle protein peptide bonds. It's a well-established technique for altering the nutritional and functional characteristics of marine protein and creating antimicrobial peptides through enzyme-driven protein hydrolysis. This technique involves the use of protease under conditions that can be precisely managed, such as the duration of hydrolysis, temperature, enzyme-to-substrate ratio and pH (Amin & Cheng, 2019; Rosa et al., 2011; Jamal et al., 2022; Jayaprakash & Perera, 2020). Over the past few decades, much of the scientific research in this area has concentrated on mollusks, specifically in the quest for antimicrobial peptides (AMPs) (Avila, 2006; Benkendorff, 2010, 2014).

Many previous studies have effectively utilized enzymatic hydrolysis for the extraction of bioactive compounds from diverse sources (Amin & Cheng, 2019; Wang et al., 2013; Jayaprakash & Perera, 2020). The capability to attain elevated extraction efficiency under favorable conditions has established enzymatic hydrolysis as a commonly employed extraction technique. Moreover, enzymatic hydrolysis is recognized for its environmentally friendly attributes, as it generally produces fewer detrimental byproducts and waste when compared to the conventional chemical methods. Consequently, enzymatic hydrolysis is highly regarded as a promising and sustainable extraction approach.

At present, there is a significant demand to establish a reliable model that optimizes variables like pH, temperature, hydrolysis duration, and enzyme-to-substrate ratio to determine the best condition for mollusks (Amin & Cheng, 2019). Both observational and statistical strategies can shed light on this optimization (Adebo et al., 2018; Hamid et al., 2015; Wang et al., 2017). In this realm, the Response Surface Methodology (RSM) stands out as an effective tool. RSM combines mathematical and statistical insights to fit empirical models with real-world data, often using linear or quadratic equations to describe the system being studied. This makes RSM an asset for research projects aiming to optimize experimental settings (Adebo et al., 2018). One of RSM's most notable advantages is its efficiency in minimizing experimental runs, reducing costs, and saving time. Such benefits have made it a popular choice for enhancing the extraction of antioxidants and antimicrobial compounds from natural origins (Hamid et al., 2015; Seema & Rajesh, 2015; Wang et al., 2017).

B. thoracites offers potential as a source for synthesizing bioactive peptides and other beneficial protein derivatives. Using proteins from this organism, enzymatic hydrolysis can create these peptides. The antibacterial properties of peptides from mollusks have been discussed in several studies (Avila, 2006; Rosa et al., 2011; Mitta et al., 1999; Jamal et al., 2022a,b; Charlet et al., 1996; Hubert, 1966). These peptides have shown effectiveness against rice diseases like the one caused by *Xanthomonas oryzae* (Sharma et al., 2000) and may serve agricultural roles, from combating pathogens to medicinal applications (Kaspar et al., 2019; Robertsen & Musiol-Kroll, 2019; Sarika et al., 2012). These

peptides also exhibit a wide array of biological benefits, including antiviral and antidiabetic to anticancer activities (Agrawal et al., 2017; Gogineni & Hamann, 2018). Additionally, their potential as antimicrobial agents have been underscored by previous studies like Sathoff et al. (2019), Datta et al. (2015), and Seo et al. (2014).

However, previous studies on *B. thoracites* protein hydrolysates have not explored the optimization of Alcalase® enzyme hydrolysis for antimicrobial potential. Therefore, this study seeks to optimize the enzymatic hydrolysis conditions with Alcalase® to maximize the antimicrobial activity of *B. thoracites* against rice pathogens.

2. Materials and Methods

Sample Collection
B. thoracites was collected from a mangrove forest at Kelanang Beach, Banting, Selangor, Malaysia, (2° 48'44.5" N, 101° 22'08.5" E). *B. thoracites* were safely packed in a plastic bag and chilled for transportation to the Plant Molecular Biology Lab (UPM).

Preparation of Crude Extract
Shipworms were cleaned and homogenised at 4°C. This mixture was dispersed with cold deionised water and packed in small plastic bags, then frozen overnight at -80°C. They were then freeze-dried until a stable weight was reached. Post-drying, the samples were ground into powder, sieved to ensure fineness, and stored in capped bottles at -20°C for future use.

Protein Hydrolysate Preparation
The Response Surface Methodology (RSM) and Central Composite Design (CCD) in Design-Expert® software were applied for optimization of conditions. 6g of *B. thoracites* was dissolved into 100mL phosphate buffers. According to the RSM design, protein and enzyme solutions were mixed to get the desired enzyme concentration. This mixture was shaken at 100 rpm and heated to 95°C for 15 minutes to deactivate the enzyme. Post-heating, the samples were centrifuged at 2600g for 15 minutes at 4°C to remove impurities. The resulting supernatant, the protein hydrolysate, was collected. After assessing the degree of hydrolysis, it was freeze-dried. The final product, *Bactronophorus thoracites* protein hydrolysates (BTPH), was then stored at -20°C for further research.

Experimental Design, Modelling and Statistical Analysis
The Design-Expert® software (version 13.0) was used to design experiments and analyze data. Using the Central Composite Design (CCD) method, four factors were assessed over five levels to study the antimicrobial activity against *P. ananatis* and *P. stewartii*. Table 1 shows the selected variables and their levels, while Table 2 presents the experiment layout. A total of 30 tests were conducted, including three central point repeats. These were randomized to account for unforeseen factors. Based on the

data, a second-order polynomial model or a simpler one was used, as shown in Equation (1).

$$Y = z_0 + \sum z_1\ A + \sum z_{12}\ AB + \sum z_{123}\ AA \qquad (1)$$

Equation (1) represents formula which "Y" symbolizes the dependent variable, which pertains to the antibacterial action against *P. ananatis* and *P. stewartii*. The term "z_0" indicates the model's average value, "z_1" is the coefficient linked to parameter A, while "z_{12}" and "z_{123}" are coefficients corresponding to the interaction terms AB and AA, respectively. The equation considers the quadratic, linear, and interactive effects of process variables on the outcomes. The importance of each process variable's coefficient was gauged using the Student's t-test. Additionally, the relevance, accuracy, and influence of process variables on the results were scrutinized using Analysis of Variance (ANOVA).

Table 1. The four variables and their associated coded levels for optimizing enzymatic hydrolysis conditions.

Symbol	Independent Variable	Coded level				
		-2	-1	0	+1	+2
A	pH	8.5	9.0	9.5	10	10.5
B	Temperature (°C)	45	50	55	60	65
C	Hydrolysis time (min)	120	180	240	300	360
D	Enzyme-to-substrate ratio (E/S) % (w/v)	1.45	1.75	2.05	2.35	2.65

Table 2. Central Composite Design (CCD) design for optimizing enzymatic hydrolysis conditions under different levels of process variables.

Run	Independent Variables			
	A	B	C	D
1	8.5	55	240	2.05
2	9	50	180	1.75
3	9	50	180	2.35
4	9	50	300	1.75
5	9	50	300	2.35
6	9	60	180	1.75
7	9	60	180	2.35
8	9	60	300	1.75
9	9	60	300	2.35
10	9.5	45	240	2.05
11	9.5	55	120	2.05
12	9.5	55	240	1.45
13	9.5	55	240	2.05
14	9.5	55	240	2.05
15	9.5	55	240	2.05
16	9.5	55	240	2.05
17	9.5	55	240	2.05
18	9.5	55	240	2.05
19	9.5	55	240	2.65
20	9.5	55	360	2.05
21	9.5	65	240	2.05
22	10	50	180	1.75
23	10	50	180	2.35
24	10	50	300	1.75
25	10	50	300	2.35
26	10	60	180	1.75
27	10	60	180	2.35
28	10	60	300	1.75
29	10	60	300	2.35
30	10.5	55	240	2.05

Independent variables: A, pH; B, Temperature (°C); C, Hydrolysis time (min); D, Enzyme to substrate ratio (% w/v).

Determination of Antimicrobial Activity

Protein hydrolysates were tested for antimicrobial effects against *P. ananatis* and *P. stewartii*, with an unhydrolyzed sample as control. They were mixed with Luria Broth and incubated at 30°C for 24 hours. Antimicrobial activity was assessed by measuring absorbance at 600 nm, following guidelines from Mohamad Asri et al. (2020). The bacterial inhibition percentage was calculated using a formula (Equation 2). The most effective samples were then freeze-dried for further analysis.

$$Inhibition\% = \frac{(24\,h\,negative\,control - 0\,h\,negative\,control) - (24\,h\,sample - 0\,h\,sample)}{0\,h\,negative\,control} \quad (2)$$

Validation of Optimum Condition

The optimal conditions for antimicrobial activity were predicted using the Design-Expert software. The verification of the model was done by hydrolyzing *B. thoracites* protein under these conditions in three tests: pH 9.5, 55°C, 240 minutes of hydrolysis, and 2.05% enzyme-to-substrate ratio. The hydrolysates were then freeze-dried and tested for antimicrobial activity. The predicted and actual activities were compared using t-test and the residual standard error (RSE). If the RSE (Equation 3) was under 5%, the predictions were considered accurate, as per methods from Ngan et al. (2014) and Zakaria et al. (2021).

$$Residual\,standard\,error\,(\%) = \left| \frac{Actual\,value - Predicted\,value}{Predicted\,value} \right| \times 100 \quad (3)$$

Effective Inhibition Concentration

The effectiveness of BTPH against bacteria was tested using methods adapted from Mohamad Asri et al. (2020) and Muhialdin et al. (2020). A bacterial culture was mixed with LB and exposed to different BTPH concentrations to find the least amount that stops bacterial growth. After incubating for 24 hours at 30°C, growth was measured. The smallest BTPH amount preventing visible growth was noted as the MIC. The MBC was determined by placing samples on agar plates before incubating the culture at 37°C for 24 hours, and observing which concentration prevented growth. These tests were repeated three times.

Data Analysis

Data is presented as the average from three repetitions ± standard deviations, using 95% confidence level.

3. Results and Discussion

Model Calibration and Variance Analysis

Table 3 displays the matrix of actual and predicted response values. Each analysis was repeated three times for accuracy. Using Analysis of Variance (ANOVA), the effects of the variables on the responses were examined. The ANOVA results showed that the models were statistically significant, with F-values of 98.68 for Y_1, *P. ananatis*, and 69.49 for Y_2, *P. stewartii*. The data suggested a less than 0.01% likelihood that these values occurred by chance. The models were deemed significant since the probability for each response was below 0.05. Based on the Central Composite Design, the antibacterial activity for *P. ananatis* (Y_1) ranged from -0.978% to 46.748%, while for *P. stewartii* (Y_2), it ranged from -2.947% to 40.768%.

Table 4 shows the quadratic models that link the independent and dependent variables for each outcome. From the ANOVA results, the R^2 values for antibacterial activities against Y_1 (*P. ananatis*) and Y_2 (*P. stewartia*), were 0.9893 and 0.9848, respectively. These values indicate a strong connection between the Central Composite Design (CCD) and the models. Additionally, the predicted R^2 values, which measure how well the model predicts response outcomes, were 0.9599 for Y_1, and 0.9271 for Y_2. This result shows a close match between experimental and model-based predictions. Previous studies, like those by Gottipati et al. (2010) and Bordbar et al. (2018), have shown that an R^2 value above 0.9 indicates a good fit. In this case, the model captures about 99% of the changes in the responses.

Typically, the R^2 value increases whenever an additional variable is incorporated into a model, regardless the significance of the statistic being evaluated. This is true irrespective of the variables number included in the model. Moreover, the adjusted R-square (Adj. R^2) is a crucial measure that determines the model's adequacy. The Adj. R^2 not only communicates the predictive power of the regression models but also considers multiple variables simultaneously. The tally value only increases when a specific variable enhances the model significantly more than what would be expected by chance alone. The adjusted R^2 values for the antibacterial activity were 0.9792 and 0.9706 for *P. ananatis* and *P. stewartii*, respectively. This result validates the models' predictive capacity in defining the optimal conditions necessary for achieving the highest antimicrobial activity of *Bactronophorus thoracites* protein hydrolysates (BTPH) and showing that most of the variability of these responses were explained by the linear model as illustrated in Figure 1. However, there are points that are located further away from this line or clustered region, suggesting discrepancies between predicted and observed values for those data points. The models for antibacterial activities Y_1 (*P. ananatis*) and Y_2 (*P. stewartii*) showed variation coefficients (CV) of 11.86% and 16.70%. Since these are below 20%, the models are therefore considered as consistent. The lack-of-fit test gave p-values of 0.7919 for Y_1 and 0.2797 for Y_2, suggesting a good fit. Thus, these models are reliable in predicting the outcomes.

Table 3. Central Composite Design (CCD) and Response Values

Run	Independent variables				Code level				Response variable (%)			
	A (pH)	B (°C)	C (min)	D (% w/v)	A	B	C	D	Y₁		Y₂	
									Actual	Prediction	Actual	Prediction
1	8.5	55	240	2.05	-2	0	0	0	-0.978	-0.503	0.060	0.281
2	9	50	180	1.75	-1	-1	-1	-1	3.788	3.844	1.591	0.623
3	9	50	180	2.35	-1	-1	-1	+1	-1.318	-2.219	17.303	17.885
4	9	50	300	1.75	-1	-1	+1	-1	12.451	13.003	10.021	10.198
5	9	50	300	2.35	-1	-1	+1	+1	7.788	7.693	15.228	16.431
6	9	60	180	1.75	-1	+1	-1	-1	3.121	4.339	-0.659	-1.317
7	9	60	180	2.35	-1	+1	-1	+1	10.249	9.406	17.638	20.243
8	9	60	300	1.75	-1	+1	+1	-1	13.752	11.944	2.382	1.825
9	9	60	300	2.35	-1	+1	+1	+1	18.316	17.764	12.271	12.355
10	9.5	45	240	2.05	0	-2	0	0	18.986	18.899	6.624	5.409
11	9.5	55	120	2.05	0	0	-2	0	1.902	1.897	12.092	10.309
12	9.5	55	240	1.45	0	0	0	-2	7.642	7.150	11.258	13.043
13	9.5	55	240	2.05	0	0	0	0	40.117	42.086	40.768	38.987
14	9.5	55	240	2.05	0	0	0	0	40.405	42.086	40.502	38.987
15	9.5	55	240	2.05	0	0	0	0	41.896	42.086	35.724	38.987
16	9.5	55	240	2.05	0	0	0	0	41.389	42.086	39.777	38.987
17	9.5	55	240	2.05	0	0	0	0	41.959	42.086	37.156	38.987
18	9.5	55	240	2.05	0	0	0	0	46.748	42.086	39.992	38.987
19	9.5	55	240	2.65	0	0	0	+2	12.352	14.268	30.768	26.073
20	9.5	55	360	2.05	0	0	+2	0	13.258	14.687	24.502	23.374
21	9.5	65	240	2.05	0	+2	0	0	18.991	20.502	-1.660	-3.356
22	10	50	180	1.75	+1	-1	-1	-1	10.977	12.320	1.182	2.275
23	10	50	180	2.35	+1	-1	-1	+1	14.024	13.618	2.483	4.774
24	10	50	300	1.75	+1	-1	+1	-1	18.991	20.502	-1.660	-3.356
25	10	50	300	2.35	+1	-1	+1	+1	10.977	12.320	1.182	2.275
26	10	60	180	1.75	+1	+1	-1	-1	14.024	13.618	2.483	4.774
27	10	60	180	2.35	+1	+1	-1	+1	18.122	16.752	24.098	23.227
28	10	60	300	1.75	+1	+1	+1	-1	19.232	18.804	12.863	14.698
29	10	60	300	2.35	+1	+1	+1	+1	5.971	3.851	-2.947	-2.415
30	10.5	55	240	2.05	+2	0	0	0	16.042	16.280	3.383	4.382

A, pH; B, Temperature (°C); C, Hydrolysis time (min); D, Enzyme-to-substrate ratio (% w/v). Response variables for antimicrobial activity (%): Y₁, *P. ananatis* and Y₂, *P. stewartii*.

Table 4. Quadratic polynomial equations for responses Y_1 (*P. ananatis*) and Y_2 (*P. stewartii*) in relation to the coded variables.

Responses	Equations	R^2	R^2 (Adj.)	R^2 (Pred.)	Regression (p-value)	F-Value	Lack of fit
Y_1	42.08 + 2.65A + 0.40B + 3.19C + 1.77D + 2.24AB - 1.18AC - 1.84AD + 0.38BC - 2.78BD + 0.18CD + 9.31 A^2 - 5.59 B^2 - 8.44 C^2 - 7.84 D^2 -	0.9893	0.9792	0.9599	< 0.0001	98.68	0.7919
Y_2	38.99 + 0.707A - 2.19B - 3.27C + 3.26D + 0.68AB - 2.84AC + 3.69AD - 1.61BC - 1.07BD + 2.76CD - 10.03 A^2 - 9.49 B^2 - 5.54 C^2 - 4.86 D^2 -	0.9848	0.9706	0.9271	< 0.0001	69.49	0.2797

Y_1 and Y_2 represent the predicted responses comprising the antimicrobial activity against *P. ananatis* and *P. stewartii*, respectively, while A, B, C, and D are independent variables values, namely pH, temperature (°C), hydrolysis time (min) and enzyme-to-substrate ratio (% w/v).
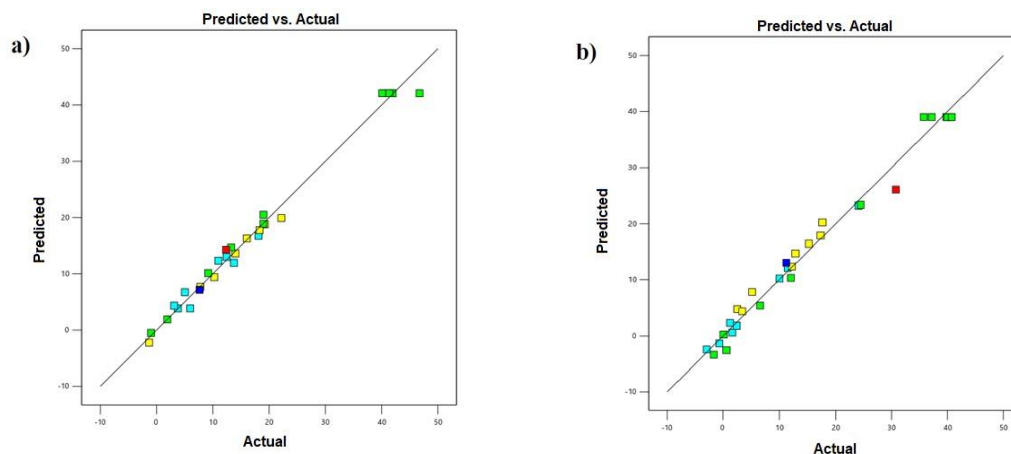
Figure 1. The predicted versus observed values for the antibacterial effect of (a) Y_1, *P. ananatis,* and (b) Y_2, *P. stewartii.*

Interpretation of Response Surface Plot and Influence of Independent Variables on Antimicrobial Activity

The interactive effects between pH (A) and temperature (B) were examined while keeping the hydrolysis duration constant at 2.05% enzyme-to-substrate ratio and 240 minutes. Figure 2(a) and Figure 3(a) depict the visual representation of these interaction effects. The graphs demonstrate that the highest antimicrobial effect was observed at pH of 9.5 and temperature of 55°C. In the pH range of 9 to 10, variations in the temperature did not seem to exert a noteworthy influence on the antimicrobial effect. The activity of Alcalase® enzyme, which is responsible for the antimicrobial effect, is believed to be influenced by the pH of the medium (Jamal et al., 2022a; Bordbar et al., 2018; Sila & Bougatef, 2016). Therefore, maintaining the pH within the optimal range is crucial for achieving maximum antimicrobial potency. Based on this investigation, the optimal pH was determined to be 9.5.

Figure 2(b) and Figure 3(b) show the effects of pH (A) and time spent on hydrolysis (C) at a set temperature of 55°C and enzyme-to-substrate ratio of 2.05%. The data reveal that the Alcalase® enzyme works best at pH of 9.5 and hydrolysis time of 240 minutes, making these the best conditions. This result matches the ideal pH range for Alcalase®, which is between 7.5 and 9.5, as noted by Zainol et al. (2021). Interestingly, the 240-minute hydrolysis time is longer than the previously suggested 60-minute period. The longer time allows the enzyme to break down the

protein more effectively, improving its ability to kill bacteria, as mentioned by Haslaniza et al. (2010). However, once past the best pH level, the enzyme's effectiveness drops, likely because it becomes less stable at high pH, as indicated by Amin et al. (2020).

Figure 2(c) and Figure 3(c) show the combined effects of pH (A) and the enzyme-to-substrate ratio (E/S) (D) at a set temperature of 55°C and hydrolysis time of 240 minutes. The data suggests that pH of 9, changes the E/S ratio either to 1.75% or 2.35% and reduces the antimicrobial strength. Earlier studies such as one by Sila & Bougatef (2016) highlighted the role of specific E/S ratios in enhancing antimicrobial effects. Hence, an E/S ratio of 2.05% seems to be the most effective for maximizing antimicrobial activity.

Figure 2(d) and Figure 3(d) demonstrate the interaction effects of temperature and enzyme-to-substrate (E/S) ratio while maintaining a constant pH of 9.5 and hydrolysis time of 240 minutes. Increased E/S ratio leads to higher concentration of the Alcalase® enzyme, resulting in greater number of amino acid peptides being cleaved. However, when the number of substrates in an enzyme reaction is low, the reaction rate is often slower and proportionate to the substrate concentration. The enzyme's affinity for the substrate, as well as the presence of any competitive inhibitors, can further influence this rate (Auwal et al., 2017; Bordbar et al., 2018).
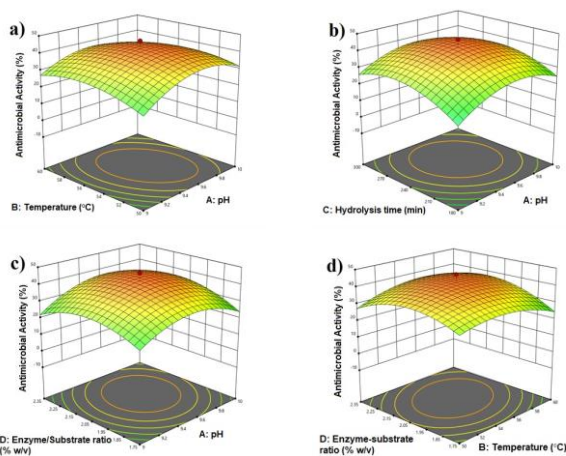
Figure 2. 3D contour plots show the variable parameters' effect on the antimicrobial activity Y_1, *P. ananatis* response. (a) pH vs temperature, (b) pH vs hydrolysis time, (c) pH vs E/S ratio, and (d) temperature vs E/S ratio.
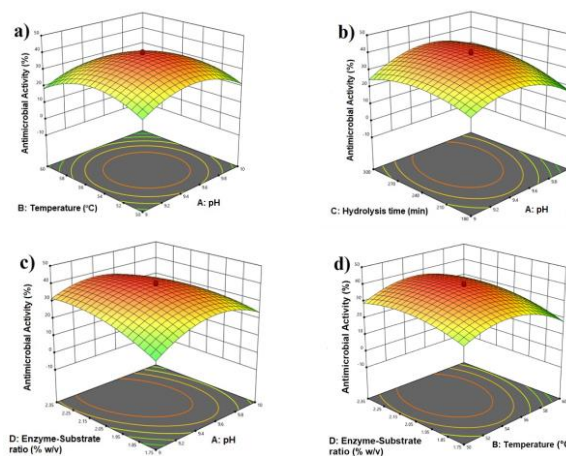

Figure 3. 3D contour plots show the variable parameters' effect on the antimicrobial activity Y_2, *P. stewartii* response. (a) pH vs temperature, (b) pH vs hydrolysis time, (c) pH vs E/S ratio, and (d) temperature vs E/S ratio.

Predicted Optimum Conditions Validation

The reliability of the obtained results was assessed by conducting validation using five independent validation sets, as shown in Table 5. This approach ensured the adequacy and reliability of the final models. The agreement between the actual and the predicted data was assessed by computing the residual standard error (RSE) percentages and contrasting them with the estimates from Equation (3). The models were deemed accurate when the RSE percentages fell below 5%, suggesting that the actual values were in close alignment with the predicted ones. As illustrated in Table 5, all RSE values came under the 5% threshold, underscoring the robustness and precision of the models.

Table 5. Actual and predicted responses.

Set	Variables				Response variables					
					Antimicrobial Activity, Y_1 (%)			Antimicrobial Activity, Y_2 (%)		
	A	B	C	D	Actual	Predicted	RSE	Actual	Predicted	RSE
1	9.1	51	190	1.8	15.952	15.364	3.827	13.419	12.884	4.156
2	9.2	52	200	1.9	27.302	26.159	4.369	27.491	28.164	-2.388
3	9.4	54	220	2	39.311	38.329	2.562	37.681	36.218	4.038
4	9.6	56	250	2.2	42.169	41.663	1.215	36.444	37.953	-3.977
5	9.8	58	270	2.3	34.222	35.184	-2.734	26.307	27.477	-4.257

Y_1 and Y_2 represent the predicted responses comprising the antimicrobial activity against *P. ananatis* and *P. stewartii*, respectively, while A, B, C, and D are independent variables values, namely pH, temperature (ºC), hydrolysis time (min) and enzyme-to-substrate ratio (% w/v).

Effective Inhibition Concentration of BTPH

The findings from this study indicated that BTPH exhibits significant antimicrobial properties. Table 6 shows that BTPH has notable antimicrobial activities, with low MICs against *P. ananatis* and *P. stewartii*. Specifically, the MIC values recorded were 250 µg/mL for *P. ananatis* and 500 µg/mL for *P. stewartii*. Additionally, the MBC for both bacterial strains was found to be 1000 µg/mL. This study's BTPH demonstrated stronger antimicrobial effects compared to those found in the past study on a peptide extracted from the mollusk *Babylonia spirata*, which showed antimicrobial activity against *Staphylococcus aureus* (1000 µg/mL) and

Aspergillus fumigatus (1000 µg/mL) (Kuppusamy & Ulagesan, 2016). The bactericidal properties of BTPH, with MBC and MIC values of ≤4, aligned with the prior findings suggesting that the antimicrobial efficacy of antimicrobial peptides (AMPs) is concentration-dependent (Arulrajah et al., 2021; Bondaryk et al., 2017). It has been reported that AMPs can disrupt intracellular activities, including inhibiting transcription (Lan et al., 2010; Zhang et al., 2008), translation (Kragol et al., 2001), and the synthesis of large molecules (Hsu et al., 2004; Patrzykat et al., 2002).

Table 6. The effects of *Bactronophorus thoracites* protein hydrolysates (BTPH) on antimicrobial activity, MIC, MBC, and bactericidal and bacteriostatic.

Sample	Microorganisms	Antimicrobial activity (%)	MIC (µg/mL)	MBC (µg/mL)	Bactericidal/ Bacteriostatic (MBC/MIC)
BTPH	*P. ananatis*	42.258±2.397	250	1000	Bactericidal
	P. stewartii	40.154±2.181	500	1000	Bactericidal
Control	*P. ananatis*	n.a	n.a	n.a	n.a
	P. stewartii	n.a	n.a	n.a	n.a

n.a = No activity; Control = *B. thoracites* crude extract; Antimicrobial activity were measured in percentage (%) and the values were expressed as mean ± standard error (SEM).

4. Conclusion

The present study effectively used RSM to optimize the enzymatic breakdown of *B. thoracites* protein. The ANOVA outcomes and the R^2 values (0.9893 for *P. ananatis* and 0.9848 for *P. stewartii*) underscored the reliability of our method. The quadratic models developed effectively highlighted the relationships between the factors adjusted and the resulting antimicrobial effects. The optimal conditions (pH 9.5, 55°C temperature, 240-minute hydrolysis time, and 2.05% enzyme/substrate ratio) matched the predictions, as the RSE was under 5%. This study also observed that the minimum concentrations needed to inhibit or kill the bacteria were 250 and 500 µg/mL. This result supports earlier research showing that BTPH's antimicrobial actions vary based on concentration. In conclusion, the produced hydrolysates showed potential as a natural defense against rice leaf blight, suggesting they could aid in disease control.

5. Acknowledgement

6. References

Adebo, O. A., Njobeh, P. B., Mulaba-Bafubiandi, A. F., Adebiyi, J. A., Desobgo, Z. S. C., Kayitesi, E. (2018). Optimization of fermentation conditions for ting production using response surface methodology, Journal of Food Processing and Preservation, 42(1): 13381.

Agrawal, S., Acharya, D., Adholeya, A., Barrow, C. J., Deshmukh, S. K. (2017). Nonribosomal peptides from marine microbes and their antimicrobial and anticancer potential, Frontiers in Pharmacology, 8(828): 1–26.

Amin, A. M., & Cheng, S. K. (2019). Optimization of enzymatic hydrolysis condition of angelwing clam (Pholas orientalis) meat using alcalase® to obtain maximum degree of hydrolysis, Malaysian Applied Biology, 48(3): 55–62.

Amin, A. M., Lee, W. S., and Sharmin, K. N. (2020). Optimisation of enzymatic hydrolysis conditions of seaweed (*Gracilaria fisheri*) protein by using Alcalase® to obtain maximum angiotensin-i-converting enzyme (ace) inhibitory activity, Malaysian Applied Biology, 49(5): 99-113.

Arulrajah, B., Muhialdin, B.J., Qoms, M.S., Zarei, M., Hussin, A.S.M., Hasan, H., Saari, N. (2021). Production of cationic antifungal peptides from kenaf seed protein as natural bio preservatives to prolong the shelf-life of tomato puree, International Journal of Food Microbiology, 359: 1-13.

Auwal, S. M., Zarei, M., Abdul-Hamid, A., Saari, N. (2017). Response Surface Optimisation for the Production of Antioxidant Hydrolysates from Stone Fish Protein Using Bromelain, Evidence-Based Complementary and Alternative Medicine 2017: 1-10.

Avila, C. (2006). Molluscan natural products as biological models: chemical ecology, histology, and laboratory culture, Progress in molecular and subcellular biology, 43:1-23.

Azizi, M. M. F., Ismail, S. I., Hata, E. M., Zulperi, D., Ina-Salwany, M. Y., Abdullah, M. A. F. (2019). First Report of *Pantoea stewartii* subsp. indologenes Causing Leaf Blight on Rice in Malaysia, Plant Disease, 103(6):1407.

Azizi, M. M. F., Zulperi, D., Rahman, M. A. A., Abdul-Basir, B., Othman, N. A., Ismail, S. I., Hata, E. M., Ina-Salwany, M. Y., Abdullah, M. A. F. (2019). First Report of *Pantoea ananatis* Causing Leaf Blight Disease of Rice in Peninsular Malaysia, Plant Disease, 103(8):2122.

Benkendorff, K. (2010). Molluscan biological and chemical diversity: Secondary metabolites and medicinal resources produced by marine molluscs, Biological Reviews, 85(4):757-775.

Benkendorff, K. (2014). Chemical diversity in molluscan communities: From natural products to chemical ecology. In: Neuroecology and Neuroethology in Molluscs: The Interface between Behaviour and Environment. Di Cosmo, A., Winlow, W., Eds.; Nova Scientific Publishers Inc.: New York, NY, USA. pp.13-41.

Bondaryk, M., Staniszewska, M., Zielińska, P., UrbańczykLipkowska Z. (2017). Natural antimicrobial peptides as inspiration for design of a new generation antifungal compounds, Journal of Fungi, 3(3): 1-36.

Bordbar, S., Ebrahimpour, A., Zarei, M., Hamid, A. A., Saari, N. (2018). Alcalase-generated proteolysates of stone fish (*Actinopyga lecanora*) flesh as a new source of antioxidant peptides, International Journal of Food Properties, 21(1):1541-1559.

Brearley A., Kashane C., Nopadon K. (2003). Pholadidae and Teredinidae (Mollusca: Bivalvia) collected from mangrove habitats on the Burrup Peninsula, Western Australia. In: Wells, F.E., Walker, D.I., Jones, D.S. (Eds.), Proceedings of the Eleventh International Marine Biological Workshop. Western Australian Museum, Perth. pp.345–361.

Charlet, M., Chernysh, S., Philippe, H., Hetru C., Hoffmann, J. A., Bulet, P. (1996). Isolation of several cysteine-rich antimicrobial peptides from the blood of a mollusk, *Mytilus edulis*, J Biol Chem, 271: 21808–21813.

Chukwu, S. C., Rafii, M. Y., Ramlee, S. I., Ismail, S. I., Hasan, M. M., Oladosu, Y. A., Magaji, U. G., Akos, I., Olalekan, K. K. (2019). Bacterial leaf blight resistance in rice: a review of conventional breeding to molecular approach, Molecular Biology Reports, 46(1):1519–1532.

Datta, A., Ghosh, A., Airoldi, C., Sperandeo, P., Mroue, K. H., Jimenez-Barbero, J., Kundu, P., Ramamoorthy, A., Bhunia, A. (2015). Antimicrobial peptides: Insights into membrane permeabilisation, lipopolysaccharide fragmentation and application in plant disease control, Scientific Reports, 5(11951):1-15.

Gogineni, V., Hamann, M. T. (2018). Marine natural product peptides with therapeutic potential: Chemistry, biosynthesis, and pharmacology, Biochimica et Biophysica Acta - General Subjects, 1862(1):81-196.

González, A. D., Franco, M. A., Contreras, N., Galindo-Castro, I., Jayaro, Y., Graterol, E. (2015). First report of *Pantoea agglomerans* causing rice leaf blight in Venezuela, Plant Disease, 99(4):552.

Gottipati, R., Mishra, S. (2010). Process optimisation of adsorption of Cr(VI) on activated carbons prepared from plant precursors by a two-level full factorial design, Chemical Engineering Journal, 160(1):99-107.

Hamed, S. M., Abd El-Rhman, A. A., Abdel-Raouf, N., Ibraheem, I. B. M. (2018). Role of marine macroalgae in plant protection & improvement for sustainable agriculture technology, Journal of Basic and Applied Sciences, 7(1):104-110.

Hamid, S. A., Halim, N. R. A., Sarbon, N. M. (2015). Optimization of enzymatic hydrolysis conditions of golden Apple Snail (*Pomacea canaliculata*) protein by Alcalase, International Food Research Journal, 22(4): 1615–1622.

Haslaniza, H., Maskat, M. Y., Wan Aida, W. M., Mamot, S. (2010). The effects of enzyme concentration, temperature and incubation time on nitrogen content and degree of hydrolysis of protein precipitate from cockle (*Anadara granosa*) meat wash water, International Food Research Journal, 17(1):147-152.

Hsu, S.T.D., Breukink, E., Tischenko, E., Lutters, M.A.G., De Kruijff, B., Kaptein, R., Bonvin, A.M.J.J., and Van Nuland, N.A.J. (2004). The nisin-lipid II complex reveals a pyrophosphate cage that provides a blueprint for novel antibiotics, Nature Structural and Molecular Biology, 11(10): 963 967.

Hubert, F. (1996). A member of the arthropod defensin family from edible Mediterranean mussels (*Mytilus galloprovincialis*), European Journal of Biochemistry, 240(1):302-306.

Jamal, S. N., Donny, D. A., Lamasudin, D. U. (2022). The Influence of Enzymatic Hydrolysis on Antimicrobial Activity Against Rice Pathogens from *Bactronophorus thoracites* (Shipworm) Protein Hydrolysate, Malay. J. Biochem. Mol. Biol., 25(3):47–57.

Jamal, S. N., Muhialdin, B. J., Saidi, N. B., Lai, K. S., Yusof, M. T., Lamasudin, D. U. (2022). The effect of lactic acid fermentation of *Bactronophorus thoracites* on antimicrobial activity against rice pathogens, Malaysian Journal of Microbiology, 18(6):592–601.

Jayaprakash, R., and Perera, C. O. (2020). Partial Purification and Characterisation of Bioactive Peptides from Cooked New Zealand Green-Lipped Mussel (*Perna canaliculus*) Protein Hydrolyzates, Foods, 9(7):1-19.

Kaspar, F., Neubauer, P., Gimpel, M. (2019). Bioactive Secondary Metabolites from *Bacillus subtilis*: A Comprehensive Review, Journal of Natural Products, 82(7):2038-2053.

Khan, J. A., Siddiq, R., Arshad, H. M. I., Anwar, H. S., Saleem, K., Jamil, F. F. (2012). Chemical control of bacterial leaf blight of rice caused by *Xanthomonas oryzae* pv. Oryzae, Pakistan Journal of Phytopayjology, 24(2):97-100.

Kragol, G., Lovas, S., Varadi, G., Condie, B.A., Hoffmann, R., Otvos, L. (2001). The antibacterial peptide pyrrhocoricin inhibits the ATPase actions of DnaK and prevents chaperone-assisted protein folding, Biochemistry, 40(10): 3016-3026.

Kuppusamy, A. Ulagesan, S. (2016). Antimicrobial activity of protein hydrolysate from marine molluscs *Babylonia spirata* (Linnaeus, 1758), Journal of Applied Pharmaceutical Science, 6(7): 73-77.

Lan, Y., Ye, Y., Kozlowska, J., Lam, J.K.W., Drake, A.F., Mason, A.J. (2010). Structural contributions to the intracellular targeting strategies of antimicrobial peptides, Biochimica et Biophysica Acta –Biomembranes, 1798(10): 1934-1943.

Lee, H. B., Hong, J. P., Kim, S. B. (2010). First Report of Leaf Blight Caused by *Pantoea agglomerans* on Rice in Korea, Plant Disease, 94(11):1372.

Lee, S. Y., Mohamed, R., Lamasudin, D. U. (2019). Morphology and molecular phylogenetic placement of a coastal shipworm (*Bactronophorus thoracites* (Gould, 1862), Teredinidae) from Peninsular Malaysia, Regional Studies in Marine Science, 29:100694.

Mitta, G., Hubert, F., Noël, T., Roch, P. (1999). Myticin, a novel cysteine-rich antimicrobial peptide isolated from haemocytes and plasma of the mussel *Mytilus galloprovincialis*, European Journal of Biochemistry, 265(1):71-78.

Mohamad Asri, N., Muhialdin, B. J., Zarei, M., Saari, N. (2020). Low molecular weight peptides generated from palm kernel cake via solid state lacto-fermentation extend the shelf life of bread, LWT, 134:110206.

Mondal, K. K., Mani, C., Singh, J., Kim, J.-G., Mudgett, M. B. (2011). A New Leaf Blight of Rice Caused by *Pantoea ananatis* in India, Plant Disease, 95(12):1582.

Muhialdin, B. J., Abdul Rani, N. F., Meor Hussin, A. S. (2020). Identification of antioxidant and antibacterial activities for the bioactive peptides generated from bitter beans (*Parkia speciosa*) via boiling and fermentation processes, LWT, 131: 109776.

Ngan, C. L., Basri, M., Lye, F. F., Fard Masoumi, H. R., Tripathy, M., Abedi Karjiban, R., Abdul-Malek, E. (2014). Comparison of Box-Behnken and central composite designs in optimisation of fullerene loaded palm-based nano-emulsions for cosmeceutical application, Industrial Crops and Products, 59:309-317.

Patrzykat, A., Friedrich, C.L., Zhang, L., Mendoza, V., Hancock, R.E.W. (2002). Sublethal concentrations of pleurocidin-derived antimicrobial peptides inhibit macromolecular synthesis in *Escherichia coli*, Antimicrobial Agents and Chemotherapy, 46(3): 605-614.

Robertsen, H. L., Musiol-Kroll, E. M. (2019). Actinomycete-derived polyketides as a source of antibiotics and lead structures for the development of new antimicrobial drugs, Antibiotics, 8(4):157.

Rosa, R. D., Santini, A., Fievet, J., Bulet, P., Destoumieux-Garzón, D., Bachère, E. (2011). Big defensins, a diverse family of antimicrobial peptides that follows different patterns of expression in hemocytes of the oyster *Crassostrea gigas*, PLoS ONE, 6(9):1-11.

Sarika, Iquebal, M. A., Rai, A. (2012). Biotic stress resistance in agriculture through antimicrobial peptides, Peptides, 36(2):322-330.

Sathoff, A. E., Velivelli, S., Shah, D. M., Samac, D. A. (2019). Plant defensin peptides have antifungal and antibacterial activity against human and plant pathogens, Phytopathology, 109(3):402-408.

Seema, R., Rajesh, B. (2015). Optimization of conditions for generation of antimicrobial peptides from milk proteins by Lactobacillus spp., African Journal of Microbiology Research, 9(24)1: 573-1585.

Seo, J. K., Lee, M. J., Jung, H. G., Go, H. J., Kim, Y. J., Park, N. G. (2014). Antimicrobial function of SHβAP, a novel hemoglobin β chain-related antimicrobial peptide, isolated from the liver of skipjack tuna, *Katsuwonus pelamis*, Fish and Shellfish Immunology, 37(1):173-183.

Sharma, Arun, Sharma, R., Imamura, M., Yamakawa, M., Machii, H. (2000). Transgenic expression of cecropin B, an antibacterial peptide from Bombyx mori, confers enhanced resistance to bacterial leaf blight in rice, FEBS Letters, 484(1):7-11.

Sila, A., Bougatef, A. (2016). Antioxidant peptides from marine by-products: Isolation, identification and application in food systems. A review, Journal of Functional Foods, 21:10-26.

Sundin, G. W., Wang, N. (2018). Antibiotic resistance in plant-pathogenic bacteria, Annual Review of Phytopathology, 56:1-20.

Toh, W. K., Loh, P. C., Wong, H. L. (2019). First report of leaf blight of rice caused by Pantoea ananatis and *Pantoea dispersa* in Malaysia, Plant Disease, 103(7):1764.

Turner, R. D. (1966). A survey and illustrated catalogue of the Teredinidae (Mollusca: Bivalvia). In: A survey and illustrated catalogue of the Teredinidae (Mollusca: Bivalvia). pp.265.

Valarmathi, P. (2020). Antibiotics- A Miracle Drug as Crop Protectants: A Review, Agricultural Reviews, 41:43-50.

Wang, X., Yu, H., Xing, R., Chen, X., Liu, S., Li, P. (2017). Optimization of the extraction and stability of antioxidative peptides from mackerel (*Pneumatophorus japonicus*) protein, BioMed Research International, 2017: 1-14.

Zainol, M. K., Abdul Sukor, F. W., Fisal, A., Tuan Zainazor, T. C., Abdul Wahab, M. R., Zamri, A. I. (2021). Optimisation of enzymatic protein hydrolysis conditions of Asiatic hard clam (*Meretrix meretrix*), Food Research, 5(4):153 - 162.

Zakaria, F., Tan, J. K., Mohd Faudzi, S. M., Abdul Rahman, M. B., Ashari, S. E. (2021). Ultrasound-assisted extraction conditions optimisation using response surface methodology from *Mitragyna speciosa* (Korth.) Havil leaves, Ultrasonics Sonochemistry, 81: 105851.

Zhang, J., Wu, X., Zhang, S.Q. (2008) Antifungal mechanism of antibacterial peptide, ABP-CM4, from *Bombyx mori* against *Aspergillus niger*, Biotechnology Letters, 30(12): 2157-2163.

HYDROTHERMAL SYNTHESIS OF NITROGEN-DOPED CQDS OF RUBUS NIVEUS LEAVES FOR FLUORESCENT pH SENSING AND PHOTOCATALYTIC APPLICATIONS

P. Negi[1a], B.S. Rawat[2b]*, N. C. Joshi[3c], W. Ahmad[4d], N. Kumar[5b], S. Upadhyay[6e], K. P. S. Parmar[7f], R. Saxena[8g], R. Dhyani[9h], P. S. Khati[10i], A.S. Rana[11j]

Abstract: The development of a fluorescent pH sensor and the treatment of wastewater with nanoparticles are both critical topics. Variations in pH impact the morphology and subsequent properties of nanoparticles, affecting their utilization in various fields, while using nanoparticles offers an improved approach for treating industrial waste. The present study examines the effects of these variables on biologically produced nitrogen-doped carbon quantum dots (NCQDs). The synthesis was achieved through a hydrothermal process using *Rubus niveus* leaf extract as a precursor. UV-Vis spectroscopy analysis revealed absorption spectra over a wide range from 200 nm to 800 nm, with prominent peaks at 236 nm and 392 nm. Additionally, the direct energy band gap of the NCQDs was found to be 3.65 eV. SEM imaging displayed flower-shaped particles, and FT-IR analysis indicated the presence of amide, CHO, N-H, and C-N functional groups. The XRD pattern revealed that the surface morphology of NCQDs is amorphous in nature. A significant response in fluorescence intensity with varying pH values was observed, confirming the potential of NCQDs as pH sensors. The reaction kinetics of Rhodamine-B (Rh-B) dye was analyzed to assess the potential of NCQDs for dye degradation, revealing pseudo-first-order kinetics with a correlation coefficient of 0.80.

Keywords: hydrothermal process, pH sensor, carbon quantum dots, energy band gap, dye degradation.

1. Introduction

Carbon quantum dots (CQDs) are emerging as a promising alternative to inorganic semiconductor materials due to their potential applications in various fields (Wang et al., 2016; Das et al., 2015; Bourlinos et al., 2013). Research highlights that low-toxicity, biocompatible, and chemically stable CQD materials are useful in drug delivery (Jallel et al., 2018), optoelectronics (Hoan et al., 2019), water treatment (Shamsipur et al., 2014),

bioimaging, biomolecules (Ge et al., 2022; Basavaiah et al., 2018), and metal ion sensors (Barati et al., 2016).

The hydrothermal carbonization method is recognized as a green synthetic approach for creating CQDs. Significant efforts have been made to develop CQD fluorescent probes for metal ion detection and other applications (Du et al., 2013; Wang et al., 2011; Lin et al., 2012; Liu et al., 2012; Salinas-Castillo et al., 2013; Mosconi et al., 2015; Pires et al., 2015).

Doped CQDs offer tunable fluorescence and excellent surface passivation. The incorporation of heteroatoms, such as nitrogen, phosphorus, and sulphur, enhances the optical properties of these particles (Carolan et al., 2017). Nitrogen-doped CQDs, in particular, interact with carbon atoms by trapping radiating electron-hole pairs, forming new optical centres, and exhibiting exceptional performance in optoelectronic, electro catalytic and luminescent applications. Carbon-bonded nitrogen introduces disorder into the hexagonal carbon rings (Li et al., 2012; Krysmann et al., 2012). The advantages of CQDs over organic fluorescent dyes include their biocompatibility, low synthesis cost, electron transmission capability, water solubility, and ease of manufacture (Qu et al., 2010; Xiao et al., 2018; Zhang et al., 2016).

pH imbalances can cause various disorders by affecting the activity of several organelles, making precise measurement of intracellular pH crucial. Various materials, such as quantum dot-encoded red fluorescent protein sensors (Tantama et al., 2011), Ag@SiO2 core-shell nanoparticles (Bai et al., 2013),

Authors information:

[a]Department of Chemistry, GRD Institute of Management & Technology, Dehradun, UK, INDIA.
[b]Department of Physics, School of Applied and Life Sciences (SALS), Uttaranchal University, Dehradun-248007, UK, INDIA.
[c]Division of Research and Innovation, Uttaranchal University, Dehradun-248007, UK, INDIA.
[d]Department of Chemistry, Graphic Era University, Dehradun, UK, INDIA.
[e]Department of Allied Health Sciences, School of Health Sciences and Technology, University of Petroleum and Energy Studies, UPES, Dehradun-248007, UK, INDIA.
[f]Department of Physics, University of Petroleum and Energy Studies, UPES, Dehradun-248007, UK, INDIA.
[g]Department of Physics, Shri Guru Ram Rai University, Dehradun-248007, UK, INDIA.
[h]Department of Applied Science, Women Institute of Technology, Dehradun, 248007, INDIA.
[i]Department of Chemistry, S.D.M. PG. College Doiwala, Dehradun-248007, UK, INDIA.
[j]Department of Physics, Shri Guru Ram Rai (P.G.) College, Dehradun-248007, UK, INDIA.
*Corresponding Author: park_bhupendra@hotmail.com

semiconducting polymer dots (Chan et al., 2011), and fluorescent quantum FRET probe dots (Dennis et al., 2012), have been developed for pH monitoring. However, these materials have limitations including bulkiness, severe toxicity, and biocompatibility issues. In contrast, CQDs have emerged as excellent candidates for pH testing due to several advantages (Han et al., 2010; Jin et al., 2010; Nie et al., 2014).

Moreover, prior studies have demonstrated that the presence of H⁺ or OH⁻ ions affects the morphology of biosynthesized metal oxide nanoparticles (Zyoud et al., 2019). Changes in pH significantly impact the hydrolysis and condensation processes during the formation of the precursor solution (Arya et al., 2021). These pH fluctuations similarly influence the morphology and characteristics of biosynthesized nanoparticles, including their optical properties (Khairol et al., 2018). Recently, various plant parts have been shown to act as reducing and capping agents to create eco-friendly, non-toxic nanoparticles for diverse applications (Sathish kumar et al., 2012; Su et al., 2012; Su et al., 2005).

Rubus niveus, locally known as Kala Hisar or Mysore raspberries, is a large, spiny shrub that commonly grows along highways, in woodlands, and in mountainous regions between 1000 and 2500 m. It is noted for its antibacterial, anticancer, wound-healing, and anti-inflammatory properties. The phytochemicals responsible for these unique qualities include saponins, tannins, flavonoids, phenols, and sugars (Blassan et al., 2014; Mullen et al., 2002).

The current study focuses on the synthesis of nitrogen-doped carbon quantum dots (NCQDs) from *Rubus niveus* leaves and examines their characteristic properties, including their capacity for photocatalytic degradation and fluorescent pH sensing.

2. Experimental Methods

Fresh *Rubus niveus* leaves were collected from a location near the campus of Uttaranchal University. We employed ethylenediamine and rhodamine-B without further purification. Double-distilled to conduct the experiments

3. Synthesis of NCQDs

The synthesis of nitrogen-doped carbon quantum dots (NCQDs) was performed using a single-step hydrothermal method (Fig. 1). Initially, the leaves were collected, washed with tap water, followed by deionized (DI) water to remove dust, and then dried in an incubator at ambient conditions. Subsequently, 5 g of the dried leaves were combined with approximately 60 ml of water and heated to 200 °C for 2 hours in a Teflon-lined autoclave. After this, 1.5 ml of ethylenediamine was added to 15 ml of the resulting carbon quantum dot (CQD) solution, which was then subjected to further heating at 200 °C for an additional 3 hours. Centrifugation was performed for about 45 minutes to remove large particles from the solution, followed by filtration using micro-level filter paper. The final solid product was obtained by drying at 75 °C.
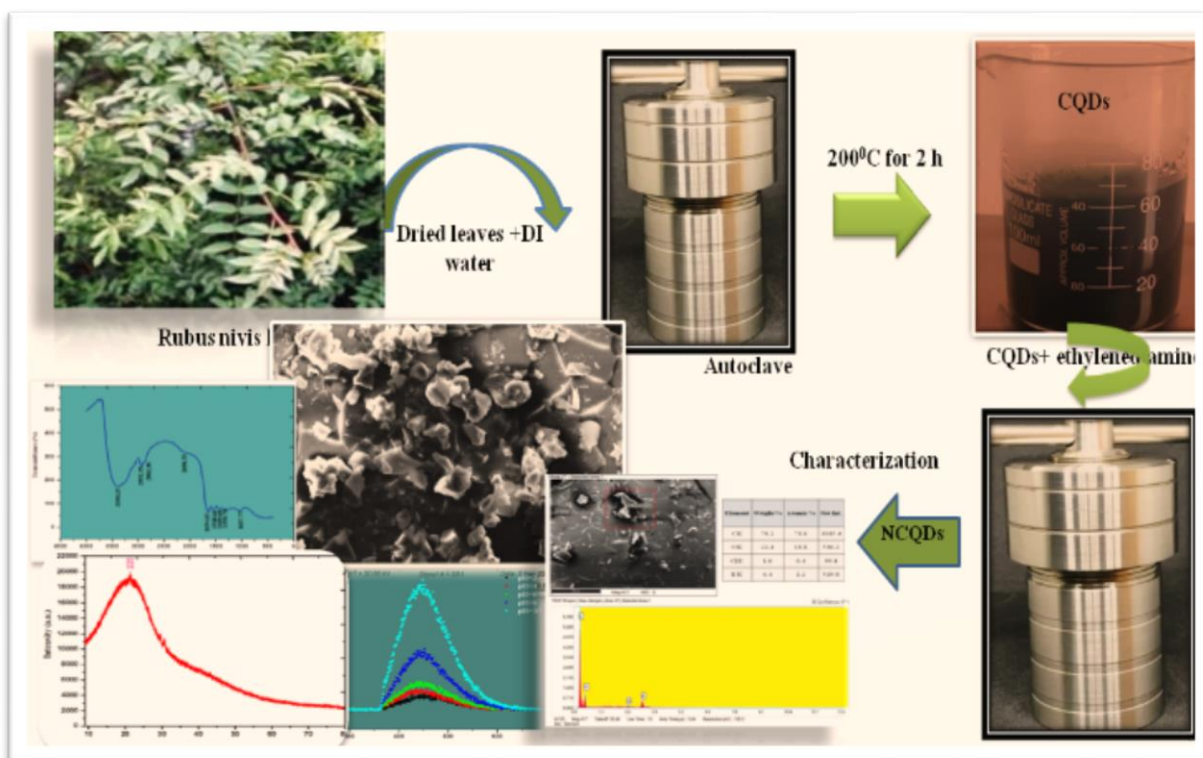

Figure 1. Schematic of the synthesis of NCQDs

4. Characterizations

UV-Vis spectral analysis, Scanning Electron Microscopy (SEM), Fourier Transform Infrared Spectroscopy (FTIR), Energy Dispersive X-ray Spectroscopy (EDX),and the X-ray powder diffraction (XRD) method were employed to describe the powder morphology of NCQDs.

Optical Properties Analysis

Analyses of absorption peaks, spectral ranges, and energy band gaps were conducted at room temperature (Fig. 2). The absorption bands were observed at 236 nm and 392 nm, with the spectral range spanning from 200 nm to 800 nm. To estimate the indirect optical energy band gap, the absorption spectrum was analyzed with reference to the absorption edge using the Tauc equation (Tauc et al., 1966), a methodology well-documented in the literature (Muhammad et al., 2011; Yakuphanoglu et al., 2005). Theenergy band gap value estimation was performed by plotting $(\alpha h v)^2$ versus photon energy $hv$and found to be 3.65eV.
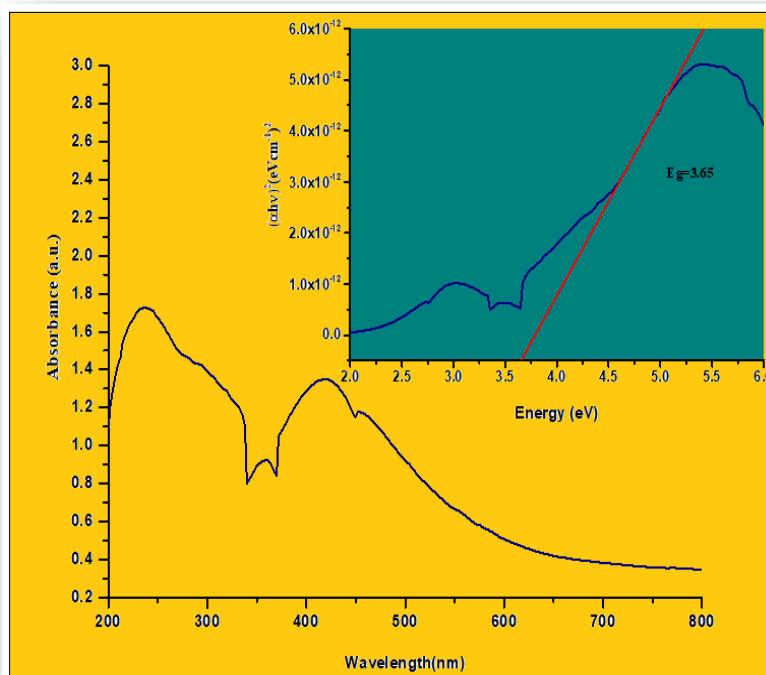
Figure 2. Plot of absorbance versus wavelength and $(\alpha h v)^2$ versus hv
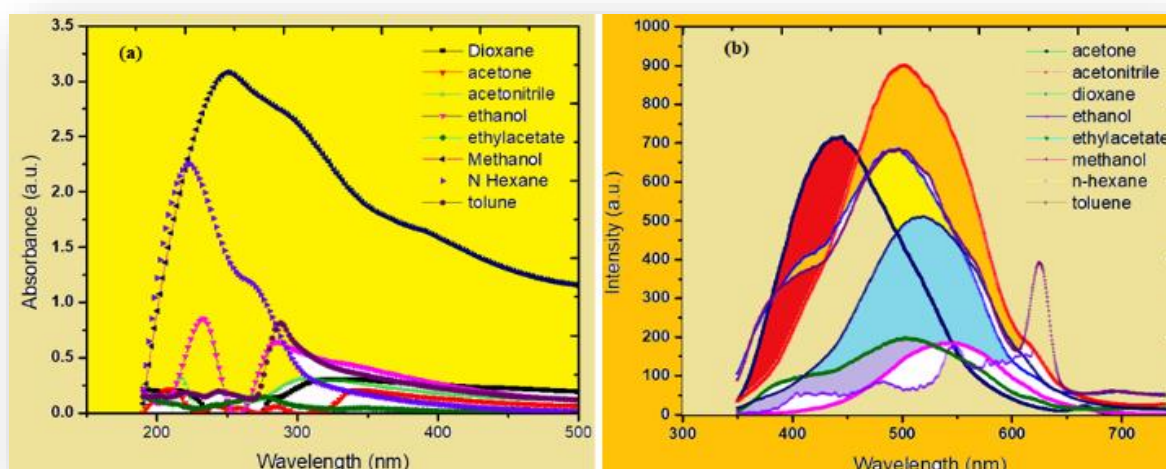
Figure 3. Plot of (a) absorbance and (b) emission versus wavelength in different solvents

The photophysical properties of NCQDs were investigated and are illustrated in Figure 3. The plots of (a) absorbance versus wavelength and (b) emission versus wavelength demonstrate the shift in peaks due to the use of different solvents, highlighting the Solvatochromic effect of the synthesized particles (Khazan et al., 2017; Dash et al., 1999). For solvents such as toluene, ethanol, dioxane, and methanol, the peaks shift towards longer wavelengths, indicating a bathochromic shift. Conversely, a hypsochromic shift is observed with ethyl acetate and acetone, with N-hexane used as the reference solvent.

The solvent-dependent shifts are attributed to the solvents' polarity and hydrogen bonding, which influence the fluorescent molecules' electronic transitions and energy levels. These findings suggest potential advantages for a broad range of industrial and technological applications.

SEM and EDX Analysis

The surface characteristics and morphological properties of NCQDs were examined using scanning electron microscopy (SEM). The SEM images of the NCQDs synthesized *from Rubus niveus* revealed flower-shaped particles with some degree of agglomeration (Fig. 4a). The observed agglomeration may be attributed to the sample preparation process.
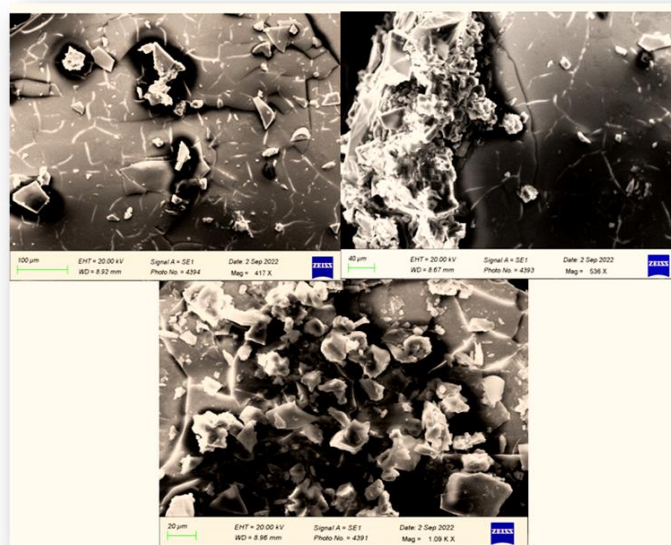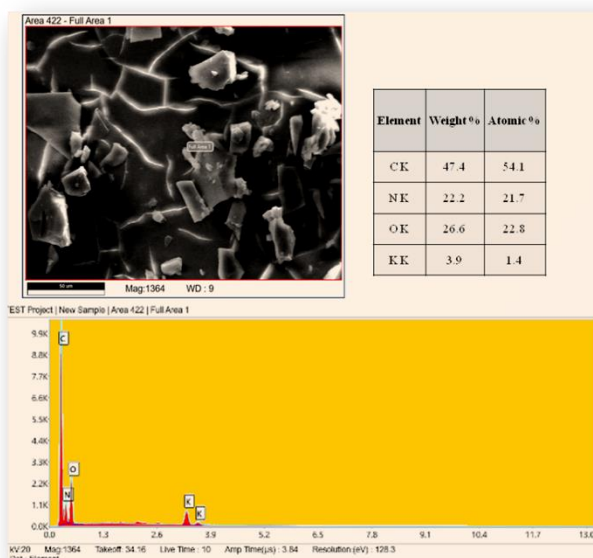

Figure 4(a). SEM morphology of NCQDs

Element	Weight %	Atomic %
CK	47.4	54.1
NK	22.2	21.7
OK	26.6	22.8
KK	3.9	1.4

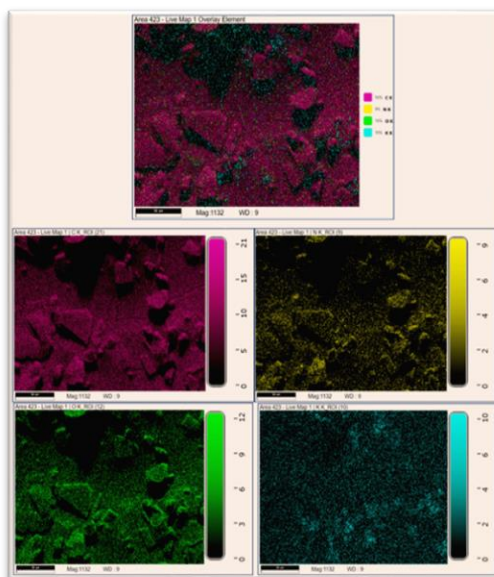**Figure 4 (b).** EDX spectrum of NCQDs

Figure.4 (b). Mapping of elements present in NCQDs

The EDX spectrum for analyzing the chemical composition of NCQDs is presented inFigure4b. The graph displays the weight and atomic percentages of the four main elements: C, N, O, and K. The presence of both carbon and nitrogen indicates successful incorporation of nitrogen into the CQDs. The detection of potassium is attributed to an incomplete washing process, which could be improved by washing with double distilled water and ethanol before drying the material. The figure shows that carbon constitutes the largest weight percentage. The presence of these elements without significant impurities confirms the purity of the synthesized NCQDs (Selva Raja et al., 2015). Elemental mapping reveals a uniform distribution of these materials throughout the synthesized NCQDs, as shown in Figure 4b.

Functional Groups Analysis

The presence of functional groups on the surface of NCQDs, which act as reducing agents during their synthesis, was investigated using FTIR analysis. A prominent peak in the FTIR spectrum (Fig. 5) at 3390 cm^{-1} corresponds to the N-H stretching vibration of secondary amines, indicating the presence of amino functional groups (Chang et al., 2022). The bands at 2932 cm^{-1} are attributed to the Fermi resonance-induced C-H stretching of aldehydes.

The C=O stretching of the amide group resultsinabandat1650cm^{-1}, while the N-H bending vibration of the amide is reflected in a troughat1548 cm^{-1}. The C-N stretching vibration of the amine is responsible for the peaks at 1350 and 1037 cm^{-1}, confirming the successful incorporation of nitrogen into the carbon dots. Furthermore, the FTIR data also verifies that the CQDs are doped with nitrogen. The presence of these functional groups, which also act as stabilizers, underscores their role in the formation of NCQDs, as observed in the plant extract.
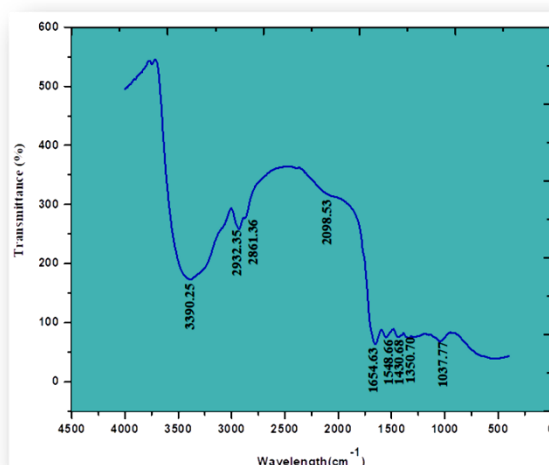

Figure 5. FT-IR spectrum for synthesized NCQDs

Crystallographic Structure Analysis

Figure (6) depicts the NCQDs' acquired XRD pattern. Comparison of the XRD pattern to the typical JCPDS card no. 00-039-1405 reveals a large and powerful diffraction peak at $2\theta=21.367$ with a hkl value of 220. This shows that synthesized NCQDs are amorphous.
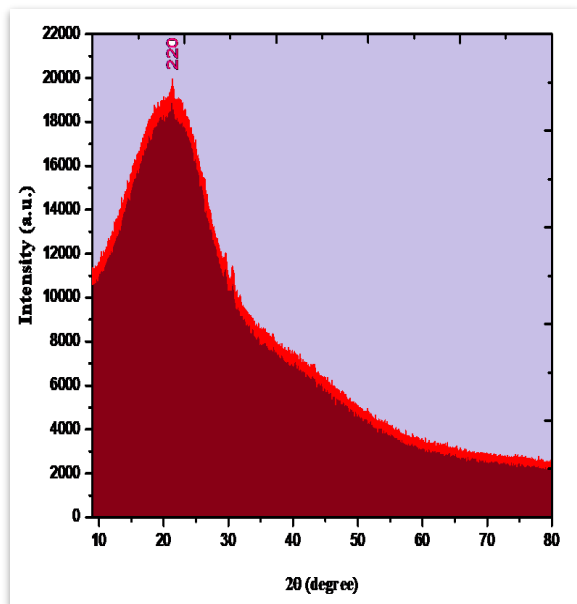

Figure 6.XRD diffractogarm for synthesized NCQDs

Analysis of p Effect on Fluorescence Emission

Figure 7a shows the produced samples, while Figure 7b illustrates the measured fluorescence intensity of solutions at various pH values. The significant shift in fluorescence intensity with wavelength, observed as the pH value changes from 2 to 10, can be explained by the numerical excitation wavelength value of the sample at 260 nm. The plot of fluorescence intensity versus pH (Figure 7c), which yields a linear correlation coefficient of 0.771, further supports this association. This demonstrates that the proposed NCQDs are promising candidates for pH measurement applications.
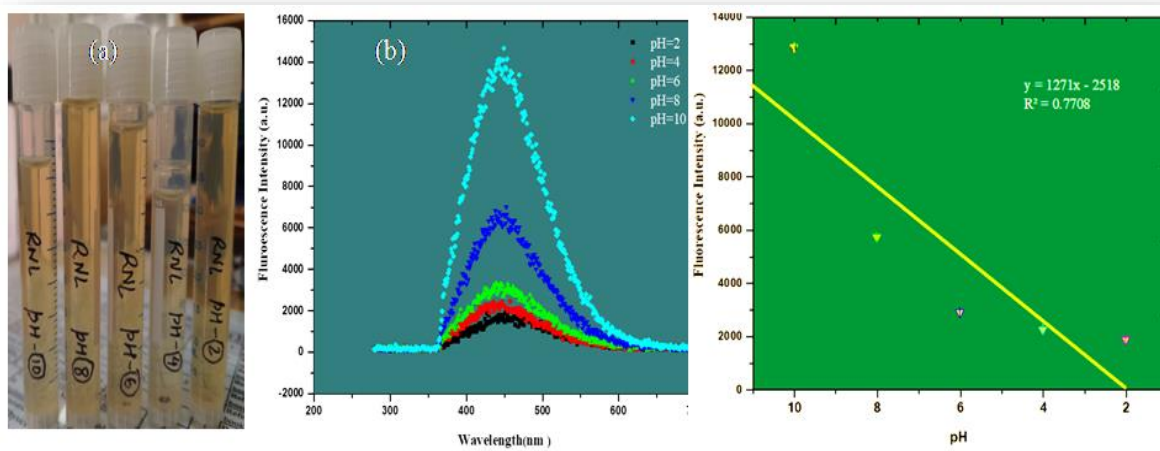

Figure 7.(a) Prepared pH samples**(b)**Intensity of fluorescence versus wavelength **(c)**Intensity versus pH values

Photocatalytic Activity

Their photocatalytic activity was evaluated under UV-visible light to assess the potential of the biosynthesized NCQDs for degrading Rhodamine-B dye. During the experiment, a solution with a fixed concentration of the dye was used, and the procedure was conducted without stirring the sample. The degradation of the dye concentration was monitored at 20-minute intervals using the peak of the pure dye as a benchmark. The results indicate that the dye concentration decreases gradually, though not significantly, over time (Figure 8b).
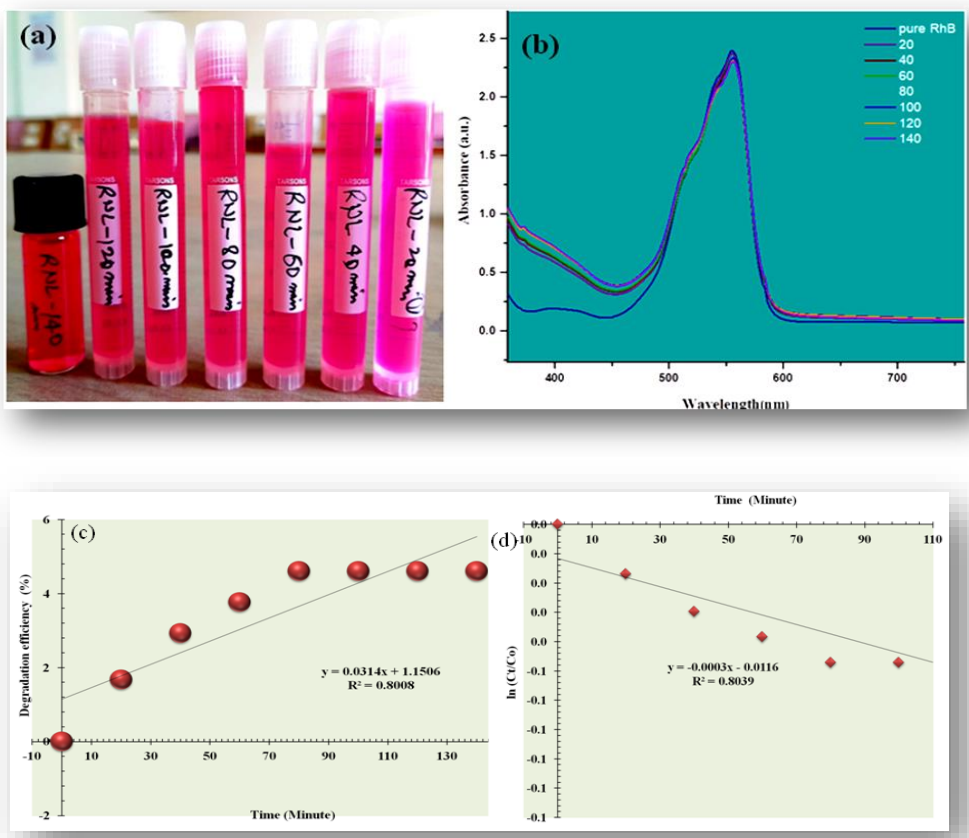
18

Figure 8. (a) Prepared samples of Rh-B dye **(b)** Plot of absorbance versus wavelength **(c)** Photocatalytic degradation efficiency of dye and **(d)** Kinetic results for the degradation of dye

Figure(8c) illustrates the variation in photocatalytic degradation efficiency over time. The kinetics of the degradation process was analyzed to determine the photocatalytic decolourization's rate constant and correlation coefficient. The correlation coefficient was found to be approximately 0.80, and the reaction rate constant was determined to be 0.003min⁻¹ (Figure8d).

degradation was determinedtobe0.80, indicating its suitability for photocatalytic applications, with potential for further enhancement through additional treatment.

5. Conclusion

Rubus niveus was utilized as the carbon source, and ethylenediamine was employed to introduce nitrogen in the hydrothermal method, successfully synthesizing NCQDs. Characterization revealed the fluorescence properties, presence of functional groups, and amorphous structure of the NCQDs. The study demonstrated that this biocompatible material can produce highly fluorescent particles. Additionally, the fluorescence intensity varied with pH, confirming the potential of NCQDs as pH sensors. The correlation coefficient for Rhodamine dye

6. Funding

7. Acknowledgement

8. Conflicts of Interest

The author(s) declare(s) that there is no conflict of interest regarding the publication of this paper

5. References

AryaS., MahajanP., MahajanS., KhoslaA., DattR., GuptaV., YoungS.-J., OrugantiS.K.(2021). Review-Influence of Processing Parameters to Control Morphology and Optical Properties of Sol-Gel Synthesized ZnO Nanoparticles. ECS J. Solid State Sci. Technol.10:23002. doi:10.1149/ 2162-8777/abe095

BaiZ. H., ChenR., SiP., HuangY. J., SunH. D., KimD. H. (2013). Fluorescent pH Sensor Based on Ag@SiO$_2$ Core-Shell Nanoparticle, ACS Applied Materials & Interfaces, 5(12): 5856-5860.

Barati A., Shamsipur M., Abdollahi H. (2016). Metal-ion-mediated fluorescent carbon dots for indirect detection of sulfide ions, Sens. Actuator B: Chem. 230: 289–297.

Basavaiah K., Tadesse A., Ramadevi D., Hagos M., Battu G.(2018).Facile green synthesis of fluorescent carbon quantum dots from citrus lemon juice for live cell imaging, Asian, J. Nanosci. Mater 1:36–46.

Blassan G., Thangaraj P., Sajeesh T., Saravanan S. (2014). Antitumor and wound healing properties of *Rubus niveus* Thunb root. J Environ Pathol Toxicol Oncol.33 (2): 145-158.

Bourlinos A.B., Karakassides M.A., Kouloumpis A., Gournis D., Bakandritsos A., Papagiannouli I. , Aloukos P., Couri S., Hola K., Zboril R., Krysmann M., Giannelis E.P. (2013). Synthesis, characterization and non-linear optical response of organophilic carbon dots, Carbon 61: 640–646.

Carolan D., Rocks C., Padmanaban D.B., Maguire P., Svrcek V., Mariott D.(22017). Environmentally friendly nitrogen-doped carbon quantum dots for next generation solar cells Sustain. Energy Fuels 1:1611–1619.

Chan Y.H., Wu C.F., Ye F.M., Jin Y.H., Smith P.B., Chiu D.T. (2011). Development of Ultrabright Semiconducting Polymer Dots for Ratiometric pH Sensing, Anal. Chem. 83(4): 1448–1455.

Chang K., Zhu Q., Qi L., Guo M., Gao W., Gao Q. (2022). Synthesis and Properties of Nitrogen-Doped Carbon Quantum Dots Using Lactic Acid as Carbon Source. *Materials*. 15(2), 466. https://doi.org/10.3390/ma15020466

Cui L., Ren X., Sun M., Liu H., Xia L. (2021).Carbon Dots: Synthesis, Properties and Applications,Nanomaterials (Basel)11: 3419.

Das B., Dadhich P., Pal P., Srivas P.K., Bankoti K., Dhara S.J. (2014).Carbon nanodots from date molasses: new nanolights for the *in vitro* scavenging of reactive oxygen species, Mater. Chem. B, 2: 6839–6847.

Dash U.N., Dash M.C. (1999). The effect of solvent polarity on the absorption and fluorescence of rhodamine dyes: a linear salvation energy relationship analysis. Journal of Luminescence 82(3): 169-180

DennisA.M., RheeW.J., SottoD., DublinS.N., BaoG. (2012).Quantum Dot–Fluorescent Protein FRET Probes for Sensing Intracellular pH, ACS Nano 6(4):2917–2924.

Dsouza, S. D. (20221). The importance of surface states in N-doped carbon quantum dots. Carbon, 183: 1–11. doi.org/10.1016/j.carbon.2021.06.088 0008

Du F., Zeng F., Ming Y., Wu S. (2013). Carbon dots-based fluorescent probes for sensitive and selective detection of iodide, Microchim. Acta 180:453-460.

Ge G. , Li L., Chen M., Wu X., Yang Y., Wang D., Zuo S., Zeng Z., Xiong W., Guo C. (2022). Green Synthesis of Nitrogen-Doped Carbon Dots from Fresh Tea Leaves for Selective Fe^{3+} Ions Detection and Cellular Imaging, Nanomaterials (Basel):12: 986.

HanJ.Y., BurgessK. (2010). Fluorescent Indicators for Intracellular pH, Chem. Rev. 110: 2709–2728.

Hoan B.T., Tam P.D., Pham V.H. (2019). Green Synthesis of Highly Luminescent Carbon Quantum Dots from Lemon Juice, J. Nanotechnol2019: 1–9.

Jallel J. A., Pramod K. (201). Artful and multifaceted applications of carbon dot in biomedicine, J. Control. Release 269: 302–321.

JinT., SasakiA., KinjoM., MiyazakiJ. (2010). A quantum dot-based ratiometric pH sensor, Chem. Commun. 46: 2408–2410.

KhairolN.F., SapaweN. (2018). Electrosynthesis of ZnO nanoparticles deposited onto egg shell for degradation of Congo red. Mater. Today Proc. 5: 21936–21939.

Khazan, A., Mohammadi A.H., Alimohammadi Z. (2017). Effects of solvent polarity on the absorption and fluorescence spectra of β-carotene in various solvents: A solvatochromic study. Journal of Luminescence 191: 89-95.

Kou, X., Jiang, S., Park, S. J., Meng, L. Y. (2020). A review: Recent advances in preparations and applications of heteroatom-doped carbon quantum dots. Dalton Trans. 49: 6915–6938.

KrysmannM.J., KelarakisA., DallasP., GiannelisE.P. (2012). Formation mechanism of carbogenic nanoparticles with dual photoluminescence emission, J. Am. Chem. Soc. 134:747–750.

LiY., ZhaoY., ChengH.H., HuH.H., ShiG.Q., DaiL.M., QuL.T.(2012). Nitrogen-doped graphene quantum dots with oxygen-rich functional groups, J. Am. Chem. Soc. 134:15–18.

Lin Z., Xue W., Chen H., Lin J.M. (22012). Classical oxidant induced chemiluminescence of fluorescent carbon dots, Chem. Commun. 48 (7). 1051e1053. doi: 10.1039/c1cc15290d

Liu C., Zhang P., Tian F., Li W., Li F., Liu W. (2011). One-step synthesis of surface passivated carbon nanodots by microwave assisted pyrolysis for enhanced multicolor photoluminescence and bioimaging, J. Mater. Chem. 21: 13163-13167.

Mosconi D., Mazzier D., Silvestrini S., Privitera A., Marega C., Franco L., Moretto A.(2015). Synthesis and photochemical applications of processable polymers enclosing photoluminescent carbon quantum dots, ACS Nano 9: 4156-4164.

Muhammad F.F., Sulaiman K. (2011). Utilizing a simple and reliable method to investigate the optical functions of small molecular organic flms-Alq3 and Gaq3 as examples. Measurement 44:1468–1474.

Mullen W., McGinn J., Lean M.J., MacLean M.R., Gardiner P., Duthie G.G.(2002). Ellagitannins, flavanoids, and other phenolics in red raspberries and their contribution to antioxidant capacity and vasorelaxation properties. J Agri Food Chem. 50:5191–6.

NieH., LiM.J., LiQ.S., Liang S.J., TanY.Y., ShengL. (2014).Carbon Dots with Continuously Tunable Full-Color Emission and Their Application in Ratiometric pH Sensing, Chem. Mater. 26(10): 3104–3112. doi.org/10.1021/cm5003669

Pancholi B., RanaA.C. (2020). Traditional Uses, Phytochemistry and Pharmacological Aspects of *Rubus niveus* thumb Plant – A Review The J.ournal of Phytopharmacology 9(6): 438-444.

Pires N.R., SantosC.M.W., SousaR.R., de PaulaR.C.M., CunhaP.L.R., FeitosaJ.P.A. (2015). Novel and fast microwave-assisted synthesis of carbon quantum dots from raw cashew gum, J. Braz. Chem. Soc. 26:1274-1282.

QuL.T., Liu V, BaekJ.B., DaiL.M. (2010). Nitrogen-doped graphene as efficient metal-free electrocatalyst for oxygen reduction in fuel cells, ACS Nano. 4:1321–1326.

Raja S., Ramesh V., Thivaharan V. (2015). Green biosynthesis of silver nanoparticles using calliandra haematocephala leaf extract, their antibacterial activity and hydrogen peroxide sensing capability, Arabian J. Chem. DOI: 10.1016/j.arabjc.2015.06.023.

Rooj B., Dutta A., Islam S., Mandal U. (2018). Green Synthesized Carbon Quantum Dots from Polianthes tuberose L. Petals for Copper (II) and Iron (II) Detection, J. Fluoresc 28: 1261–1267.

Salinas-Castillo A., Ariza-Avidad M., Pritz C., Camprubí-Robles M., Fern andez B., Ruedas-Rama M.J., Megia-Fernandez A., Lapresta-Fern andez A., Santoyo-Gonzalez F., Schrott-Fischer A., Capitan-Vallvey L.F. (2013). Carbon dots for copper detection with down and upconversion fluorescent properties as excitation sources, Chem. Commun. 49: 1103-1105.

Sathishkumar G., Gobinath C., Karpaga K., Hemamalini V., Premkumar K., Sivaramakrishnan S. (2012). Phyto-synthesis of silver nanoscale particles using Morinda citrifolia L. and its inhibitory activity against human pathogens, Colloids Surf., B. 95:235-240.

Shamsipur M., Rajabi H. (2014). Pure zinc sulfide quantum dot as highly selective luminescent probe for determination of hazardous cyanide ion, Mater. Sci. Eng. C 36: 139–145.

SinghR., Dutta S. (2018). Synthesis and characterization of solar photoactive TiO2 nanoparticles with enhanced structural and optical properties, Adv. Powder Technol. 29: 211–219.

Su B.N., Pawlus A.D., Jung H.A., Keller W.J., McLaughlin J.L., Kinghorn A. D. (2005). Chemical Constituents of the Fruits of Morinda citrifolia (Noni) and their antioxidant Activity, J. Nat. Prod. 68:592-595.

TantamaM., HungY.P., YellenG.J.(2011).Imaging Intracellular pH in Live Cells with a Genetically Encoded Red Fluorescent Protein Sensor, Am. Chem. Soc. 133: 10034-10037.

Tauc J., Grigorovici R., Vancu A. (1966). Optical properties and electronic structure of amorphous germanium. Physica status solidi (b), 15:627-637.

Wang H., Sun P., Cong S., Wu J., Gao L., Wang Y., Dai X., Yi Q., Zou G. (2016).Nitrogen-Doped Carbon Dots for "green" Quantum Dot Solar Cells, Nanoscale Res. Lett., 11: 1–6.

Wang X., Qu Q., Xu B., Ren J., Qu X. (2011). Microwave assisted one-step green synthesis of cell-permeable multicolor photoluminescent carbon dots without surface passivation reagents, J. Mater. Chem. 21: 2445-2450.

XiaoL., SunH. (2018). Novel properties and applications of carbon nanodots, Nanoscale Horizons, 3(6): 565–597.

Yakuphanoglu F., Erten H. (2005). Refractive index dispersion and analysis of the optical constants' of an ionomer thin flm. Opt Appl 35(4):969.

ZhangJ., YuS.-H. (2016). Carbon dots: large-scale synthesis, sensing and bioimaging, Mater. Today 19(7):382–393.

ZyoudA.H., ZubiA., ZyoudS.H., HilalM.H., ZyoudS., QamhiehN., HajamohideenA., HilalH.S.(2019). Kaolin-supported ZnO nanoparticle catalysts in self-sensitized tetracycline photodegradation: Zero-point charge and pH effects. Appl. Clay Sci. 182, 105294. doi:10.1016/j.clay.2019.105294

GREEN ROUTE SYNTHESIS OF COPPER OXIDE (CuO) NANOPARTICLES FOR THE DEGRADATION OF COMMERCIAL DYES USING *VICIA FABA* LEAF EXTRACT

P. Rastogi[1a], P. Negi[2b*], B. S. Rawat[3a], N. C. Joshi[4d]

Abstract: The release of toxic dyes into water effluents by various industries has become a global concern. Therefore, developing novel, straightforward, and economically viable methods or materials for purifying these hazardous pigments is imperative. This study aims to synthesize copper oxide nanoparticles (CuO-NPs) through a green route using *Vicia faba* leaf extract. UV-Vis spectroscopy reveals an absorption band ranging from 200 nm to 300 nm, with a major absorption peak at 212 nm and an energy band gap of 5.29 eV. FTIR, SEM, EDX, and XRD techniques characterise the synthesised CuO nanoparticles. FTIR analysis identifies functional groups including hydroxyl (OH), aromatic C-H, C=C stretching, carbonyl (C=O), and Cu-O stretching vibrations. Scanning electron microscopy reveals flower-like particles, while EDX analysis confirms the formation of CuO nanoparticles. The XRD pattern indicates a crystalline structure with an average particle size of 27.44 nm. A plot of $(\alpha h v)^2$ versus photon energy (hv) was generated to determine the energy band gap, yielding a value of 5.29 eV. Rhodamine-B and methylene blue (MB) dyes were employed to evaluate the photocatalytic degradation of the synthesized CuO-NPs, resulting in correlation coefficients of 0.7154and 0.9702, respectively. Furthermore, the rate constants of these dye reactions were found to be 0.0406min^{-1} and0.0343 min^{-1}.

Keywords: nanoparticles, photocatalytic degradation, Vicia faba, methylene blue, rhodamine-B.

1. Introduction

Industrial and household wastewater effluents pose significant threats to both human health and aquatic life (Joshi et al. 2022). Industrial effluents may contain hazardous substances, including pesticides, unprocessed colored dyes, and organic dyes. Upon exposure to sunlight, organic dyes undergo photocatalysis, reducing the dissolved oxygen in water. The absorption of sunlight by dye molecules generates highly reactive oxygen species, which react with oxygen molecules and contaminants, leading to a depletion of dissolved oxygen levels. Moreover, dyes can form complexes with oxygen, hindering its dissolution in water and further reducing the availability of oxygen for aquatic life (Dutta et al. 2021; Farré et al. 2008). The widespread use of industrial dyes in the paper, pharmaceutical, textile, and leather industries negatively impacts water resources and disrupts aquatic ecosystems. Consequently, it is crucial to remove these toxic dyes from the environment.

Various strategies have been considered for the treatment of the harmful substances. However, these methods often only change the phase of the contaminants rather than completely degrading them. To address these challenges, nanostructures have been explored for their potential to degrade dyes (Kumar et al. 2018). These nanostructures include metal oxide nanoparticles, zeolites, nanorods, and others (Sharma et al.

2017). The use of metal oxide nanoparticles has proven to be one of the most effective and promising methods for removing hazardous contaminants from water (Anjum et al. 2016). Nanoparticles offer several advantages, and their production can be achieved through various methods, including chemical processes. However, the use of harmful toxic chemicals and certain processes in chemical methods cannot be ignored. Given that metal nanoparticles come into contact with the human body, there is a pressing need to develop eco-friendlier methods, such as biological synthesis, to mitigate the detrimental effects of chemical nanoparticle synthesis protocols. Biological synthesis involves the extraction of nanoparticles from plant material, microorganisms, and enzymes (Asemani et al. 2019).

Copper nanoparticles are of great importance due to their applications in gas sensors, lubricants, superconductors, and dye-sensitized solar cells (Mandke et al. 2012). Copper oxide nanoparticles also possess significant biological properties, including antifouling, antimicrobial, and antifungal activities (Crisan et al. 2022). Several methods can be employed to synthesize copper oxide nanoparticles, including chemical reduction, microwave irradiation, and electrochemical methods (Mandke et al. 2012; Dang et al. 2011; Naveena et al. 2022). With increasing awareness, there is a growing focus on the development of eco-friendly synthesis methods for nanoparticles. The use of plants, microorganisms, and enzymes for synthesizing non-toxic, biologically benign metal nanoparticles is gaining importance (Kulkarni et al. 2014). The phyto constituents present in plants and microorganisms mediate the synthesis of nanoparticles by acting as capping agents.

Authors information:

[a]Department of Physics, School of Applied and Life Sciences (SALS), Uttaranchal University, Dehradun-248007, UK, INDIA.
[b]Department of Chemistry, GRD Institute of Management & Technology, Dehradun, UK, INDIA.
[c]Division of Research and Innovation, Uttaranchal University, Dehradun-248007, UK, INDIA.
*Corresponding Author: park_bhupendra@hotmail.com

Vicia faba is an erect, rigid annual legume that is widely cultivated in most parts of the world. Its leaves are 8-15 cm long and grey-green in color (Singh et al. 2013). The bean plant exhibits several medicinal properties, including antidiabetic, diuretic, and antihypertensive effects, and can also fix atmospheric nitrogen (Köpke et al. 2010). Moreover, it is a rich source of phenolic compounds (Valente et al. 2018).

The current study aims to synthesize copper oxide nanoparticles using a green synthesis method with aqueous *Vicia faba* leaf extract and subsequently use these nanoparticles to degrade harmful dyes such as Rhodamine-B and methylene blue.

2. Materials and Method

Analytical-grade chemicals, including copper (II) sulfate pentahydrate, Rhodamine-B (Rh-B), and methylene blue (MB), were utilized in this study. The leaves of *Vicia faba* were collected from the local region of Dehradun in March. The Agricultural Department of Uttaranchal University authenticated the collected plant material.

Fresh, healthy plant leaves were thoroughly washed with double-distilled water to remove contaminants. After drying in the shade for five days to eliminate moisture, the plant material was finely ground into a powder. Subsequently, 500 ml of deionized water was mixed with 20 g of powdered plant material on a magnetic stirrer with a hot plate at 65°C for eight hours. The resulting extract was then filtered using Whatman filter paper.

3. Synthesis of CuO-NPs

Copper oxide nanoparticles (CuO-NPs) were synthesized from *Vicia faba* by mixing 1 mM copper sulfate with 10g of the extract. The mixture was then combined with a 1 M NaOH solution to achieve a pH of approximately 8. The solution was stirred with a magnetic stirrer for 10 hours at 40°C. Subsequently, the solution containing the precipitate was centrifuged, and the precipitate was separated and transferred to a Petri dish. It was then dried in a hot air oven at 100°C. After drying, the precipitate was finely powdered and stored in a vial for further characterization (Fig. 1).
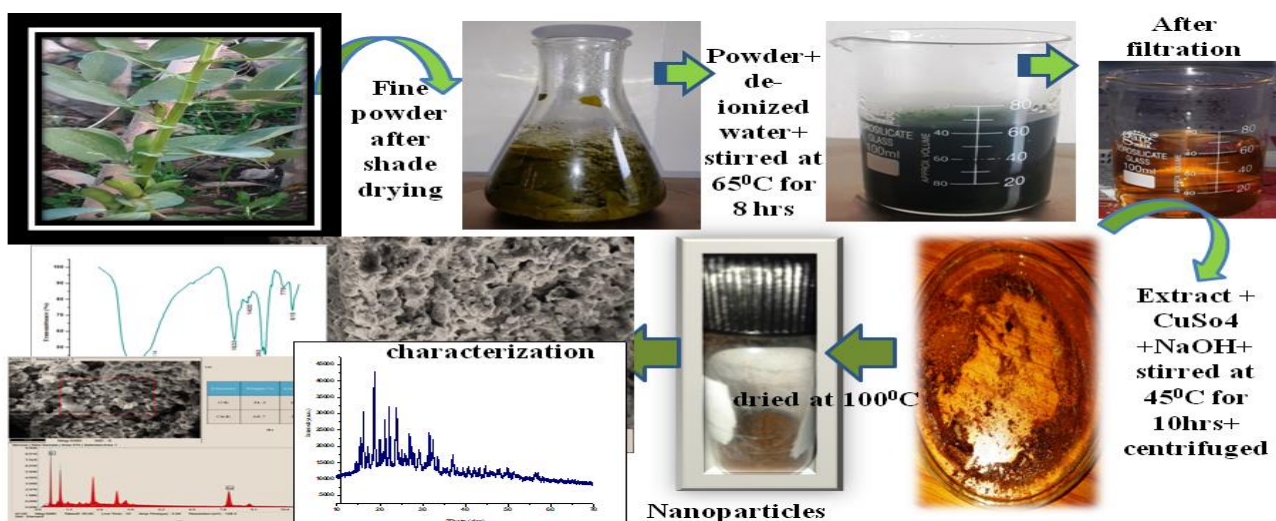

Figure 1. Scheme for the synthesis of CuO-NPs

4. Results and Discussion

SEM & EDX Analysis

SEM analyses were employed to characterize the morphology of CuO-NPs. However, due to the sample preparation process, the SEM analysis revealed the presence of agglomerated particles with a roughly flower-like shape (Fig. 2).
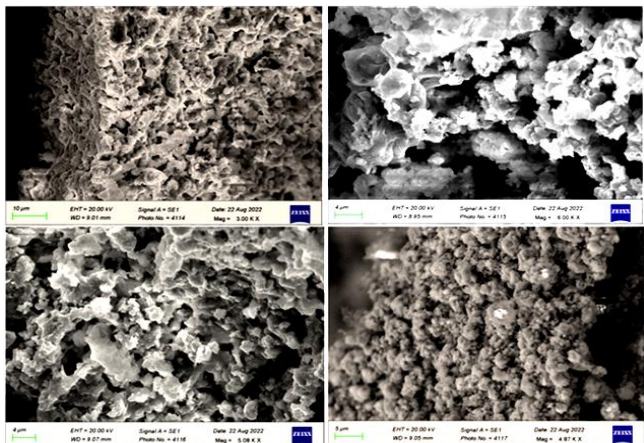

Figure 2. SEM morphology of nanoparticles

For confirmation of the elements present in CuO-NPs, EDX analysis was conducted (Fig. 3). The EDX results revealed the presence of characteristic copper and oxygen, with weight percentages of 68.7% and 31.3%, respectively, and intensity peak values of 4353.1 and 5997.3. These results confirm the successful synthesis of CuO-NPs using the *Vicia faba* leaf extract. It is noteworthy that the additional peaks observed in the EDX analysis may be attributed to the presence of organic groups, which could potentially be removed by washing the extract with ethanol and distilled water.
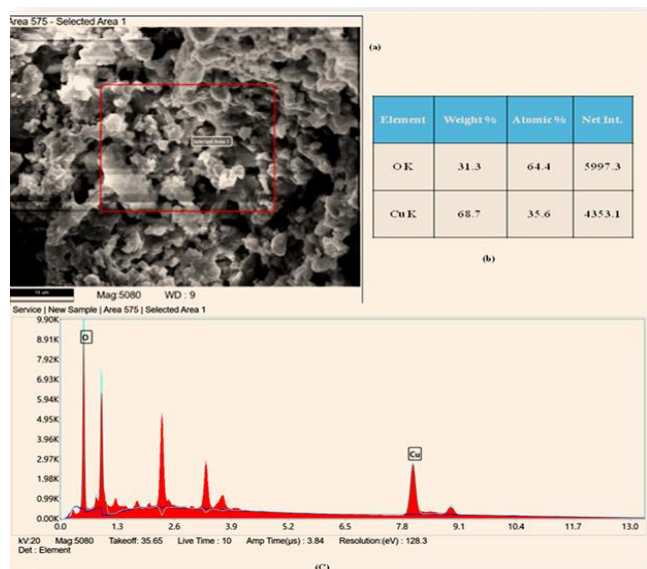

Figure 3. EDX spectrum of nanoparticles
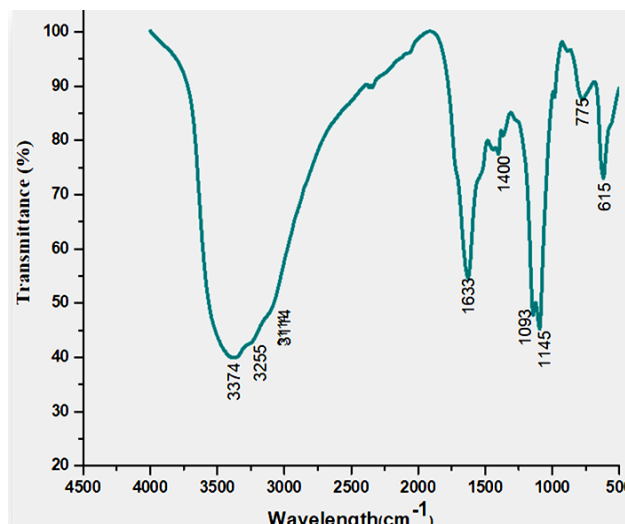
FT-IR Analysis

Figure 4. FT-IR spectra of synthesized nanoparticles

FTIR analysis was conducted to identify the various functional groups in volvedin the Nanoparticles (Fig.4).Thespectraobtained from the *Vicia faba* leaf extract exhibited distinct bands at 3374cm⁻¹, 3255cm⁻¹, 3114cm⁻¹, 1633cm⁻¹, 1400cm⁻¹, 1145cm⁻¹, 1093cm⁻¹, 775cm⁻¹, and 615 cm⁻¹. The prominent peak at 3374 cm⁻¹ indicated the presence of a hydroxyl (OH) functional group, commonly found in alcohols and phenolic compounds (Rajendran et al., 2022). The band at 3114 cm⁻¹ can be attributed to the stretching vibrations of aromatic C-H bonds, while the absorption band at 1400 cm⁻¹ is due to the fundamental vibrations of aromatic C=C bonds (alkene group). The presence of a carbonyl (C=O) group is suggested by a dip near 1633 cm⁻¹, and the absorption band around 1093 cm⁻¹ indicates Cu-O stretching vibrations. Additionally, the smaller peaks observed in the 775-615 cm⁻¹ range are attributed to the bending vibrations of aromatic C-H bonds out of the plane. These findings suggest that flavonoids and other phenolic compounds in the *Vicia faba* leaf extract play a stabilizing role on the surface of the produced metal oxide nanoparticles. This stabilization contributes to their reducing properties and facilitates the reduction of Cu^{2+} ions to form CuO-NPs.

XRD Analysis

X-ray Diffraction (XRD) analysis (Fig. 5) of the synthesized CuO nanoparticles confirms their crystalline structure. The XRD pattern exhibits distinct diffraction peaks at 2θ angles of approximately 35.48°, 38.65°, 46.08°, 48.74°, 58.22°, 61.51°, 66.22°, 67.98°, and 75.01°, corresponding to the lattice planes (111), (111), (112), (202), (202), (113), (311), (113), and (004), respectively. These results from the XRD spectrum provide strong evidence for the presence of copper oxide nanoparticles, and their structural characteristics are consistent with the SEM image.
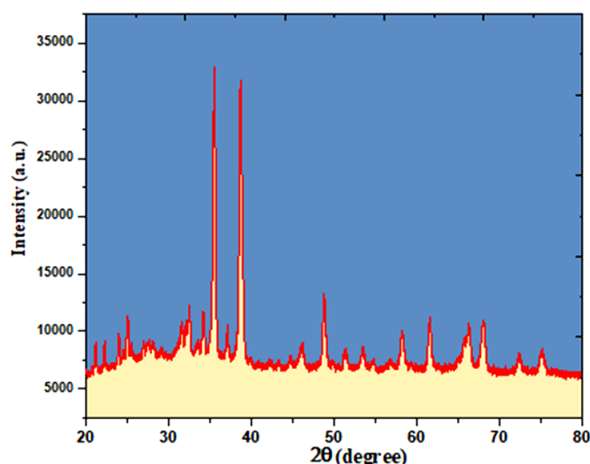
Figure 5. XRD Spectrum of synthesized nanoparticles

Table 1 presents the assigned peak values (2θ), d-spacing values, relative intensity, and particle size estimation of the particles. The Debye-Scherrer equation, detailed below, was used to evaluate the particle size, which was determined to be 27.44 nm (Jenkins et al., 1996). The Scherrer constant and X-ray wavelength were set at 0.89 and 0.15418, respectively. Furthermore, the indexed peak values were compared with the standard card for the anatase phase of the powder sample (JCPDS card no: 01-080-1916), confirming a match.

Table 1. Average particle size, d-spacing and lattice parameters

Peak position (2θ)	Peak height (cts)	Full width half max (2θ)	d-spacing [Å]	Relative Intensity (%)	hkl	Particle size [Å]
35.4890	32719.89	0.295	2.47	100.00	111	291
38.6470	31706.50	0.236	2.27	96.90	111	369
46.0810	8800.19	0.472	1.92	26.90	112	186
48.7390	13178.78	0.276	1.82	40.28	202	325
58.2240	9899.62	0.394	1.55	30.26	202	236
61.5060	11161.57	0.315	1.47	34.11	-113	301
66.2220	10482.79	0.315	1.38	32.04	-311	309
67.9830	10740.92	0.354	1.35	32.83	113	277
75.0110	8217.02	0.768	1.24	25.11	004	176

Optical Properties Analysis

A UV-visible spectrophotometer at room temperature was employed for investigating the absorption peaks, range of the absorption spectrum, and energy band gap (Fig 6).
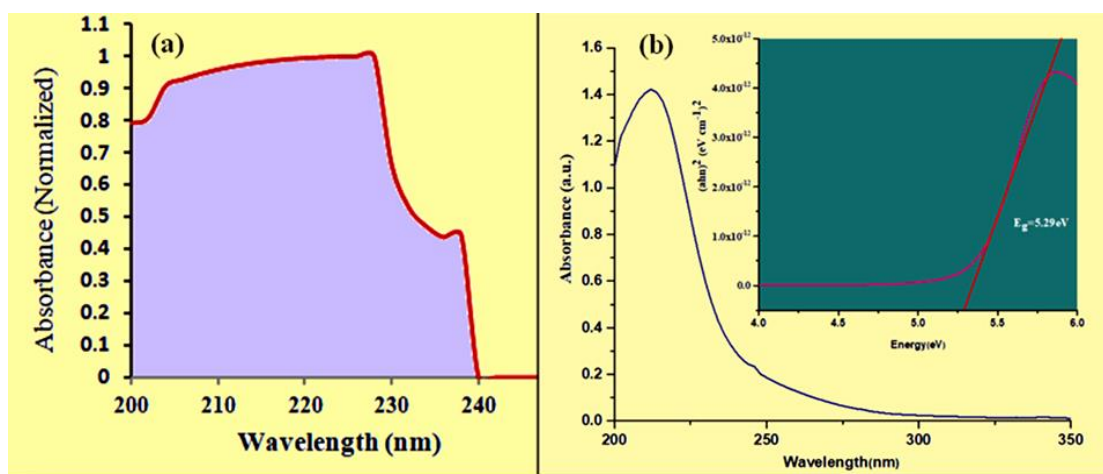

Figure 6. Plot of absorbance against wavelength of (a) *Vicia faba* leaves extract and (b) *Vicia faba* CuO-NPs along with (αhν)^2 versus hν

25

The absorption spectrum of *Vicia faba* leaf extract was observed in the range from 200 nm to 240 nm, displaying distinct peaks at 204 nm, 228 nm, and 238 nm. In contrast, the absorption spectrum of *Vicia faba* CuO-NPs spanned a broader range from 200 nm to 300 nm, with a prominent peak at 212 nm. The presence of multiple peaks in the plant extract spectrum may be attributed to various compounds with different absorption properties. Additionally, the pronounced peak at 212 nm confirms the successful formation of CuO-NPs. To ensure consistency in examining the absorption spectra, ethanol was used as the solvent for both the plant extract and CuO-NPs.

Considering the absorption edge, the indirect optical energy band gap was estimated from the absorption spectrum. Tauc's equation was employed for this estimation, supported by existing literature (Muhammad et al., 2011; Yakuphanoglu et al., 2005). The energy band gap value was determined by plotting $(\alpha h\nu)^2$ versus photon energy (hν), yielding a value of 5.29 eV. The relationship between the absorption coefficient (α) and the energy of the incident photon (hν) is given by the equation mentioned below (Tauc et al., 1996).

$$\alpha h\nu = \alpha_0 \left(h\nu - E_g\right)^n$$

where E_g is the energy band gap, ν is the incident photon frequency, α_0 is the energy independent constant, and n defines the type and nature of transitions.

Investigation of Photocatalytic Potential

To evaluate the photocatalytic activity of CuO-NPs, the degradation of Methylene blue (MB) and Rhodamine-B (Rh-B) dyes in aqueous solutions was examined. The mechanism for the decomposition of these dyes on the surface of CuO-NPs is detailed in the literature (Devi & Singh, 2014).

Standard solutions with a concentration of 20 mg/L for both Rhodamine-B and Methylene blue dyes were prepared. Each standard dye solution (10 ml) was mixed with 1 mg to 13 mg of CuO-NPs, at 2 mg intervals, in separate test tubes. The solutions were then exposed to direct sunlight with an intensity of 9.2 W/m². The absorption spectra were analyzed using a UV-visible spectrophotometer at 663 nm for MB and 547 nm for Rh-B, with measurements taken at 15-minute intervals. The photocatalytic degradation efficiency (PDE) was calculated using the formula (Chen et al., 2015):

PDE (%) = [Initial concentration of dye (C$_o$) − remaining dye concentration after time t (C)x100]/ Initial concentration of dye (C$_o$)

The degradation of the aqueous solution under sunlight exposure was investigated, and the results are presented in Figures 7(a) and 8(a) for Rh-B and MB dyes, respectively. The suspensions of CuO-NPs were separated by taking 3 mL aliquots and subjecting them to centrifugation. MB was completely decomposed within 105 minutes in the presence of CuO-NPs as the catalyst, while Rh-B was degraded within 75 minutes.
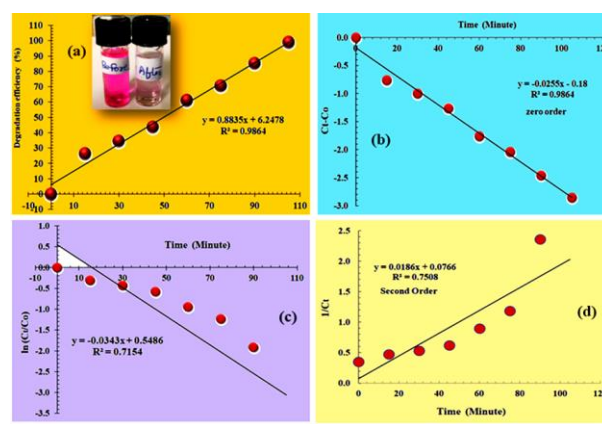

Figure 7(a). Photocatalytic degradation efficiency of Rh-B **Figure 7(b-d).** Kinetic results for the degradation of Rh-B

Additionally, degradation was confirmed by recording absorption spectra at 663 nm for MB and 547 nm for Rh-B dye. According to Sharma and Dutta (Sharma et al., 2015), hydroxyl radicals are identified as the primary reactive oxygen species responsible for the degradation process. Furthermore, the kinetics of the selected dyes' photocatalytic degradation were investigated and presented in Figure 7(b) for Rh-B and Figure 8(b) for MB dye.

To determine the kinetic rate of the reaction, the experimental results were analyzed using zero-order, first-order, and second-order reaction kinetics, as outlined by Mukhlish et al. (2013).

$$C_t - C_o = -k_o t, \; zero \; order \; (1)$$

$$\ln(C_t/C_o) = -k_1, \; First \; order \; (2)$$

$$1/ C_t = k_2 t, \; Second \; order \; (3)$$

From the table (Table 2), it can be predicted that for Rh-B, the coefficient of determination (R^2) is higher for the zero-order reaction (0.9864) compared to the first-order (0.7154) and second-order (0.7508) reactions. Conversely, for MB, the first-order reaction exhibits the highest R^2 (0.9702) compared to the zero-order (0.9501) and second-order (0.8225) reactions.

Furthermore, the rate constants for Rh-B are 0.0255 min^{-1} (zero-order), 0.0343 min^{-1} (first-order), and 0.0186 min^{-1} (second-order). For MB, the rate constants are 0.0124 min^{-1} (zero-order), 0.0406 min^{-1} (first-order), and 0.1298 min^{-1} (second-order). These results suggest that the discoloration of Rh-B and MB dyes can be primarily explained by zero-order and first-order reactions, respectively.
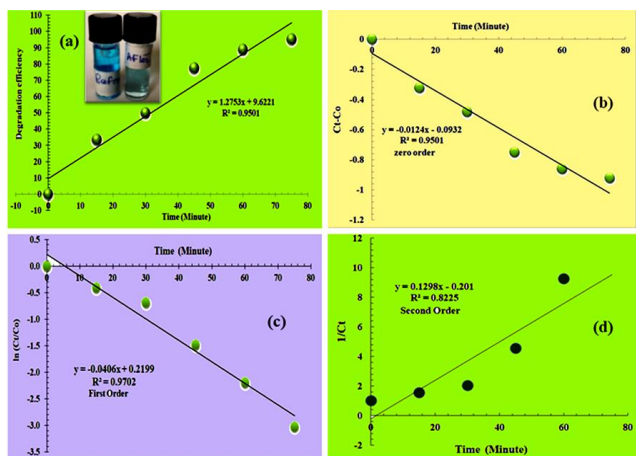
Figure 8(a). Photocatalytic degradation efficiency of MB **Figure 8(b-d).** Kinetic results for the degradation of MB

Figure 9. Photocatalytic degradation rate constant variation of MB under the effect of CuO-NPs load

Figure 9 illustrates the variation in the rate constant (min^{-1}) of MB at different amounts (mg) of CuO-NPs extracted from *Vicia faba* leaves. The experiments maintained a constant dye concentration, as previously mentioned. The results indicate an initial gradual increase in the rate constant up to 9 mg/10 ml, followed by a subsequent faster decrease. The examination of the rate constant (min^{-1}) for Rh-B is not considered with different amounts, as it remains constant for the zero-order reaction over time and is not affected by changes in reactant concentration.
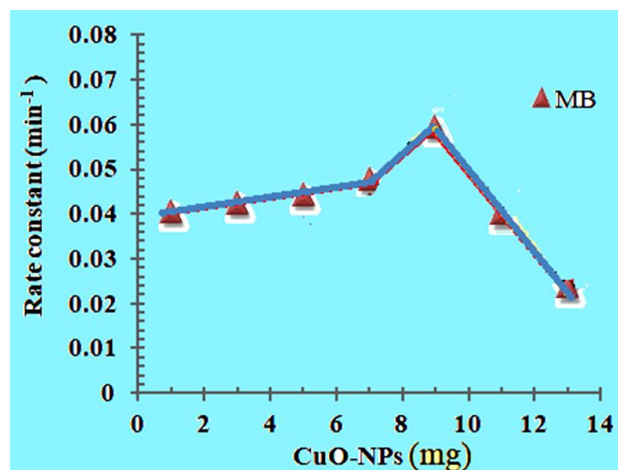
The enhanced degradation efficiency of the MB dye with an increasing amount of CuO-NPs catalyst can be attributed to the greater availability of active sites on the catalyst's surface, which accelerates the formation rates of radicals. However, when the catalyst amount exceeds 9 mg/10 ml, the rate constant decreases due to light scattering and reduced light penetration through the solution. At higher catalyst loadings, the deactivation of activated molecules by collisions with ground-state molecules becomes more dominant in the reaction, leading to a reduced reaction rate (Neppolian et al., 2001).

Table 2. Parameters used and results of kinetic of degradation of dyes.

Parameters	Dye	
	Rh-B	**MB**
Solution	aqueous	aqueous
equation of kinetics	y = -0.0255x - 0.18 (zero-order)	y = -0.0124x - 0.0932 (zero-order)
	y = -0.0343x + 0.5486 (first-order)	y = -0.0406x + 0.2199 (first-order)
	y= 0.0186x + 0.0766(second-order)	y = 0.1298x - 0.201 (second-order)
correlation coefficient (R^2)	R^2 = 0.9864(zero-order)	R^2 = 0.9501 (zero-order)
	R^2 = 0.7154(first-order)	R^2 = 0.9702 (first-order)
	R^2 = 0.7508 (second-order)	R^2 = 0.8225 (second-order)
rate constant of reaction	0.0255min^{-1}(zero-order)	0.0124 min^{-1} (zero-order)
	0.0343 (first-order)	0.0406 min^{-1} (first-order)
	0.0186 (second-order)	0.1298 min^{-1} (second-order)

5. Conclusion

In the present study, *Vicia faba* leaf extract was effectively utilized to synthesize CuO nanoparticles (CuO-NPs), which exhibited a flower-shaped morphology with an average size of 27.44 nm. The formation of CuO-NPs was confirmed through absorption spectrum analysis, and the crystalline structure of the synthesized nanoparticles was validated using X-ray diffraction (XRD).

The synthesized CuO-NPs were employed in the degradation of Methylene Blue (MB) and Rhodamine B (Rh-B) dyes, with notable efficacy observed, particularly in the case of Methylene Blue.

Based on the present findings, it can be concluded that the green synthesis of nanoparticles using *Vicia faba* leaf extract represents an environmentally friendly approach, as it does not release secondary chemical by products. Furthermore, these nanoparticles have demonstrated their suitability for the degradation of toxic industrial dyes.

6. Funding

7. Acknowledgement

8. Conflicts of Interest

The author(s) declare(s) that there is no conflict of interest regarding the publication of this paper.

9. References

Anjum, M., Miandad, R., Waqas, M., Gehany, F., Barakat, M.A. (2016). Remediation of wastewater using various nano-materials. Arab. J. Chem, doi:10.1016/j.arabjc.2016.10.004

Asemani, M., Anarjan, N. (2019). Green synthesis of copper oxide nanoparticles using *JUGLANS REGIA* leaf extract and assessment of their physico-chemical and biological properties. Green Processing and Synthesis, 8 (1), 557-567. doi.org/10.1515/gps-2019-00252011.

Chen, W., Zheng, L., Jia, R., Wang, N. (2015). Cloning and expression of a new manganese peroxidase from Irpex lacteus F17and its application in decolorization of reactive black 5. Process Biochemistry, 50(11), 1748–1759.

Crisan, M.C., Teodora, M., and Lucian, M. (2022). Copper Nanoparticles: Synthesis and Characterization, Physiology, Toxicity and Antimicrobial Applications. Appl. Sci.., *12*(1), 141; https://doi.org/10.3390/app12010141

Dang, T.M.D., Le, T.T.T., Fribourg-Blanc, E., Dang, M.C. (2011). Synthesis and optical properties of copper nanoparticles prepared by a chemical reduction method. Adv Nat Sci: Nanosci Nanotechnol 2(1):015009. doi 10.1088/2043-6262/2/1/015009

Devi, H. S., Singh, T. D. (2014). Synthesis of copper oxide nanoparticles by a novel method and its application in thedegradation of Methyl orange. Advance in Electronic and Electric Engineering, 4(1), 83–88.

Dutta, S., Banerjee, P., Das, P., Mukhopadhyay, A. (2021). Phytogenic synthesis of nanoparticles and their application in photo catalysis of dye rich effluents, Photocatalytic Degradation of Dyes, Elsevier, 647-694

Farré, M. la, Pérez, S., Kantiani, L., Barceló, D. (2008). Fate and toxicity of emerging pollutants, their metabolites and transformation products in the aquatic environment. TrAC-Trends Anal. Chem, 27, 991–1007. doi:10.1016/j.trac.2008.09.010

Jenkins, R., Snyder, R. L. (1996). Introduction to X-Ray Powder Diffractometry, (1st ed). New York, USA, John Wiley and Sons, 554.

Joshi, N.C., Gururani, P., Gairola, S.P. (2022). Metal Oxide Nanoparticles and their Nanocompositebased Materials as Photocatalysts in the Degradation of Dyes. Biointerface Research in Applied Chemistry, 12(5), 6557-6579. doi.org/10.33263/BRIAC125.65576579

Köpke, U., Nemecek, T. (2010). Ecological services of faba bean. Field Crops Research, 115, 217–233. doi.org/10.1016/j.fcr.2009.10.012

Kulkarni, N., and Muddapur, U. (2014). Biosynthesis of Metal Nanoparticles: A Review, Journal of Nanotechnology, Article ID 510246, 8 pages http://dx.doi.org/10.1155/2014/510246

Kumar, M., Mehta, A., Mishra, A., Singh, J., Rawat, M., Basu, S. (2018). Biosynthesis of tin oxide nanoparticles using Psidium Guajava leave extract for photocatalytic dye degradation under sunlight. Mater. Lett, 215, 121–124. doi.org/10.1016/j.matlet.2017.12.07

Mandke, M.V., Pathan, H.M. (2012). Electrochemical growth of copper nanoparticles: structural and optical properties. J Electroanal Chem, 686, 19–24. doi.org/10.1016/j.jelechem.2012.09.004

Muhammad, F.F., Sulaiman, K. (2011). Utilizing a simple and reliable method to investigate the optical functions of small molecular organic flms-Alq3 and Gaq3 as examples. Measurement, 44(8), 1468–1474. doi.org/10.1016/j.measurement.2011.05.017

Mukhlish, M. B., Najnin, F., Rahman, M. M., Uddin, M. J. (2013). Photocatalytic degradation of different dyes using TiO2 withhigh surface area: a kinetic study. Journal of Scientific Research, 5(2), 301–314.

Naveena, D., Dhanabal, R., Bose, A. C. (2022). Investigating the effect of La doped CuO thin film as absorber material for solar cell application.Optical Materials, Volume 127, 112266. doi.org/10.1016/j.optmat.2022.112266

R. Singh, R., Dutta,S. (2018). Synthesis and characterization of solar photoactive TiO_2 nanoparticles with enhanced structural and optical properties, Adv. Powder Technol, 29 211–219, doi:http://dx.doi.org/10.1016/j.apt.2017.11.005.

Rajendran, R., Pullani, S., Thavamurugan, S., Radhika, R., Prabha, A.L. (2022). Green Fabrication of silver nanoparticles from Salvia species extracts: characterization and anticancer activities against A549 human lung cancer cell line. Applied Nanoscience, 5(7),1515-1519. https://doi.org/10.1007/s13204-021-02130w.

Sharma, R., Dutta, K. (2015).Studies on the drastic improvement of photocatalytic degradation of acid orange-74 dye by TPPO capped CuO nanoparticles in tandem with suitable electron capturingagents, RSCAdv. 5, 43815–43823, doi:http://dx.doi.org/10.1039/c5ra04179a.

Sharma, V.K., Feng, M. (2017). Water depollution using metal-organic frameworks-catalyzed advanced oxidation processes: A review. J. Hazard. Mater, 372, 3-16. doi:10.1016/j.jhazmat.2017.09.043

Singh, A. K., Bharati, R.C., Manibhushan, N. C., and Pedpati, A. (2013). An assisment of faba bean (*Vicia faba* L.) current status and future prospect. African Journal of Agricultural Research, Vol. 8(50), pp. 6634-6641, 26 December, do: 10.5897/AJAR2013.7335

Tauc, J., Grigorovici, R., Vancu, A. (1966). Optical properties and electronic structure of amorphous germanium. Physica status solidi (b), 15(2), 627-637. doi.org/10.1002/pssb.19660150224

Valente, I. M., Maia, M.R.G., Malushi, N., Oliveira, H.M., Papa, L., Rodrigues, J.A., Fonseca, A.J.M., Cabrita, A.R.J. (2018). Profiling of phenolic compounds and antioxidant properties of European varieties and cultivars of *Vicia faba* L. pods. Phytochemistry, 152, 223–229, doi:10.1016/j.phytochem.2018.05.011

Yakuphanoglu, F. Erten, H. (2005). Refractive index dispersion and analysis of the optical constants' of an ionomer thin flm. Opt Appl, 35(4), 969.

DEVELOPMENT OF A SPECTROPHOTOMETRIC DETERMINATION OF PREDNISOLONE IN DIFFERENT DOSAGE FORMS

Hasan M. Luaibi[1a], Khalid Waleed S. Al-Janabi[2b], Ali Khalil Mahmood[3b], Takleef Dheyab Sallal[4c], and Tayser Sumer Gaaz[5d,e]*

Abstract: A sensitive, accurate, and affordable colorimetric method was developed for assaying prednisolone (PRZ) in various medicinal forms. The procedure involves the oxidation of PRZ by ferric ions, followed by complexation of the resulting ferrous ions with ferricyanide to produce a greenish-blue product. Common complexation conditions were thoroughly investigated. The mole ratio of $FeCl_3 \cdot 6H_2O$ to $K_3Fe(CN)_6$ was 8:1. The proposed mechanism of complexation was suggested and considered. Various parameters were optimized, including the reduction of the colorimetric reaction temperature to 50°C and the duration of heating and analysis to 20-30 minutes. The calibration curve was linear over the range of 1-60 µg/mL. The limit of detection (LOD) and the limit of quantification (LOQ) were 0.5 µg/mL and 1 µg/mL, respectively. Spiking actual samples with standard PRZ showed recoveries within the 97.3-100.1% range. The method exhibited high precision, with an RSD% of less than 1.5%. Additionally, the study confirmed that common pharmaceutical excipients did not interfere. Real medicinal samples, including tablets, syrup, eye drops, and creams, were successfully examined for direct analysis of PRZ using the developed methodology, demonstrating its suitability for routine analysis of various PRZ-containing drug formulations.

Keywords: colorimetric analysis, UV-Vis, derivatization, pharmaceuticals, prednisolone, steroid determination.

1. Introduction

Prednisolone Prednisolone (PRZ), a synthetic steroid, inhibits the release of inflammatory chemicals in the body. It is five times more potent than cortisone acetate, with less sodium and fluid retention, which mitigates stomach issues. PRZ and prednisone are corticosteroids frequently used to treat inflammatory and immunological diseases. PRZ is humans' active form of prednisone (Xu et al., 2007). It is commonly used to treat inflammation, ulcerative colitis, gland disorders (endocrine), lupus, allergic disorders, psoriasis, and other conditions affecting the eyes, skin, nervous system, lungs, blood cells, or stomach (Albayati & Jassam, 2019). However, it should be avoided in patients with fungal infections and in those taking certain drugs, including vitamins and herbal products. Additionally, PRZ reduces the immune system's response to various syndromes, such as swelling, discomfort, and allergy symptoms (Schuster et al., 2005).

Synthetic corticosteroids are incorporated in many pharmaceutical preparations, leading to numerous studies on their assay within different pharmaceutical mixtures. Balaji et al. (2008) developed a voltammetric approach using a β-cyclodextrin-modified carbon paste electrode to test PRZ along with other corticosteroids (Balaji et al., 2008). Colorimetric absorption spectroscopy is generally used for regular analytical quantifications, provided the active material's allowable percentage in the remedy is not less than ±10% (Evtifeeva et al., 2016).

Traditional chromatographic methods (Raut et al., 2014; Razzaq et al., 2017), HILIC (Hydrophilic Interaction Liquid Chromatography) (Ali & Rasheed, 2020), and spectrophotometric methods (Kashyap et al., 2012) have been employed for PRZ determination. El Gammal et al. evaluated PRZ in various pharmaceutical mixtures using micellar liquid chromatography (El Gammal et al., 2018), while Lemus Gallego et al. used micellar electrokinetic chromatography (Lemus Gallego & Pérez Arroyo, 2003). Gas chromatography and a mass spectrometer have also been used to quantify PRZ (Iannella et al., 2019). Primpray et al. separated and quantified steroids, including PRZ, in adulterated herbal medications using electrochemical analysis (Primpray et al., 2019).

Another study employed the quality-by-design tactic (QbD) to develop a spectroscopic technique for PRZ assay by varying seventeen parameters (Bhusnure et al., 2015).

The spectrophotometric quantification method for PRZ was validated using identical model blends analyzed by one analyst on various spectrometers in two different laboratories. Evtifeeva et al. quantified PRZ spectroscopically directly at 243.5 nm without derivatization (Evtifeeva et al., 2016). Additionally, PRZ was

Authors information:

[a]Department of Renewable Energy, College of Energy and Environmental Sciences, Al-Karkh University of Science, Baghdad, IRAQ. E-mail: hasan.luaibi@gmail.com[1]

[b]Department of Chemistry, College of Education for Pure Sciences/ Ibn Al-Haitham, University of Baghdad, Baghdad, IRAQ. E-mail: Khalid.janabi@gmail.com[2]; ali.khalil.mahmood@gmail.com[3]

[c]Ministry of Education, Baghdad, IRAQ. E-mail: sallaltakleef535@gmail.com[4]

[d]Technical College Al-Musaib, Al-Furat Al-Awsat Technical University, Babil, IRAQ. E-mail: taysersumer@atu.edu.iq[5]

[e]Prosthetics and Orthotics Engineering Department, College of Engineering and Technologies, Al-Mustaqbal University, Babylon, IRAQ. E-mail: tayser.sumer.gaaz@uomus.edu.iq[5]

*Corresponding Author: tayser.sumer.gaaz@uomus.edu.iq

determined by dropping the mercury electrode (DME) on the differential pulse voltammeter (Smajdor et al., 2016).

Derivative spectrometry is a significant analytical practice that avoids overlapping spectra in chemical mixtures (Abdul Kareem & Al-Janabi, 2018; Al-Janabi, 2013; Al-Janabi et al., 2020c, 2020a, 2020b; Hammod, Al-Janabi, et al., 2020; Hannoun & Al-Janabi, 2020; Radhi & Al-Janabi, 2020). A study reported a colorimetric procedure for assaying dexamethasone after fluoranil derivatization (Al-Janabi et al., 2020b).

The current work aimed to demonstrate a simple, sensitive, and economically viable colorimetric method for quantifying PRZ within pharmaceutical formulations without preliminary separation steps. The method is based on the oxidation of PRZ in an acidic medium with ferric ions, followed by the complexation of ferrous ions with ferricyanide. This approach offers stability and high sensitivity, and common excipients present in pharmaceutical preparations did not interfere with the PRZ assay.

2. Materials and Method

Apparatus
Spectrophotometric analyses were performed using a double beam UV-Visible Spectrometer (T80+ PG Instruments Ltd., UK), with a path length of 1 cm, and quartz cuvettes.

Material
All reagents and materials were of analytical grade. Prednisolone powder, with a purity of 99.8%, was obtained from the State Company for Drug Industry and Medical Appliances (SDI), Samarra, Iraq.

Preparing the Stock and Working Solutions:
Standard working solutions of PRZ were prepared in methanol at concentrations of 1, 2, 5, 10, 20, 30, 40, 50, and 60 µg/mL. Standard solutions of potassium hexacyanoferrate (III), $K_3Fe(CN)_6$, referred to hereinafter as potassium ferricyanide, and ferric chloride $FeCl_3·6H_2O$, were prepared in distilled water at a concentration of 0.5% (w/v) individually.

An aliquot of 10 mL of each PRZ standard was mixed with 2 mL of 4N sulfuric acid, followed by 2 mL of ferric chloride (0.5% w/v), and 0.5 mL of ferrate solution (0.5% w/v). The mixture was warmed to 50°C in a water bath for 25±5 minutes, with intermittent shaking, before being diluted with distilled water. The resulting colored products were stable for over an hour and examined at 778 nm.

Preparation of Sample Solutions from Pharmaceutical Dosage Forms
Pharmaceutical samples were prepared for colorimetric PRZ quantification, comparing the medicine's designated dosage to the analyzed results. Sample preparation varied based on the physical state of the medicine, such as tablets, creams, or drops, and was then subjected to colorimetric analysis as outlined in the suggested procedure.

An exact amount of powdered tablets, equivalent to the pure form of PRZ, was dissolved in 10 mL of methanol (Dikran et al., 2017). The mixture was filtered and rinsed with 10 mL of alcohol. The filtrate and washing were diluted with distilled water in a 100 mL volumetric flask to the required concentration. For creams, 5 g of cream was weighed and gently heated, swirling in 50 mL of methanol. Eye drops were diluted directly with methanol. The original concentration of PRZ in the eye drops was simulated by diluting various aliquots of pre-prepared solutions with methanol (Mahmood, 2017). Recovery was intensively studied by spiking the drug (tablet and syrup) with different amounts of standard PRZ solutions over the range of 1-20 µg/mL.

Optimum settings were obtained by adjusting one factor at a time while keeping the others unchanged. The influence of ferric chloride and ferricyanide concentrations was studied as a function of absorbance, maintaining the PRZ amount constant. Maximum absorbance was achieved with a concentration of 4.0×10^{-2} M for $FeCl_3·6H_2O$ and 5.0×10^{-3} M for $K_3Fe(CN)_6$, which were therefore adopted as optimal.

3. Results and Discussion

PRZ was directly assayed in the UV region of the spectrum at a peak maximum of 236.4 nm (Figure 1). However, this absorbance presents a significant drawback, as it interferes with many other active medicinal compounds that absorb in the same spectral range. To mitigate this issue, PRZ is derivatized to produce a colored product that absorbs in the visible region, a technique known as a bathochromic shift, or redshift (Skoog et al., 2017). This approach overcomes interference from other compounds. The common reversible redox system of ferricyanide/ferrocyanide (Mortimer, 2017) was utilized as the basis for detecting PRZ spectrophotometrically, demonstrating no interference with common excipients.
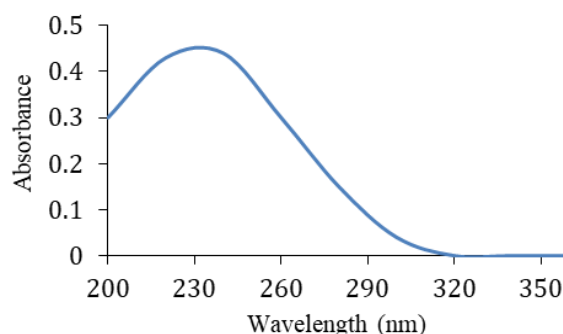
Figure 1. The UV absorption spectrum of the PRZ solution with a maximum peak of 236.4 nm.

The proposed method demonstrates no interaction between the active compound of PRZ and common excipients or other additives. The method's efficacy for quantifying pharmacological formulations was evaluated, with assay outcomes reflecting accuracy and precision. The investigated PRZ is oxidized by ferric chloride ($FeCl_3·6H_2O$) in an acidic medium, producing ferrous (II) ions (Singh & Verma, 2008) (Figure 2).

Figure 2. The oxidation of PRZ by ferric chloride to produce the PRZ dione derivative and ferrous chloride in an acidic medium

The complexation conditions for the proposed procedure of Singh & Verma (2008) were thoroughly studied and optimized. The mole ratio of FeCl₃·6H₂O to K₃Fe(CN)₆ was determined to be 8:1. The mechanism of the complexation reaction was considered and suggested.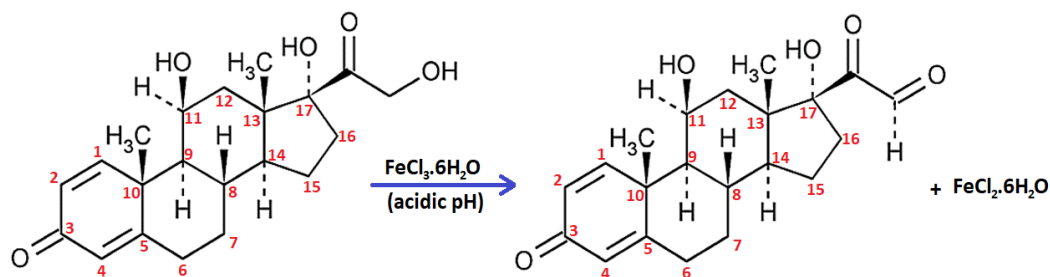 Improvements were observed in various parameters, such as lowering the colorimetric reaction temperature to 50 °C and reducing the time between heating and analysis to 20-30 minutes. A linear calibration curve was constructed over the 1–60 µg/mL range.

The LOD and LOQ were determined to be 0.5 µg/mL and 1 µg/mL, respectively. Real medicinal samples of tablets, syrup, eye drops, and creams containing PRZ were spiked and analyzed with standard PRZ, yielding recoveries between 97.3% and 100.1%.

In the acidic medium, ferric ion acts as an oxidizing agent for PRZ. The reduction of ferric ion to ferrous ion by PRZ involves the oxidation of the 2-hydroxyacetyl side chain on C17 of PRZ into two adjacent carbonyl groups, forming a dione. FTIR analysis confirms the formation of the oxidized PRZ dione derivative through the appearance of a sharp C-H stretching peak at 2725 cm⁻¹ and a C=O stretching peak at 1711 cm⁻¹, as shown in Figure 3.
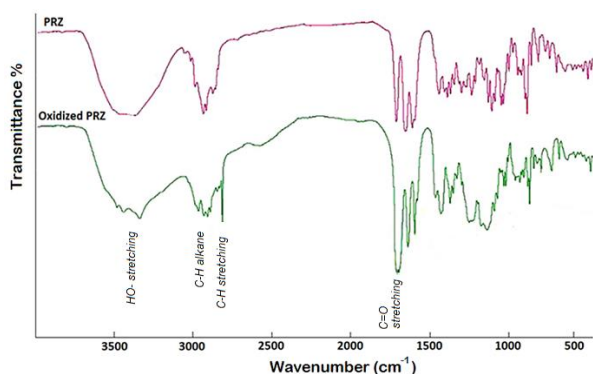
Figure 3. An overlaid FTIR spectra of PRZ and PRZ oxidized dione derivative confirming the formation of PRZ dione derivative by the appearance of a sharp peak of C-H stretching at 2725 cm⁻¹ and C=O stretching peak at 1711 cm⁻¹

The ferrous (II) ion resulting from the PRZ oxidation reacts with potassium ferricyanide to produce a bluish-green complex of potassium ferrocyanide (Lillie & Donaldson, 1974) (Figure 4), which has an absorbance maximum at 778 nm, as shown in Figure 5.
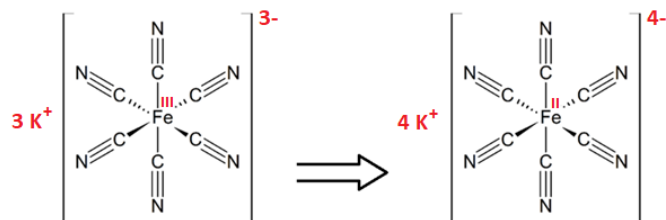
Figure 4. Reduction of Ferricyanide to Ferrocyanide (Mortimer, 2017).
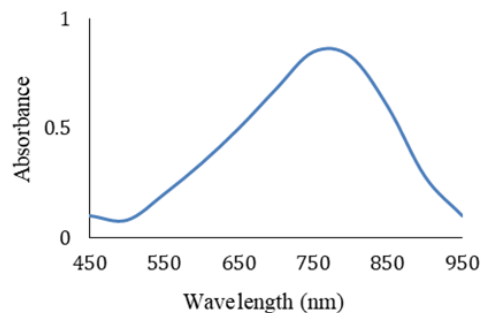
Figure 5. UV/Vis spectrum for the resulting colored complex with maximum absorbance at 778 nm.

The optimal amount of FeCl₃·6H₂O relative to K₃Fe(CN)₆ was determined by adding different concentrations of FeCl₃·6H₂O to a fixed amount (5.0×10^{-3} M) of K₃Fe(CN)₆. Spectrophotometric analyses were performed against a blank containing the same ratio of reagents, with the same amount of FeCl₃·6H₂O added to both the sample and the blank each time. The optimal ratio was found to be 8:1 (Figure 6).
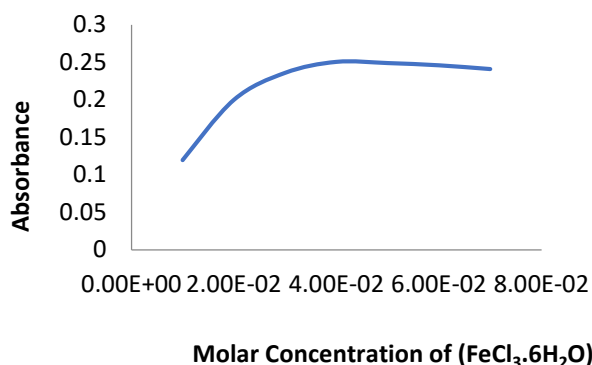
Figure 6. Effect of adding different concentrations of $FeCl_3.6H_2O$ to 5.0×10^{-3} M of $K_3Fe(CN)_6$

The color reaction between 4.0×10^{-2} M $FeCl_3 \cdot 6H_2O$ and 5.0×10^{-3} M $K_3Fe(CN)_6$ occurred at room temperature; however, color development was faster at elevated temperatures. The absorbance maximum was detected within 20 to 30 minutes of heating at 50 °C, after which the color began to gradually fade, as shown in Figure 7. The anticipated cause of the color fading is the thermal decomposition of the colored complex.
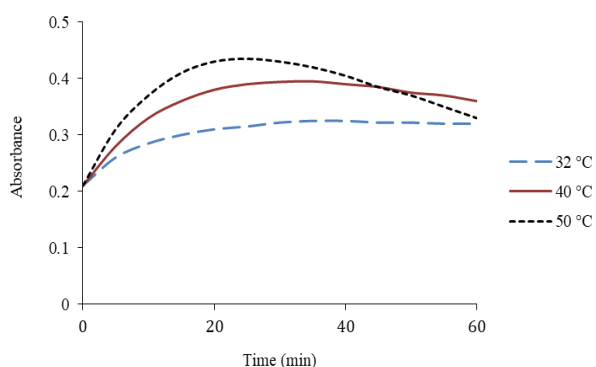
Figure 7. The influence of reaction temperature on absorbance as a function for time and color development.

PRZ aliquots (20 µg/mL) were analyzed using the proposed method with ten replicates. The mean absorbance value was 0.2506 AU, with a relative standard deviation (RSD%) of 0.75%. After optimizing the spectrophotometric analysis conditions, a calibration curve was established, demonstrating linearity in accordance with Beer's law over the range of 1 to 60 µg/mL. The optimal temperature for the colorimetric reaction was found to be 50 °C, with the measurement optimal within 20-30 minutes

after the onset of the colorimetric reaction at λ_max of 778 nm. The limit of detection (LOD) and limit of quantification (LOQ) were determined to be 0.5 and 1 µg/mL, respectively, with a correlation coefficient of 0.9989 (Figure 8). Additionally, statistical data were calculated for three PRZ concentrations (5, 10, 40 µg/mL) with five replicates each. The RSD was less than 1.5%, and the relative errors ranged from -0.520% to +1.002% (Table 1).
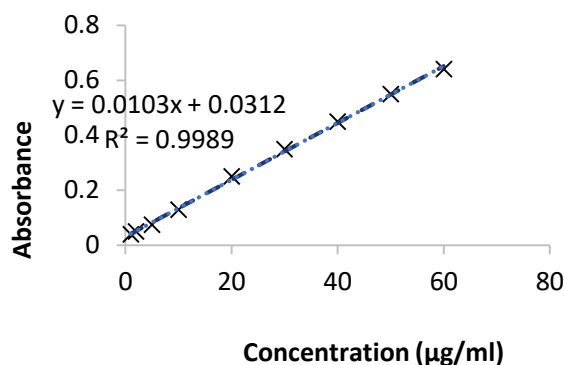
Figure 8. PRZ calibration curve under optimal conditions, linearity obtained for the range (1 to 60 µg/mL).

Table 1. Some statistical parameters for the proposed method

Concentration (µg/mL)		Rel. Error %	RSD%
Taken	Found*		
5	5.0501	+1.002	1.4022
10	9.9480	-0.520	0.9601
40	39.778	+0.555	0.8125

* Average of five measurements.

Assaying Different Forms of PRZ Pharmaceuticals:

The stability of the colored product was found to be over 1 hour when left at room temperature. The method was applied to quantify PRZ in tablets, including its pure form and in proprietary drugs from various pharmaceutical manufacturers. The readings, taken with n=5 replicates, were reproducible. The analysis results, as shown in Table 2, indicate no significant differences compared to the dosages prescribed by the manufacturers.

Table 2. Quantification of PRZ tablets from various manufacturers using the proposed approach.

Brand name	Generic name	Dosage (mg)	Found* (mg)	Error (mg)	RSD%
SDI, Iraq	Prisolone 5	5	4.87	-0.13	1.023
Accord, UK	Prednisolone 5	5	5.03	+0.03	0.902
Wockhardt, UK	Prednisolone 5 mg	5	4.98	-0.02	0.888
Care Formulation Lab, India	PREDTORE (eye drop) 1%	5	4.89	-0.11	1.303
GPO, Thailand	Prednisolone (Cream) 0.5%	10	9.84	-0.16	1.390

* Mean value of n = 5.

Using widely available chemicals, such as ferric chloride as the color agent and sulfuric acid as the acidity modifier, renders this method highly cost-effective. The overall duration of the proposed procedure is less than one hour, while still maintaining high sensitivity and accuracy.

The method was validated for precision, linearity, recovery, and accuracy. By analyzing a series of standard PRZ solutions within the specified range, the linearity of the proposed method for assaying PRZ was evaluated. Quantification was performed according to the experimentally validated parameters.

Separate analyses at various concentrations of PRZ were conducted to assess the repeatability of the readings and the precision of the method. The resulting readings exhibited a relative standard deviation (RSD%) of less than 1.5%, indicating excellent precision.

The method's selectivity, including the matrix effect, was also investigated. Solutions of PRZ in two different pharmaceutical matrices (tablets and syrup) were spiked with varying amounts of pure PRZ. The resulting measurements demonstrated the method's high selectivity, as there was no interference from excipients in the assay of PRZ using the recommended procedure. The recoveries obtained (n=3) ranged from 97.3% to 100.1%, reflecting satisfactory precision of the method, as shown in Table 3.

Table 3. Various amounts of pure PRZ were spiked into real pharmaceutical samples of PRZ (n = 3).

PRZ dosage forms	Initial concentration (μg/mL)	After Spiking (μg/mL)	Found (μg/mL)	Relative error (%)	Recovery (%)
Tablet	10	11	10.96	0.36	99.6%
Tablet	10	13	12.98	0.15	99.8%
Tablet	10	15	14.82	1.20	98.8%
Tablet	10	20	19.95	0.25	99.8%
Tablet	10	30	30.03	0.10	100.1%
Syrup	10	11	10.70	2.73	97.3%
Syrup	10	13	12.80	1.54	98.5%
Syrup	10	15	14.73	1.80	98.2%
Syrup	10	20	19.70	1.50	98.5%
Syrup	10	30	29.95	0.17	99.8%

4. Conclusion

The proposed colorimetric method has been validated for the assay of PRZ in both its pure form and commercial pharmaceutical preparations. The method demonstrated accuracy, reproducibility, and cost-effectiveness for PRZ quantification. The results obtained were satisfactory. Additionally, the method does not require a separation step, as there is no interference from common excipients. Therefore, the developed technique is suitable for routine analysis of prednisolone.

5. References

Abdul Kareem, R. Q., & Al-Janabi, K. W. S. (2018). Determination of the Degree of Consumption (DoC) of Lube Engine Oils Using Fluorescence Spectroscopy. *Ibn AL- Haitham Journal For Pure and Applied Science*, *31*(1), 124. https://doi.org/10.30526/31.1.1860.

Albayati, T. M., & Jassam, A. A. A. (2019). Synthesis and characterization of mesoporous materials as a carrier and release of prednisolone in drug delivery system. *Journal of Drug Delivery*

Science and Technology, *53*, 101176. https://doi.org/10.1016/j.jddst.2019.101176.

Ali, A. S., & Rasheed, A. S. (2020). Application of hydrophilic interaction chromatography methods for prednisolone acetate determination in their pure and tablet, syrup dosage forms. *Plant Archives*, *20*(1), 2807–2812. http://plantarchives.org/20-1/2807-2812%20(6042).pdf.

Al-Janabi, K. W. S. (2013). Quantification of Acrylamide content in Potato Chips and Iraqi "Harissa." *Ibn Al-Haitham Journal for Pure and Applied Sciences*, *26*(3), 236–244.

Al-Janabi, K. W. S., Mahmood, A. K., & Luaibi, H. M. (2020a). Determination of the Dissociation Constants of Metformin from a Second Derivative UV Spectrum. *International Journal of Research in Pharmaceutical Sciences*, *11*(1), 790–796. https://pharmascope.org/index.php/ijrps/article/view/1896.

Al-Janabi, K. W. S., Mahmood, A. K., & Luaibi, H. M. (2020b). Development of a simple colorimetric determination of dexamethasone. *International Journal of Drug Delivery Technology*, *10*(2), 255–258. https://doi.org/10.25258/ijddt.10.2.12.

Al-Janabi, K. W. S., Mahmood, A. K., & Luaibi, H. M. (2020c). Quantitative Analysis of Some Aromatic Amino Acids By Spectrophotometric Mathematical Derivatization. *Biochemical and Cellular Archives*, *20*(2), 6435–6439.

Balaji, K., Reddy, G. V. R., Reddy, T. M., & Reddy, S. J. (2008). Determination of prednisolone, dexamethasone and hydrocortisone in pharmaceutical formulations and biological fluid samples by voltammetric techniques using b-cyclodextrin modified carbon paste electrode. *African Journal of Pharmacy and Pharmacology*, *2*(8), 157–166. https://doi.org/https://doi.org/10.5897/AJPP.9000096.

Bhusnure, O. G., Manoj, B., Todkar, V., & Giram, P. S. (2015). Analytical Method Development and Validation of Prednisolone Sodium Phosphate by QbD Approach. *IOSR Journal of Pharmacy and Biological Sciences Ver. III*, *10*(6), 2319–7676. https://doi.org/10.9790/3008-10636475.

Dikran, S. B., Mohammed, A. K., & Mahmood, A. K. (2017). Uni and Multivariate Optimization for the Spectrophotometric Determination of Cimetidine Drug via Charge-Transfer Complex Formation. *Ibn AL-Haitham Journal For Pure and Applied Science*, *28*(3), 113–128.

El Gammal, R. N., Hammouda, M. E. A., El-Wasseef, D. R., & El-Ashry, S. M. (2018). Simultaneous determination of gatifloxacin and prednisolone in their bulk powder, synthetic mixture and their combined ophthalmic preparation using micellar liquid chromatography. *Journal of Chromatographic Science*, *56*(4), 367–374. https://doi.org/10.1093/chromsci/bmy011..

Evtifeeva, O. A., Proskurina, K. I., Ganeva, E. V., & Zhukova, T. V. (2016). Evaluation of Metrological Characteristics for Quantitative Spectrophotometric Determination of Prednisolone by an Optical Absorbance Method. *Pharmaceutical Chemistry Journal*, *49*(12), 847–853. https://doi.org/10.1007/s11094-016-1385-2.

Hammod, N. M., Al-Janabi, K. W. S., & Hasan, S. A. (2020). Determination of some volatile organic compounds in the water produced at al-ahdab oilfield in the governorate of Wasit, Iraq using headspace SPE-GC-FID. *Indian Journal of Forensic Medicine and Toxicology*, *14*(1), 994–999. https://doi.org/10.37506/v14/i1/2020/ijfmt/193034.

Hammod, N. M., Al-janabi, K. W. S., & Hasan, S. A. (2020). TRACKING OF THE EXISTENCE OF POLYCYCLIC AROMATIC HYDROCARBONS (PAH) IN WATER RESOURCES AROUND AND AWAY FROM AL-AHDAB OIL FIELD IN WASIT GOVERNORATE OF IRAQ. *Plant Archives*, *20*(2), 5047–5052.

Hannoun, W. A., & Al-Janabi, K. W. S. (2020). Spectrophotometric determination of isopropamide iodide based on ion-pair complex formation with thymol blue. *Indian Journal of Forensic Medicine and Toxicology*, *14*(2), 1043–1049. http://medicopublication.com/index.php/ijfmt/article/view/3045.

Iannella, L., Botrè, F., Colamonici, C., Curcio, D., & de la Torre, X. (2019). Development and validation of a method to confirm the exogenous origin of prednisone and prednisolone by GC-C-IRMS. *Drug Testing and Analysis*, *11*(11–12), 1615–1628. https://doi.org/10.1002/dta.2715.

Kashyap, R., Subrahmanyam, E. V. S., & Sharbaraya, A. R. (2012). Development evelopment and validation of UV spectroscopy method for the estimation of prednisolone in bulk and dosage form. *Journal of Chemical and Pharmaceutical Research*, *4*(2), 1090–1096. https://www.jocpr.com/articles/development-and-validation-of-uv-spectroscopy-method-for-the-estimation-of-prednisolone-in-bulk-and-dosage-form.pdf

Lemus Gallego, J. M., & Pérez Arroyo, J. (2003). Simultaneous Determination of Hydrocortisone and Zn-Bacitracin by Spectrophotometric Derivative and Multivariate Methods. *Microchimica Acta*, *141*(3–4), 133–141. https://doi.org/10.1007/s00604-002-0940-6

Mahmood, A. K. (2017). Development Of Two Different Spectrophotometric Methods For The Determination Of Atropine Drug In Pure Form And Pharmaceutical Preparations. *Ibn AL-Haitham Journal For Pure and Applied Science*, *25*(3), 226–241.

Mortimer, R. J. (2017). Spectroelectrochemistry, Applications. In *Encyclopedia of Spectroscopy and Spectrometry* (pp. 160–171). Elsevier. https://doi.org/10.1016/B978-0-12-803224-4.00288-0

Primpray, V., Chailapakul, O., Tokeshi, M., Rojanarata, T., & Laiwattanapaisal, W. (2019). A paper-based analytical device coupled with electrochemical detection for the determination of dexamethasone and prednisolone in adulterated traditional medicines. *Analytica Chimica Acta*, *1078*, 16–23. https://doi.org/10.1016/j.aca.2019.05.072.

Radhi, N. A. A., & Al-Janabi, K. W. S. (2020). Spectrophotometric determination of Di phenyl hydramine HCl in pure and pharmaceutical formulations using Thymol blue. *Annals of Tropical Medicine and Public Health*.

Raut, G. S., Shirkhedkar, A. A., Ugale, V. G., & Surana, S. J. (2014). Simultaneous determination of Prednisolone acetate and Moxifloxacin hydrochloride in bulk and in eye drop using RP-HPTLC. *Journal of Liquid Chromatography and Related Technologies*, *37*(4), 528–537. https://doi.org/10.1080/10826076.2012.749495.

Razzaq, S. N., Ashfaq, M., Khan, I. U., Mariam, I., Razzaq, S. S., & Azeem, W. (2017). Simultaneous determination of dexamethasone and moxifloxacin in pharmaceutical formulations using stability indicating HPLC method. *Arabian Journal of Chemistry*, *10*(3), 321–328. https://doi.org/10.1016/j.arabjc.2014.11.016.

Schuster, D., Laggner, C., & Langer, T. (2005). Why drugs fail-a study on side effects in new chemical entities. *Current Pharmaceutical Design*, *11*(27), 3545–3559.

Singh, D. K., & Verma, R. (2008). Spectrophotometric Determination of Corticosteroids and Its Application in Pharmaceutical Formulation. *Iranian Journal of Pharmacology & Therapeutics*, *7*(1), 61–65. http://ijpt.iums.ac.ir/article-1-155-en.html.

Skoog, D. A., Holler, F. J., & Crouch, S. R. (2017). *Principles of Instrumental Analysis*. Cengage Learning. https://books.google.iq/books?id=D13EDQAAQBAJ.

Smajdor, J., Piech, R., & Paczosa-bator, B. (2016). *A Novel Method of High Sensitive Determination of Prednisolone on Renewable Mercury Film Silver Based Electrode*. 394–400. https://doi.org/10.1002/elan.201500262.

Xu, J., Winkler, J., & Derendorf, H. (2007). A pharmacokinetic/pharmacodynamic approach to predict total prednisolone concentrations in human plasma. *Journal of Pharmacokinetics and Pharmacodynamics*, *34*(3), 355–372. https://doi.org/10.1007/s10928-007-9050-8.

MULTI-ENTITY STOCK DEPENDENT MODEL WITH CAPACITY AND MANUFACTURE COST RESTRAINT'S

Atma Nand[1a], N. S. Chauhan[2b]

Abstract: Inventory has an impact on the manufacturing process as well as supply chain operations. The fundamental goal of this research paper is to optimize the cost associated with inventories and to provide flow less continuous production process in time. Normally, demand rate of any entity in inventory control model are treated as predictable and at the same time constant too, and that the cost associated to unit inventory must be independent and non-variable in nature. Nevertheless, in practical circumstances, the unit price and demand rate of an entity may be interconnected. When the asking for an article is enormous, an entity is manufactured in huge quantities and the static charges of manufacturing being diffused over a multiple component. Henceforth, per unit article cost decreases significantly. i.e., per unit article cot and the demand of an article are related under inverse variation. So, better to consider the demand rate of an article as a variable constraint than to fixed one. In this research article, a mathematical model for multiple articles through permitted and restricted shortage and per article cost based on demand accompanied by upper and lower limits viz restricted storage space and manufacturing expenses has been constructed. Overall, investigating the simultaneous effect of storage space and manufacturing expenses in an inventory model provides valuable insights that enable cost optimization, resource allocation, capacity planning, and risk mitigation. It helps companies make informed decisions and improve their overall operational efficiency and profitability. The Multi-Entity Stock Dependent Model with Capacity and Manufacture Cost Restraints can be customized and used in a variety of sectors that include managing inventory across numerous entities and complicated supply chain networks. Here are a few examples of industries that can benefit from such a model: manufacturing industry, the retail and distributor sector, e-commerce companies, pharmaceutical and healthcare industry, automotive industry and food and beverage industry. The article cost is explored at this juncture in a fuzzy atmosphere and solutions of the model being obtained through KKT condition. Finally, a conclusion is offered in the final portion.

Keywords: Integrated inventory model, restricted shortages, KKT, fuzzification, variable constraint.

1. Introduction

The economic order quantity model has an essential and key functioning in the field of inventory. When applying the EOQ model to particular practical scenarios encountered in real life, it is difficult to precisely estimate the cost associated with the various terminology of inventory viz, setup, carrying, shortage, demand etc. Only approximate values may be found. Mostly, the situation which are unpredictable and not certain are studied under the influence of stochastic inventory theory.

Inventory control is a crucial area for both real-world applications and research reasons. The most often used inventory model is the Economic Order Quantity model, in which the sequential operations are classed as supply and demand. The first quantitative treatment of inventory was the basic EOQ model. This model was created by Harris (1915) later, Hadley & Whitin (1963) analysed several inventory methods.Abu Hashan Md Mashudand et al. (2021), Mishra U et al. (21), [1]Rahman et al. (2022), [2]Rahman et al. (2022) studies the two warehouse inventory problems to get rid of stockout situation but renting or owning two warehouse increases the investment and overall profitability of the entire model decreases. Miah et al. (2021) developed limited time price discount inventory model but restricted this model for the electronic products only. This model could be more generalize to cover more industries.[1]Roy D et al. (2022), [2]Roy D et al. (2022) studies the inventory models with preservation technology and cap-and-trade policy. Sultana et al. (2022) described the role of the discount policy and its impact on the inventory control model. They extended the earlier work of Shaikh A. A. et al. (2017, 2020) in which author considered fully backlogged inventory model and application of preservation facility with ramp type demand. Md. Alamin Khan et al. (2017) proposed the solution of nonlinear system of equation that could be raised during the development of mathematical formulation of inventory model.

The fundamental goal of this mathematical model is to optimize the cost associated with inventories and to provide flow less continuous production process in time. Normally, demand rate of any entity in inventory control model are treated as predictable and at the same time constant too, and that the cost associated to unit inventory must be independent and non-variable in nature. Nevertheless, in practical circumstances, the unit price and demand rate of an entity may be interconnected. When the asking for an article is enormous, an entity is manufactured in

Authors information:

[a]Department of Mathematics, SALS, Uttaranchal University, Dehradun-248007, INDIA. E-mail: atmanand.prasad@gmail.com[1].
[b]Department of Mathematics, Faculty of Engineering (FOE), Teerthanker Mahaveer University, Moradabad-244001, INDIA.
*Corresponding Author: atmanand.prasad@gmail.com

huge quantities and the static charges of manufacturing being diffused over a multiple component. Henceforth, per unit article cost decreases significantly. i.e., per unit article cot and the demand of an article are related under inverse variation. So, better to consider the demand rate of an article as a variable constraint than to fixed one.

In this chapter, a mathematical model for multiple articles through permitted and restricted shortage and per article cost based on demand accompanied by upper and lower limits viz restricted storage space and manufacturing expenses has been constructed. The article cost is explored at this juncture in a fuzzy atmosphere and solutions of the model being obtained through KKT condition. Finally, a conclusion is offered in the final portion.

2. K-K-T Conditions

Taha (2007) presented how to achieve the optimum solution of a nonlinear programming issue associated to inequality restrictions by applying the Kuhn-Tucker criteria. The construction of the Kuhn-Tucker conditions is based on the Lagrangean approach. Assume that the issue is stated by

Minimize $y = f(x)$ ……..1

Associated to $h_\sigma(x) \geq 0, \sigma = \{x : x \in N\}$. ……..2

The non-negative restrictions $x \geq 0$, if any, are included into the limitations of a natural numbers. The inequality restrictions can be imposed to the equations by implementing non-negative slack variables. Suppose s_σ^2 the amount of slack eliminated from the σth constraint $h_\sigma(x) \geq 0$.

Let $\varepsilon = (\varepsilon_1, \varepsilon_2, \dots \dots, \varepsilon_n)$, ……..4
$h(x) = (g_1(x), g_2(x), \dots, g_n(x))$ ……..5
and $s^2 = (s_1^2, s_2^2, \dots \dots, s_n^2)$ ……..6

Then the Lagrangean functions are given by

$$H(x, s, \varepsilon) = f(x) - \varepsilon[h(x) - s^2]$$ ……..7

Considering the fractional differentiation of H associated to $x, s,$ and ε criteria that are also sufficient if the objective function and solution domain meet the following limitations:

Sense of optimization	Prerequisite conditions	
	Objective function	Solution space
Maximization	Concave	Convex Set
Minimization	Convex	Convex Set

The following is a summary of the requirements for determining if the Kuhn-Tucker conditions are satisfied:

Problem	Kuhn-Tucker conditions	
1. Max z = $f(x)$ associated to $k^\sigma(x) \leq 0, x \geq 0, \sigma = 1, 2, \dots n$	$\dfrac{\partial}{\partial x_j} f(x) - \sum\limits_{\sigma=1}^{n} \varepsilon_\sigma \dfrac{\partial}{\partial x_j} k^\sigma(x) = 0$	……..8
	$\varepsilon_\sigma k^\sigma(x) = 0, k^\sigma(x) \leq 0, \sigma = 1, 2, \dots. n$	……..9
	$\varepsilon_\sigma \geq 0, \sigma = 1, 2, \dots \dots n$	……..10
2. Max z = $f(x)$ associated to $k^\sigma(x) \geq 0, x \geq 0, \sigma = 1, 2, \dots n$	$\dfrac{\partial}{\partial x_j} f(x) - \sum\limits_{\sigma=1}^{n} \varepsilon_\sigma \dfrac{\partial}{\partial x_j} k^\sigma(x) = 0$	……..11
	$\varepsilon_\sigma k^\sigma(x) = 0, k^\sigma(x) \geq 0, \sigma = 1, 2, \dots. n$	……..12
	$\varepsilon_\sigma \geq 0, \sigma = 1, 2, \dots \dots n$	……..13

Karush was one who firstly introduced and developed the K-K-T conditions in 1939.

3. Formulation and Evaluation of The Model

Let the stock volume of σth entity ($\sigma \in N$) be R_σ for instance $t = 0$. In specified range $(0, T_\sigma (= t_{1\sigma} + t_{2\sigma}))$, demand being fulfilled by systematic declination of stock level. This technique results in the inventory level being 0 at the time $t_{1\sigma}$ then the range is allowed to experience shortages in the domain $(t_{1\sigma}, T_\sigma)$.

Figure 3.1 interpret a mathematical model with stock backorder. R_σ is the maximum inventory quantity and Q is the order quantity for one period? Also, $t_{1\sigma}$ indicates the time needed for the R_σ entities to be required. The length of time during one period over whichbackorder will be incurred will be given byFigure-1.
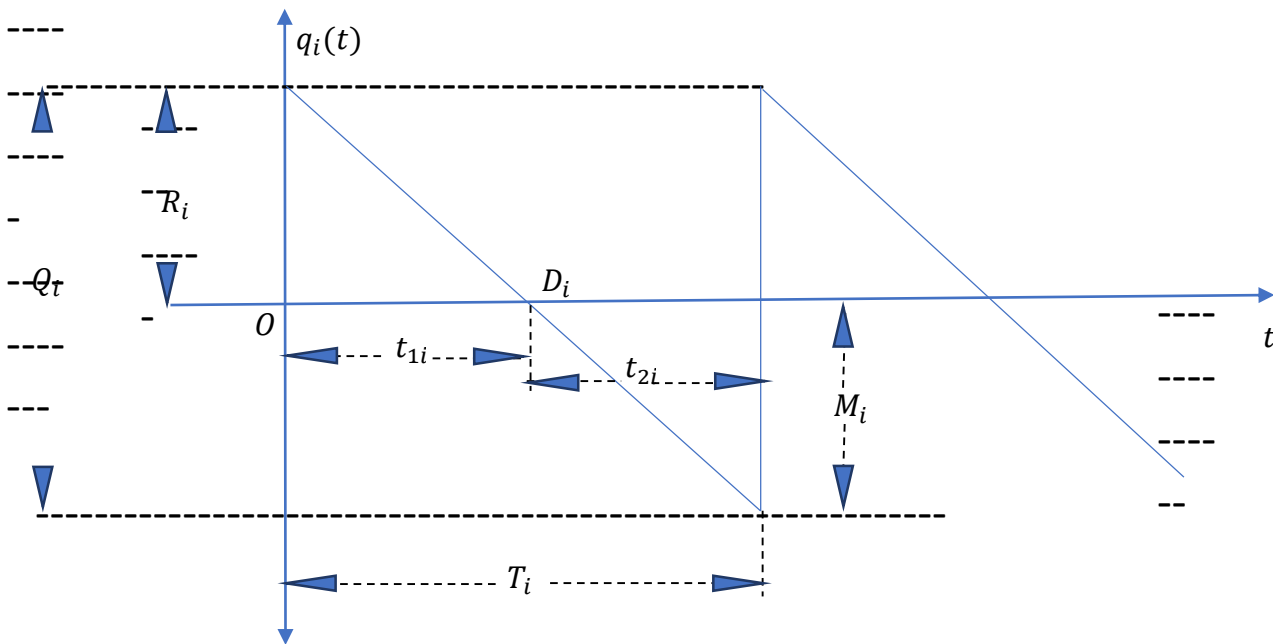
Figure -1 Stock level of the σth entity

Let $q_\sigma(t)$ be the on-hand inventory at time t ($0 \leq t \leq$ T). In this model, uniform replenishment rate starts with inventory level q_σ. The inventory level decreases with demand. Ultimately the inventory reaches 0 at the end of the cycle time $t_{1\sigma}$.

The derivative function describing inventory level $q_\sigma(t)$ of σth entity in the range $0 \leq t \leq T_\sigma$ is given by

$$\frac{dq_\sigma(t)}{dt} = \begin{cases} -D_\sigma, \text{for } 0 \leq t \leq t_{1\sigma} \\ -D_\sigma, \text{for } t_{1\sigma} \leq t \leq T_\sigma \end{cases} \qquad \ldots\ldots.14$$

With the conditions $q_\sigma(0) = R_\sigma (= Q_\sigma - M_\sigma), q_\sigma(T_\sigma) = -M_\sigma$ and $q_\sigma(t_{1\sigma}) = 0$ $\qquad \ldots\ldots.15$

On every interval a certain quantity of shortfall is permitted and there is a penalty cost m_1 per entity of unmet demand per unit time.

$$\text{For } 0 \leq t \leq t_{1\sigma} \qquad \ldots\ldots.16$$

$$\qquad \ldots\ldots.17$$

$$\int_0^t dq_\sigma(t) = - \int_0^t D_\sigma \, dt$$

$$q_\sigma(t) - q_\sigma(0) = -D_\sigma t \qquad \ldots\ldots.18$$

Hence, $q_\sigma(t) = R_\sigma - D_\sigma(t) \qquad \ldots\ldots.19$

For $t_{1\sigma} \leq t \leq T_\sigma \qquad \ldots\ldots.20$

$$\qquad \ldots\ldots.21$$

$$\int_{t_{1\sigma}}^t dq_\sigma(t) = - \int_{t_{1\sigma}}^t D_\sigma \, dt$$

$q_\sigma(t) - q_\sigma(t_{1\sigma}) = -D_\sigma(t - t_{1\sigma}) \qquad \ldots\ldots.22$

Hence, $q_\sigma(t) = D_\sigma(t_{1\sigma} - t) \qquad \ldots\ldots.23$

Thus $q_\sigma(t) = R_\sigma - D_\sigma(t)$, for $0 \leq t \leq t_{1\sigma} \qquad \ldots\ldots.24$

$D_\sigma(t_{1\sigma} - t)$ for $t_{1\sigma} \leq t \leq T_\sigma \qquad \ldots\ldots.25$

Also $D_\sigma t_{1\sigma} = R_\sigma \qquad \ldots\ldots.26$

$M_\sigma = D_\sigma t_{2\sigma} \qquad \ldots\ldots.27$

$Q_\sigma = D_\sigma T_\sigma \qquad \ldots\ldots.28$

The holding cost is related to the cost of carrying (or holding) inventory. This cost frequently encompasses the expenditures such as rent for space, usage for storage, interest on the money locked-up, insurance of stored equipment, manufacturing, taxes, depreciation of equipment and furnishings utilised, etc.

This is derived by evaluating the integral in the range $\qquad \ldots\ldots.29$ $(0, t_{1\sigma})$

$$\text{Holding cost} = H_\sigma \int_0^{t_{1\sigma}} q_\sigma(t) dt \qquad \ldots\ldots.30$$

$$= \frac{H_\sigma (Q_\sigma - M_\sigma)^2}{2D_\sigma} \qquad \ldots\ldots.31$$

$$= \frac{H_\sigma T_\sigma (Q_\sigma - M_\sigma)^2}{2Q_\sigma} \qquad \ldots\ldots.32$$

Since, $Q_\sigma = D_\sigma T_\sigma \qquad \ldots\ldots.33$

The penalty cost for running out of stock (i.e., when an entity cannot be provided on the customer's demand) is known as the shortfall cost. This cost encompasses the loss of projected profit via sales of items and loss of goodwill in terms of permanent loss of customers, and it is tied to lost earnings in future sales. Thus, the shortfall cost is calculated by evaluating the integral in the range $(t_{1\sigma}, T_\sigma)$. This is because the shortage develops only after all the present stockpiles are consumed. Hence,

$$\text{Shortage cost} = n_\sigma \int_{t_{1\sigma}}^{T_\sigma} -q_\sigma(t) \, dt \qquad \ldots\ldots.34$$

$$= -n_\sigma \left[\{T_\sigma q_\sigma(T_\sigma) - t_{1\sigma} q_\sigma(t_{1\sigma})\} - \int_{t_{1\sigma}}^{T_\sigma} t(-D_\sigma) \, dt \right] \qquad \ldots\ldots.35$$

Since, $dq_\sigma(t) = -D_\sigma \, dt$ for $t_{1\sigma} \leq t \leq T_\sigma \qquad \ldots\ldots.36$

The shortage cost becomes,

$$\text{Shortage cost} = n_\sigma \left[\{T_\sigma(-M_\sigma) - 0\} + D_\sigma \int_{t_{1\sigma}}^{T_\sigma} t \, dt \right] \qquad \ldots\ldots.37$$

$$= n_\sigma T_\sigma M_\sigma - \frac{n_\sigma D_\sigma}{2}[T_\sigma^2 - t_{1\sigma}^2] \qquad \ldots\ldots.38$$

But $T_\sigma = \frac{Q_\sigma}{D_\sigma}$

$t_{1\sigma} = \frac{R_\sigma}{D_\sigma} = \frac{(Q_\sigma - M_\sigma)}{D_\sigma}$ and $Q_\sigma = R_\sigma + M_\sigma \qquad \ldots\ldots.39$

$$= n_\sigma M_\sigma T_\sigma = \frac{n_\sigma D_\sigma}{2}\left[\frac{Q_\sigma^2}{D_\sigma^2} - \frac{R_\sigma^2}{D_\sigma^2}\right] \qquad \ldots\ldots.40$$

$$= n_\sigma M_\sigma T_\sigma - \frac{n_\sigma}{2D_\sigma}[\{R_\sigma + M_\sigma\}^2 - R_\sigma^2] \qquad \ldots\ldots.41$$

$$= \frac{n_\sigma M_\sigma^2}{2D_\sigma} \qquad \ldots\ldots.42$$

$$= \frac{n_\sigma M_\sigma^2 T_\sigma}{2Q_\sigma} \qquad \ldots\ldots.43$$

Since, $D_\sigma = \frac{Q_\sigma}{T_\sigma}$

The cost of manufacturing each component of the system is provided by

Production cost = $P_\sigma Q_\sigma$

Additionally, each entity's setup price is provided by

Setup cost = S_σ

The total cost is defined as the sum of production cost, setup cost, holding cost and shortage cost.

$$TC = p_\sigma Q_\sigma + S_\sigma + \frac{H_\sigma T_\sigma (Q_\sigma - M_\sigma)^2}{2Q_\sigma} + \frac{n_\sigma M_\sigma^2 T_\sigma}{2Q_\sigma}, \text{ for } \sigma = \qquad \ldots\ldots.44$$

$1, 2, \ldots, n.$

The overall average cost of the σth entity of the system is then given by

$$TC(p_\sigma, Q_\sigma, M_\sigma) = p_\sigma D_\sigma + \frac{S_\sigma D_\sigma}{Q_\sigma} \qquad \ldots\ldots.45$$
$$+ \frac{H_\sigma (Q_\sigma - M_\sigma)^2}{2Q_\sigma} + \frac{n_\sigma M_\sigma^2}{2Q_\sigma}$$

The unit price of an entity is often thought of as being constant and independent in nature, and the classical inventory concerns are formed by taking these assumptions into account. By making the assumption that the demand rate and unit price are constants and independent of one another, Silver & Peterson (1985) developed an inventory model. However, in real-world situations, a company's unit price and demand rate may be connected. When there is a high demand for something, it is produced in vast quantities and the fixed production costs are spread among a lot of different goods. As a result, the entity's unit cost declines, making its unit price inversely linked to its demand. This strategy was used by Jung & Klein (2001) to propose and resolve the Economic Order Quantity problem. The inventory model with demand-dependent unit pricing is solved in the current study by utilising the Karush Kuhn-Tucker method.

4. Assumptions of the Inventory Model

Under the following presumptions, a multi-entity stock non-restricted shortage model has been developed.
Instant replenishment is available.
No lead time exists.
Demand is correlated with unit price as $p_\sigma = A_\sigma^\beta D_\sigma^{-\beta}$
where $A_\sigma (> 0)$ and $\beta (\beta > 1)$ being non-variable, non-imaginary numbers chosen to provide the best fit of the estimated price function $A_\sigma > 0$ is a necessary constraint as individually D_σ and P_σ need to positive.

5. Objective Function of the Model

The objectives of the issue are as follows:
According to the objective of modelling, the total cost of materials must minimise in the system which comprises three parts with shortage cost.
The annual total cost rendering to the fundamental valuation of the mathematical model for economic order quantity is:

Overall cost = manufacture cost + setup cost + holding cost + shortage cost

$$TC(p_\sigma, Q_\sigma, M_\sigma) = p_\sigma D_\sigma + \frac{S_\sigma D_\sigma}{Q_\sigma} \qquad \ldots\ldots.46$$
$$+ \frac{H_\sigma (Q_\sigma - M_\sigma)^2}{2Q_\sigma} + \frac{n_\sigma M_\sigma^2}{2Q_\sigma}$$

Substituting for p_σ gives

$$TC(D_\sigma, Q_\sigma, M_\sigma) = A_\sigma^\beta D_\sigma^{1-\beta} + \frac{S_\sigma D_\sigma}{Q_\sigma} \qquad \ldots\ldots.47$$
$$+ \frac{H_\sigma (Q_\sigma - M_\sigma)^2}{2Q_\sigma} + \frac{n_\sigma M_\sigma^2}{2Q_\sigma}$$

for $\sigma = 1,2,3,\ldots\ldots n$

The inventory model's primary goal is to reduce the overall cost specified by

$$\text{Min } TC(D_\sigma, Q_\sigma, M_\sigma) \qquad \ldots\ldots.48$$
$$= \sum_{\sigma=1}^{n} \left[A_\sigma^\beta D_\sigma^{1-\beta} + \frac{S_\sigma D_\sigma}{Q_\sigma} \right.$$
$$\left. + \frac{H_\sigma (Q_\sigma - M_\sigma)^2}{2Q_\sigma} + \frac{n_\sigma M_\sigma^2}{2Q_\sigma} \right]$$

6. Constraints of the Model

The following limitations have been put on the proposed model: In order to achieve the ideal overall cost, it is necessary to take into account a variety of resource limitations. The amount of warehouse floor space that can be used to store the items is limited.

$$\text{i.e; } \sum_{\sigma=1}^{n} w_\sigma Q_\sigma \leq W \qquad \ldots\ldots.49$$

The amount that can be invested in overall production costs is finite and may have a maximum investment level.

$$\text{i.e; } \sum_{\sigma=1}^{n} p_\sigma Q_\sigma \leq B \qquad \ldots\ldots.50$$
$$\Rightarrow \text{i.e; } \sum_{\sigma=1}^{n} A_\sigma^\beta D_\sigma^{-\beta} Q_\sigma \leq B \qquad \ldots\ldots.51$$

7. Uncertain Stock Model

When $p_\sigma's$ are uncertain decision constraints, the above crisp formulation underneath uncertain situation reduces to

$$\text{Min } TC(p_\sigma, D_\sigma, Q_\sigma, M_\sigma) \qquad \ldots\ldots.52$$
$$= \sum_{\sigma=1}^{n} \left[A_\sigma^\beta D_\sigma^{1-\beta} + \frac{S_\sigma D_\sigma}{Q_\sigma} \right.$$
$$\left. + \frac{H_\sigma (Q_\sigma - M_\sigma)^2}{2Q_\sigma} + \frac{n_\sigma M_\sigma^2}{2Q_\sigma} \right]$$

associated to the limitations

$$\sum_{\sigma=1}^{n} w_\sigma Q_\sigma \leq W \qquad \ldots\ldots.53$$
$$\sum_{\sigma=1}^{n} A_\sigma^\beta D_\sigma^{-\beta} Q_\sigma \leq B \qquad \ldots\ldots.54$$

Where $\widetilde{p_\sigma} = A_\sigma^\beta D_\sigma^{-\beta}$ and $\widetilde{p_\sigma}$ represents fuzzification of the parameters.

8. Karush Kuhn-Tucker Conditions f2or Solving the Stock Model

The impartial function of a stock model is

$$M\sigma n \ TC \ (D_\sigma, Q_\sigma, M_\sigma) \qquad \ldots\ldots.55$$

$$= \sum_{\sigma=1}^{n} \left[A_\sigma^\beta D_\sigma^{1-\beta} + \frac{S_\sigma D_\sigma}{Q_\sigma} + \frac{H_\sigma(Q_\sigma - M_\sigma)^2}{2Q_\sigma} + \frac{n_\sigma M_\sigma^2}{2Q_\sigma} \right]$$

associated to the constraints

$$\sum_{\sigma=1}^{n} w_\sigma Q_\sigma \leq W \qquad \ldots\ldots.56$$

$$\sum_{\sigma=1}^{n} A_\sigma^\beta D_\sigma^{-\beta} Q_\sigma \leq B \qquad \ldots\ldots.57$$

Here the decision constraints are the demand D_σ, lot size Q and the shortage level M_1. The problem is, to solve the above inventory model with these decision variables associated to the inequality constraints (3.3) and (3.4) in order to minimize the overall cost function. The problem is solved for a unit entity. For a single entity the objective function and the constraints can be written as follows.

$$\text{Min } TC \ (D, Q, M) = \sum_{\sigma=1}^{n} \left[A^\beta D^{1-\beta} + \frac{SD}{Q} + \frac{H(Q-M)^2}{2Q} + \frac{nM^2}{2Q} \right] \qquad \ldots\ldots.58$$

associated to the inequality constraints

$$wQ \leq W \qquad \ldots\ldots.59$$
$$A^\beta D^{-\beta} Q \leq B \qquad \ldots\ldots.60$$

To minimize the objective function, the Lagrangean function has been constructed by introducing the variables s_1 and s_2 as follows:

9. Relationship Function

The relationship function for the vague variable P_σ is defined as follows

$$\mu_{p_\sigma}(X) = \begin{cases} 1, p_\sigma \leq L_{L_\sigma} \\ \dfrac{U_{L_\sigma} - p_\sigma}{U_{L_\sigma} - L_{L_\sigma}}, L_{L_\sigma} \leq p_\sigma \leq U_{L_\sigma} \\ 0, p_\sigma \geq U_{L_\sigma} \end{cases}$$

Here U_L and L_L are superior bound and inferior bound of P_σ correspondingly.

10. Numerical Example

To illustrate the suggested mathematical model for stock with and without shortage instances, the following input data are examined in correct units for a single entity. A numerical example has been constructed for a single entity with the set of input parametric values given in Table-l.

Table-1 The input values of parameters in the mathematical model

Parameter	Notation	Value (in rupees)
Number of entities	n	1
Constant	A_1	20
Setup cost of the entity 1	S_1	80
Holding cost of the entity 1	H_1	0.7
Storage space for the entity 1	w_1	3sq.ft.
Storage space available	W	280sq.ft.
Total investment cost	B	40
Shortage cost per unit entity	n_1	10
Lower limit of the component cost of the entity 1	L_{L_1}	1
Upper limit of the component cost of the entity 1	U_{L_1}	2

For the above data, the objective function becomes

$$G = 20^\beta D^{1-\beta} + 80DQ^{-1} + 0.35(Q-M)^2 Q^{-1} + 5M^2 Q^{-1} - \varepsilon_1(280 - 3Q - s_1^2) - \varepsilon_2(40 - 20^\beta D^{-\beta} Q - s_2^2) \qquad \ldots\ldots.62$$

$$G = 20^\beta D^{1-\beta} + 80DQ^{-1} + 0.35Q - 0.7M + 5.35M^2 Q^{-1} - \varepsilon_1(280 - 3Q - s_1^2) - \varepsilon_2(40 - 20^\beta D^{-\beta} Q - s_2^2) \qquad \ldots\ldots.63$$

Differentiating (63) partially with respect to D, Q and M respectively we get

By the Kuhn-Tucker conditions

$$\frac{\partial G}{\partial D} = 0 \Rightarrow (1-\beta)20^{\beta}D^{-\beta} + 80Q^{-1} - \beta\varepsilon_2 20^{\beta}D^{-\beta-1}Q = 0 \qquad \ldots\ldots.67$$

$$\frac{\partial G}{\partial Q} = 0 \Rightarrow 80DQ^{-2} + 0.35 - 5.35\,Q^{-2}M^2 + 3\varepsilon_1 + \varepsilon_2 20^{\beta}D^{-\beta} \qquad \ldots\ldots.68$$
$$= 0$$

$$\frac{\partial G}{\partial M} = -0.7 + 10.7Q^{-1}M = 0 \qquad \ldots\ldots.69$$

Hence, an optimal solution has been obtained by solving the Equations (6), (7) & (8) by implementing K-K-T conditions with demand D, portion size Q and the deficiency level M as the decision constraints by varying the parametric value β. Also, an optimum solution has been obtained by fuzzifying the unit cost and the results are discussed in Table 2.

The value of the parameter β has been chosen between 2 and 3. The most suitable values are obtained for the parametric values β such as 2.4, 2.5, 2.6 and 2.8 by trial-and-error method that minimizes the objective function.

A sensitivity analysis for optimum solution with shortages corresponding to the parameter β is given in Table 2.

Table-2 Optimal results for the model with shortages

β	P_1	μ_{p_σ}value	D_1	Q_1	M_1	Expected Total cost
2.4	1.2853	0.7147	18.014	62.092	4.061	55.151
2.5	1.3053	0.6947	17.978	62.899	4.114	54.872
2.6	1.3278	0.6722	17.934	63.627	4.161	54.633
2.8	1.3806	0.6194	17.824	64.834	4.240	54.197

In Table 2, a study of expected total cost with demand and lot size including shortages is given for different values of β. We can conclude that when demand decreases, lot size increases but the annual total cost decreases.

$$\frac{\partial G}{\partial D} = (1-\beta)20^{\beta}D^{-\beta} + 80Q^{-1} - \beta\varepsilon_2 20^{\beta}D^{-\beta-1}Q \qquad \ldots\ldots.64$$

$$\frac{\partial G}{\partial Q} = 80DQ^{-2} + 0.35 - 5.35\,Q^{-2}M^2 + 3\varepsilon_1 + \varepsilon_2 20^{\beta}D^{-\beta} \qquad \ldots\ldots.65$$

$$\frac{\partial G}{\partial M} = -0.7 + 10.7Q^{-1}M \qquad \ldots\ldots.66$$

From the above table it follows that 1.2853 has the extreme relationship value 0.7147. Henceforth the enforced optimal resolution is $Q_1 = 62.092$, $D_1 = 18.014$, $M_1 = 4.061$ and Minimum expected total cost 55.151.

11. Sensitivity Analysis

Sensitivity examination is investigated to check in what way the productivity of the mathematical model is influenced by modifications or errors in its input parameters based on the numerical example. The outcomes are demonstrated through the assistance of numerical example. A model with and without shortage is discussed in this chapter.

One of the most fundamental inventory models is the stochastic model. The model is significant because it continues to be one of the most widely used inventory models in the sector and acts as a foundation for more sophisticated inventory models.

The values of ambiguous variables needed for decision-making are obtained by solving the inventory model using the Kuhn-Tucker condition technique. The maximum membership function value of 0.7147 corresponds to the best values of the choice variables and the overall cost. Hence the optimal solution is $Q_1 = 62.092$, $D_1 = 18.014$, $M_1 = 4.061$ and TC = 55.151.Results due to different values of β for the model has been calculated and depicted in the following Figures 2, 3, 4, 5 and 6.

Figure 2 Effect of change in demand level with respect to β
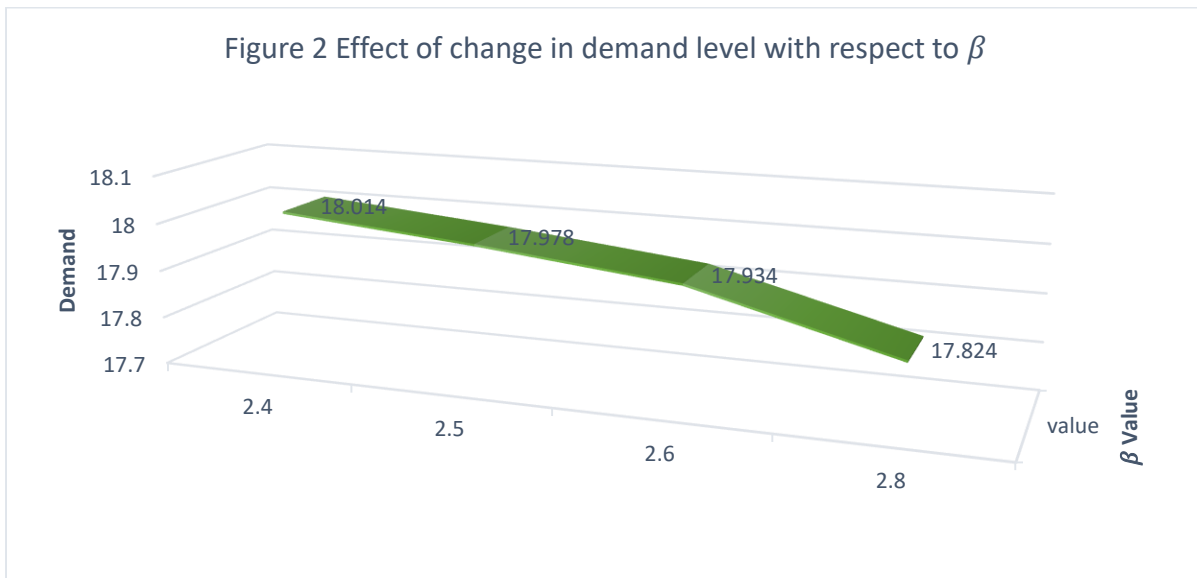
The above Figure 2 shows that as the value of the parameter β increases from 2.4 to 2.8, the value of the demand decreases from 18.014 to 17.824.

Figure 3 Effect of change in unit price with respect to β
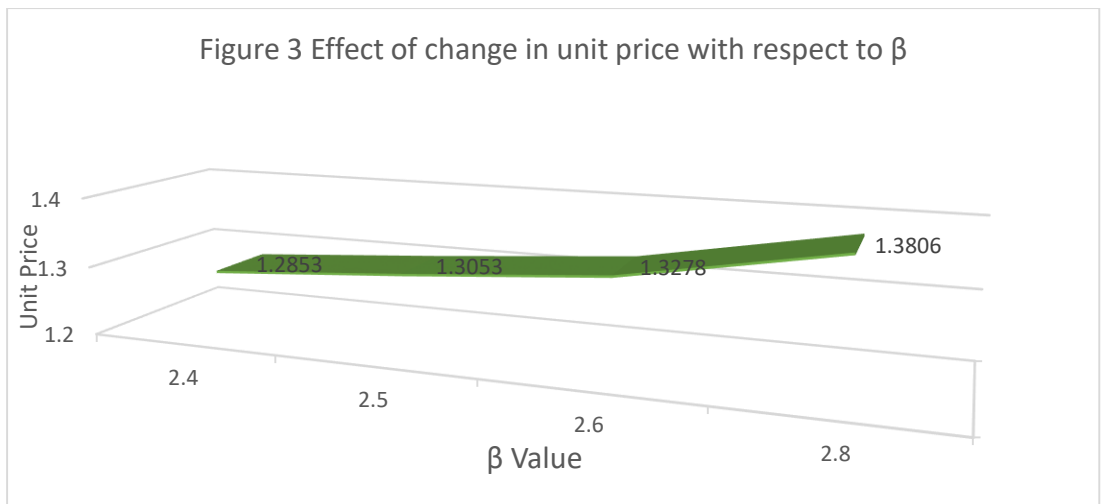
The above Figure 3 shows that as the value of the parameter β increases from 2.4 to 2.8, the value of the unit price increases from 1.2853 to 0.1.3806.

Figure 4a Effect of change in demand with respect to β

Figure 4b Effect of change in ordering quantity with respect to β
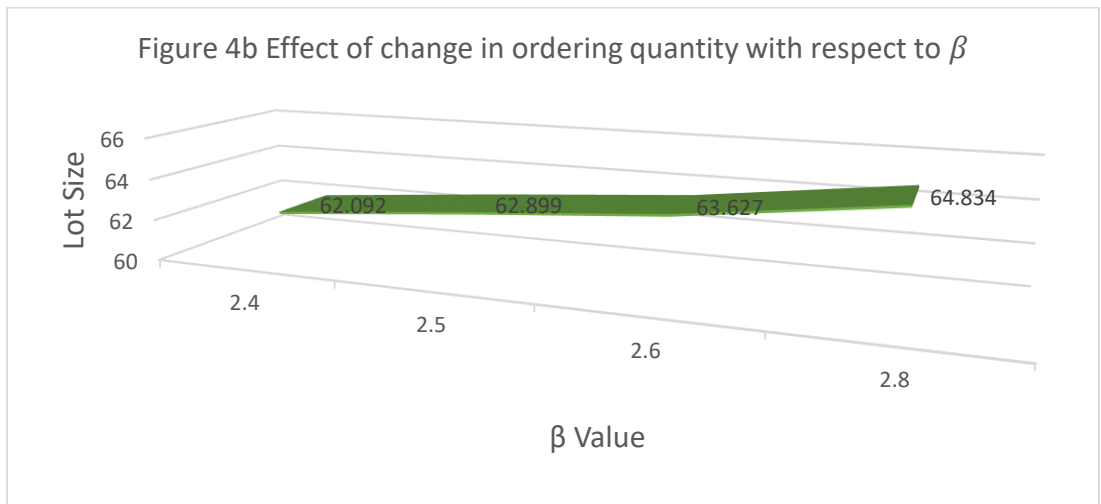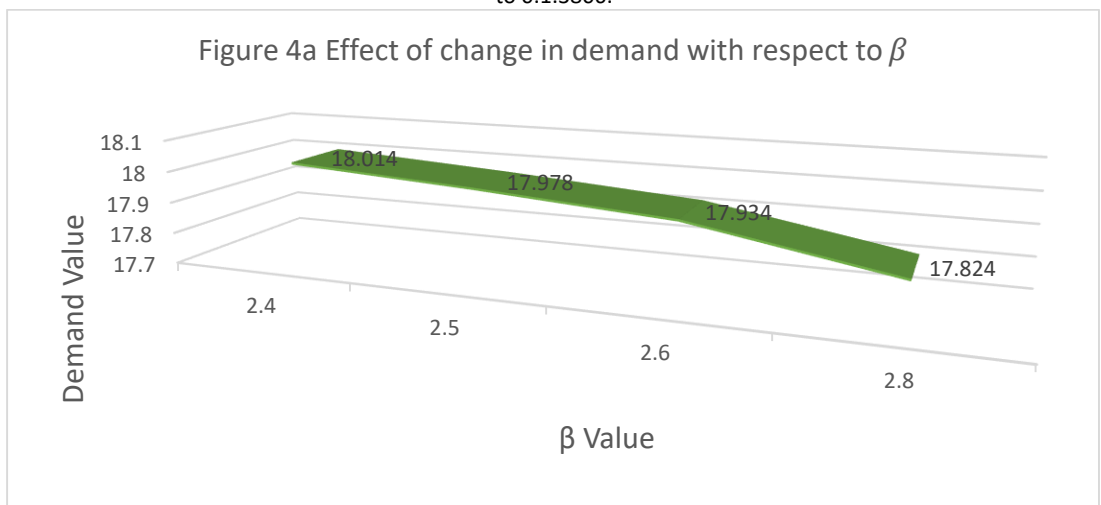
The above Figure 4 shows that as the value of the parameter β increases from 2.4 to 2.8, the value of the lot size increases from 62.092 to 64.834.

Figure 5 Effect of change in shortage level with respect to β
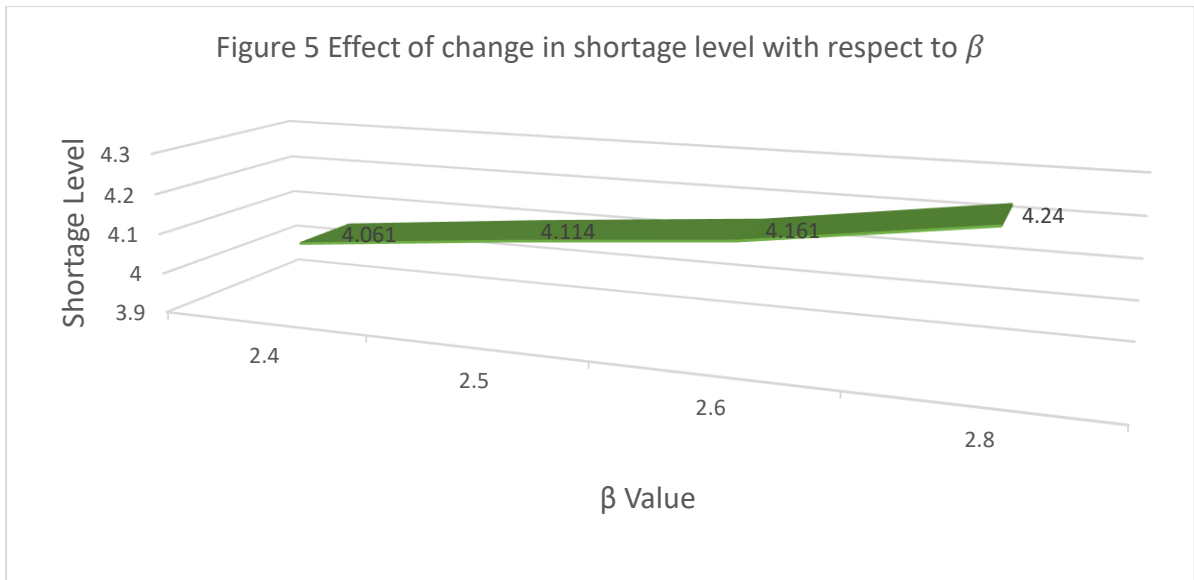
The above Figure 5 shows that as the value of the parameter β increases from 2.4 to 2.8, the value of the shortage level increases from 4.061 to 4.240.

Figure 6 Effect of change in total cost with respect to β

The above Figure 6 shows that as the value of the parameter β increases from 2.4 to 2.8, the value of the annual total cost decreases from 55.151 to 54.197.
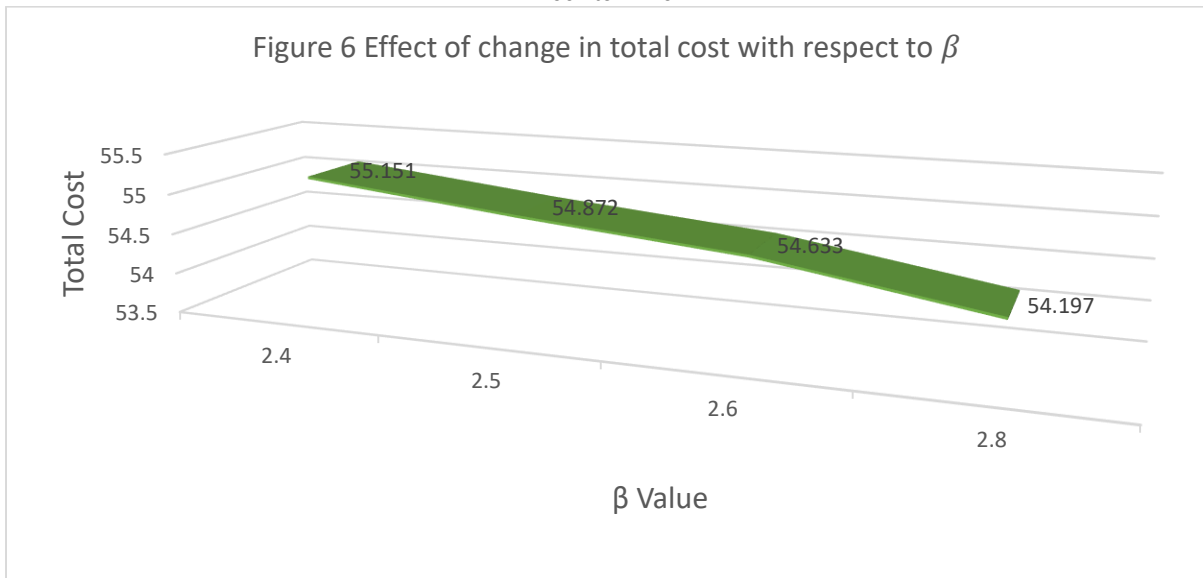
12. Inventory Model Without Shortages as a Singular Instance

It is possible to get the scenario without a shortage by inserting in the preceding model. The only variables that affect the total cost function in this scenario are demand and lot size. An inventory model without shortages can be reduced to

$$M\sigma n\, TC\, (D_\sigma, Q_\sigma) = \sum_{\sigma=1}^{n} \left[A_\sigma^\beta D_\sigma^{1-\beta} + \frac{S_\sigma D_\sigma}{Q_\sigma} + \frac{H_\sigma Q_\sigma}{2} \right] \quad \dots\dots.70$$

associated to the constraints

$$\sum_{\sigma=1}^{n} w_\sigma Q_\sigma \le W \quad \dots\dots.71$$

$$\sum_{\sigma=1}^{n} A_\sigma^\beta D_\sigma^{-\beta} Q_\sigma \le B \quad \dots\dots.72$$

For a single entity the inventory model can be stated as

$$M\sigma_n TC\, (D, Q) = A^\beta D^{1-\beta} + \frac{SD}{Q} + \frac{HQ}{2} \quad \dots\dots.73$$

associated to the constraints

$$wQ \le W \text{ and} \quad \dots\dots.74$$

$$A^\beta D^{-\beta} Q \le B \quad \dots\dots.75$$

The Lagrangean function corresponding to this objective function can be written as

$$G = A^\beta D^{1-\beta} + SDQ^{-1} + 0.5HQ - \varepsilon_1(W - wQ - s_1^2) - \varepsilon_2(B - A^\beta D^{-\beta}Q - s_2^2) \quad \dots\dots.76$$

Differentiating the above functionpartially with respect to D and Q gives the following derivatives.

$$\frac{\partial G}{\partial D} - (1-\beta)A^\beta D^{-\beta} + SQ^{-1} - \varepsilon_2 \beta A^\beta D^{-\beta-1}Q \quad \dots\dots.77$$

By Karush Kuhn-Tucker conditions

$$\frac{\partial G}{\partial D} = 0 \Longrightarrow (1 - \beta)A^{\beta}D^{-\beta} + SQ^{-1} - \varepsilon_2\beta A^{\beta}D^{-\beta-1}Q = 0 \quad \dots\dots..78$$

$$\frac{\partial G}{\partial D} = 0 \Longrightarrow -SDQ^{-2} + 0.5H + \varepsilon_1 w + \varepsilon_2 A^{\beta}D^{-\beta} = 0 \quad \dots\dots..79$$

Solving the Equations (14) and (15) gives the required optimum solution. Ideal resolution in deprived of shortages is assumed in the subsequent Table 3 for the same set of input values given in Table I.

Table 3 Optimal values for various values of for no-shortage case

β	p_1	μ_{p_1} value	D_1	Q_1	Expected Total cost
2.4	1.3405	0.6595	17.701	59.538	56.519
2.5	1.3624	0.6376	17.673	60.268	56.282
2.6	1.3857	0.6143	17.642	60.967	56.059
2.8	1.4407	0.5593	17.555	62.223	55.649

In this case, it follows that the minimum annual total cost corresponds to the determined relationship function value is 0.6595. Hence the optimal result satisfying the constraints are $D_1 = 17.701$, $Q_1 = 59.538$ and the minimum total cost is equal to 56.519. The graphical representations are shown in the Figure 7, 8,9 and 10.

Figure 7 Effect of change in demand level with respect to β
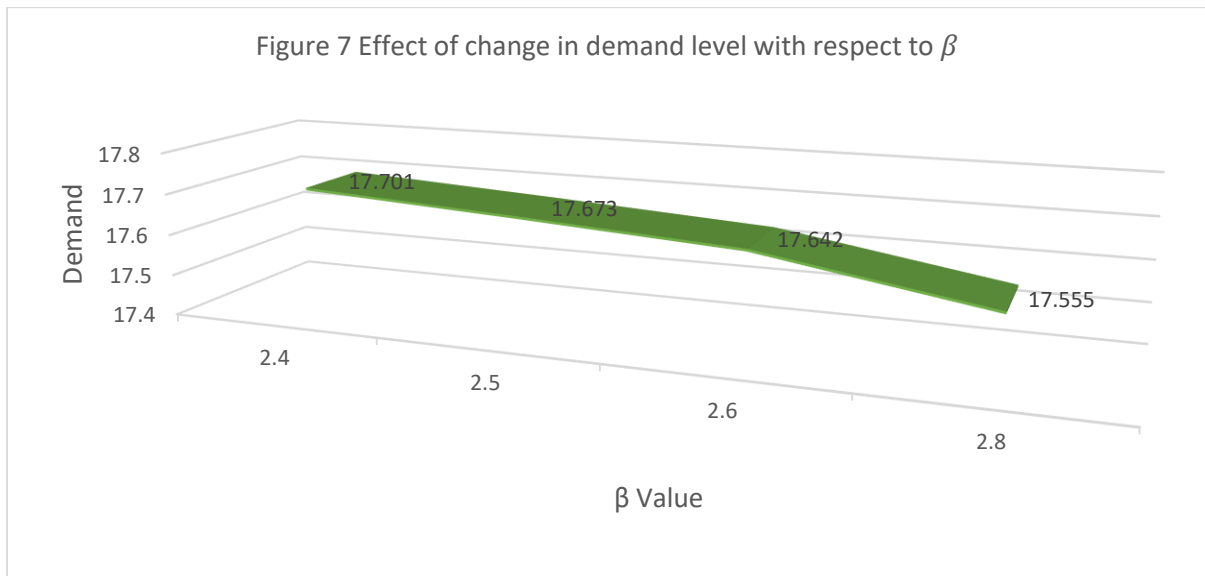
The above Figure 7 shows that as the value of the parameter β increases from 2.4 to 2.8, the value of the demand decreases from 17.701 to 17.555.

Figure 8 Effect of change in ordering quantity with respect to β
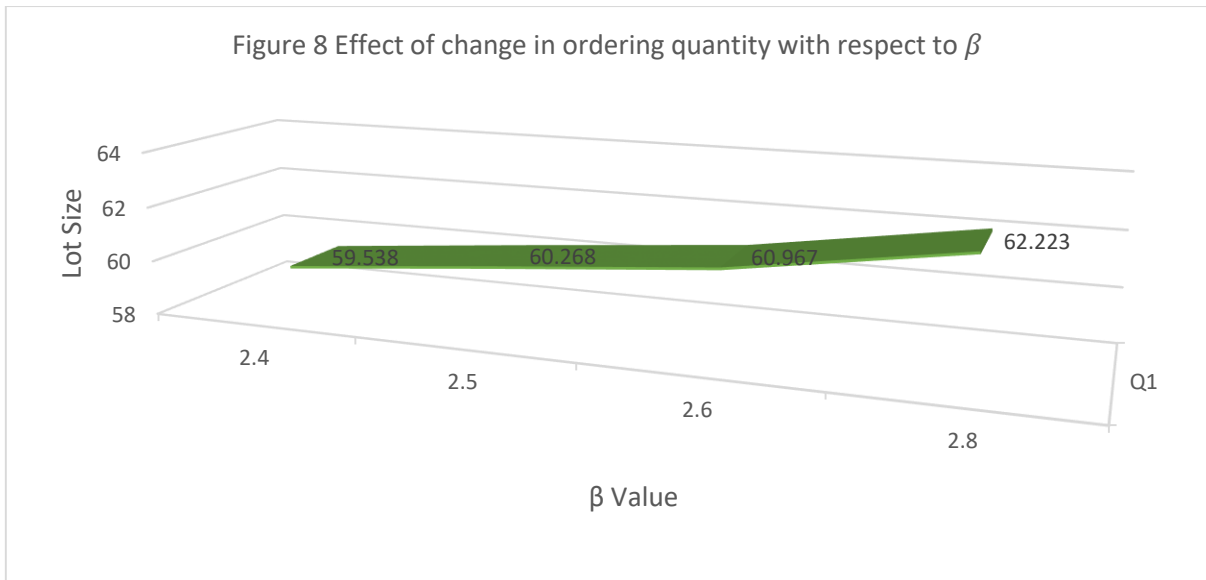
The above Figure 8 shows that as the value of the parameter β increases from 2.4 to 2.8, the value of the lot size increases from 59.538 to 62.223.

Figure 9 Effect of change in unit price with respect to β
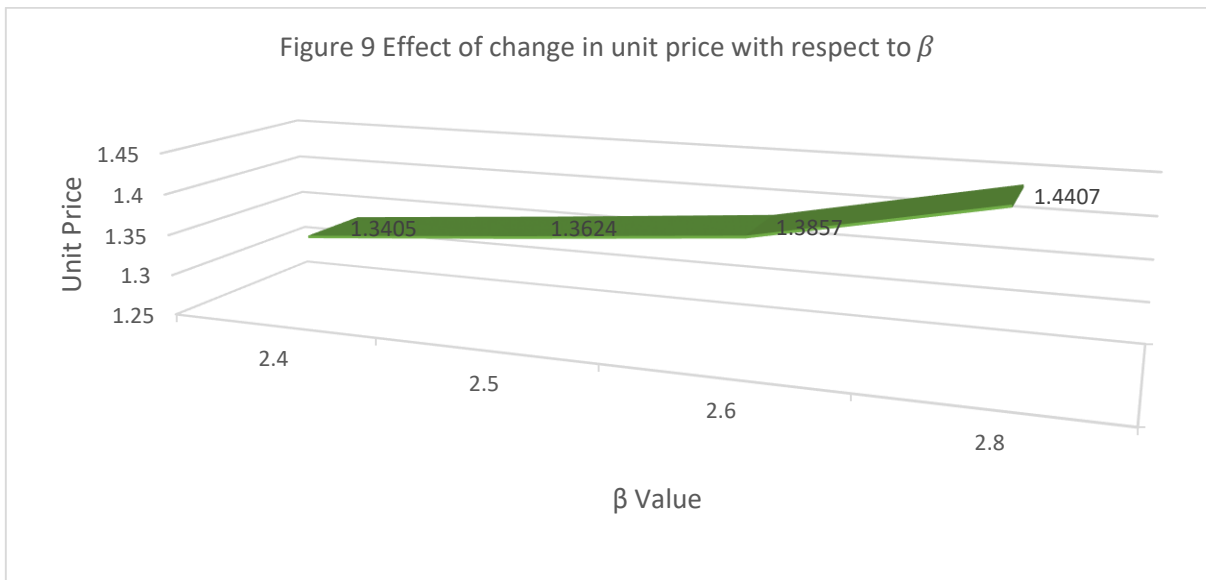
The above Figure 9 shows that as the value of the parameter β increases from 2.4 to 2.8, the value of the unit price increases from 1.3405 to 1.4407.
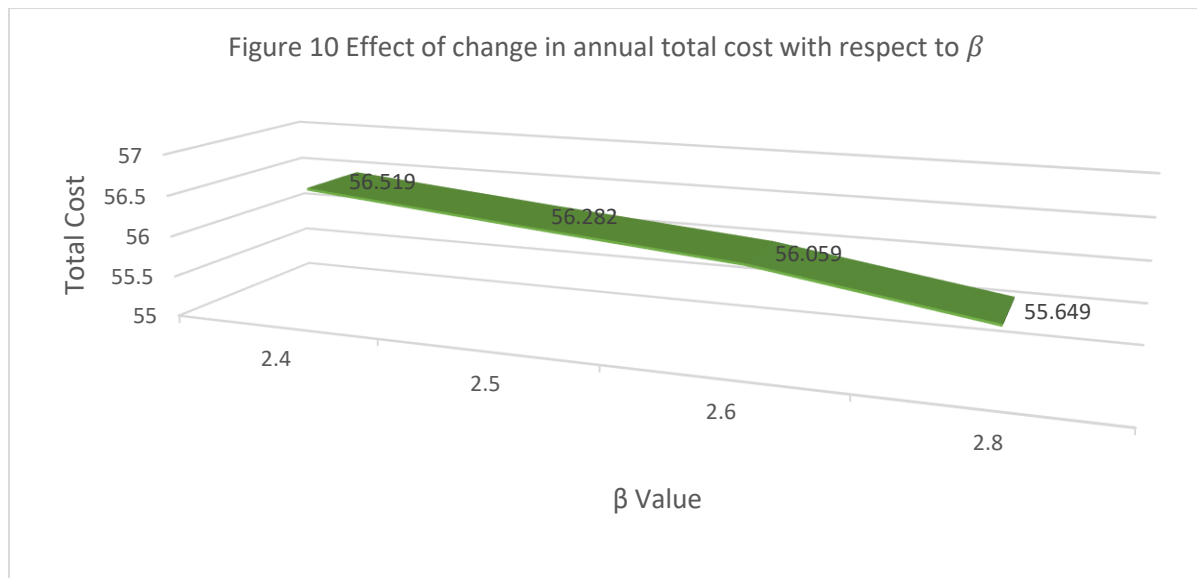
Figure 10 Effect of change in annual total cost with respect to β

The above Figure 10 shows that as the value of the parameter β increases from 2.4 to 2.8, the value of the total cost decreases from 56.519 to 55.649.

13. Summary

In this research article, a mathematical model for multiple articles through permitted and restricted shortage and per article cost based on demand accompanied by upper and lower limits viz restricted storage space and manufacturing expenses has been constructed. The article cost is explored at this juncture in a fuzzy atmosphere and solutions of the model being obtained through KKT condition. A comparison study of the findings for with shortage case(Table-2) and without shortage case(Table-3) is done. In the numerical examples(Table-1), it is found that the optimum total cost in the shortage scenario is less than that of the without shortage case.

The purpose behind developing this model is to provide several managerial insights and constructive conclusion such as: the model aids managers in deciding how best to distribute resources among various supply chain organizations.To maximise overall performance, managers may take well-informed decisions on production schedules, capacity utilisation, and cost-cutting strategies. Managers may minimise stockouts, assure product availability, and optimise inventory levels while taking capacity constraints and production costs into account.It offers information on how adjustments to production procedures, capacity use, and inventory allocation might result in cost reductions.It assists managers in determining the impact of variable demand, capacity constraints, or cost variations on inventory management. Organizations may use this information to establish risk-mitigation measures such as safety stock management, contingency planning, and alternate sourcing choices.The model serves as a framework for assessing and improving supply chain performance. Managers may identify areas for improvement and apply specific initiatives to increase overall performance by analysing key performance metrics such as inventory turnover, order fulfilment rates, and manufacturing cost ratios

Ultimately, it helps businesses to make efficient decisions about inventory management, resource allocation, and cost reduction. Managers may boost efficiency, cut costs, enhance customer happiness, and establish a competitive edge in their respective sectors by recognising the interdependencies between storage space, production expenditures, and other restrictions.

One of the possible extensions of this chapter is to establish particular conditions that guarantee the global optimality of solutions. It is also conceivable to consider the life cycle to be a stochastic function. When this model would cover the time value of money and inflation, a better reflection of real-life scenarios could be presented.

14. References

Bardhan, S., Pal, H., &Giri, B. C. (2019). Optimal replenishment policy and preservation technology investment for a non-instantaneous deteriorating item with stock-dependent demand. *Operational Research*, *19*(2), 347-368.

Barman, A., Das, R., & De, P. K. (2021). Optimal pricing, replenishment scheduling, and preservation technology investment policy for multi-item deteriorating inventory model under shortages. *International Journal of Modeling, Simulation, and Scientific Computing*, *12*(05), 2150039.

Erlenkotter, D. (1990). Ford Whitman Harris and the economic order quantity model. *Operations Research*, *38*(6), 937-946.

Hadley, G. W., & Whitten, T. (1963). TM, 1963. Analysis of Inventory systems. *Englewood Cliffs, NJ*, *1963*.

Mashud, A. H. M., Wee, H. M., & Huang, C. V. (2021). Preservation technology investment, trade credit and partial backordering

model for a non-instantaneous deteriorating inventory. *RAIRO-Operations Research*, *55*, S51-S77.

Md. Alamin Khan, A. H. M. M., M. A. Halim. (2017). Numerous Exact Solutions Of Nonlinear Partial Differential Equations By Tan–Cot Method. Journal of Mechanics of Continua Mathematical sciences, 11(2), 37-48.

Md Mashud, A. H., Pervin, M., Mishra, U., Daryanto, Y., Tseng, M.-L., & Lim, M. K. (2021). A sustainable inventory model with controllable carbon emissions in green-warehouse farms. Journal of Cleaner Production, 298, 126777. doi:https://doi.org/10.1016/j.jclepro.2021.126777

Miah, M. S., Islam, M. M., Hasan, M., Mashud, A. H. M., Roy, D., & Sana, S. S. (2021). A Discount Technique-Based Inventory Management on Electronics Products Supply Chain. Journal of Risk and Financial Management, 14(9), 398.

Mishra, V. K. (2014). Controllable deterioration rate for time-dependent demand and time-varying holding cost. *Yugoslav Journal of Operations Research*, *24*(1), 87-98.

Mishra, U., Mashud, A. H. M., Tseng, M.-L., & Wu, J.-Z. (2021). Optimizing a Sustainable Supply Chain Inventory Model for Controllable Deterioration and Emission Rates in a Greenhouse Farm. Mathematics, 9(5), 495.

Nath, B. K., & Sen, N. (2021). A partially backlogged two-warehouse EOQ model with non-instantaneous deteriorating items, price and time dependent demand and preservation technology using interval number. *International Journal of Mathematics in Operational Research*, *20*(2), 149-181.

Pal, H., Bardhan, S., &Giri, B. C. (2018). Optimal replenishment policy for non-instantaneously perishable items with preservation technology and random deterioration start time. *International Journal of Management Science and Engineering Management*, *13*(3), 188-199.

Rahman, M. M., Ahmed, R., Mashud, A. H. M., Malik, A. I., Miah, S., & Abedin, M. Z. (2022). Consumption-Based CO2 Emissions on Sustainable Development Goals of SAARC Region. Sustainibility, 14(3), 1467.

Rahman, M. M., Anan, N., Mashud, A. H. M., Hasan, M., & Tseng, M.-L. (2022). Consumption-based CO2 emissions accounting and scenario simulation in Asia and the Pacific region. Environmental Science and Pollution Research, 29(23), 34607-34623. doi:10.1007/s11356-021-18265-w

Roy, D., Hasan, S. M. M., Rashid, M. M., Hezam, I. M., Al-Amin, M., Chandra Roy, T., . . . Mashud, A. H. M. (2022). A Sustainable Advance Payment Scheme for Deteriorating Items with Preservation Technology. Processes, 10(3), 546.

Roy, D., &Mashud, A. H. M. (2022). Optimizing profit in a controlled environment: Assessing the synergy between preservation technology and cap-and-trade policy. Journal of King Saud University - Science, 34(3), 101899. doi:https://doi.org/10.1016/j.jksus.2022.101899

Shaikh, A. A., Mashud, A. H. M., Uddin, M. S., & Khan, M. A.-A. (2017). Non-instantaneous deterioration inventory model with price and stock dependent demand for fully backlogged shortages under inflation. International Journal of Business Forecasting and Marketing Intelligence, 3(2), 152-164.

Shaikh, A. A., Panda, G. C., Khan, M. A.-A., Mashud, A. H. M., & Biswas, A. (2020). An inventory model for deteriorating items with preservation facility of ramp type demand and trade credit. Int. J. Math. Oper. Res., 17(4), 514-551.

Silver, E. A., & Peterson, R. (1985). *Decision systems for inventory management and production planning* (Vol. 18). Wiley.

Sultana, S., Mashud, A. H. M., Daryanto, Y., Miah, S., Alrasheedi, A., &Hezam, I. M. (2022). The Role of the Discount Policy of Prepayment on Environmentally Friendly Inventory Management. Fractal and Fractional, 6(1), 26.

Yang, H. L., & Chang, C. T. (2013). A two-warehouse partial backlogging inventory model for deteriorating items with permissible delay in payment under inflation. *Applied Mathematical Modelling*, *37*(5), 2717-2726.

Zia, N. P., &Taleizadeh, A. A. (2015). A lot-sizing model with backordering under hybrid linked-to-order multiple advance payments and delayed payment. *Transportation Research Part E: Logistics and Transportation Review*, *82*, 19-37.

ANALYTIC STUDY OF THERMOHALINE CONVECTIVE STABILITY IN A COUPLE-STRESS FLUID

Reeta Devi[1a], Shalu Choudhary[2b*], Poonam Sharma[3c], Amit Mahajan[4d], Sunil[5e], Manoj Kumar Sharma[6b]

Abstract: This study examines stability by conducting a nonlinear stability analysis on the thermohaline flow of a steady, viscous, incompressible couple-stress fluid, utilizing a generalized energy method. It is observed that the linear and nonlinear thresholds are the same, and the physics of the onset of convection is fully captured. The couple-stress and solute gradient parameters are found to have a stabilizing effect on the system.

Keywords: Stability, energy method, Couple-stress fluid, thermohaline convection, Rayleigh number.

1. Introduction

Hydrodynamic stability theory has been the subject of intensive study for decades, as it predominantly concerns the identification of critical Rayleigh number values that depict the stability region [see Joseph (1965, 1966); Straughan (2004)]. While linear theory does not guarantee stability, it does establish conditions for the instability of hydrodynamic systems. Under certain conditions, the energy technique of nonlinear theory ensures the stability of hydrodynamic systems but cannot conclusively prove instability. Thus, the use of a nonlinear approach to study the effects of finite perturbations on flow becomes vital. Initial credit for the energy method goes to Reynolds (1895) and Orr (1907), but it was later improved by Serrin (1959) and Joseph (1965, 1966, 1976). This classical energy technique, successful in many problems [Rionero, 1968; Galdi, 1985; Galdi & Straughan, 1985], has been confronted in many situations. Later, numerous authors (Galdi & Padula, 1990; Straughan, 2004; Rionero & Mulone, 1988; Mulone & Rionero, 1989) employed and improved the classical energy theory, and its generalization is now considered more successful in analyzing many complex theories.

Industrial and technological applications of couple-stress fluids, which include pumping fluids like synovial joint fluid, synthetic fluids, liquid crystals, animal blood, and the theory of lubrication, have attracted researchers to study the properties and behaviors of such fluids. The mathematical relation for Couple-stress fluid flow, as proposed by Stokes (1966), has distinct characteristics like couple stress forces, body couples, and non-symmetric stress tensors. Stokes (1984) provides an excellent description of this theory. Sunil et al. (2013, 2014, 2019) examined the stability problem of couple-stress fluid using the energy method. It is observed that the critical thermal Rayleigh values for linear instability and nonlinear stability coincide, indicating that subcritical instabilities are not present. It is known that saline can easily adhere or suspend in any fluid, and in certain cases, like animal blood, saline is present in the fluid. It is, therefore, important to consider this aspect when studying the stability of couple-stress liquids.

This paper aims to discuss the thermohaline convective stability in couple-stress fluids and analyze the impact of the presence of couple stress and solute concentration on convection, utilizing both linear and nonlinear methods of stability. The calculated critical Rayleigh number values depict the onset of convection and also provide an estimate of the stability region. These estimates may be useful for experiments to control heat transfer in such liquids. This paper identifies research opportunities and challenges for future research and has, to the best of our knowledge, not appeared in the literature thus far.

Authors information:
[a]Department of Mathematics, Government Post Degree College, Kangra, (H.P.), 176047, INDIA.
[b]Department of Mathematics, Uttaranchal University, Dehradun, Uttarakhand, 248007, INDIA.
[c]Department of Mathematics, NSCBM Government Degree College, Hamirpur, (H.P.), 177005, INDIA.
[d]Department of Applied Sciences, NIT Delhi,110040, INDIA.
[e]Department of Mathematics and Scientific Computing, NIT Hamirpur,(H.P.),177005, INDIA.
*Corresponding Author: chaudhary.shalu40@gmail.com

2. Mathematical Model

Consider a layer of couple stress fluid between two parallel plates d distance apart, extending infinitely in the horizontal direction, with constant viscosity. The temperature $T_{a,v}$ at the lower and upper surfaces $z = d/2$ and $-d/2$ is considered to be

fixed as T_l, T_u, respectively. The temperature gradient $\beta_T \left(= \left| \frac{dT}{dz} \right| \right)$ is maintained across the layer. The fluid layer heated and soluted from below confines with stress free boundaries and a gravitational force acting vertically downward along the z-direction.
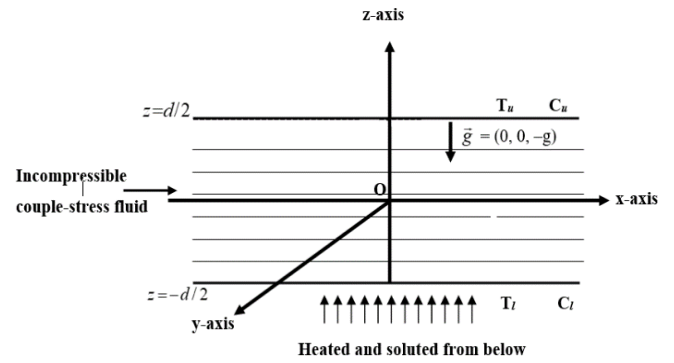

Figure 1. Pictorial representation of the mathematical model.

The governing equations of the convective system of the fluid with couple stress forces (by using Boussinesq approximation) are (Sunil et al., 2011; Choudhary & Sunil, 2019):

$$\nabla \cdot \vec{q}_s = 0 \tag{1}$$

$$\rho_r \left(\frac{\partial}{\partial t} + \vec{q}_s \cdot \nabla \right) \vec{q}_s = -\nabla p_1 + \rho_r [1 - \alpha(T - T_{a\,v}) + \alpha'(C - C_{a\,v})]\vec{g} + (\mu - \mu'\nabla^2)\nabla^2 \vec{q}_s \tag{2}$$

$$\frac{\partial T}{\partial t} + \vec{q}_s \cdot \nabla T = \kappa \nabla^2 T, \tag{3}$$

$$\frac{\partial C}{\partial t} + \vec{q}_s \cdot \nabla C = \kappa' \nabla^2 C. \tag{4}$$

Here, ρ_f is the fluid density ρ_r is the reference density, $\vec{q}_s$ is the fluid velocity, $\vec{g}$ is the acceleration due to gravity, t is the time, p_1 is the pressure field, μ is the coefficient of viscosity, μ' is the coefficient of visco-elasticity, κ is the thermal diffusivity, κ' is the solute diffusivity, α is the thermal expansion coefficient and α' is the solute expansion coefficient. The solute concentrations $C_{a\,v}$ at the lower and upper planes are fixed as C_l, C_u, respectively, while maintaining the solute gradient $\beta_C \left(= \left| \frac{dC}{dz} \right| \right)$ across the layer. The basic state ('b') is quiescent, and is given by:

$$\vec{q}_s = \vec{0}, \quad p_1 = p_{1b}(z), \quad \rho_f = \rho_{f\,b}(z) = \rho_r(1 + \alpha\beta_T z - \alpha'\beta_C z), \quad T = T_b(z) = -\beta_T z + T_{a\,v}, C = C_b(z)$$
$$= -\beta_C z + C_{a\,v}, \quad \beta_T = \frac{T_l - T_u}{d}, \quad \beta_C = \frac{C_l - C_u}{d}, \tag{5}$$

To perform stability analysis, let us introduce perturbations $\vec{q}_s'$, p_1', ρ', θ and γ representing velocity, pressure, density, temperature and concentration, respectively, to the basic state. The perturbations equations are:

$$\rho_0 \frac{\partial \vec{q}_s'}{\partial t} + \rho_r \vec{q}_s' \cdot \nabla \vec{q}_s' = -\nabla p_1' + \mu\nabla^2 \vec{q}_s' - \mu'\nabla^4 \vec{q}_s' + \rho_r g(\alpha\theta - \alpha'\gamma)\boldsymbol{k}, \tag{6}$$

$$\nabla \cdot \vec{q}_s' = 0, \tag{7}$$

$$\frac{\partial \theta}{\partial t} + \vec{q}_s' \cdot \nabla \theta = \kappa\nabla^2\theta + \beta_T w \tag{8}$$

$$\frac{\partial \gamma}{\partial t} + \vec{q}_s' \cdot \nabla \gamma = \kappa'\nabla^2\gamma + \beta_C w. \tag{9}$$

Boundary conditions (BC's) on $\vec{q}_s'$, θ, γ which satisfy a plane tilling periodicity are:

$$\vec{q}_s' = 0, \quad \theta = 0, \quad \gamma = 0 \text{ at } z = \pm\frac{d}{2} \tag{10}$$

3. Stability Analysis by Generalized Energy Method

To analyze stability, the perturbation equations (6) – (9) are written in non-dimensional form (dropping *) as follows:

$$\frac{\partial \vec{q}_s}{\partial t} + \vec{q}_s \cdot \nabla \vec{q}_s = -\nabla p_1 + \nabla^2 \vec{q}_s - F_C \nabla^4 \vec{q}_s + R^{\frac{1}{2}} \theta \boldsymbol{k} - \frac{S^{\frac{1}{2}}}{Le} \gamma \boldsymbol{k} \tag{11}$$

$$\nabla \cdot \vec{q}_s = 0, \tag{12}$$

$$\frac{\partial \theta}{\partial t} + \vec{q}_s \cdot \nabla \theta = \nabla^2 \theta + R^{\frac{1}{2}} w, \tag{13}$$

$$\frac{\partial \gamma}{\partial t} + \vec{q}_s \cdot \nabla \gamma = \frac{1}{Le} \nabla^2 \gamma + S^{\frac{1}{2}} w \tag{14}$$

The below mentioned dimensionless quantities and parameters are used for non dimensionalizing the perturbed equations

$$t^* = \frac{\mu}{\rho_0 d^2} t, \quad \vec{q}^*{}_s = \frac{d}{\nu} \vec{q}'_s, \quad p_1{}^* = \frac{d^2}{\rho_r \nu^2} p'_1, \quad \theta^* = \frac{R^{\frac{1}{2}}}{\beta_T d} \theta, \quad \gamma^* = \frac{S^{\frac{1}{2}}}{\beta_C d} \gamma, z^* = \frac{1}{d} z, R = \frac{g \alpha \beta_T \rho_r d^4}{\mu \kappa}, \quad S$$
$$= \frac{g \alpha' \beta_C \rho_r d^4}{\mu \kappa'}, Le = \frac{\kappa}{\kappa'} \quad \text{and} \quad F_C = \frac{1}{\nu} \frac{\mu'}{\rho_r d^2} \tag{15}$$

Here, R is the thermal Rayleigh number, S is the solute Rayleigh number, F_c is the couple-stress parameter and Le is the Lewis number.

Multiplying equations (11) by $\vec{q}_s$ (13) by θ, (14) by γ and integration over V and utilizing the given conditions, we obtain:

$$\frac{1}{2} \frac{d \|\vec{q}_s\|^2}{dt} = -\|\nabla \vec{q}_s\|^2 - F_c \|\nabla^2 \vec{q}_s\|^2 + R^{\frac{1}{2}} \langle w\theta \rangle - S^{\frac{1}{2}} \langle w\gamma \rangle, \tag{16}$$

$$\frac{1}{2} \frac{d\|\theta\|^2}{dt} = -\|\nabla\theta\|^2 + R^{\frac{1}{2}} \langle w\theta \rangle, \tag{17}$$

$$\frac{1}{2} \frac{d\|\gamma\|^2}{dt} = -\frac{1}{Le} \|\nabla\gamma\|^2 + S^{\frac{1}{2}} \langle w\gamma \rangle \tag{18}$$

Here, the symbol $\langle \cdot \rangle$ is for integration over V and $\| \cdot \|$ is the $L^2(V)$ norm.

From Eq. (16) – (17), an L^2 energy $E_0(t)$ is constructed and the change of $E_0(t)$ is

$$\frac{dE_0}{dt} = I_a - D_a, \tag{19}$$

where

$$E_0 = \frac{1}{2} \|\theta\|^2 + \frac{\lambda_1}{2} \|\vec{q}_s\|^2 - \frac{\lambda_2}{2} \|\gamma\|^2, \tag{20}$$

$$I_a = (1 + \lambda_1) R^{\frac{1}{2}} \langle w\theta \rangle - \lambda_1 \frac{S^{\frac{1}{2}}}{Le} \langle w\gamma \rangle - \lambda_2 S^{\frac{1}{2}} \langle w\gamma \rangle, \tag{21}$$

$$D_a = \|\nabla\theta\|^2 + \lambda_1 \|\nabla \vec{q}_s\|^2 + \lambda_1 F_c \|\nabla^2 \vec{q}_s\|^2 - \frac{\lambda_2}{Le} \|\nabla\gamma\|^2, \tag{22}$$

with λ_1 and λ_2 being positive coupling parameters.

In equation (20), the term $\frac{\lambda_2}{2} \|\gamma\|^2$ has a negative sign, which indicates that the system consumes energy due to the solute concentration. The energy consumed by the solute is less than the energy produced by the velocity and temperature. The energy dissipated by the solute is less than the energy dissipated by these two factors. This always ensures that all the RHS terms of equations (20) and (22) are less than the LHS terms.

We define

$$m_{max} = \max_H \frac{I_a}{D_a} \tag{23}$$

where H is the space of admissible solutions, and take m_{max}, so that

$$\frac{dE_0}{dt} \leq -e_0 D_a \tag{24}$$

with $e_0 = 1 - m_{max}$.

Using Poincare inequality, it is established that

$$D_a \geq \pi^2 \left(\|\theta\|^2 + \lambda_1(1 + \pi^2 F_c)\|\vec{q}_s\|^2 - \frac{\lambda_2}{Le}\|\gamma\|^2 \right) \geq E_0 \tag{25}$$

Eq. (25) is hold if $\frac{\lambda_2}{Le}\|\gamma\|^2 < \lambda_1(1 + \pi^2 F_c)\|\vec{q}_s\|^2$.

Using the (24) and (25), one finds

$$\frac{dE_0}{dt} \leq -e_0 E_0,$$

and by integration of this between limits 0 and t, the energy estimate is

$$E_0(t) \leq exp(-e_0 t)E_0(0). \tag{26}$$

Thus, the exponential fast decay of E assures conditional stability for all $E_0(0)$.

Variational Problem

Equation (23) is solved by using calculus of variation to maximize at the critical value m_{max}. By using the transformations $\hat{\vec{q}}_s = \sqrt{\lambda_1}\vec{q}_s$ and $\hat{\gamma} = \sqrt{\lambda_2}\gamma$, the Euler-Lagrange equations are given as (by dropping caps)

$$-2F_c\nabla^4\vec{q}_s + 2\nabla^2\vec{q}_s + R^{\frac{1}{2}}(1 + \lambda_1)\frac{1}{\lambda_1^{\frac{1}{2}}}\theta\hat{\vec{k}}$$
$$- S^{1/2}(1 + \lambda_2)\frac{1}{\lambda_1^{\frac{1}{2}}\lambda_2^{\frac{1}{2}}}\gamma\hat{\vec{k}} = 2\nabla\eta, \tag{27}$$

$$2\nabla^2\theta + R^{1/2}(1 + \lambda_1)\frac{1}{\lambda_1^{\frac{1}{2}}}w = 0 \tag{28}$$

$$\frac{2}{Le}\nabla^2\gamma + S^{\frac{1}{2}}\left(\lambda_2 + \frac{\lambda_1}{Le}\right)\frac{1}{\lambda_1^{\frac{1}{2}}\lambda_2^{\frac{1}{2}}}w = 0 \tag{29}$$

where η is introduced as Lagrange's multiplier, due to the solenoidal property of $\vec{q}_s$.

The third component of curlcurl of equation (27) is written as

$$-2F\nabla^6 w + 2\nabla^4 w + R^{\frac{1}{2}}(1 + \lambda_1)\frac{1}{\lambda_1^{\frac{1}{2}}}\nabla_1^2\theta$$
$$- S^{1/2}\left(\lambda_2 + \frac{\lambda_1}{Le}\right)\frac{1}{\lambda_1^{\frac{1}{2}}\lambda_2^{\frac{1}{2}}}\nabla_1^2\gamma = 0 \tag{30}$$

Now, consider a plane tiling solution

$$(w, \theta, \gamma) = [W(z), \Theta(z), \Gamma(z)]g(x, y) \tag{31}$$

Here, $\nabla_1^2 g + a^2 g = 0$, where 'a' is the non-zero wave number (Straughan, 2001; Chandrasekhar, 1981). Thus, the equations (28)-(30) are represented as

$$-2F_c(D^2 - a^2)^3 W + 2(D^2 - a^2)^2 W$$
$$- \frac{R^{\frac{1}{2}}a^2}{\lambda_1^{\frac{1}{2}}}(1 + \lambda_1)\Theta$$
$$+ \frac{S^{\frac{1}{2}}a^2}{\lambda_1^{\frac{1}{2}}\lambda_2^{\frac{1}{2}}}\left(\lambda_2 + \frac{\lambda_1}{Le}\right)\Gamma = 0, \tag{32}$$

$$2(D^2 - a^2)\Theta + \frac{R^{1/2}}{\lambda_1^{\frac{1}{2}}}(1 + \lambda_1)W = 0 \tag{33}$$

$$\frac{2}{Le}(D^2 - a^2)\Gamma + \frac{S^{\frac{1}{2}}}{\lambda_1^{\frac{1}{2}}\lambda_2^{\frac{1}{2}}}\left(\lambda_2 + \frac{\lambda_1}{Le}\right)W = 0 \tag{34}$$

and the BC's are

$$W = 0, \quad D^2 W = 0, \quad D^4 W = 0, \quad \Theta = 0, \quad \Gamma = 0$$
$$\text{at } z = \pm\frac{1}{2} \tag{35}$$

The functions W, Θ and Γ, satisfying (35) are given by

$$W = l_0 \cos \pi z, \Theta = m_0 \cos \pi z \Gamma = n_0 \cos \pi z, \tag{36}$$

where l_0, m_0 and n_0 are constants. Using solution (36) in (32)-(34), the polynomial equations with coefficients of l_0, m_0 and n_0 are obtained. Condition for existence of nontrivial solution of these equations' yields

$$R_e = \frac{4(1+x)^3\{1 + F_1(1+x)\}}{x\frac{1}{\lambda_1}(1 + \lambda_1)^2} + \frac{S_1 Le\left(\lambda_2 + \frac{\lambda_1}{Le}\right)^2}{\lambda_2(1 + \lambda_1)^2} \tag{37}$$

52

where $R_e = \frac{R}{\pi^4}$, $S_1 = \frac{S}{\pi^4}$, $x = \frac{a^2}{\pi^2}$, $F_1 = \pi^2 F_c$.

The optimal value of λ_1 and λ_2 is obtained from the conditions $\frac{dR_e}{d\lambda_1} = 0$ and $\frac{dR_e}{d\lambda_2} = 0$, respectively, and are found to be

$$\lambda_1 = 1 \text{ and } \lambda_2 = \frac{1}{Le}. \qquad (38)$$

Using (38) in equation (37), the Rayleigh number becomes

$$R_e = \frac{(1+x)^3[1+F_1(1+x)]}{x} + S_1. \qquad (39)$$

R_e attains minimum when

$$3F_1 x^4 + 2(1 + 4F_1)x^3 + 3(1 + 2F_1)x^2 - (1 + F_1) = 0. \qquad (40)$$

From the condition $\frac{dR_e}{dx} = 0$, the critical wave number values are derived numerically using the Newton-Raphson method. From equation (39), the required critical thermal Rayleigh number R_{ce} is obtained.

It is thus crucial to perform a standard normal mode technique on the perturbed equations (6) − (9), without including nonlinear terms, to investigate linear instability and determine their solution in the form (31) for the comparison of nonlinear results. Using the boundary conditions (35), the thermal Rayleigh number is obtained as

$$R_\ell = \frac{(1+x)^3[1+F_1(1+x)]}{x} + S_1 = R_e. \qquad (41)$$

Equation (35) simplifies to $R_\ell = \frac{(1+x)^3}{x} = R_e$, in the absence solute gradient $(S_1 = 0)$ and of couple stress parameter $(F_1 = 0)$, i.e., the linear instability boundary ≡ the nonlinear stability boundary, indicating no sub-critical instabilities region exists.

Table 1. Dependence of the R_c on (F_1).

F_1	x_c	R_c
0	0.5	106.75
1	0.387	116.46
2	0.366	125.99
3	0.357	135.49
4	0.351	144.99
5	0.348	154.48
6	0.346	163.97
7	0.344	173.45
8	0.343	182.94
9	0.342	192.42
10	0.341	201.90

Table 2. Dependence of the R_c on S_1, for various values of F_1.

S_1	R_c $\begin{pmatrix} F_1 = 1 \\ x_c = 0.387 \end{pmatrix}$	R_c $\begin{pmatrix} F_1 = 5 \\ x_c = 0.348 \end{pmatrix}$	R_c $\begin{pmatrix} F_1 = 9 \\ x_c = 0.342 \end{pmatrix}$
100	116.46	154.48	192.42
200	216.46	254.48	292.42
300	316.46	354.48	392.42
400	416.46	454.48	492.42
500	516.46	554.48	592.42
600	616.46	654.48	692.42
700	716.46	754.48	792.42
800	816.46	854.48	892.42
900	916.46	954.48	992.42

4. Results and Discussion

The critical wave number $x_c = x_{ce} = x_{c\ell}$ and critical thermal Rayleigh number $R_c = R_{ce} = R_{c\ell}$ were a function of couple stress parameter F_1 and solute gradient S_1. The variations given in Tables 1 and 2 are illustrated graphically in Figures 2 and 3.
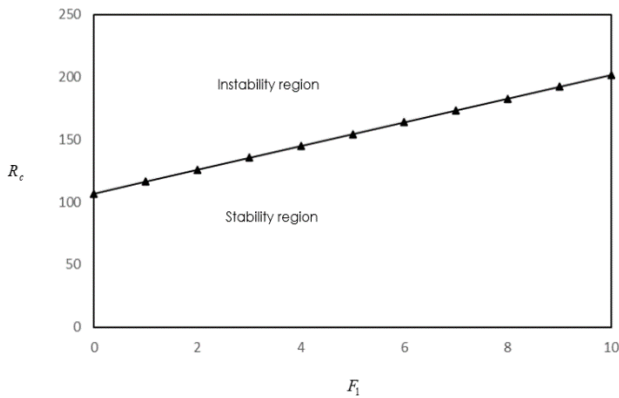

Figure 2. Plot of R_c versus F_1 for S_1=100.

From figure 2, it is found that the convection is advanced due to couple-stress parameter F_1, as R_c increases with an increase in F_1. Therefore, this parameter attempts to stabilize the convection in fluid. Additionally, the linear and nonlinear Rayleigh numbers are found to be the same. Table 1 shows that the couple-stress fluid stabilizes thermally more as compared to the standard fluid.
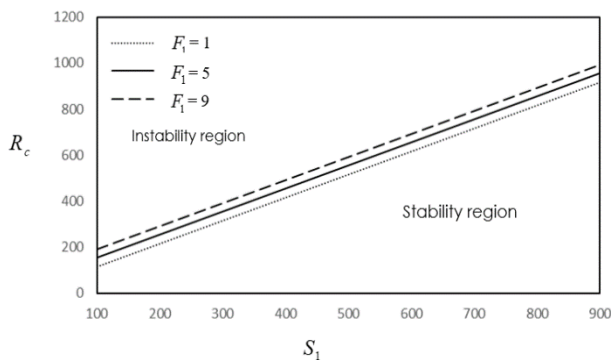

FIGURE 3. Plot of R_c versus S_1 for different values of F_1.

The variation of R_c with variation in S_1 for various values of F_1 is given in Table 2 and Figure 3. This clearly demonstrates the stabilizing effect of the solute parameter S_1 because R_c increases with an increase in S_1.

5. Conclusion

The results obtained using the generalized energy technique for the nonlinear system are the same as those obtained by linear theory, indicating that the boundaries of stability and instability coincide. There is no possibility of the existence of any subcritical instability. This finding is significant because it suggests that by controlling the parameter values, the fluid can be stabilized, and heat transfer can also be controlled. An increase in the values of parameters shows that the couple stresses and the presence of solute stabilize the system. Consequently, couple stress fluids are observed to be more stable than ordinary fluids. Therefore, in applications where higher stability requirements exist, such fluids can be utilized.

The study could be enhanced by including the effects under rigid type boundary conditions and also by considering viscosity as a function of temperature and pressure.

6. Acknowledgement

5. References

Chandrasekhar S. (1981) *Hydrodynamic and Hydromagnetic Stability*, New York, Dover.

Choudhary S. & Sunil (2019) Global stability for double-diffusive convection in a couple-stress-fluid saturating a porous medium, *Studia Geotechnica et Mechanica* **41(1)**:13. DOI: https://doi.org/10.2478/sgem-2018-0044

Galdi G. P. (1985) Nonlinear stability of the magnetic Bénard problem via a generalized energy Method, *Archive of Rational Mechanics and Analysis* **87**:167-186. DOI: https://doi.org/10.1007/BF00280699.

Galdi G. P.& Straughan B. (1985) A nonlinear analysis of the stabilizing effect of rotation in the Bénard problem, *Proceedings of the Royal Society of London A.* **402**:257-283. DOI:10.1098/rspa.1985.0118

Galdi G. P. & Padula M. (1990) A new approach to energy theory in the stability of fluid Motion, *Archive of Rational Mechanics and Analysis* **110**:187-286. DOI: https://doi.org/10.1007/BF00375129

Joseph D. D. (1965) On the stability of the Boussinesq equations, *Archive of Rational Mechanics and Analysis* **20**:59- 71. DOI: https://doi.org/10.1007/BF00250190.

Joseph D. D. (1966) Nonlinear stability of the Boussinesq equations by the method of energy,*Archive of Rational Mechanics and Analysis* **22**: 163-184.DOI: https://doi.org/10.1007/BF00266474.

Joseph D. D. (1976) *Stability of Fluid Motions*, Springer Verlag, New York.Rionero S. (1968) Metodivariazionali per la stabilitfiasintotica in media in magnetoidrodinamica, *Annali di Matematica Pura ed Applicata***78**:339-364. DOI: https://doi.org/10.1007/BF02415121.

Orr W. McF. (1907) Stability or instability of the steady motions of a perfect liquid, *Proceedings of the Royal Irish Academy A.* **27**:9-68:69-138.

Reynolds O. (1895) On the dynamical theory of incompressible viscous fluids and the determination of the criterion, *Philosophical Transactions Royal Society of London A.* **186**:123-164. DOI: http://dx.doi.org/10.1098/rsta.1895.0004

Rionero S. &Mulone G. (1988) A non-linear stability analysis of the magnetic Bénard problem through the Lyapunov direct method, *Archive for Rational Mechanics and Analysis* **103**:347-368. DOI: DOI:10.1007/BF00251445

Mulone G. & Rionero S. (1989) On the nonlinear stability of the rotating Bénard problem via the Lyapunov direct method, *Journal of Mathematical Analysis and Applications* **144**:109-127. DOI:10.1016/0022-247X (89)90362-4

Serrin J. (1959) On the stability of viscous fluid motions, *Archive Rational Mechanics and Analysis***3**:1-13. DOI: https://doi.org/10.1007/BF00284160.

Stokes V. K. (1966) Couple stresses in fluids,*Physics* of *Fluids***9**:1709.

Stokes V. K. (1984) *Theories of Fluids with Microstructure*, Springer, New York.

Straughan B. (2004) *The Energy Method, Stability, and Nonlinear Convection,* Springer Verlag, New York.

Sunil, Choudhary S. & Bharti P. K. (2013) Global stability for thermal convection in a couple-stress fluid with temperature and pressure dependent viscosity, *Studia Geotechnica et Mechanica* **35(3)**: 85-102. DOI:10.2478/sgem-2013-0032

Sunil, Choudhary S. & Mahajan A. (2014) Conditional stability for thermal convection in a rotating couple-stress fluid saturating a porous medium, *Special Topics & Reviews in Porous Media* **5(2)**:119-132. DOI: 10.1615/SpecialTopicsRevPorousMedia.v5.i2.30

Sunil, Choudhary S.& Mahajan A. (2019) Stability analysis of a couple-stress fluid saturating a porous medium with temperature and pressure dependent viscosity using a thermal non-equilibrium model,*Applied Mathematics and Computation* **340(1)**:15-30. DOI: https://doi.org/10.1016/j.amc.2018.08.025

Sunil, Devi R. & Mahajan A. (2011) Global stability for thermal convection in a couple stress fluid, *International Communications in Heat and Mass Transfer* **38**: 938–942. DOI: https://doi.org/10.1016/j.icheatmasstransfer.2011.03.030

CONSTRUCTING QUANTUM ANGULAR MOMENTUM $\hat{L}_3$ IN A SPECIFIC DIRECTION BY USING THE U(1) GROUP

Ahmad Aqwa Rosli[1a]* and Nurisya Mohd Shah[2a,b]

Abstract: The purpose of this work is to investigate the mathematical structure of finite quantum angular momentum in a specific direction L_3 which can be constructed from the representation of the U(1) group. The angular momentum eigenstate is invariant under Abelian rotation symmetry. The character group of U(1) is constructed to show that there exists an additive unitary operator for the angular momentum eigenstate, and the rotation eigenstate is invariant under it. The Weyl relation is proved by showing that the angle $e^{i\phi}$ and angular momentum L_3 are the canonical conjugate pair of observables.

Keywords: group, character group, group representation, quantum angular momentum.

1. Introduction

Traditionally, a quantisation scheme, such as the transcription of the Lie algebra structure from phase space to Hilbert space has been used to represent the observables of a physical system as self-adjoint operators on Hilbert space. We refer to Busch et al., (1997), Dirac, (1981), Isham, (1984), Sundermeyer, (1982) as reading materials to provide some methods of quantisation. The physical system of interest in this work is a quantum system with Abelian rotation symmetry. The reason is because angular momentum is a conserved quantity when the system has rotational symmetry (Hall, 2013). The discussion of angle and angular momentum observables has appeared in the past decades (Berry, 1977; Bizarro, 1994; Yamada, 1982) but with different spirit and objectives. They used Weyl-Wigner formulation to study rotation-angle and angular momentum in the quantum system. Recent developments in this technique can be seen in Weinbub and Ferry, (2018). In this work, the role of U(1) group and its character group are analysed to formulate the quantum angular momentum $\hat{L}_3$ in specific direction.

The U(1) group has been used to study various kinds of physical systems. For instance, in quantum harmonic oscillator. It has U(1) symmetry which is rotations in the position-momentum plane (Iwai, 1982). This implies that the Hamiltonian's eigenvalues, which represent the system's energy, will be integers multiplied by some fixed value. In addition, U(1) can act on complex-valued wavefunctions by pointwise phase transformations to describe quantum particles (Das, 2020). This technique is used to study how particles interact with electromagnetic fields, and the electric charge of the state is the physical interpretation of the operator's eigenvalue. For the recent discussion on this area see Zhang and Feng, (2023). For the case of quantum angular momentum, since the group SO(2) is the circle group for rotations in $\mathbb{R}^2$ plane and it is isomorphic to U(1) (Woit et al., 2017) then the group U(1) can be seen as a group of rotation in complex plane. The eigenvalues of the generator $\hat{L}_3$ are integers that are not continuous, implying that the quantum angular momentum on specific direction has different behaviour compared to classical angular momentum.

The paper is structured as follows. Section 2 focuses on constructing angular momentum $\hat{L}_3$ by applying the representation of U(1) group and shows that the angular momentum is invariant under rotation symmetry. In Section 3 the character group of U(1) is used to construct the additive unitary group of shift operator for angular momentum and prove that the angle eigenstate is invariant under these operators. Section 4 is devoted to proving the Abelian rotation symmetry and additive unitary shift operator for angular momentum satisfy the Weyl canonical commutation relation. In the final section, the conclusion of this work is stated.

Authors information:

[a]Laboratory of Computational Sciences and Mathematical Physics, Institute for Mathematical Research (INSPEM), Universiti Putra Malaysia, 43400 Serdang, Selangor, MALAYSIA. E-mail: ahmadaqwa@gmail.com[1]; risya@upm.edu.my[2]

[b]Department of Physics, Faculty of Science, Universiti Putra Malaysia, 43400 Serdang, Selangor, MALAYSIA. E-mail: risya@upm.edu.my[2]

*Corresponding Author: ahmadaqwa@gmail.com

2. The Representation of U(1) Group

In the three-dimensional space, if one chooses a particular direction, then the group of rotation on that particular axis can be identified with the abelian group U(1).

Definition 1. The U(1) group
- The elements of the group are points on the unit circle which are denoted by a unit complex number $e^{i\phi}$, or an angle $\phi \in \mathbb{R}$ with ϕ and $\phi + 2\pi k$ denoting the same group element for $k \in \mathbb{Z}$.
- Multiplication of group elements is complex multiplication:
$$e^{i\phi_1} e^{i\phi_2} = e^{i(\phi_1+\phi_2)},$$
where $\phi_1, \phi_2 \in \mathbb{R}$. So, in terms of angles the group law is addition (mod 2π)
- It is an Abelian group.

Definition 2. An irreducible representation of U(1) is given by,
$$U_k : U(1) \to GL(1,\mathbb{C}) \cong \mathbb{C}^\times$$
$$: e^{i\phi} \mapsto e^{ik\phi}$$
where $k \in \mathbb{Z}$ and $\mathbb{C}^\times$ is an invertible group of complex numbers. The map U_k has some properties:
- It satisfies the homomorphism rules $U_k(\phi_1 + \phi_2) = U_k(\phi_1)U_k(\phi_2)$.
- It has periodicity property: $U_k(2\pi) = U_k(0) = 1$.
- It has unitary property: $\overline{e^{ik\phi}} e^{ik\phi} = 1 = e^{ik\phi} \overline{e^{ik\phi}}$.

Any unitary representation U can be written as a direct sum,
$$U = U_1 \oplus U_2 \oplus \dots \oplus U_n, \tag{1}$$
where U_i for $i = 1, 2, \dots, n$ are the irreducible representation. Since U(1) is commutative, all irreducible representations will be one dimensional. Now, we can write a unitary representation of U in terms of its irreducible representation as the following:
$$U(e^{i\phi}) = \begin{pmatrix} e^{ik_1\phi} & \dots & \dots & 0 \\ 0 & e^{ik_2\phi} & \dots & 0 \\ \dots & \dots & & \dots \\ 0 & 0 & \dots & e^{ik_n\phi} \end{pmatrix} = e^{i\hat{L}_3\phi}. \tag{2}$$

Hence, we can define the generator $\hat{L}_3$ as the following,
$$\hat{L}_3 = \begin{pmatrix} k_1 & \dots & \dots & 0 \\ 0 & k_2 & \dots & 0 \\ \dots & \dots & & \dots \\ 0 & 0 & \dots & k_n \end{pmatrix}. \tag{3}$$

If we let $U(\phi) = e^{i\hat{L}_3\phi}$, and differentiate it with respect to ϕ, we get the following equation,
$$-i\frac{d}{d\phi}U(\phi) = \hat{L}_3 U(\phi). \tag{4}$$

This implies the generator $\hat{L}_3 = -i\frac{d}{d\phi}$. If $\psi(0)$ is the unit vector that describes our system at $\phi = 0$, then the unit vector which describes our system at angle ϕ is given by,
$$\psi(\phi) = U(\phi)\psi(0). \tag{5}$$
By substituting $\psi(0)$ into both sides of equation (4), then we obtain the following equation:
$$-i\frac{d}{d\phi}\psi(\phi) = \hat{L}_3\psi(\phi). \tag{6}$$

The equation above is exactly the equation for quantum angular momentum on a specific z-axis. The operator $\hat{L}_3$ is called the angular momentum operator on the z-axis and it governs the quantum system with Abelian rotation symmetry.

Observe that $U(\phi)$ can be written as the following,
$$U(\phi) = e^{i\hat{L}_3\phi} = \sum_{k=1}^{n} e^{ik\phi} |k\rangle\langle k|, \tag{7}$$
where $|k\rangle$ is the eigenbasis for $\hat{L}_3$. By substituting the eigenbasis $|k\rangle$ into the right-hand side of equation (4) gives,
$$\hat{L}_3(U(\phi)|k\rangle) = e^{ik\phi}(\hat{L}_3|k\rangle),$$
$$= ke^{ik\phi}|k\rangle,$$
$$= U(\phi)\hat{L}_3|k\rangle.$$

Therefore, the unitary operator $U(\phi)$ and the angular momentum generator $\hat{L}_3$ commute,
$$[U(\phi), \hat{L}_3] = 0. \tag{8}$$

Physically, this implies that if the state has well-defined eigenvalue of $\hat{L}_3$ at angle zero, then it will continue to have the same value at any other angle ϕ. In other words, the angular momentum is invariant under rotation symmetry.

3. Character Group of U(1)

A character for any Abelian group G is a homomorphism $\chi: G \to \mathbb{C}^\times$, where $\mathbb{C}^\times$ is a group of invertible complex numbers. The character forms an Abelian group under multiplication. The group is called dual group and denoted as $G^\wedge$. When U_k is a irreducible unitary representation then the character corresponds to,
$$\chi_k(\phi) = \text{Tr}(U_k(\phi)). \tag{9}$$
This equation implies that,
$$\chi_k(\phi) = \text{Tr}(e^{ik\phi}) = e^{ik\phi} = U_k(\phi). \tag{10}$$

So, the irreducible unitary representation of the U(1) can be specified by its character. Physically, it means if we interpret χ_k as particle moving with angular momentum k on the circle and $\chi_{\delta k}$ as moving with angular momentum δk, then $\chi_k \cdot \chi_{\delta k}$ should be interpreted as moving with angular momentum $k + \delta k$.

Recall that, by solving equation (6), the eigenvector $|k\rangle$ is given as $\psi_k(\phi) = e^{ik\phi}$ where $k \in \mathbb{Z}$. This is exactly the characters $\chi_k(\phi)$. Since the characters form a group $G^\wedge$, then we can introduce an additive unitary group of shift operator:
$$V(k) = e^{ik\hat{\Phi}} = \sum_{\phi} e^{ik\phi} |\phi\rangle\langle\phi|, \tag{11}$$
where $|\phi\rangle$ is the eigenvector for operator $V(k)$. By using the Fourier transform the eigenvector $|\phi\rangle$ can be written in terms of $|m\rangle$ as,
$$|\phi\rangle = \frac{1}{\sqrt{2\pi}} \sum_{m} e^{ik\phi} |m\rangle. \tag{12}$$
Thus,
$$V(k)|\phi\rangle = e^{ik\phi}|\phi\rangle. \tag{13}$$

This shows that the improper eigenvectors are invariant under additive unitary group of shift operator $V(k)$.

4. Weyl Canonical Commutation Relation for Angle and Angular Momentum

In quantum mechanics, canonical commutation relation (CCR) of observables plays a special role as it relates the fundamental relation between observables. For example, position and momentum. The observables which form the CCR are called canonically conjugate pair of observables and they imply the Heisenberg uncertainty principle. There is another way of writing it by using exponential and it is called Weyl canonical commutation relation.

Recall that, the unitary group of operators for rotation and additive unitary shift operator angular momentum are given by $U(\phi) = e^{i\hat{L}_3\phi}$ and $V(k) = e^{ik\hat{\Phi}}$ respectively. Those act as $U(\phi)|\phi'\rangle = |\phi + \phi'\rangle$ and $V(k)|\phi'\rangle = e^{ik\phi'}|\phi'\rangle$. Thus for any state $|\phi'\rangle$:

$$U(\phi)V(k)|\phi'\rangle = e^{ik\phi'}U(\phi)|\phi'\rangle = e^{ik\phi'}|\phi + \phi'\rangle,$$

$$V(k)U(\phi)|\phi'\rangle = V(k)|\phi + \phi'\rangle = e^{ik(\phi+\phi')}|\phi + \phi'\rangle,$$

Hence, we find the relation,

$$V(k)U(\phi) = e^{ik\phi}U(\phi)V(k). \qquad (14)$$

This implies that angular momentum and angle are the pair of canonically conjugate self-adjoint operators.

5. Conclusion

In this work, the finite quantum angular momentum in a specific direction, $\hat{L}_3$ can be constructed by the unitary representation of the U(1) group. The eigenstate of $\hat{L}_3$ is invariant under rotation symmetry. We have constructed the character of U(1) group and shown that the angular momentum eigenstate is invariant under the additive unitary operator. The finding has also shown that the angle $e^{i\phi}$ and the angular momentum $\hat{L}_3$ are the canonical conjugate observables. This is because they satisfied the Weyl canonical commutation relation.

6. Acknowledgement

7. References

Berry, M. V. (1977). Semi-classical mechanics in phase space: a study of Wigner's function. *Philosophical Transactions of the Royal Society of London. Series A, Mathematical and Physical Sciences*, *287*(1343), 237-271.

Bizarro J. P. (1994). Weyl-Wigner formalism for rotation-angle and angular-momentum variables in quantum mechanics, *Physical Review A*, *49*(5):3255.

Busch P., Grabowski M., Lahti P. J. (1997). *Operational quantum physics* (Vol. 31). Springer Science & Business Media.

Das A. (2020). *Lectures on quantum field theory*. World Scientific.

Dirac P. A. M. (1981). *The principles of quantum mechanics* (No. 27). Oxford University Press.

Hall B. C. (2013). *Quantum theory for mathematicians*. Springer.

Isham C. J. (1984). Topological and global aspects of quantum theory. In *Relativity, groups and topology. 2*. edited by B. S. Dewitt and R. Stora, North-Holland: Amsterdam, 1984, pp. 1059-1290.

Iwai T. (1982). The symmetry group of the harmonic oscillator and its reduction. *Journal of Mathematical Physics*, *23*(6):1088-1092.

Sundermeyer K. (1982). *Constrained dynamics with applications to Yang-Mills theory, general relativity, classical spin, dual string model*. New York, USA: Springer-Verlag.

Weinbub, J., & Ferry, D. K. (2018). Recent advances in Wigner function approaches. *Applied Physics Reviews*, *5*(4).

Woit, P., Woit, & Bartolini. (2017). *Quantum theory, groups, and representations*. New York, NY, USA: Springer International Publishing.

Yamada K. (1982). Angular-momentum—angle commutation relations and minimum-uncertainty states. *Physical Review D*, *25*(12):3256.

Zhang, K. Y., & Feng, W. Z. (2023). Explaining the W boson mass anomaly and dark matter with a U (1) dark sector. *Chinese Physics C*, *47*(2), 023107.

MATHEMATICAL MODEL OF NICKEL-GRAPHENE COMPOSITE INKS FOR JETTING PROPERTIES IN INKJET PRINTING

Neha Thakur[1a]*, Parasuraman Swaminathan[2b], Hari Murthy[3a]

Abstract: The droplet formation process in inkjet printing is studied numerically and verified through a simulation model. The droplet formation process decides the printing quality of the coating, and a mathematical model is developed to understand the complete process from droplet formation to detachment. The Navier-Stokes equation is used to mathematically derive the droplet radius ($r_{numerical}$). COMSOL multiphysics is used for simulation and the radius ($r_{simulation}$) is calculated from the droplet mass. The $r_{numerical}$ and $r_{simulation}$ are compared for inks containing nickel, graphene, and nickel-graphene composite ink it is observed that the composite ink radiuses have the lowest difference ($r_{simulation}$ - $r_{numerical}$ = 0.085 µm). A droplet is formed at 1.47 mm from the nozzle inlet, for nickel-graphene ink, and after 1.5mm for other pristine inks. The results are verified through Z number, velocity profile, and droplet mass. The droplet formation observed from the velocity profile is earliest at 120 µs. It is seen that a stable droplet is generated at 100µs for nickel-graphene ink and at 200 µs for individual inks.

Keywords: Drop formation, inkjet printing, COMSOL multiphysics, composite ink, nickel-graphene ink.

1. Introduction

Inkjet Printing (IJP) is one of the material printing techniques that has shown remarkable throughput in recent years. Printing technology is preferred over other conventional deposition techniques because of their lower deposition time, compactness, reduced number of patterning steps, and adaptation to different substrates. Farraj et al., (2014) discussed two types of IJP techniques that have been developed: continuous inkjet (CIJ) and drop-on-demand (DOD), wherein the former, continuous ink flow occurs, and droplets are formed irrespective of whether the character is available or not. CIJ can print features up to 20-50 µm with a preferred viscosity of up to 16 mPa.s. In DOD, the droplet is formed only when the character is present resulting in lower resource wastage. The viscosity range for DOD lies between 20-40 mPa.s. According to Hoath et al., (2016), each droplet maintains a ligament that prolongs from the main droplet body towards the nozzle. The main functioning of the IJP relies on droplet formation, which in turn depends on the ink's rheological properties (viscosity, surface tension, and density). The ink contains active agents, precursors, dispersing medium, and surfactants, which must be selected appropriately as suggested by Murthy et al. (2021). The droplet generation process is divided into four stages - droplet generation, flight mode, drop impingement, and drop hardening. A droplet is said to be generated when the fluid mass accumulated exceeds the surface tension force that holds the fluid onto the surface. A behavior change occurs because the liquid drop takes a shape that minimizes the free energy (ψ) of the system, contributed by the three interfaces (solid, liquid, and gas), given by

Kulkarni et al., (2016):

$$\psi = \sigma_{LS} A_{LS} + \sigma_{SG} A_{SG} + \sigma_{LG} A_{LG} \qquad (1)$$

σ_{LS}, σ_{LG}, and σ_{SG} are the surface energy for liquid-solid, liquid-gas, and solid-gas interface, respectively. A_{LG}, A_{LS}, and A_{SG} are the areas of liquid-gas, liquid-solid, and solid-gas interface, respectively.

For a homogenous surface, the surface tension should be balanced as:

$$\sigma_{SG} = \sigma_{LS} + \sigma_{LG} \cos\phi_{eq} \qquad (2)$$

where, ϕ_{eq} represents the equilibrium contact angle, given as the angle between the liquid/gas interface as it meets the solid surface.

$$\cos\phi_{eq} = \frac{\sigma_{SG} - \sigma_{LS}}{\sigma_{LG}} \qquad (3)$$

Drop impingement occurs when a droplet hits the substrate and the extent of surface wetting is determined by ϕ_{eq}. The droplet behavior varies from equilibrium or stable state to spread, recede, rebound, partial rebound, and oscillate depending upon the wetting conditions discussed by Davydzenka et al., (2016) as given in **Table** 1. The splashing of the droplet is determined by the Weber number (We) and Reynold's number (Re) used for determining the Z-number. Z-number is used to confirm the ink printability. The ideal values for the Z number are between 1-10, where below 1, the fluid will not flow because of insufficient energy, and for Z >10, the fluid will too viscously be creating satellite droplets. The ideal relation between Re and We for inkjet printing applications is defined by Derby (2015) as given in Figure 1.

Authors information:

[a]Dept. of Electronics and Communication Engineering, CHRIST (Deemed to be University), Bengaluru, Karnataka, INDIA.
[b]Dept. of Metallurgical and Materials Engineering, Indian Institute of Technology, Madras, Tamil Nadu, INDIA.
*Corresponding Author: neha.thakur@res.christuniversity.in
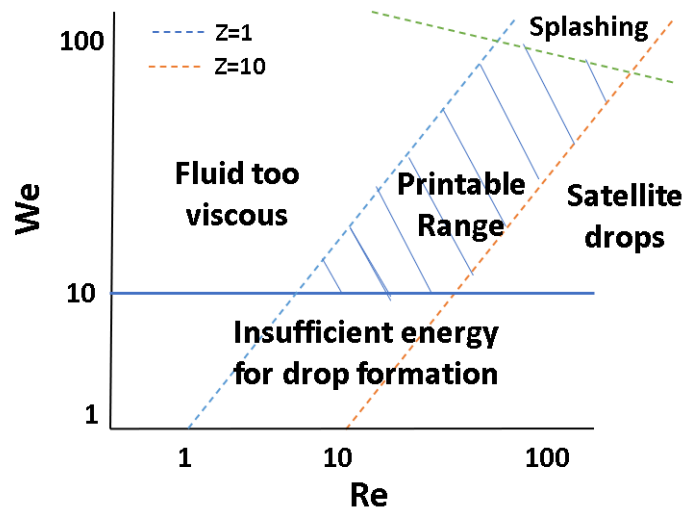
Figure 1. Relationship between Re and We which influences the ink printability.

Table 1. Wetting conditions for different contact angles

ϕ_{eq}	Expression	Wettability	Example
0	$\sigma_{LG} = \sigma_{SG} - \sigma_{LS}$	Complete wetting	
0 to 90º		Partial wetting	
90º	$\sigma_{SG} = \sigma_{LS}$	Equilibrium	
90º to 180º		Partial non-wetting	
180º	$\sigma_{LG} = \sigma_{LS} - \sigma_{SG}$	Non-wetting	

The proposed work involves a mathematical multiphase (liquid ink and air) fluid flow model. The model is developed to determine the droplet's behavior during formation and travel toward the substrate. To date, the droplet radius is not calculated mathematically as per the author's knowledge, and the proposed work will be helpful for users working on coating techniques like inkjet printing. The droplet radius is calculated and the input parameters are varied to predict the droplet radius prior to printing. As a case study, nickel-graphene ink has been used for simulation in the literature. Nickel-graphene composites exhibit strong sp^2 hybridization between the 2p orbital of graphene and the 3d orbital of nickel with a low lattice mismatch of ~1.2% and an inter-metal separation of 0.21 nm. The strong chemical interaction between graphene and nickel makes it an excellent electrical conductor for electronic applications summarized by Thakur et al., (2021). Takuya et al., (2023) derived a model to determine the breakup length of the droplet stream from the ligament.

2. Materials and Methods

The fluid interface and convection with air are represented as part of a laminar two-phase flow, by considering the level set method, considering the inks as Newtonian fluid. Mathematical and simulation models are used to obtain droplet radius for multiphase flow (MPF). Before realizing the MPF model, the single-phase flow (SPF) model is derived.

Single Phase Flow (SPF)

Figure 2 shows the channel area where the fluid flow occurs is considered a cylindrical coordinate (r, θ, z), where 'r' is the nozzle radius, 'θ' is the angle between the reference direction (z) on the chosen plane and the line from the origin to the projection on the plane, and 'z' is the distance from the inlet to the point of reference. Assuming that the direction of fluid flow is in z-direction towards the substrate, implies v_r =0, v_θ =0, and that there is no effect of gravity. The Navier Stokes (NS) equation is written by Rev et al., (2018):

$$\rho\left(\frac{\partial \vec{v}}{\partial t} + (\vec{v}.\vec{\nabla})\vec{v}\right) = -\vec{\nabla}P + \mu\nabla^2\vec{v} \tag{4}$$

where, 'μ' is viscosity (mPa.sec), 'ρ' is density (kg/m³), 'P' is pressure (Pa), and 'v' is velocity (m/sec).
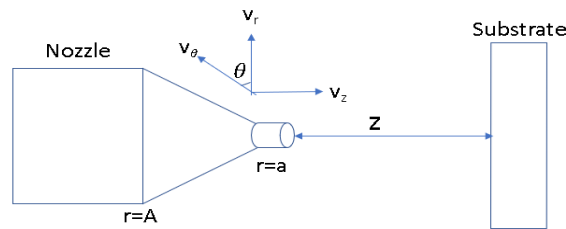
Figure 2. The cylindrical coordinate system for the proposed nozzle schematics

Solving the above NS equation for the 'r' coordinate and 'θ' based on the condition that v_r =0, v_θ =0, we get:

$$-\frac{\partial P}{\partial r} = 0 \tag{5}$$

and
However, solving for the 'z' coordinate, we get:

$$-\frac{1}{r}\frac{\partial P}{\partial \theta} = 0 \tag{6}$$

$$\frac{\partial P}{\partial z} = \mu\left[\frac{1}{r}\frac{\partial}{\partial r}\left(r\frac{\partial v_z}{\partial r}\right)\right] = constant \tag{7}$$

If P_1 is the inlet pressure, P_2 is the outlet pressure, with L being the surface length, then for the ink to flow across the 'z' direction P_1 should be greater than P_2, and the pressure gradient is given as:

$$\frac{\Delta P}{L} = -\mu\left[\frac{1}{r}\frac{d}{dr}\left(r\frac{dv_z}{dr}\right)\right] \tag{8}$$

The velocity in the z direction, v_z is obtained:

$$v_z = -\frac{1}{2\mu}\frac{\Delta P}{L}\frac{r^2}{2} + C_1\ln(r) + C_2 \tag{9}$$

The boundary conditions for single-phase flow are given as:

- No slip condition at the wall, i.e., $\frac{dv_z}{dr} = 0$ (r=a)
- No fluid velocity at the outer radius of the nozzle, i.e., v_z= 0 (at r=A)

Applying the boundary conditions to obtain the constants C_1 and C_2, we get

$$C_1 = \frac{1}{2\mu}\frac{\Delta P}{L}a^2 \tag{10}$$

$$C_2 = \frac{1}{2\mu}\frac{\Delta P}{L}\left(\frac{A^2}{2} - a^2\ln(A)\right) \tag{11}$$

Thus, the generalized velocity for SPF is obtained as:

$$v_z(r) = -\frac{1}{2\mu}\frac{\Delta P}{L}\left[\frac{r^2}{2} - a^2\ln(r) - \frac{A^2}{2} + a^2\ln(A)\right] \tag{12}$$

The volume flow rate is calculated as:

$$Q = \frac{\pi}{8\mu}\frac{\Delta P}{L}(A^2 - a^2)(A^2 - 3a^2) \tag{13}$$

Multiphase Flow (MPF)

Two phases are considered for deriving the numerical model having velocities v_{z1} and v_{z2}, pressure P_1 and P_2, viscosities μ_1, and μ_2 for the phase 1 and phase 2 respectively, 'r' is the variable radius of the flow across the length of the nozzle, 'R_d' is the radius of the fluid flow. The velocities for phase 1 and phase 2 are given as:

$$v_{z1} = -\frac{1}{2\mu_1}\frac{\partial P_1}{\partial z}\frac{r^2}{2} + C_{11}\ln(r) + C_{21} \tag{14}$$

$$v_{z2} = -\frac{1}{2\mu_2}\frac{\partial P_2}{\partial z}\frac{r^2}{2} + C_{12}\ln(r) + C_{22} \tag{15}$$

The boundary conditions for multiphase flow are given as:

- No slip condition at the wall, i.e., $v_{z1}=0$ (r=a)
- At the starting point, there is no change in the velocity, i.e., $\frac{dv_{z2}}{dr} = 0$ (at r=0)
- Same travel velocity for the two fluids, i.e., $v_{z1}(R_d)= v_{z2}(R_d)$
- Constant shear stress for both fluids, i.e., $\zeta_1(R_d) = \zeta_2(R_d)$

Applying the boundary conditions to obtain the following constants:

$$C_{21} = \frac{1}{2\mu_1}\frac{\partial P_1}{\partial z}\frac{a^2}{2} - C_{11}\ln(a) \tag{16}$$

$$C_{12} = 0 \tag{17}$$

$$C_{11} = \frac{V_{tp} + \frac{1}{4\mu_1}\frac{\partial P_1}{\partial z}\left(R_d{}^2 - a^2\right)}{ln\left(\frac{R_d}{a}\right)} \tag{18}$$

$$C_{22} = \frac{1}{2\mu_2}\frac{\partial P_2}{\partial z}\frac{R_d{}^2}{2} + V_{tp} \tag{19}$$

$$C_{21} = \frac{1}{2\mu_1}\frac{\partial P_1}{\partial z}\frac{a^2}{2} - \frac{4V_{tp} + \frac{\partial P_1}{\partial z}\left(R_d{}^2 - a^2\right)}{4\mu_1\,ln\left(\frac{R_d}{a}\right)}ln(a) \tag{20}$$

After substituting the values of all constants, velocities and flow rates of the two phases are given by Li et al., (2021):

$$v_{z1} = -\frac{1}{2\mu_1}\frac{\partial P_1}{\partial z}\frac{r^2}{2} + \frac{4V_{tp} + \frac{\partial P_1}{\partial z}\left(R_d{}^2 - a^2\right)}{4\mu_1\,ln\left(\frac{R_d}{a}\right)}ln\left(\frac{r}{a}\right) + \frac{1}{2\mu_1}\frac{\partial P_1}{\partial z}\frac{a^2}{2} \tag{21}$$

$$v_{z2} = -\frac{1}{2\mu_2}\frac{\partial P_2}{\partial z}\frac{r^2}{2} + \frac{1}{2\mu_2}\frac{\partial P_2}{\partial z}\frac{R_d{}^2}{2} + V_{tp} \tag{22}$$

$$Q_1 = \frac{\pi}{\mu_1}\left\{\left[\frac{\partial P_1}{\partial z}\left(\frac{R_d{}^2 - a^2}{2}\right)\right]\left[\frac{R_d{}^2 - a^2}{4} - E_1\right] - \frac{E_1}{2}\right]\right\} \tag{23}$$

$$Q_2 = \pi\left\{\frac{1}{\mu_2}\frac{\partial P_2}{\partial z}\frac{R_d{}^4}{8} + R_d{}^2 V_{tp}\right\} \tag{24}$$

The droplet formation process is derived with respect to fluid velocity (v_z) and volume flow rate (Q). The numerical droplet diameter ($d_{numerical}$) and radius ($r_{numerical}$) as the function of nozzle diameter (d_N) and nozzle radius (r_N) respectively and also the function of volume flow rate, is given as:

$$d_{numerical} = d_N \sqrt[3]{\left(1 - \frac{6Q_2}{\pi Q_1}\right)} \qquad (25)$$

$$r_{numerical} = r_N \sqrt[3]{\left(1 - \frac{6Q_2}{\pi Q_1}\right)} \qquad (26)$$

Simulation Model

The drop-on-demand process uses COMSOL multiphysics software to understand the different stages involved in the droplet formation process. Due to the nozzle geometry, an axis-symmetric 2D model is used to simplify the calculations. Initially, the space between the nozzle and the substrate is filled with air. The ink is ejected through the nozzle and forced to flow out of the nozzle forming a droplet that eventually changes shape and cuts off from the nozzle. The droplet is constantly changing shape and travels towards the substrate. The properties of the fluid are expected to be different in the nanochannel in comparison to the bulk which is given by Rudyak et al., (2011). The adaptive mesh refinement functionality of COMSOL multiphysics is used to refine the mesh around the ink and air interface. A similar model is developed by Tofan et al., (2022) for modelling 3D droplet movement using a DoD inkjet printhead model. The functionality divides the simulation into several time intervals and locally refines the mesh in the region where the phase interface is present in each interval to increase calculation accuracy.

The following assumptions are made to simplify the simulation process

1. The fluid and surrounding air are incompressible.
2. Heat transfer will be neglected, and the ink will be assumed to have constant properties throughout the problem. No liquid evaporation takes place.
3. Laminar flow
4. The liquid properties are constant with time.

The droplet size and velocity are controlled during the ejection by applying a rectangular function as shown in **Figure 3** to the inlet velocity forcing a pressure increase inside the modelled nozzle. It helps to set the pulse length and maximum inlet fluid velocity magnitude, which affects the resulting velocity of the ejected droplet, though magnitude has a larger influence on the droplet velocity. The nozzle geometry is created using the dimensions given in **Table 2** and is shown in **Figure 4**.
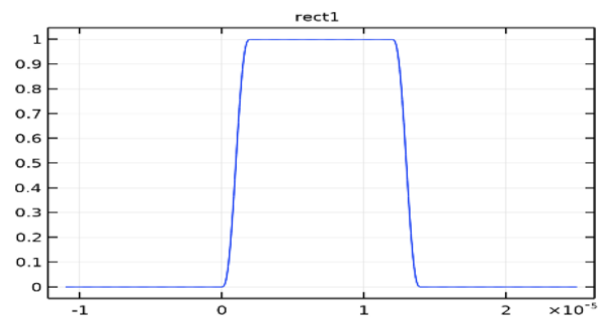

Figure 3. Rectangular function of the increasing pressure in the nozzle

Table 2. Dimensions of the nozzle geometry used for simulation

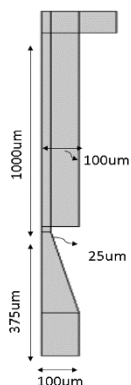| Name	Value (μm)
Inlet Radius	100
Nozzle Length	375
Nozzle Radius	25
Throat Length	25
Distance to target	1000
Air Channel Width	100

Figure 4. Nozzle geometry used for simulation model

The boundary condition selected for simulation is the same as for the fully developed flow. According to the COMSOL Module User's guide by Burlington et al., (2018), the level set method is selected, and the value for the level set function (φ) is '0' for the air and '1' for ink. In the transition layer close to the interface, φ goes from 0 to 1 smoothly, with the interface moving together with the fluid velocity. For the simulation, the physics-controlled mesh has been used with a minimum element size of 3.18 μm, and a curvature factor of

0.3. The wetted wall conditions used were the wall condition used was Navier slip, slip length 10 μm, and the contact angle as pi/2. The range used for computation was (0, 10 x 10^{-6}, 500 x 10^{-6}) using a PARDISO solver. From the simulation report, droplet mass is obtained, which is further used to calculate the droplet radius. The material properties used for simulation are given in **Table 3**.
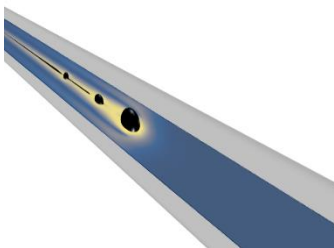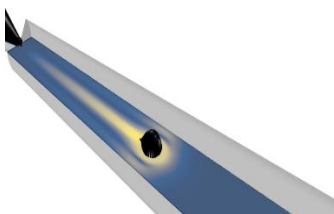
Table 3. Material properties used for simulation

Material	Density (kg/m³)	Surface Tension (mN/m)	Viscosity (mPa.s)
Air	1		
Graphene	1300	10	33.45
Nickel	7810	72	44

3. Results and Discussion

The droplet formed for all inks along with its position and formation time is given in **Table 4**. It can be seen from the simulation model; that the droplet is formed earliest at 1.47 mm from the nozzle inlet in the nickel-graphene ink.

Table 4. Droplet formation in the simulation model

Ink	Nickel	Graphene	Nickel-graphene
Result			
Droplet position	@1.5456mm	@2.667mm	@ 1.47mm
Time	20μs	20μs	20μs

Viscosities and surface tension for nickel ink and graphene ink are shown in **Table 5**. For each value, the numerical and simulation droplet radius is calculated and compared. The case with the least difference (nickel viscosity 44 mPa.sec, graphene viscosity 33.4 mPa.sec) in the radius values is chosen for further analysis.

Table 5. Numerical and simulation radius calculated for the existing rheological properties from the literature

Ink used	Viscosity (mPa.s)	Surface Tension (mN/m)	Oh	Mass (μg)	Numerical radius(μm)	Simulation Radius (μm)	Ref
Liquid nickel	44	72	0.166	0.21	39.86	41.67	Cherne et al. (2002)
Ni ink	25	15	0.207	0.2	39.21	41.66	Altay et al., (2018)
NiO nano fluid	22.4	45.9	0.106	0.2	39.22	41.66	Ramachandran et al., (2020)
Graphene ink	43.5	15	0.402	0.2	71.30	41.67	Chen et al., (2020)
Graphene ink	15	72	0.14	0.22	73.60	41.67	Secor et al., (2015)
Graphene ink	33.4	10	0.83	0.2	41.67	41.97	Gao et al., (2014)

Nickel-graphene (Ni-G) composite ink is considered and the radius is calculated to be around ~41.66 μm which is close to the simulated radius of 41.67 μm. The density, viscosity, and surface tension of the nickel-graphene ink were taken as 4555 kg/m^3, 38.87 mPa.s, and 72 mN/m respectively. The droplet mass was found to be 14x10^{-11} kg. It is observed that Ni-G ink composite gives better results in comparison to the individual inks. It is discernible that all three inks are coming in the printability range of 1 to 10.

There is continuous change in the fluid velocity and to understand the exact fluid flow mechanism with respect to velocity five points (A, B, C, D, and E) are considered at different time intervals from 20 to 180μs. The mechanism at each point of time is described in **Table 6**. It is apparent that Ni-G composite ink droplets are detached earliest at 1.124 mm as shown in **Figure 5**.

Table 6. Velocities at different stages of droplet formation for nickel, graphene, and nickel-graphene composite

	Significance	Time (μs)	Ni (m/s)	G (m/s)	Ni-G (m/s)
A	The droplet is ejected from the nozzle with maximum pressure	20	10	9.12	9.94
B	The droplet is followed by a ligament with maximum length, mass, and volume	80	9.79	8.72	9.03
C	Almost spherical droplet is formed	100	10.8	9.05	9.19
D	Droplet is detached	120	9.71	10.4	9.37
E	The droplet starts moving toward the substrate	180	9.49	9.5	9.05

The droplet mass is determined up to 500 μs, and the values are graphically represented in **Figure 6**. The droplet mass results are obtained from the droplet mass curve generated by COMSOL multiphysics. For Ni ink and graphene ink, the stable (or constant) droplet mass is achieved at 200 μs whereas for Ni-G composite ink the stable droplet mass is achieved at 100 μs. The emphasis is

given on droplet mass because the droplet mass indicates the droplet volume and the radius can be calculated from the volume.

For Ni ink and graphene ink, the stable droplet mass is achieved at 200 μs whereas for Ni-G composite ink the stable droplet mass is achieved at 100 μs. The droplet mass remains fixed once the droplet is ejected from the nozzle.

Future work would be focused on understanding the impact of more parameters and deepening into the droplet behavior, along with the validation of the results through physical experimentation. The proposed numerical work as an implementation study with COMSOL is useful for scientists working on the modelling of inkjet printing. By using COMSOL, the numerical modelling of the motion of inkjet droplets has been achieved, and the length of the dropped thread, the moment when the drop is pulled out of the thread when the droplet forms a spherical shape, droplet mass, droplet volume, droplet conditions on impact, and the final state of the droplet can be studied. In addition, it is now possible to configure different nozzle parameters, and different ejection pressures, test different inks as well, and consider different ink precursors given by Tofan et al., (2021).
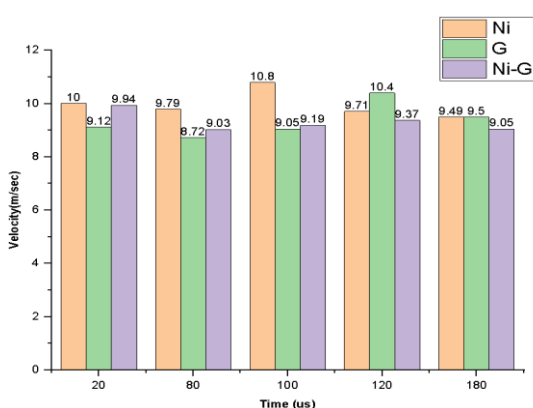

Figure 5. Velocity plot for nickel, graphene, and nickel-graphene composite. The graph indicates the velocity of droplets at different stages from ejection to detachment.
The nickel ink droplet is detached at 1.165mm, graphene at 1.248mm, and nickel-graphene ink composite at 1.124mm
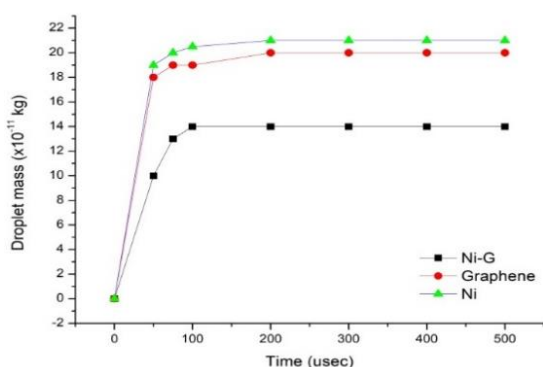

Figure 6. Droplet mass plot for nickel, graphene, and nickel-graphene composite

4. Conclusion

The droplet formation and detachment process are studied by modelling the inkjet nozzle numerically and through simulation. From both the models the droplet radius is derived and calculated. For verification purposes, three inks (Ni, G, and Ni-G) are chosen, and it is conspicuous that for Ni-G composite ink the difference in the droplet radius is 0.085 μm which is the least among all the three inks. Various analyses based on the Z parameter, velocity profile, and droplet mass are calculated for all the inks, and the most optimized results are obtained for the Ni-G ink composite. The stable droplet mass is achieved at $100\mu s$ for Ni-G ink whereas for others is obtained at $200\mu s$ and the droplet is formed earliest in Ni-G ink. Composite inks are expected to have better properties than their individual components and hence can play a crucial role in the future for various electronics and biosensing applications. In the future, the experimental work will be performed in three phases. The first phase includes ink formulation and characterization, keeping in mind the rheological properties of the present research. In the second phase, the formulated ink will be used to generate droplets and the droplets formed will be compared with the droplets in the simulation model. In the third phase, the droplet radius is calculated and will be compared with the numerical and simulation model.

5. Acknowledgements

6. References

Altay BN, Jourdan JS, Turkani VS, et al. (2018) Fundamental Mechanism of Ink Film Roughness The Impact of Substrate and Process on the Electrical Performance of Screen-Printed Nickel Electrodes. *ACS Appl. Energy Mater.* 1: 7164-7173

Burlington M. (2018) *CFD Module User's Guide; COMSOL*.

Chen H, Zhang Y, Ma Y, et al. (2020) Sand-Milling Exfoliation of Structure Controllable Graphene for Formulation of Highly Conductive and Multifunctional Graphene Inks. 12: 56319-56329

Cherne FJ, Baskes MI, Deymier PA. (2002) Properties of liquid nickel: A critical comparison of EAM and MEAM calculations. *Phys Rev B - Condens Matter Mater Phys*. 65.

Derby B. (2015) 3D Printing — Review Additive Manufacture of Ceramics Components by Inkjet Printing. *Engineering*. 1:113-123.

Farraj Y, Grouchko M, Magdassi S, Koch F., Wittkotter M., Muller M., Reinhold I., Zapka W. (2014). Ink-jet printed copper complex MOD ink for plastic electronics, *International Conference on Digital Printing Technologies*. 51: 1587-1590

Gao Y, Shi W, Wang W, Leng Y, Zhao Y. (2014) Inkjet printing patterns of highly conductive pristine graphene on flexible substrates. *Ind Eng Chem Res*. 53: 16777-16784.

Hoath S. D. (2016) Fundamentals of Inkjet Printing: The Science of Inkjet and Droplets. (Hoboken, ed.). *John Wiley & Sons.*

Kulkarni VS., Shaw C. (2016). Surfactants, Lipids, and Surface Chemistry. *Essent Chem Formul Semisolid Liq Dosages*

Li D (2001) *Interface Science and Technology*.

Murthy H., Thakur N., and NS. (2022). Nickel-Based Inks for Flexible Electronics - A Review on Recent Trends. *Journal of Adv Manuf Syst*. 21: 591-624.

Ramachandran H, Jahanara MM, Nair NM, Swaminathan P. (2020) Metal oxide heterojunctions using a printable nickel oxide ink. *RSC Adv*. 10: 3951-3959

Rev. BS. (2018) On the development of the Navier–Stokes equation byNavier. *Hist Phys Relat Sci*. 40: 1-12.

Rudyak V. Ya., Belkin (2011) A. A. Egorov V. V. IDA. Simulation of flows in nanochannels by the molecular dynamics method. *Nanosyst Physics, Chem Math*. 2:100-112.

Secor EB, Ahn BY, Gao TZ, Lewis JA, Hersam MC. (2015) Rapid and Versatile Photonic Annealing of Graphene Inks for Flexible Printed Electronics. *Adv Mater*. 27

Takuya O., Tsubouchi S., and Suwa Y. (2023). Analysis of the Ink-stream Break-Up Phenomenon in Continuous Inkjet Printing. *ACS Omega.* 8: 34442-34447.

Thakur N, Murthy H. (2021) Nickel-Based Inks for Inkjet Printing : A Review on Latest Trends. 11: 20-35.

Tofan T., Borodinas S., Kacianauskas R., and Jasevicius R. (2022). Modeling 3D Droplet Movement Using a Drop-on-Demand Inkjet Printhead Model. *Processes MDPI*: 10, 147.

Tofan Tim, Kruggel Emdem Harald, Turla Vytautas JR. (2021) Numerical Modeling of the Motion and Interaction of a Droplet of an Inkjet Printing Process with a Flat Surface. *Appl Sci*. 11: 527.

NUMERICAL ASSESSMENT OF SOME SEMI-ANALYTICAL TECHNIQUES FOR SOLVING A FRACTIONAL-ORDER LEPTOSPIROSIS MODEL

Khadeejah James Audu[1a]*, Abdgafar Tunde Tiamiyu[2b], Jeremiah Nsikak Akpabio[3c], Hijaz Ahmad[4d,e,f] and Majeed Adebayo Olabiyi[5g]

Abstract: This research aims to apply and compare two semi-analytical techniques, the Variational Iterative Method (VIM) and the New Iterative Method (NIM), for solving a pre-formulated mathematical model of Fractional-order Leptospirosis. Leptospirosis is a significant bacterial infection affecting humans and animals. By implementing the VIM and NIM algorithms, numerical experiments are conducted to solve the leptospirosis model. Comparing the obtained findings demonstrates that VIM and NIM are effective semi-analytical methods for solving systems of fractional differential equations. Notably, our study unveils a crucial dynamic in the disease's spread. The application of VIM and NIM offers a refined depiction of the biological dynamics, highlighting that the susceptible human population gradually decreases, the infectious human population declines, the recovered human population increases, and a significant rise in the infected vector population is observed over time. This nuanced portrayal of the disease's dynamics is crucial for understanding the intricate interplay of Leptospirosis among human and vector populations. The study's outcomes contribute valuable insights into the applicability and performance of the methods in solving the Fractional Leptospirosis model. Results indicate rapid convergence and comparable outcomes for both methods.

Keywords: Leptospirosis model, fractional differential equation, variational iterative method, semi-analytical methods, new iterative method.

1. Introduction

Over time, mathematics has been utilized to comprehend the modes of disease transmission throughout the world. Infectious diseases are those that are transmitted from one individual to another, whereas non-infectious diseases are typically caused by environmental or genetic factors. Infectious diseases have commonly been regarded as the adversaries of human health throughout history and have remained the leading causes of pain and death in underdeveloped nations. It is common knowledge that the spread of a communicable disease involves disease-related parameters such as the infectious agent, infectious periods, incubation period, mode of transmission, resistance, and susceptibility. Leptospirosis is a bacterial infection that poses significant health risks to both humans and animals, with a global impact on public health. Understanding the dynamics of leptospirosis is crucial for effective disease management and prevention. Mathematical modeling has proven to be a valuable tool for studying infectious diseases, providing insights into their transmission patterns, and informing control strategies (Aslan et al., 2021; Ali et al., 2022; Akogwu, 2022; Falade et al., 2021; Gallego & Simov, 2021; Pan et al., 2021; Ozlem, 2020; Peter et al., 2022; Khan et al., 2021; Gomez et al., 2022; Raouf et al., 2022; Ramashis & Biswa, 2022).

Due to the difficulties of finding analytical solutions for fractional order differential equations, semi-analytical approximation methods are given to solve such fractional order differential equation problems. This research aims to utilize the Variational Iterative Method (VIM) and New Iterative Method (NIM), for the numerical solution of the fractional-order Leptospirosis model occurring in five compartments of the Leptospirea environment. These methods have been demonstrated to be excellent mathematical tools for a variety of bio-mathematical phenomena for linear and nonlinear fractional systems of ordinary differential equations. They are promising numerical methods that combine analytical and iterative approaches to approximate solutions of differential equations.

Authors information:

[a]Department of Mathematics, Federal University of Technology, Minna, NIGERIA. E-mail: k.james@futminna.edu.ng[1]

[b]Department of Mathematics, The Chinese University of Hong Kong, HONG KONG. E-mail: abdgafartunde@yahoo.com[2]

[c]Department of Biostatistics and Data Science, The University of Texas Health Sciences, Houston, USA. E-mail: jeremian.n.akpabio@uth.tmc.edu[3]

[d]Department of Mathematics, Faculty of Science, Islamic University of Madinah, Medina, SAUDI ARABIA. E-mail: hijaz.ahmad@neu.edu.tr[4]

[e]Near East University, Operational Research Center in Healthcare, Nicosia, TURKEY. E-mail: hijaz.ahmad@neu.edu.tr[4]

[f]Department of Mathematics and Informatics, Azerbaijan University, Baku, AZERBAIJAN. E-mail: hijaz.ahmad@neu.edu.tr[4]

[g]Department of Mathematics, Federal University of Technology, Minna, NIGERIA. E-mail: majeedstanstazsstarwhite@gmail.com[5]

*Corresponding Author: k.james@futminna.edu.ng

The VIM, proposed by Ji-Huan He in 1999 and later modified in 2007, involves constructing an auxiliary function using a variational principle and iteratively improving the solution. It is a semi-analytical method used to solve various differential equations, including fractional differential equations, boundary value problems and integro-differential equations (Ahmad, 2018; Tebyakin et al., 2023; Narayanamoorthy & Mathankumar, 2018; Shirazian, 2023; Shihab et al., 2023).

The NIM is a well-known method, which is introduced by Daftardar and Jafari (2006) and later called the Daftardar-Jafari method. It is a simple and efficient semi-analytical method for solving differential equations with applications in various fields. The NIM employs an iterative scheme to linearize the problem and refine the solution. It has been successfully applied to differential equations fractional differential equations and partial differential equations (Falade & Tiamiyu, 2020a; Batiha et al., 2023; Falade & Tiamiyu, 2020b).

Both methods have the advantage of providing accurate solutions with reduced computational efforts compared to purely numerical methods. However, they have some limitations. The dependency on initial approximations can be a drawback, requiring careful selection and additional effort. Convergence analysis and stability considerations are also important, particularly when dealing with complex systems or equations with discontinuities. The proposed research is justified due to the importance of understanding and managing leptospirosis, the advantages offered by these methods, and their potential contributions to the field of mathematical modeling in epidemiology.

The literature review reveals the suitability of the two methods for solving diverse mathematical problems. While these methods have been applied to various mathematical equations, their specific application to leptospirosis modeling remains limited. This study aims to fill this research gap by assessing the performance of these methods in solving a fractional leptospirosis model. The novelty and contribution of this research lie in the application and assessment of the two methods, to solve a Fractional model of leptospirosis. While the model formulation itself may have been established, the research introduces a fresh perspective by exploring and evaluating the effectiveness of VIM and NIM in the context of solving the leptospirosis model. By evaluating the performance of these methods in the context of leptospirosis, this study offers insights into their suitability and effectiveness in capturing the dynamics of the disease. The findings contribute to the existing body of knowledge by expanding the understanding of how these methods can be applied to infectious disease modeling, potentially leading to improved disease management strategies.

The structure of this study is as follows: The second section covers a description and formulation of the model and a qualitative analysis of the model, which includes the local stability analysis and Reproduction number. The third section covers a brief introduction to Fractional calculus and some semi-analytical methods, employed for solutions to fractional order derivatives. Section four is concerned with computational experiments of the model, and its Results which are illustrated graphically to illustrate the impact of various variables and characteristics regarding the disease. Furthermore, a discussion of the result is also presented in Section 5. Finally, we conclude the research in Section 6.

2. Model Formulation

The Leptospirosis Model formulation

Considering the works of Khan et al. (2014); Bhalraj et al. (2021) and Aslam et al. (2021), we will use some assumptions in this section to create a deterministic mathematical model of the Leptospirosis virus. This is accomplished by studying how the virus spreads between humans and vectors (cattle). The model is categorized into three compartmental models for humans and two for vectors (cattle). The category of Susceptible $\left(S^H \right)$ humans is made up of people who are recruited at a constant rate g_1 and get infected at a rate B_1 and B_2 in connections to infected humans and vectors respectively. The number of vulnerable population of humans who can become infected fluctuates due to changes in the birth rate or immigration. This category increases by the rate λ_H for those who can become vulnerable again, and it decreases by the rate μ_H for those who die naturally. The rate of change in the susceptible category can therefore be characterized as:

$$\frac{dS^H(t)}{dt} = g_1 + \lambda_H R^H - \mu_H S^H - \mathrm{B}_1 S^H I^H - \mathrm{B}_2 S^H I^V \tag{1}$$

The category of infected humans $\left(I^H \right)$ tends to increase among vulnerable individuals infected at rates B_1 and B_2, and decreases due to natural and induced mortality rates μ_H and δ_H, respectively. Those who recover from the sickness at a slower rate contribute further to the decline. Consequently, the rate of change of infected humans is depicted as:

$$\frac{dI^H(t)}{dt} = B_1 S^H I^H + B_2 S^H I^V - \left(\delta_H + \chi_H + \mu_H\right) I^H \tag{2}$$

The recovery category of human inhabitants $\left(R^H\right)$ grows at a rate χ_H of the transition from infected to recovered compartments. Then, it is reduced by those who recovered from being infectious due to immunity at rate λ_H and by the natural death of recovered inhabitants of rate μ_H. As a result, the community of recovered individuals is changing at the following rate:

$$\frac{dR^H(t)}{dt} = \chi_H I^H - \lambda_H R^H - \mu_H R^H \tag{3}$$

The category of susceptible vectors $\left(S^V\right)$ is created by the recruitment rate g_2. It decreases due to the natural mortality of vectors at rate χ_V and advancement to the infected group at rate B_3. Therefore, the following equation can be used to describe how this category works:

$$\frac{dS^V(t)}{dt} = g_2 - \chi_V S^V - B_3 S^V I^H \tag{4}$$

The infected category of vector inhabitants $\left(I^V\right)$ grows after receiving the virus. The natural death rate χ_V, and induced mortality rate δ_V of the infected vectors cause a decrease. Therefore, the behavior of this category can be modeled using the following equation:

$$\frac{dI^V(t)}{dt} = B_3 S^V I^H - \delta_V I^V - \chi_V I^V \tag{5}$$

With the above assumptions, the non-linear differential equation framework is provided by

$$\frac{dS^H(t)}{dt} = g_1 + \lambda_H R^H - \mu_H S^H - B_1 S^H I^H - B_2 S^H I^V$$

$$\frac{dI^H(t)}{dt} = B_1 S^H I^H + B_2 S^H I^V - \delta_H I^H - \chi_H I^H - \mu_H I^H$$

$$\frac{dR^H(t)}{dt} = \chi_H I^H - \lambda_H R^H - \mu_H R^H \tag{6}$$

$$\frac{dS^V(t)}{dt} = g_2 - \chi_V S^V - B_3 S^V I^H$$

$$\frac{dI^V(t)}{dt} = B_3 S^V I^H - \delta_V I^V - \chi_V I^V$$

Therefore, the entire human population is denoted by the equation $N^H(t) = S^H(t) + I^H(t) + R^H(t)$, whereas the population of vectors (cattle) is denoted by the equation $N^V(t) = S^V(t) + I^V(t)$.

The Fractional Order Leptospirosis Model

According to Chen et al., (2021), the integer-order derivatives of the Leptospirosis epidemic model in (6), are substituted with a fractional-order operator of the Caputo type. The fractional model is controlled by a set of nonlinear differential equations of fractional order α, which are described in the following way:

$$_C D_t^\alpha S^H(t) = g_1 - \mu_H S^H - B_1 S^H I^H - B_2 S^H I^V + \lambda_H R^H$$

$$_C D_t^\alpha I^H(t) = B_1 S^H I^H + B_2 S^H I^V - \delta_H I^H - \chi_H I^H - \mu_H I^H$$

$$_C D_t^\alpha R^H(t) = \chi_H I^H - \lambda_H R^H - \mu_H R^H \tag{7}$$

$$_C D_t^\alpha S^V(t) = g_2 - \chi_V S^V - B_3 S^V I^H$$

$$_C D_t^\alpha I^V(t) = B_3 S^V I^H - \delta_V I^V - \chi_V I^V$$

where $_C D_t^\alpha$ represents Caputo fractional derivative regarding order α.

Reproduction Number of the Model

The reproduction number will be computed by utilizing the matrix method of the next generation. Based on the next-generation matrix idea, the fundamental reproduction number is the next-generation matrix's spectral radius " FV^{-1} ". That is the fundamental reproduction quantity is given as $\mathfrak{R}_0 = \rho\left[FV^{-1}\right]$. To derive the reproduction number, we utilize the second and fourth equations in (7) to obtain

$$\overset{\square}{F} = \begin{pmatrix} \beta_1 S^H I^H + \beta_2 S^H I^V \\ \beta_3 S^V I^H \end{pmatrix}, \quad \overset{\square}{V} = \begin{pmatrix} K_1 I^H \\ K_3 I^V \end{pmatrix} \tag{8a}$$

And then linearize to generate

$$\left.\begin{array}{l} F = \begin{bmatrix} \dfrac{\partial \overset{\square}{F}_1}{\partial I^H} & \dfrac{\partial \overset{\square}{F}_1}{\partial I^V} \\ \dfrac{\partial \overset{\square}{F}_2}{\partial I^H} & \dfrac{\partial \overset{\square}{F}_2}{\partial I^V} \end{bmatrix} = \begin{bmatrix} \beta_1 S^H & \beta_2 S^H \\ \beta_3 S^V & 0 \end{bmatrix} \\[3em] V = \begin{bmatrix} \dfrac{\partial \overset{\square}{V}_1}{\partial I^H} & \dfrac{\partial \overset{\square}{V}_1}{\partial I^V} \\ \dfrac{\partial \overset{\square}{V}_2}{\partial I^H} & \dfrac{\partial \overset{\square}{V}_2}{\partial I^V} \end{bmatrix} = \begin{bmatrix} K_1 & 0 \\ 0 & K_3 \end{bmatrix} \end{array}\right\} \tag{8b}$$

where matrix F represents the partial derivatives of the infected compartments in the human equations with respect to the infected compartments in both human and vector populations. Similarly, matrix V represents the partial derivatives of the infected compartments in the vector equations. After some algebraic manipulations and matrix multiplication, it results into

$$FV^{-1} = \begin{bmatrix} \dfrac{\beta_1 S^H}{K_1} & \dfrac{\beta_2 S^H}{K_3} \\ \dfrac{\beta_3 S^V}{K_1} & 0 \end{bmatrix} \quad and, \mathfrak{R}_0 = \rho \begin{bmatrix} \dfrac{\beta_1 S^H}{K_1} & \dfrac{\beta_2 S^H}{K_3} \\ \dfrac{\beta_3 S^V}{K_1} & 0 \end{bmatrix} \tag{9}$$

where $K_1 = \delta_H + \gamma_H + \mu_H$ and $K_3 = \delta_v + \gamma_v$, then we have the following eigenvalues of the FV^{-1} matrix follows

$$\lambda_1 = \frac{K_3 B_1 g_1 \gamma_V + \sqrt{4 K_1 \mu_H K_3 B_3 g_2 B_2 g_1 + K_3^2 g_1 B_1^2 \gamma_V^2}}{2 \gamma_V K_1 \mu_H K_3}$$

$$\lambda_2 = -\frac{K_3 B_1 g_1 \gamma_V + \sqrt{4 K_1 \mu_H K_3 B_3 g_2 B_2 g_1 + K_3^2 g_1 B_1^2 \gamma_V^2}}{2 \gamma_V K_1 \mu_H K_3} \tag{10}$$

Hence, the reproduction number is represented as

$$\mathfrak{R}_0 = \rho\left[FV^{-1}\right] = \frac{K_3 B_1 g_1 \gamma_V + \sqrt{4 K_1 \mu_H K_3 B_3 g_2 B_2 g_1 + K_3^2 g_1 B_1^2 \gamma_V^2}}{2 \gamma_V K_1 \mu_H K_3} \tag{11}$$

Stability of the Leptospirosis Free Equilibrium (LFE)

The leptospirosis-free equilibrium $\gamma_{LFE} = \left(S_*^H, I_*^H, R_*^H, S_*^H, I_*^H\right)$ is achieved when the population is free of disease. A total of zero will be assigned to all affected categories. As such, the leptospirosis-free equilibrium meets the conditions.

$$\chi_{LFE} = \left(S_*^H, I_*^H, R_*^H, S_*^H, I_*^H\right) = \left(\frac{b_1}{\mu_H}, 0, 0, \frac{b_2}{\gamma_V}, 0\right) \tag{12}$$

To assess the stability of the disease-free equilibrium, we computed the Jacobian matrix in (12) to get

$$J_M = \begin{pmatrix} -\mu_H & -K_4 & \lambda_H & 0 & -K_5 \\ 0 & K_6 - K_1 & 0 & 0 & K_7 \\ 0 & \gamma_H & -K_2 & 0 & 0 \\ 0 & -K_8 & 0 & -\gamma_V & 0 \\ 0 & K_9 & 0 & 0 & -K_3 \end{pmatrix} \tag{13}$$

where $K_2 = \lambda_H + \mu_H$, $K_4 = K_6 = \dfrac{g_1 B_1}{\mu_H}$, $K_5 = K_7 = \dfrac{g_1 B_2}{\mu_H}$, $K_8 = K_9 = \dfrac{g_2 B_3}{\gamma_V}$, and obtain its eigenvalue as follows.

$$\lambda_1 = -\mu_H$$
$$\lambda_2 = -\gamma_V$$
$$\lambda_3 = -K_2$$
$$\lambda_4 = -\frac{K_1}{2} - \frac{K_3}{2} + \frac{K_6}{2} + \frac{\sqrt{K_1^2 - 2K_3 K_1 - 2K_6 K_1 + K_3^2 + 2K_3 K_6 + K_6^2 + 4K_9 K_7}}{2} \tag{14}$$
$$\lambda_5 = -\frac{K_1}{2} - \frac{K_3}{2} + \frac{K_6}{2} - \frac{\sqrt{K_1^2 - 2K_3 K_1 - 2K_6 K_1 + K_3^2 + 2K_3 K_6 + K_6^2 + 4K_9 K_7}}{2}$$

This demonstrates that the real parts of the eigenvalues are negative. As a result, the equilibrium of the leptospirosis at free disease state is said to be asymptotically stable if the real parts of λ_4 and λ_5 are negative too.

Table 1. Values of Parameters Used in Computations.

Parameters	Description	Value	Source
μ_H	Human's natural death rate	0.0121	(Khan et al., 2021)
λ_H	Coefficient of susceptible humans after recovery	0.0008	(Paist & Thamchai, 2021)
δ_H	Coefficient of Induced human death from disease	0.00001	(Altaf et al., 2014)
δ_V	Induced vector death from disease per time	0.001	(Khan et al., 2022)
γ_H	Human recovery coefficient	0.025	(Khan et al., 2022)
γ_V	Vector's natural death rate	0.0018	(Altaf et al., 2014)
B_1	Transmission between Susceptible human and infected human	0.000014	Assumed
B_2	Transmission between Susceptible human and infected vector	0.00002	Assumed
B_3	Transmission between Susceptible vector and infected human	0.007	Assumed
g_1	Rate of human recruitment	0.121	(Chong et al., 2022)
g_2	Rate of vector recruitment	0.002	(Khan et al., 2022)

3. Fractional Calculus

Although fractional calculus is quite old as calculus itself, it has only been in recent decades that its practical applications and mathematical virtues have come to light (Mukdasai et al., 2022; Ayoade et al., 2018; Darzi & Agheli (2018)). The evolution of several definitions, some of which modified pre-existing ones,

may be seen. The sequel provides a few of the more significant ones employed in this work.

Definition 1: A function $U(t)$ [i, j] associated with the Riemann-Liouville (RL) fractional integral operator of order α is represented as

$$I^{\alpha}U(t) = \frac{1}{\Gamma(\alpha)}\int_0^t (t-s)^{\alpha-1}U(s)ds, \quad \alpha > 0, \quad i < t < j \tag{15}$$

where the function of gamma α is expressed in the format $\Gamma(\alpha) = \int_0^{\infty} e^{-t}s^{\alpha-1}ds$

Also, the properties in connection with Riemann-Liouville are;

(i). $I^{\alpha}I^{\beta}U(t) = I^{\alpha+\beta}U(t)$

(ii). $I^{\beta}I^{\alpha}U(t) = I^{\alpha}I^{\beta}U(t)$

(iii). $I^{\beta}t^{\alpha} = \frac{\Gamma(\alpha+1)}{\Gamma(\alpha+\beta+1)}t^{\alpha+\beta}$

Definition 2: For a function $U(t)$ within $i \le t \le j$, concerning Caputo derivative operator of order α is expressed as

$$D_t^{\alpha}U(t) = J^{r-\alpha}D^r U(t)$$

$$= \frac{1}{\Gamma(r-\alpha)}\int_0^t (t-s)^{r-1-\alpha}\left(\frac{d}{ds}\right)^r U(s)ds^{\alpha} \tag{16}$$

where $r-1 < \alpha < r, \ r \in \mathbb{N} \ and \ t > 0$. The associated properties of the Caputo style are;

(i). $I^{\alpha}D^{\alpha}U(t) = U(t)$

(ii). $D^{\beta}t^{\alpha} = \frac{\Gamma(\alpha+1)}{\Gamma(\alpha-\beta+1)}t^{\alpha-\beta}$

(Sources: Mousa & Altaie, 2022; Zabidi et al., 2020; Falade et al., 2023)

By considering a numerical approach for the functional relation in the format.

$$D_t^{\alpha}U(t) + fU(t) + NU(t) = g(t) \tag{17}$$

where N is considered a nonlinear operator, f is a linear function and g is an inhomogeneous term. This section aims to expand the applicability of the NIM and VIM techniques to find approximate results for fractional nonlinear differential systems designated as

$$D_t^{\alpha_1}U_1(t) = f_1(U_1, U_2, \cdots, U_k) + N_1(U_1, U_2, \cdots, U_k) + g_1(t)$$
$$D_t^{\alpha_2}U_2(t) = f_2(U_1, U_2, \cdots, U_k) + N_2(U_1, U_2, \cdots, U_k) + g_2(t)$$
$$\vdots$$
$$D_t^{\alpha_k}U_k(t) = f_k(U_1, U_2, \cdots, U_k) + N_k(U_1, U_2, \cdots, U_k) + g_k(t) \tag{18}$$

where D_t^α is the Caputo-style derivative of U_k of order α_k, subject to some initial criteria such as

$$U_1(0)=h_1, \quad U_2(0)=h_2, \quad \cdots, \quad U_n(0)=h_k, \text{ for } 0\prec\alpha_k\leq 1$$

The Variational Iterative Method (VIM)

The VIM's ideas as well as its applicability to a wide range of different types of linear and nonlinear differential equations are discussed in (Alwehebi et al., 2023; Yin et al., 2013). In the VIM, Lagrange multipliers enforce constraints in the auxiliary function, and Euler-Lagrange equations guide the iterative process to improve accuracy. By using Lagrange multipliers, VIM handles constraints and enhances solution accuracy. To use the VIM to find a solution for the system of nonlinear fractional differential in (18), rewrite the problem so that it takes the format.

$$D_t^{\alpha_1}U_1(t) - f_1(U_1, U_2, \cdots, U_k) - N_1(U_1, U_2, \cdots, U_k) - g_1(t)$$
$$D_t^{\alpha_2}U_2(t) - f_2(U_1, U_2, \cdots, U_k) - N_2(U_1, U_2, \cdots, U_k) - g_2(t)$$
$$\vdots \qquad\qquad (19)$$
$$D_t^{\alpha_k}U_k(t) - f_k(U_1, U_2, \cdots, U_k) - N_k(U_1, U_2, \cdots, U_k) - g_k(t)$$

where $0\prec\alpha_k\leq 1$ concerning some initial criteria $U_1(0)=h_1, \quad U_2(0)=h_2, \quad \cdots, \quad U_n(0)=h_k$. The correction functional with respect to the system of nonlinear fractional equations in (19) is approximately formulated as:

$$U_1^{n+1}(t)=U_1^n(t)+\int_0^t \lambda_1\left[D_t^{\alpha_1}U_1(s)-f_1\left(U_1^n(s),\cdots,U_k^n(s)\right)-N_1\left(U_1^n(s),\cdots,U_k^n(s)\right)-g_1(s)\right]ds$$

$$U_2^{n+1}(t)=U_2^n(t)+\int_0^t \lambda_2\left[D_t^{\alpha_2}U_2(s)-f_2\left(U_1^n(s),\cdots,U_k^n(s)\right)-N_2\left(U_1^n(s),\cdots,U_k^n(s)\right)-g_2(s)\right]ds$$

$$\vdots \qquad\qquad (20)$$

$$U_k^{n+1}(t)=U_k^n(t)+\int_0^t \lambda_k\left[D_t^{\alpha_k}U_k(s)-f_k\left(U_1^n(s),\cdots,U_k^n(s)\right)-N_2\left(\overline{U_1^n(s)},\cdots,\overline{U_k^n(s)}\right)-g_2(s)\right]ds$$

the term situated as the second one from the right is referred to as the correction where $D_t^{\alpha_k}U_k(t)=\dfrac{1}{\Gamma(r-\alpha)}\int_0^t (t-s)^{r-\alpha-1}U^r(s)ds$, and $\lambda_1, \lambda_2, \cdots, \lambda_k$ signifies confined variations and are generic Lagrange multipliers. The Lagrange multiplier λ can be obtained by $\lambda=(-1)^n\dfrac{1}{(-1+n)!}(t-\xi)^{n-1}$, where n represents the number of recurrences of the differentials. To utilize Lagrange multipliers in the VIM approach, we begin by introducing these multipliers into the auxiliary functional formulation. These additional terms are brought in to enforce constraints or boundary conditions imposed on the problem one is working on. This inclusion of Lagrange multipliers transforms the auxiliary function into a function that depends on both the unknown function and these multipliers. They can be found best using variation theory and by making the above functions (20) fixed, we get the following fixed conditions:

$$\lambda_j'(s)\big|_{s=t}=0$$
$$1+\lambda_j(s)\big|_{s=t}=0, \qquad j=1,2,\cdots,k$$

Thus, the multipliers of Lagrange can be denoted as $\lambda_j=-1 \ \ for \ j=1,2,\cdots,k$. Replacing $\lambda_j=-1$ in the correctional functional equation (20) gives the resulting iteration formulations:

$$U_1^{n+1}(t)=U_1^n(t)-\int_0^t \lambda_1\left[D_t^{\alpha_1}U_1(s)-f_1\left(U_1^n(s),U_2^n(s),\cdots,U_k^n(s)\right)-g_1(s)\right]ds$$

$$U_2^{n+1}(t)=U_2^n(t)-\int_0^t \lambda_2\left[D_t^{\alpha_2}U_2(s)-f_2\left(U_1^n(s),U_2^n(s),\cdots,U_k^n(s)\right)-g_2(s)\right]ds$$

$$\vdots \qquad\qquad (21)$$

$$U_k^{n+1}(t)=U_k^n(t)-\int_0^t \lambda_k\left[D_t^{\alpha_k}U_k(s)-f_1\left(U_1^n(s),U_2^n(s),\cdots,U_k^n(s)\right)-g_k(s)\right]ds$$

74

From these first estimates $U_1^0 = h_1, \quad U_2^0 = h_2, \quad \cdots, \quad U_k^0 = h_k$, we may derive all the approximations $U_1^n, \quad U_2^n, \quad \cdots, \quad U_k^n$. Lastly,

$j = 1, 2, \cdots, k$, we use the nth term $U_j^N(t)$ to approximatively solve $U_k(t) = \lim_{j \to \infty} U_j^N(t)$.

The New Iterative Method (NIM)

The NIM was developed in the 21st century and has recently become an extremely well-known method in the connected sciences. The method can be used to solve ordinary and partial differential equations without making any assumptions about diminishing or linearizing effects. This makes it the best alternative method. NIM is based on simple ideas and is straightforward to implement on computers with symbolic computation software such as Maple. This method is superior to numerical methods because it eliminates rounding errors and requires fewer computing resources. In many circumstances, it has been demonstrated to be more effective than other procedures (Zada et al., 2021; Nawaz et al., 2020) to name a few. Considering the basic NIM procedure for a given functional equation depicted as:

$$
\begin{aligned}
D_t^{\alpha_1} U_1(t) &= f_1(t) + N\left[D_t^{\alpha_1} U_1(t) \right] \\
D_t^{\alpha_2} U_2(t) &= f_2(t) + N\left[D_t^{\alpha_2} U_2(t) \right] \\
&\vdots \\
D_t^{\alpha_k} U_k(t) &= f_k(t) + N\left[D_t^{\alpha_k} U_k(t) \right]
\end{aligned}
\tag{22}
$$

where N is considered a nonlinear operator from Banach's space $(B \to B)$, $f(t)$ is a known function, and $0 \prec \alpha_k \leq 1$ for all

values ranging from 1 to inclusive, On both sides of equation (22), the fractional integral operator I^{α_k} is applied, which is the inverse of D^{α_k} (the operator). We seek to obtain the new iterative solutions and the expansion of the solution to equation (22), concerning NIM's interpretation, can be presented in the following manner/series format:

$$
\begin{cases}
U_1(t) = \sum_{h=0}^{\infty} U_h^1(t) \\
U_2(t) = \sum_{h=0}^{\infty} U_h^2(t) \\
\vdots \\
U_k(t) = \sum_{h=0}^{\infty} U_h^k(t)
\end{cases}
\tag{23}
$$

Based on the idea of Daftardar-Geiji and Jaffari (2006), the nonlinear function that is seen on the right-hand side of (22) can be broken down into the following components:

$$
\begin{aligned}
N\left[\sum_{h=0}^{\infty} D_t^{\alpha_1} U_h^1(t) \right] &= N\left(U_0^1 \right) + \sum_{h=0}^{\infty} \left[N\left(\sum_{h=0}^{k} D_t^{\alpha_1} U_h^1(t) \right) - N\left(\sum_{h=0}^{k-1} D_t^{\alpha_1} U_h^1(t) \right) \right] \\
N\left[\sum_{h=0}^{\infty} D_t^{\alpha_2} U_h^2(t) \right] &= N\left(U_0^2 \right) + \sum_{h=0}^{\infty} \left[N\left(\sum_{h=0}^{k} D_t^{\alpha_2} U_h^2(t) \right) - N\left(\sum_{h=0}^{k-1} D_t^{\alpha_2} U_h^2(t) \right) \right] \\
&\vdots \\
N\left[\sum_{h=0}^{\infty} D_t^{\alpha_k} U_h^k(t) \right] &= N\left(U_0^k \right) + \sum_{h=0}^{\infty} \left[N\left(\sum_{h=0}^{k} D_t^{\alpha_k} U_h^k(t) \right) - N\left(\sum_{h=0}^{k-1} D_t^{\gamma_k} U_h^k(t) \right) \right]
\end{aligned}
\tag{24}
$$

When equations (23) and (24) are substituted into equation (22), we get:

$$\sum_{h=0}^{\infty} U_h^1 = f_1(t) + N\left(U_0^1\right) + \sum_{h=0}^{\infty}\left[N\left(\sum_{h=0}^{k} D_t^{\alpha_1} U_h^1(t)\right) - N\left(\sum_{h=0}^{k-1} D_t^{\alpha_1} U_h^1(t)\right)\right]$$

$$\sum_{h=0}^{\infty} U_h^2 = f_2(t) + N\left(U_0^2\right) + \sum_{h=0}^{\infty}\left[N\left(\sum_{h=0}^{k} D_t^{\alpha_2} U_h^2(t)\right) - N\left(\sum_{h=0}^{k-1} D_t^{\alpha_2} U_h^2(t)\right)\right] \qquad (25)$$

$$\vdots$$

$$\sum_{h=0}^{\infty} U_h^k = f_k(t) + N\left(U_0^k\right) + \sum_{h=0}^{\infty}\left[N\left(\sum_{h=0}^{k} D_t^{\alpha_k} U_h^k(t)\right) - N\left(\sum_{h=0}^{k-1} D_t^{\alpha_k} U_h^k(t)\right)\right]$$

The relation of recurrence can be written as

$$\left.\begin{aligned}
U_0^1 &= f_1 \\
U_1^1 &= N\left(U_0^1\right) \\
U_{h+1}^1 &= N\left(U_0^1 + U_1^1 + \cdots + U_h^1\right) - N\left(U_0^1 + U_1^1 + \cdots + U_{h-1}^1\right) \\
U_0^2 &= f_2 \\
U_1^2 &= N\left(U_0^2\right) \\
U_{h+1}^2 &= N\left(U_0^2 + U_1^2 + \cdots + U_h^2\right) - N\left(U_0^2 + U_1^2 + \cdots + U_{h-1}^2\right) \\
&\vdots \\
U_0^k &= f_k \\
U_1^k &= N\left(U_0^k\right) \\
U_{h+1}^k &= N\left(U_0^k + U_1^k + \cdots + U_h^k\right) - N\left(U_0^k + U_1^k + \cdots + U_{h-1}^k\right) \\
h &= 1, 2, 3, \cdots
\end{aligned}\right\} \qquad (26)$$

Then it leads to the relation

$$\left(U_0^1 + U_1^1 + U_2^1 + \cdots + U_{h+1}^1\right) = N\left(U_0^1 + U_1^1 + U_2^1 + \cdots + U_h^1\right)$$

$$\left(U_0^2 + U_1^2 + U_2^2 + \cdots + U_{h+1}^2\right) = N\left(U_0^2 + U_1^2 + U_2^2 + \cdots + U_h^2\right)$$

$$\vdots \qquad (27)$$

$$\left(U_0^k + U_1^k + U_2^k + \cdots + U_{h+1}^k\right) = N\left(U_0^k + U_1^k + U_2^k + \cdots + U_h^k\right)$$

and we obtain

$$\sum_{v=0}^{\infty} U_k = f + N\left[\sum_{v=0}^{\infty} U_k\right] \qquad (28)$$

Finally, the solutions of $n-$term estimations of (22) are provided by $U = U_0 + U_1 + U_2 + \cdots + U_{n-1}$

4. Computational Experiments

This section illustrates the numerical solution of model (7) based on the fractional order model of leptospirosis. Because fractional order differential equations lack accurate analytical solutions, semi-analytical approximation methods are presented to overcome this fractional order differential equation problem.

Regarding the numerical solution of the system (7), we employed the VIM and NIM discussed in the previous section, to proffer numerical solutions.

Application of VIM on Fractional Order Leptospirosis Model

By applying the VIM formula to solve the Leptospirosis Fractional order model (7), we obtain the correction functional as follows;

76

$$S_{k+1}^{H}(t) = S_{k}^{H}(t) - \int_{0}^{t}\left[D_{t}^{\alpha_{1}}S_{k}^{H}(s) - g_{1}(s) + B_{1}S_{k}^{H}(s)I_{k}^{H}(s) + B_{1}S_{k}^{H}(s)I_{k}^{V}(s) - \mu_{H}R_{k}^{H}(s)\right]ds$$

$$I_{k+1}^{H}(t) = I_{k}^{H}(t) - \int_{0}^{t}\left[D_{t}^{\alpha_{2}}I_{k}^{H}(s) - B_{1}S_{k}^{H}(s)I_{k}^{H}(s) - B_{1}S_{k}^{H}(s)I_{k}^{V}(s) + (\delta_{H} + \chi_{H} + \mu_{H})I_{k}^{H}(s)\right]ds$$

$$R_{k+1}^{H}(t) = R_{k}^{H}(t) - \int_{0}^{t}\left[D_{t}^{\alpha_{3}}R_{k}^{H}(s) - \chi_{H}I_{k}^{H}(s) + \lambda_{H}R_{k}^{H}(s) + \mu_{H}R_{k}^{H}(s)\right]ds \qquad 29$$

$$S_{k+1}^{V}(t) = S_{k}^{V}(t) - \int_{0}^{t}\left[D_{t}^{\alpha_{4}}S_{k}^{V}(s) - g_{2}(s) + \chi_{V}S_{k}^{V}(s) + B_{3}S_{k}^{V}(s)I_{k}^{H}(s)\right]ds$$

$$I_{k+1}^{V}(t) = I_{k}^{V}(t) - \int_{0}^{t}\left[D_{t}^{\alpha_{5}}I_{k}^{V}(s) - B_{3}S_{k}^{V}(s)I_{k}^{H}(s) + \delta_{V}I_{k}^{V}(s) + \chi_{V}I_{k}^{V}(s)\right]ds$$

The initial conditions of the variables are $S_{0}^{H} = 100, I_{0}^{H} = 20, R_{0}^{H} = 30, S_{0}^{V} = 50 \text{ and } I_{0}^{V} = 10$ combined with values of the parameters in Table 1 are inserted in the above equation. In the numerical simulations, we integrate available data, grounding the simulations in empirical findings. Simultaneously, assumed values are strategically introduced to address uncertainties in specific regional data, enhancing adaptability. These choices contribute to a comprehensive numerical framework, combining existing knowledge with thoughtful assumptions for exploring the dynamic intricacies of Leptospirosis spread. As such, the solution as follows.

$$
\begin{aligned}
S^{H} = {} & 100 - 4.45200000t - 2.801171767t^{2} + 0.01213769126t^{3} - 0.00009045352718t^{4} \\
& - 8.052530390 \times 10^{-6}t^{5} + 3.062550894 \times 10^{-8}t^{6} - 8.342872503 \times 10^{-8}t^{7} + 6.802098552 \times 10^{-9}t^{8} \\
& - 1.103747079 \times 10^{-10}t^{9} - 1.771925258 \times 10^{-14}t^{10} + 4.545999430 \times 10^{-16}t^{11} + \ldots
\end{aligned}
$$

$$
\begin{aligned}
I^{H} = {} & 20 - 20.77680000t - 9.124152759t^{2} + 1.015793230t^{3} + 0.00406576125t^{4} \\
& + 5.855770683 \times 10^{-6}t^{5} - 3.030395707 \times 10^{-6}t^{6} + 8.337606600 \times 10^{-8}t^{7} - 6.802285196 \times 10^{-9}t^{8} \\
& + 1.103747079 \times 10^{-10}t^{9} + 1.771925258 \times 10^{-14}t^{10} - 4.545999430 \times 10^{-16}t^{11} + \ldots
\end{aligned}
$$

$$
\begin{aligned}
R^{H} = {} & 30 + 18.4520000t + 7.672734943t^{2} - 1.009207206t^{3} - 0.003975024183t^{4} \\
& + 2.196671850 \times 10^{-6}t^{5} - 3.215390123 \times 10^{-8}t^{6} + 5.265691836 \times 10^{-11}t^{7} + 1.866364860 \times 10^{-13}t^{8} \\
& - 20.82085239t^{3/2} + 1.435417448t^{5/2} - 0.1351859757t^{7/2} + \ldots
\end{aligned}
$$

$$
\begin{aligned}
S^{V} = {} & 50 - 27.87600000t - 9.327890169t^{2} + 0.8135892032t^{3} - 0.6357144870t^{4} \\
& + 0.05420793935t^{5} - 0.007615697802t^{6} + 0.0004096108888t^{7} - 0.00001842953807t^{8} \\
& + 2.825726738 \times 10^{-7}t^{9} + 2.822955643 \times 10^{-9}t^{10} + 31.45469766t^{3/2}
\end{aligned}
$$

$$
\begin{aligned}
I^{V} = {} & 10 + 27.88800000t + 9.314597411t^{2} - 0.8181215464t^{3} + 0.6355509391t^{4} \\
& - 0.05420606038t^{5} + 0.007615269121t^{6} + 0.00001842953780t^{8} - 0.0004096012571t^{7} \\
& - 2.825726739 \times 10^{-7}t^{9} - 2.822955643 \times 10^{-9}t^{10} - 1.363464346 \times 10^{-14}t^{11}
\end{aligned}
$$

Application of NIM on Fractional Order Leptospirosis Model

Applying the NIM procedure to compute the Leptospirosis Fractional order model in (7), we obtain the following equations.

$$S^H(t) = S^H(0) - I_t^{\alpha_1}\left[g_1(s) - B_1 S^H(t) I^H(t) - B_1 S^H(t) I^V(t) + \mu_H R^H(t) \right]$$

$$I^H(t) = I^H(0) - I_t^{\alpha_2}\left[B_1 S^H(t) I^H(t) + B_1 S^H(t) I^V(t) - (\delta_H + \chi_H + \mu_H) I^H(t) \right]$$

$$R^H(t) = R^H(0) - I_t^{\alpha_3}\left[\chi_H I^H(t) - \lambda_H R^H(t) - \mu_H R^H(t) \right] \tag{30}$$

$$S^V(t) = S^V(0) - I_t^{\alpha_4}\left[g_2(s) - \chi_V S^V(t) - B_3 S^V(t) I^H(t) \right]$$

$$I^V(t) = I^V(0) - I_t^{\alpha_5}\left[B_3 S^V(t) I^V(t) - \delta_V I^V(t) - \chi_V I^V(t) \right]$$

After transforming the unknown terms into infinite series and evaluating the nonlinear terms concerning the new iterative concept, the estimated solution is presented as

$$\begin{aligned}
S^H = {}& 100 - 1.255886013\sqrt{t} + 0.01709961999t - 6.580429508 \times 10^{-7} t^2 - 5.188031459 \times 10^{-8} t^3 \\
& - 2.014517145 \times 10^{-13} t^4 - 2.299607981 \times 10^{-22} t^5 - 0.0008179322706 t^{3/2} + \ldots
\end{aligned}$$

$$\begin{aligned}
I^H = {}& 20 - 5.861027069\sqrt{t} + 1.361509842\,t + 0.00001565159704 t^2 + 5.188112813 \times 10^{-8} t^3 \\
& + 2.014517145 \times 10^{-13} t^4 + 2.299607981 \times 10^{-22} t^5 - 0.2685318063 t^{3/2} + \ldots
\end{aligned}$$

$$\begin{aligned}
R^H = {}& 30 + 5.205213097\sqrt{t} - 1.231544819t - 0.00001423242583 t^2 - 7.715173144 \times 10^{-13} t^3 \\
& + 0.2428377159 t^{3/2} - 1.171556959 \times 10^{-8} t^{5/2}
\end{aligned}$$

$$\begin{aligned}
S^V = {}& 50 - 7.997951536\sqrt{t} + 0.01247840000t + 0.0002898312344 t^2 + 0.001303355628 t^3 \\
& - 7.080468976 \times 10^{-11} t^4 - 8.254818517 \times 10^{-20} t^5 - .2469258630 t^{3/2} + \ldots
\end{aligned}$$

$$\begin{aligned}
I^V = {}& 10 + 7.867059552\sqrt{t} - 0.01924160000t - 0.0004539436269 t^2 - 0.001303355628 t^3 \\
& + 7.080468976 \times 10^{-11} t^4 + 8.254818517 \times 10^{-20} t^5 + 0.2469494953 t^{3/2} + \ldots
\end{aligned}$$

Here, we present comprehensive tabular and graphical representations of the numerical assessment results for VIM and NIM techniques applied to solve the Fractional-order leptospirosis model (7). The Tables offer a detailed analysis of the outcomes obtained during the experimentation process.

Table 2. Comparison between VIM and NIM for Leptospirosis Human Fractional Model.

Days	VIM $S^H(t)$	NIM $S^H(t)$	VIM $I^H(t)$	NIM $I^H(t)$	VIM $R^H(t)$	NIM $R^H(t)$
0	100.00000	100.00000	20.0000000	20.0000000	30.00000	30.000000
1	99.68757617	99.60453810	18.56993202	18.27423993	31.26700102	31.53055749
2	99.45781321	99.44169743	17.56498476	17.62715340	32.15214960	32.10325260
3	99.26794909	99.31711830	16.77181856	17.15411336	32.84640998	32.52145021
4	99.10396857	99.21234079	16.11664599	16.76983370	33.41622348	32.86087923
5	98.95839873	99.12021483	15.55883537	16.44144656	33.89830128	33.15072160
6	98.82661250	99.03707419	15.07272349	16.15217727	34.31587841	33.40586948
7	98.70551628	98.96074062	14.64102175	15.89210873	34.68462057	33.63512621
8	98.59294782	98.88979530	14.25173000	15.65481035	35.01539483	33.84419968
9	98.48735654	98.82325248	13.89646415	15.43583678	35.31577455	34.03703533
10	98.38761633	98.76039476	13.56945680	15.23196689	35.59094024	34.21649175

Table 3. Comparison between VIM and NIM for The Leptospirosis Vector Fractional Model.

Days	VIM $S^V(t)$	NIM $S^V(t)$	VIM $I^V(t)$	NIM $I^V(t)$
0	50.00000000	50.000000	10.0000000	10.0000000
1	48.10115515	47.46426898	11.89953979	12.49366212
2	46.79834431	46.40363800	13.20261734	13.53646822
3	45.79384992	45.58256866	14.20713973	14.34369900
4	44.98219532	44.88429720	15.01866656	15.03019388
5	44.30484125	44.26375440	15.69578809	15.64027672
6	43.72483161	43.69790510	16.27549453	16.19660039
7	43.21744123	43.17311249	16.78253423	16.71257461
8	42.76572616	42.68052253	17.23386667	17.19690544
9	42.35807446	42.21400716	17.64111347	17.65561817
10	41.98672198	41.76912096	18.01204373	18.09308338

Graphical representations of the SIR-SI compartment dynamics within the context of our study on Fractional leptospirosis modeling provide visual insights into the disease spread and transmission patterns. Below, you will find a series of informative graphs illustrating the behavior of this compartment.
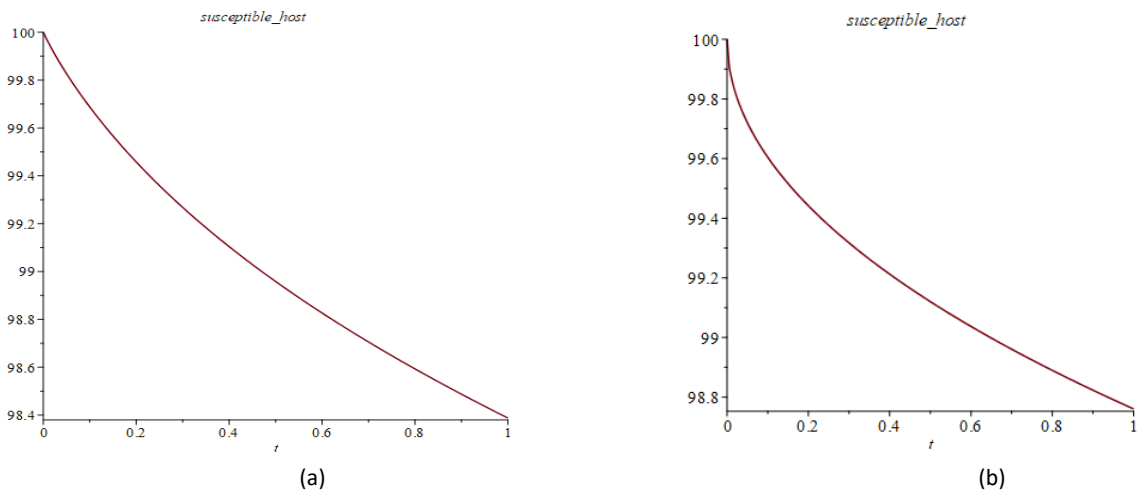
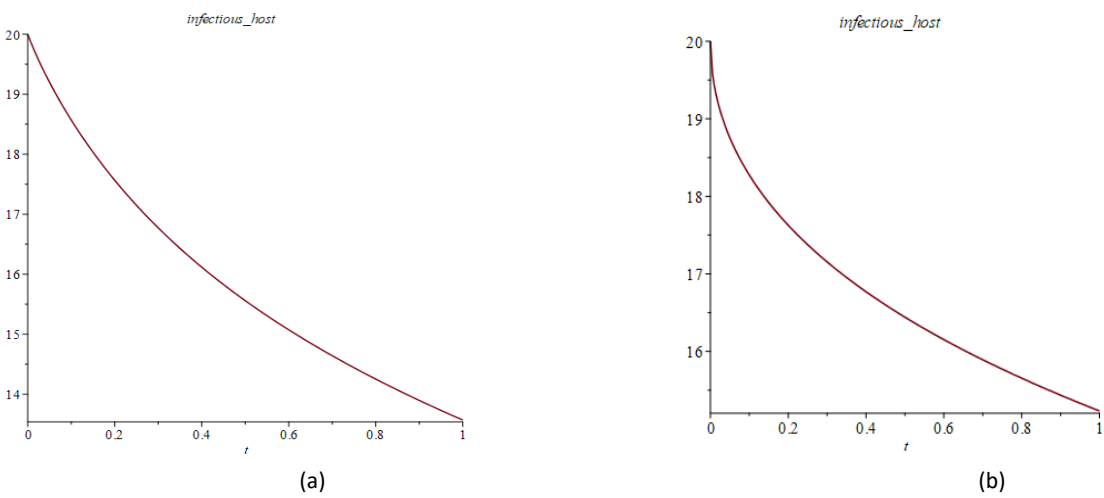**Figure 1.** Plots of the model (7) for Susceptible humans when α = 0.5; (a) VIM (b) NIM.

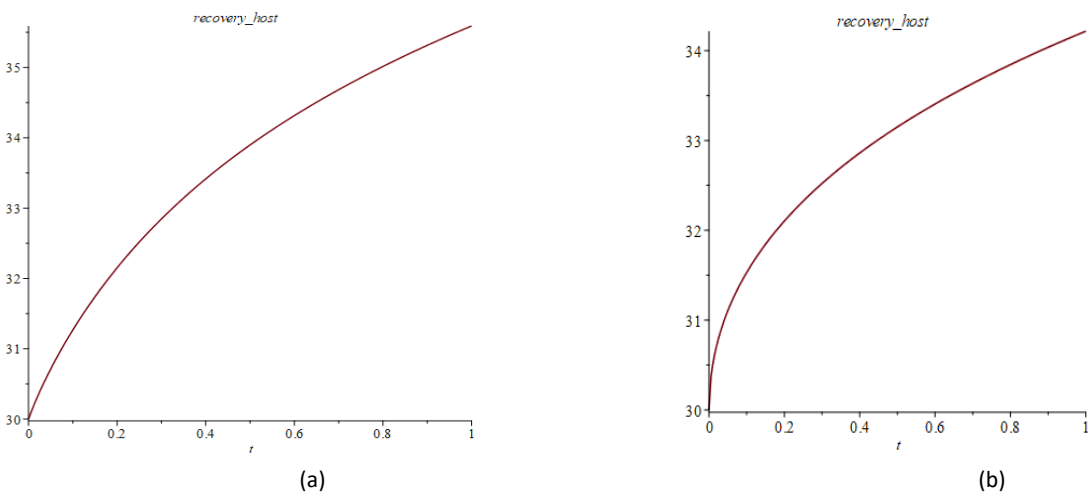**Figure 2.** Plots of the model (7) concerning Infected humans when α = 0.5; (a) VIM (b) NIM.

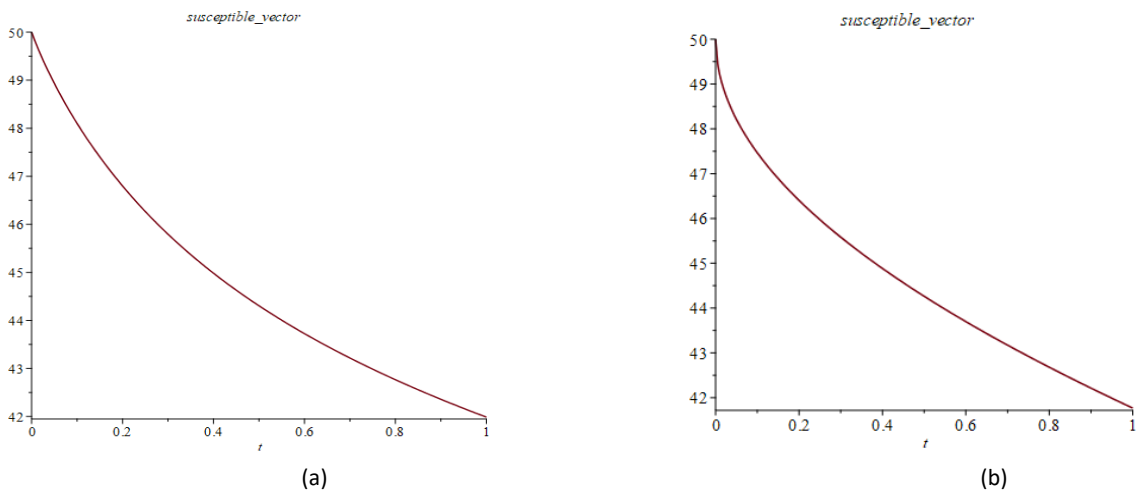**Figure 3.** Plots for model (7) regarding Recovery human when α = 0.5; (a) VIM (b) NIM.

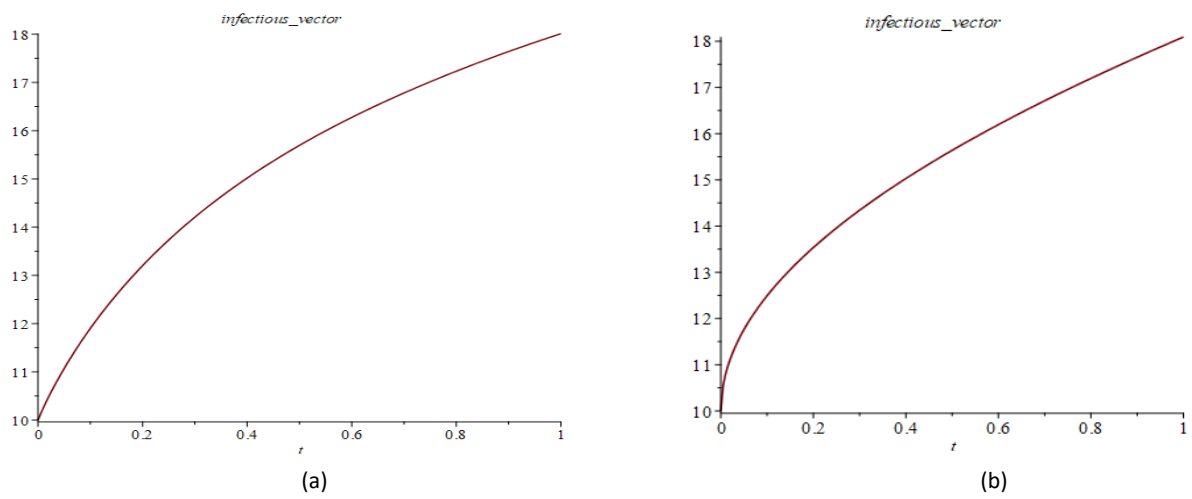**Figure 4:** Plots of model (7) for Susceptible vector when α = 0.5; (a) VIM (b) NIM.

Figure 5: Plots of (7) concerning Infected vector when α = 0.5; (a) VIM (b) NIM.

The graphical representation for better visualization of Tables 2 and 3 is presented below.
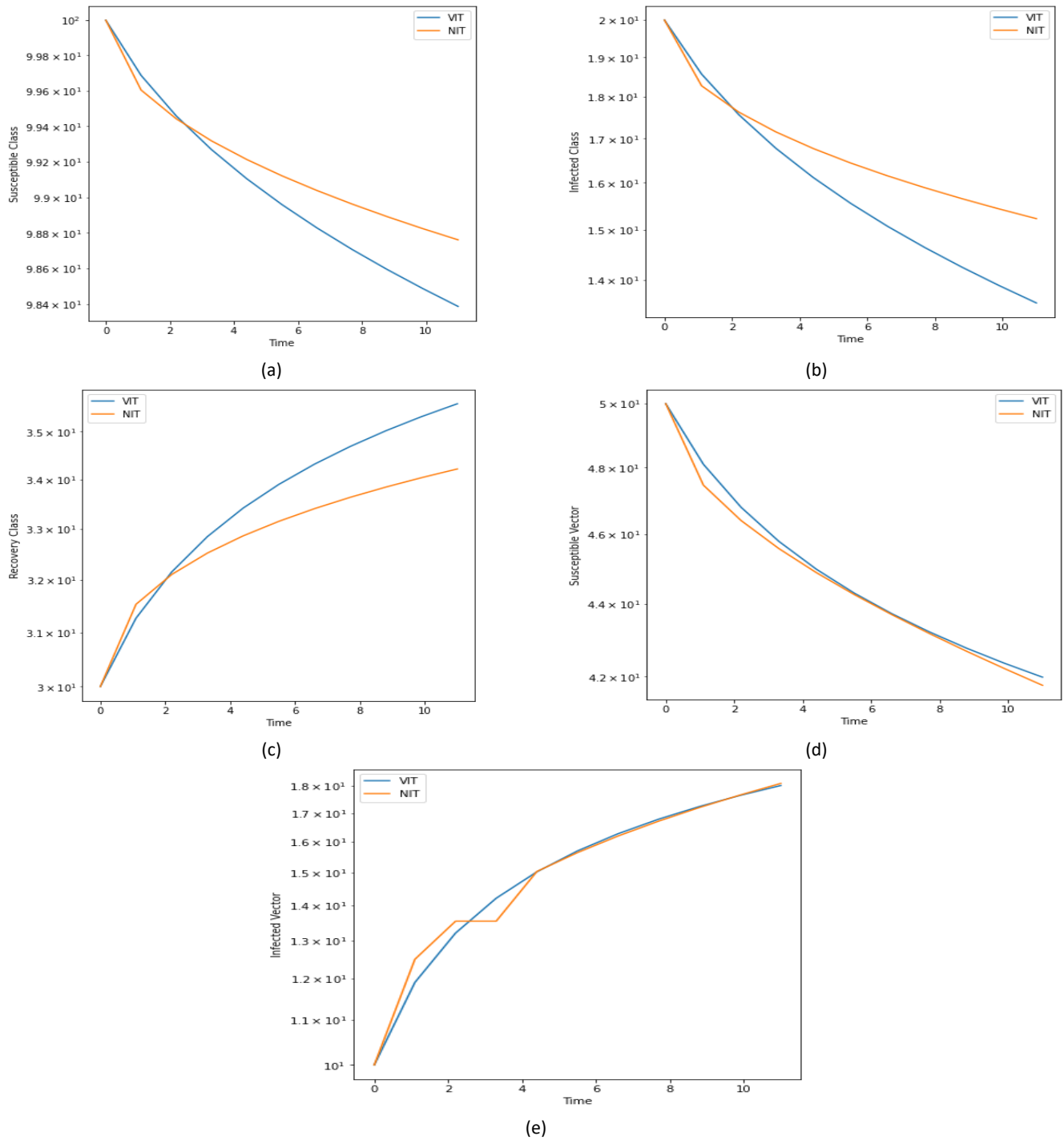

(a)

(b)

(c)

(d)

(e)

Figure 6: Plot (a - e) showing a comparison of VIM and NIM for the SIR-SI Fractional leptospirosis model.

5. Discussion of Results

Table 2 presents a comparison of the VIM and NIM methods in terms of their impact on susceptible, infected, and recovered human populations over 10 days. The two methods started with the same values for susceptible humans, infected humans, and recovered humans on day 0. Both methods led to a gradual decrease in the number of susceptible humans and an increase in the number of recovered humans over the 10 days, but the rate of change varied. On day 10, the VIM method showed a slightly higher percentage of susceptible humans and a lower percentage of infected humans compared to the NIM method, indicating that it is slightly more effective in reducing the number of susceptible humans, while the NIM method is slightly less effective in reducing the number of infected humans. Overall, both methods were effective in reducing the number of susceptible and infected humans and increasing the number of recovered humans, but the VIM method had a slightly better performance in reducing the

number of susceptible humans and the NIM method had a slightly worse performance in reducing the number of infected humans.

Table 3 presents the susceptible and infected vectors at different times for both methods. At time zero, the susceptible vector had a value of 50 and the infected vector had a value of 10. Both methods resulted in a decrease in the values of the susceptible vector and an increase in the values of the infected vector over time, but the rates of change varied. The trend continued with VIM showing slightly higher values than NIM. However, VIM performed slightly better than NIM, as indicated by higher values for the susceptible vector and lower values for the infected vector. These differences may be attributed to the different numerical procedures employed by the two methods.

The graphs in Figures 1, 2, and 3 displaying the populations of susceptible humans, infected humans, and recovered humans are generated from a comparative assessment of the VIM and NIM. In Figures 1, and 2, both methods demonstrated a gradual decline in the count of susceptible and infected humans while they depict a concurrent rise in the count of recovered humans in Figure 3. Figures 4 and 5 display changes in the populations of susceptible and infected vectors at different time points for NIM and VIM approaches. It is shown that, both methods led to a reduction in the number of susceptible vectors in Figure 4 and an increase in the number of infected vectors in Figure 5.

Figure 6 illustrates the comparison of the behavior of various classes (compartments) being examined under values of α in terms of their disease status. The dynamics of all model populations are depicted, revealing that at α=0.5, most populations decline except for classes of recovery human and infected vector. It becomes evident that the class of Susceptible humans decreases with VIM, by approximately 1.6% and 1.2% with NIM, (a), and Infectious humans also decrease with VIM by 6.43% and NIM by 4.77%, (b). Conversely, the class of susceptible vectors gradually decreases by 8.01% and 8.23% as captured by both VIM and NIM respectively, (d), while the class of recovered human increases by approximately 35.59% with VIM and 34.22% with NIM, (c), and a notable increase is observed in the infected vector in (e).

It is important to note that these results are based on the specific conditions and parameters of the model used in this study and may not be generalizable to other models or scenarios. Further studies may be needed to validate these findings and explore the effectiveness of other numerical methods for solving similar models.

6. Conclusion

In this study, a fractional Leptospirosis model was simulated using the VIM and the NIM. As regards the model, the solutions obtained from the two methods are relatively close. We compared the effectiveness of these two methods by analyzing their results on a simulated population using a susceptible-infected-recovered (SIR) model. Our analysis showed that both VIM and NIM can be effective in modeling the spread of infectious diseases. However, we found that VIM performed slightly better than NIM in terms of accuracy and convergence rate. Specifically, VIM showed a faster convergence rate and smaller error values compared to NIM. Overall, the findings suggest that VIM can be a useful tool for modeling the spread of infectious diseases. However, further research is needed to explore the potential of these methods in modeling more complex infectious disease scenarios. In conclusion, this study highlights the importance of using effective simulation/solving methods in understanding the dynamics of infectious diseases. Future research could explore the applicability of VIM and NIM in solving diseases with multiple strains, spatial dynamics, or dynamic human behaviors.

These findings could affect future research or practical applications such as developing a real-time simulation/tool that integrates current data to predict the future spread of the disease, aiding public health officials in making timely and informed decisions. As well as to optimize intervention strategies, such as vaccination campaigns or public health measures, with the aim of minimizing the impact of the disease. By using VIM and NIM, we were able to gain insights into the spread of diseases in human populations and vector populations and identify the strengths and weaknesses of these two methods. Overall, the VIM method is a better approach for simulating the fractional Leptospirosis fractional model. The results obtained will aid in advancing our understanding and potential management strategies for leptospirosis. Finally, all computations and algorithms are implemented using version 2021 of the Maple software.

7. Acknowledgement

8. References

Ahmad, H. (2018). Variational iteration method with an auxiliary parameter for solving

differential equations of the fifth order, *Nonlinear Science Letters* A, 9(1), 27–35.

Altaf, K. M., Islam S., & Afzal, K. S. (2014). Mathematical Modeling Towards the Dynamical Interaction of Leptospirosis. *Applied Mathematics and Information Sciences*, 8, 1049-1056.

Alwehebi, F., Hobiny, A., & Maturi, D. (2023). Variational Iteration Method for Solving Time Fractional Burgers Equation Using Maple. *Applied Mathematics*, 14, 336-348.

Akogwu, B. O. (2022). Approximate Solutions of Malaria Disease Transmission Model: Using Mult-Step Differential Transform Method, *FUDMA Journal of Science*, 6(6), 182-194.

Ali, Z., Rabiei F., Rashidi, M. M., & Khodadadi, T. (2022). A fractional-order mathematical model for COVID-19 outbreak with the effect of symptomatic and asymptomatic transmissions. *European Physical Journal Plus*, 137, 395.

Aslan, I. H., Baca-Carrasco, D., Lenhart, S., & Velasco-Hernandez, J. X. (2021). An age structure model with impulse actions for

Leptospirosis in livestock cattle. *Journal of Biological Systems*, *29*(1), 75–105.

Ayoade, A, A., Ibrahim, M. O., & Odetunde, O. (2018). Analytical Solution of a Fractional Order Cholera Model. *Nigerian Journal of Scientific Research,* 17, 158-164.

Batiha, B., Ghanim, G., & Batiha, K. (2023). Application of the New Iterative Method (NIM) to the Generalized Burgers–Huxley Equation, *Symmetry*, 15.

Bhalraj,A., & Azmi-Mohd, H. (2021). Analytical and Numerical Solutions of Leptospirosis Model. *International Journal of Mathematics and Computer Science*, *16*(3), 949–961.

Chen, Y., Liu, F. Yu, Q. & Li, T. (2021). Review of fractional epidemic models. *Applied Mathematical Modelling*, 97, 281–307.

Chong, J. W., Tiong, W. K., Labadin, J. 1., & Sahak, N. (2022). Mathematical modeling of Leptospirosis spread in Malaysia. *Mathematical Modeling and Computing*, *9*(1), 18–25.

Daftardar-Gejji, V., Jafari, H. (2006). An iterative method for solving nonlinear functional equations, *Journal of Mathematical Analysis and Applications*, *316*(2), 753–763.

Darzi, R. & Agheli, B. (2018). An analytic approach for the system of fractional differential equations by means of innovative homotopy perturbation method. *Mathematica Moravica*, *22*(1), 93-105.

Falade, K. I., & Tiamiyu, A. T. (2020a). Computatıonal Algorıthm for the Numerıcal Solutıon of Systems of Volterra Integro-Dıfferentıal Equatıons, *Academic Journal of Applied Mathematical Sciences*, 6, 66-76.

Falade, K. I., & Tiamiyu, A. T. (2020b) Numerical solution of partial differential equations with fractional variable coefficients using new iterative method (NIM), *Mathematical Sciences and Computing*, 3, 12-21.

Falade, K. I., Tiamiyu, A. T., & Isa U. (2021). Numerical Comparison of Runge-Kutta (Rk5) and New Iterative Method (Nim) for solving Metastatic Cancer Model. *Malaysian Journal of Computing*, 6, 758-771.

Falade, K. I., Tiamiyu, A. T., Adio, A. K., Tahir, H. M., Abubakar, U. M., & Badamas, S. M. (2023). Computational Relationship of the Surface Area, and Stiffness of the Spring Constant on Fractional Bagley-Torvik Equation. *Turkish Journal of Science & Technology*, *18*(1), 23-31.

Gomez, A. A., Lopez, M. S., Mullere, G. V., Lopez, L. R., Sione, W., & Giovina, L. (2022). Modeling Leptospirosis outbreaks in relation to hydroclimatic variables in the northeast of Argentina. *Heliyon* 8(2022).

Gallego, M. A., Simoy, M. V. (2021). Mathematical modeling of leptospirosis: A dynamic regulated by environmental carrying capacity. *Chaos, Solitons & Fractals,* 152, 114-125.

He, J. H. (2007). Variational iteration method-some recent results and new interpretations. *Journal of Computational and Applied Mathematics*, *207*(1), 3-17.

Khan, M. F., Alrabaiah, H., Altaf, S. M., Farooq, K. M., Mamat, M. & Asjad, M. I. (2021). A new fractional model for vector-host disease with saturated treatment function via singular and non-singular operators. *Alexandria Engineering Journal*, 60, 629–645.

Khan, M. A., Saeed, I., & Khan, S. A. (2014). Mathematical Modeling towards the dynamical Interaction of Leptospirosis. *Applied Mathematics and Information Sciences*, *8*(3), 1049-1056.

Mousa, M. G., & Altaie, H. O. (2022). Efficient analytical method for the solution of some fractional-order nonlinear differential equations. *International Journal of Nonlinear Analytical Application*, *13*(2), 401–408.

Mukdasai, K., Sabir, Z., Asif, M., Raja, Z., Sadat, R., Ali, M. R., & Singkibud, P. (2022). A numerical simulation of the fractional order Leptospirosis model using the supervised neural Network. *Alexandria Engineering Journal,* 61, 12431–12441.

Nawaz, R., Ali N., Zada, L., Shah, Z., Tassaddiq, A., & Alreshidi, N. A. (2020). Comparative analysis of natural transform decomposition method and new iterative method for fractional foam drainage problem and fractional order modified regularized long-wave equation," *Fractals, 28*(7) article 2050124.

Ngoma, H. D., Kiogora, R. P., & Chepkwony, I. (2022). A Fractional Order Model of Leptospirosis Transmission Dynamics with Environmental Compartment. Global *Journal of Pure and Applied Mathematics*, 18, 81-110.

Ozlem, D. O. (2020). Modeling the impact of temperature on fractional order dengue model with vertical transmission. *International Journal of Optimization and Control: Theories and Applications*, 10, 85-93.

Paisanwarakiat, P., & Thamchai, P. (2021). Optimal Control of a Leptospirosis Epidemic Model. *Science and Technology Asia*, *26*(1), 9-17.

Pan, W., Li, T., & Ali, S. (2021). A fractional order epidemic model for the simulation of outbreaks of Ebola. *Advances in Difference Equations*, 161, 1-21.

Peter, O. J., Oguntolu, F. O., Mayowa, M. O., Oyeniyi, A. O., Jan, R., & Khan, I. (2022). Fractional order mathematical model of monkeypox transmission dynamics. *Physica Scripta*, 97, 084005.

Ramashis B., & Biswa, F. (2022). Fractional optimal control of compartmental SIR model of COVID-19: Showing the impact of effective vaccination., *International Federation of Automatic Control*, *55*(1), 616–622.

Raouf, R., Zarin, A., & Yusuf, U. W. (2022). Existence theory and numerical solution of leptospirosis disease model via exponential decay law. *AIMS Mathematics*, *7*(5), 8822–8846.

Shihab, M. A., Taha, W. M., Hameed, R. A., Jameel, A., & Ibrahim, S. M. (2023). Implementation of variational iteration method for various types of linear and nonlinear partial differential equations. *International Journal of Electrical and Computer Engineering*, *13*(2), 2131-2141.

Shirazian, M. (2023). A new acceleration of variational iteration method for initial value problems. Mathematics and Computer in Simulation, 204, 640-644.

Tebyakin, A. D., Kalutsky, L. A., Yakovleva, T. V., & Krysko, A. V. (2023). Application of Variational Iterations Method for Studying Physically and Geometrically Nonlinear Kirchhoff Nanoplates: A Mathematical Justification. *Axioms*, 12,

Tomar, S., Singh, M., Vajravedu, K., & Ramos, H. (2023). Simplifying the variational iteration method: A new approach to obtain the Lagrange multiplier. *Mathematics and Computer in Simulation*, 204, 640-644.

Yin, F., Song, J., & Cao, X. (2013). A General Iteration Formula of VIM for Fractional Heat- and Wave-Like Equations. *Journal of Applied Mathematics*, Article ID 428079.

Zabidi, N. U., Abdul-Majid, Z., Kilicman, A., & Rabiei, F. (2020). Numerical Solutions of Fractional Differential Equations by Using Fractional Explicit Adams Method, *Mathematics*, *8*(1675), 1-23.

Zada, L., Nawaz, R., Ahsan, S., Nisar, K. S., & Baleanu, D. (2021). New iterative approach for the solutions of fractional order inhomogeneous partial differential equations, *AIMS Mathematics*, *6*(2), 1348–1365.

INVESTIGATION OF WETTABILITY, ANTIBACTERIAL ACTIVITY, THERMAL INSULATION, AND MECHANICAL CHARACTERISTICS OF ELASTOMER BLEND ADHESIVES WITH HIGH-DENSITY FIBERBOARD WOOD AND ALUMINUM

Maha K. Majeed[1a], Seenaa I. Hussein[2a]*

Abstract: Attention has recently been given to finding alternative and sustainable raw material sources for wood and metal adhesives, such as polyvinyl alcohol (PVA), corn starch (CS), arabic gum (AG), and dextrins (D). Modifying polymer dispersion using unique substances, such as modifying reactive elastomer liquid (EL) using PVA, CS, AG, or D results in sufficiently moisture-resistant adhesive joins. In the present study, the physical characteristics of EL/blended with the natural polymers PVA, CS, AG, and D, based on high-density fiberboard (HDF) wood and aluminum (Al) adhesives and coatings, were investigated and compared to those of pure EL. The EL was blended with PVA, CS, AG, or D at a ratio of 60/40 (w/w) to form EL/blends. The chemical structures, surface and interface morphology, adhesion strengths (including shear strength and pull-off strength), surface roughness, wettings, color intensity, and thermal insulation of the prepared EL and EL/blends were investigated. A scanning electron microscopy (SEM) investigation confirmed filler dispersion and adhesion between the blends, and coated HDF wood, or Al. The developed EL/AG blend had a pull-off strength of 144±5 and 102±3 MPa and a shear strength of 771±11, and 52±3 N with HDF wood and Al substrate, respectively. The EL/PVA blend had a maximum surface roughness value 4.57 µm, and its average water contact angle (WCA) was 85.6°. A plasma jet was used to treat the surface roughness and hence the wettability of the pure EL and the EL/blends, for example, plasma treatment decreased the roughness of the EL/AG blend from 4.36 to 3.28 µm. WCA, and hence wettability, was also significantly influenced by plasma treatment, for example, plasma treatment decreased the WCA of the pure EL from 71.7±0.4° to 30.7±0.7°. The lightness value of the EL/blends was less than that of the pure EL, indicating that (the color adhesives have darkened). Similarly, the yellowness-blueness and redness-greenness values of the EL/blends were greater than those of the pure EL,(rendering the blended adhesives more reddish and bluish). The EL/AG blend was found to have a minimum thermal conductivity (of 0.27 W/m.K), indicating maximum insulation.

Keywords: Elastomers, adhesives, wettability, mechanical, color, thermal insulation, antibacterial, plasma.

1. Introduction

Sealant and adhesive substances pervade our environment and are used in almost every company and sector, as a result, significant efforts have been made to develop these compounds (Sunday, 2015; Ali *et al.*, 2021; Almashhadani, 2021; Kun & Pukánszky, 2017). Polar compounds with ionic groups, *i.e.,* hydrophilic molecules, readily absorb and dissolve in polar solvents such as water, where they generate hydrogen bonds. Thus, hydrophilic substances are polar (molecules) that easily establish hydrogen bonds and dissolve in water (Al-Lhaibi & Al-Shabander, 2022).

Natural polymers such as polyvinyl alcohol (PVA), corn starch(CS), and arabic gum (AG), have unique qualities that include non-toxicity, water solubility, and biodegradability, as well as physical traits such as high optical clarity (Hussein *et al.*, 2020; Abd-Elnaiem *et al.*, 2022). Surface coating and engineering boost polymer performance by applying synthesized film coatings, rendering it suitable for use in energy harvesting, water

treatment, and insulating barriers. The relevance of thin layers of polymeric substances on metal production is influenced by various factors such as lightweight and shock-resistant (Ali *et al.*, 2023). Homogeneous or heterogeneous blends of at least two polymers or co-polymers are known as polymer blends or as polymer mixtures. The polymers can interact chemically or physically, and their physical characteristics diverge from those of their parent components (Ali *et al.*, 2021). Polymer blends can be classified into five broad categories, each of which has received extensive research: Thermoplastic-thermoplastic, thermoplastic-rubber, thermoplastic-thermosetting, rubber-thermosetting, and polymer-filler blends (Parameswaranpillai *et al.*, 2014). Elastomers (EL) are polymers that, at typical ambient temperatures, are above their glass transition temperatures and are amorphous in their unstretched condition (Christenson *et al.*, 2005). The EL polymer was utilized in this investigation and had the following characteristics: strong, waterproof, flexible, chemically resistant, and temperature resistant up to 120 °C. They often have low glass transition temperatures, which fall between −50 and −70 °C. A network of cross-links holds the irregularly shaped chain molecules that make up EL together, preventing the chains as a whole from moving around but allowing individual

Authors information:

[a]Physics Department, College of Science, University of Baghdad, Baghdad, IRAQ. E-mail: mahakhalid6431124@gmail.com[1]; seenaa.hussein@sc.uobaghdad.edu.iq[2]
*Corresponding Author: seenaa.hussein@sc.uobaghdad.edu.iq

chain segments to move locally. The network of cross-links may result from physical connections between chain molecules or covalent bonding (Ebewele, 2000). The method used to synthesize polymer blends affected the structural and mechanical properties of polymer blends especially the adhesion strength (Awaja *et al.*, 2009).

Wood and Al have been used as natural building materials, furniture, tools, vehicles, and ornamental items since the dawn of time due to their distinctive properties and relative availability. Engineers, architects, and carpenters should have more accurate knowledge of wood variation to use it more effectively (Mohammed *et al.*, 2022). High-density fiberboard (HDF) wood is prepared when natural wood has a high density and a low amount of chemical additives. HDF wood is a scientific word that informally means the wood is of high quality and hence expensive (Henke *et al.*, 2022).

Certain polymers are more susceptible to bacterial attack due to the physical qualities of their surfaces or the chemical makeup of the polymer. The microbial population increases in polymers as it is usually used in humid conditions with large levels of organic materials (Hussein *et al.*, 2019). The use of hydrogen peroxide (H_2O_2), a silane coupling agent, and an olefin monomer as an oxidant, a cross-linking agent, and a comonomer, respectively, allowed for the creation of high-performance starch-based wood adhesives (Zhang *et al.*, 2015). It was demonstrated that starch-based wood adhesives' bonding strengths equal 7.88 MPa and 4.09 MPa in dry and wet conditions, respectively. The addition of silicon dioxide (SiO_2) as a filler affected the adhesive qualities of PVA (Hameed, 2016). Their findings revealed that the increases in SiO_2 content, increase the tensile strength and enable it to be used as an adhesive. High-performance, environmentally friendly starch-based glue was synthesized using cassava starch as the primary raw ingredient (Chen *et al.*, 2022). The plywood with modified starch adhesive demonstrated the maximum wet shear strength, 1 MPa, at a pH of 4.5 to 5.5, which was 163% greater than the nontreated starch adhesive.

The need for sustainable and alternative raw materials has increased as a result of the world's energy problems and reliance on petroleum resources. Unfortunately, the limitations include workability at low temperatures, poor water resistance, and limited heat resistance. It is generally known that D, AG, and CS are not moisture-resistant polymers, therefore can be used in damp settings significantly reducing their strength. Adhesive connections that withstand moisture may be created by blending EL and AG, D, PVA, or CS. Therefore, this study aims to improve the shear strength, pull-off adhesions, color intensity, thermal insulation, wearability, and antibacterial activity of EL mixed with naturally mentioned polymers so it may be used for HDF wood and Al coatings and adhesives. In addition, the effect of surface treatment by plasma jet on the wettability and roughness was investigated and compared.

2. Methods and Materials

Materials

The adhesives are EL, and EL blends with AG, D, PVA, or CS. The EL polymer ($\rho \sim 1.1$ g cm^{-3}) was purchased from Sika Gulf manufactures products in Bahrain. AG is a complex blend of macromolecules with a variety of sizes and compositions, with a high concentration of carbohydrates and a negligibly low concentration of proteins less than 3%. In comparison to other gums, AG has a comparatively low viscosity and a high-water solubility. The D, dextrin, is a white or yellow powder, has ρ equals 1.8 g cm^{-3}, and a boiling point of 865.2 °C. Both the AG and D were purchased from the Chinese company Shanghai Clinical Research Center. PVA is a synthetic polymer that easily dissolves in water, its idealized chemical structure is $[CH_2CH(OH)]_n$, and its ρ equals 1.19 g cm^{-3}. Both PVA and CS have no color (white) and were acquired from the Spanish company Panreac Corn Co., Ltd. The commercially HDF wood and Al adherent substrate were obtained from local markets and their thicknesses are 3 cm and 3 mm, respectively.

Preparation of EL and EL Blends

El and EL/(AG, D, PVA, or CS) blends were produced with weight ratios of 60/40 (w/w). Around 1 g of AG, D, PVA, or CS was suspended, at 70 °C, in 10 ml of deionized water for 1 h while continuously magnetically stirred until the solution became transparent. Then, 40% of the formed solutions were mixed separately with 60% of EL polymer and the mixture was agitated again at room temperature (RT~25°C) for ½ h. The produced samples were then placed into a mold with a 20 cm diameter and fixed at RT for 24 h to ensure full drying and water removal. The thickness of the synthesized polymer layers was calculated by an electronic digital micrometer to be 2 mm.

Characterization

Fourier transform infrared spectroscopy (FTIR) model Shimazu's FTIR-8400S on KBr pellets was used to record an infrared spectrum of EL and EL blends. The FTIR spectrum of EL and EL blends was performed at RT in the range of 4000-400 cm^{-1} to examine chemical bonding between their components. The morphology of the synthesized EL and EL blends, as well as their adherence to HDF wood or Al substrates, were investigated using an SEM model INSPECT S 50 operating at 5 kV.

The PosiTest pull-off adhesion tester was used to evaluate the force required to separate the coating from its substrate as the hydraulic pressure increased. Pressure shown on a digital liquid-crystal display (LCD) shows how effectively the coating clings to the substrate. The PosiTest determines the maximum tensile pull-off force that the coating can bear before detaching (pull-off strength) to evaluate the coating's adhesion. The dolly, adhesive, coating layers, and substrates are among the fractured surfaces that develop along the system's weakest plane and function as breaking points. **Fig. 1** displays the EL and EL blends prepared for the pull-off adhesion test.
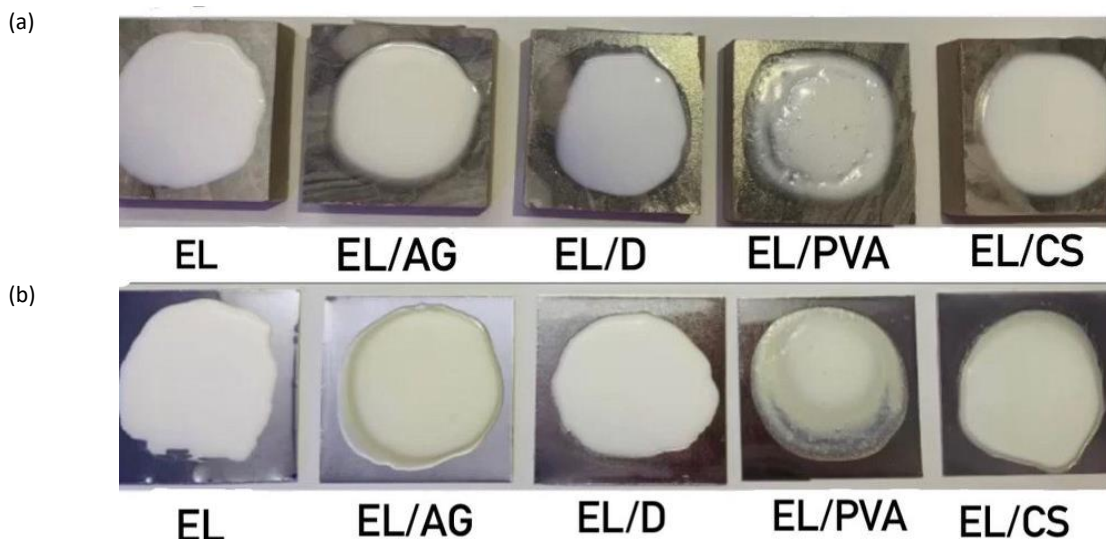
(a)

(b)

Figure 1. EL, EL/AG, EL/D, EL/PVA, and EL/CS blends prepared for the pull-off adhesion test with **(a)** HDF wood and **(b)** Al substrates.

Single-Lap joints were mechanically evaluated in Quasi-Static conditions using an Intron 4502 electromechanical tensile testing device. In compliance with ASTM D 1002 standard, cross-head speed was set at 1.3 mm min⁻¹. Each sample was subjected to at least six evaluations and the test was performed at RT. A Single-Lap joint may exhibit stiff adhesion and act as a solid with linear elastic properties, according to a shear strength theory. Following these hypotheses, the adhesive will experiences pure shear stress, which is fixed across the entire overlapping range. **Fig. 2** presents the illustration blends for HDF wood and Al substrates.
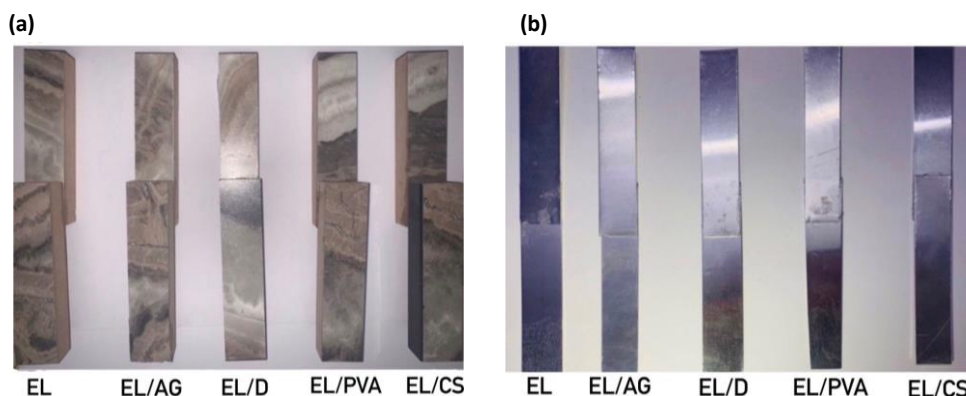
(a)   **(b)**

Figure 2. EL, EL/AG, EL/D, EL/PVA, and EL/CS blend samples for **(a)** HDF wood and **(b)** Al substrates.

The sessile drop method is utilized to determine WCA and hence the surface wettability. The liquid droplet (typically water) is produced with a syringe pump, and then the WCA was examined using a camera. The WCA of the droplet on the substrate is identified and calculated by software attached to the camera for 10 s and measured more than 100 times and the average was estimated. Surface roughness, a measure of rough surface, is the vertical deviation of a physical surface from its homogeneous ideal shape. The crucial function that roughness plays in numerous processes, including friction and adhesion, is frequently measured.

A Konica CM-3600d colorimeter was used to determine color coordinates in the CIELAB color space L* (lightness), a* (redness: green to red), and b* (yellowness: blue to yellow). The following equation was used to estimate the average values of total color change (ΔE) for the investigated polymers (Kubo *et al.*, 2013):

$$\Delta E = \sqrt{(a^* - a)^2 + (b^* - b)^2 + (L^* - L)^2} \tag{1}$$

where L*, a*, and b* are standard values meanwhile L, a, and b are the values of investigated samples.

The thermal conductivity coefficient (K), thermal insulation, and passing thermal energy (e) were calculated using Lee's formula. The methods are further explained in our earlier study (Ali *et al.*, 2021). The value of K was determined using the following equations (Hussein *et al.*, 2020; (Al-Sharuee, 2019):

$$K = \frac{e d_s}{T_B - T_A}\left[T_A + \frac{2}{r}\left(d_A + \frac{d_s}{4}\right)T_A + \frac{d_s T_B}{2r}\right] \tag{2}$$

where *e* is the amount of thermal energy passing through a unit area per second through a disk sample and estimated by (Hussein *et al.*, 2020; (Al-Sharuee, 2019):

$$e = \frac{IV}{\pi r^2 (T_A + T_B) + 2\pi r [d_A T_A + \frac{d_s (T_A + T_B)}{2} + d_B T_B + d_C T_C]} \quad (3)$$

here T_A, T_B, and T_C are the temperature (°C) of the disks A, B, and C, meanwhile, d_A, d_B, and d_C are their thicknesses (Hussein *et al.*, 2020), respectively. The IV is the thermal energy transfers through the heating coil unit, r is the radius of the disk (mm), and d_s is the thickness of the sample (mm).

The disc diffusion technique with Muller-Hinton agar was used to assess the materials' in vitro antibacterial activity. Sample membranes were sliced into 6 mm diameter discs, which were then put on the bacterial culture, and an inhibitory zone measurement are performed in millimeters (mm) scale. For mixed adhesives, the samples were examined at 37 °C for 6 h against Gram-negative bacteria Escherichia coli (E. coli) and Gram-positive Staphylococcus aureus (S. aureus).

Plasma Surface Treatment

The plasma is generated by a system consisting of a quartz tube (T-shaped) with two entrances: the first to enter the high-voltage electrode, while the second entrance to enter the Ar gas and an outlet for the generated plasma torch. In this setup, the flow rate of pure Ar gas is controlled by a flowmeter. Optical emission spectroscopy (OES) was applied to diagnose the Ar plasma jet by electronically observing the excited species and their intensities in the discharges generated by the dielectric barrier discharge plasma Jet. Surwit device model S3000-UV-NIR was used to record the spectra with a range of 250-950 nm. The optical fiber was placed 1 cm away from the plasma torch and was inclined at an angle of 45°.

3. Results and Discussion

FTIR Analysis

Fig. 3 depicts the FTIR spectra used to describe the structure of the EL and EL/blends. The main observed peaks in the FTIR for EL are located at 3440.8, and 3431.1 cm^{-1} corresponding to sp C–H stretching. The detected bands at 2999.1-2879 cm^{-1}, and 1573.8 cm^{-1} are ascribed to a long chain of –CH$_2$- group and C=C stretching mode of the aromatic ring, respectively. In addition, the bands at 646, 1012.5 cm^{-1} are attributed to C–O which are commonly used as the fingerprint region of liquid rubber (Gharde *et al.*, 2015). The FTIR spectrum of the EL/AG blend showed bands at 3436.9 and 3286.4 cm^{-1}, which are characteristics of the O–H stretching vibration. The detected bands at 3213.1 cm^{-1}, 2960 cm^{-1}, and 2341 cm^{-1} are designated to sp^2 C–H stretching, sp^3 C–H stretching, and C–H stretching, respectively. The C=C bond can be detected at 1413.7, and 1639.3 cm^{-1}, while the C–O–C bending vibrations were observed at 1170, 800.4, 642.2, and 522 cm^{-1}. By inspection of this result, it was observed that the characteristics bands of EL were detected at 3436.9, 2960, 1573.8, and 642.2

cm^{-1}. While the bands at 3286.4, 3213.1, 1639.3, 1413.7, 1170, 800.4, and 522 cm^{-1} are related to the presence of AG in the blend (Petrović et al. 2017). From these results, it was concluded that there is no interaction between AG and EL since there are no new bands are observed and the EL and AG exist in the blend.
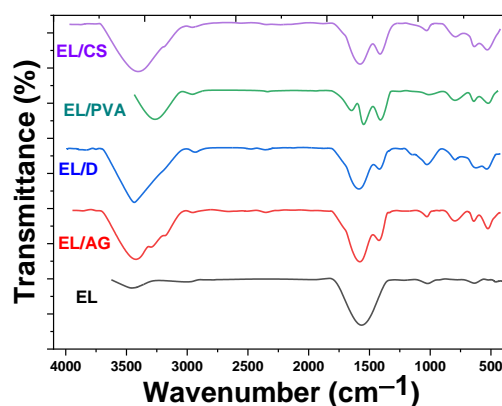

Figure 3. FTIR spectra of EL, EL/AG, EL/D, EL/PVA, and EL/CS blends.

The FTIR spectrum of EL/D polymer showed characteristic bands of EL at 1554, and 1021 cm^{-1}. On the other hand, the characteristics bands of D can be observed at 3432 cm^{-1} (O–H stretching vibration), 2937 cm^{-1} (C–H stretching of the –CH$_2$ group), 1413 cm^{-1} (C–O–H bending mode), 795 cm^{-1} (ring deformation modes of the a-D-(1-4) and a-D-(1-6) linkages), 638 cm^{-1} (the flexural vibration peak of O–H), and 525 cm^{-1} (the bending vibrations of the hydroxide groups outside of their plane (Tohry *et al.*, 2022)). From this result, there is no new bond related to the interaction between EL and D, but the two substances are presented separately in the blend. The FTIR spectrum of EL/PVA displayed bands at 3284 cm^{-1} (O–H stretching), 2955 cm^{-1} (asymmetric stretching of CH$_2$), 1642 cm^{-1} (O–H bending vibration), 1410 cm^{-1} (CH$_2$ bending), 800 cm^{-1} (C–C stretching), 648 cm^{-1} (C–H out of plane bending), and 510 cm^{-1} (Kharazmi *et al.*, 2015), which are the characteristics bands of PVA. While the detected bands at 1555 cm^{-1} and 1018 cm^{-1} are the main bands of EL. No new band was detected due to the interaction of EL and PVA, however, they existed in a separate phase in the blend. The FTIR spectrum of EL/CS showed bands at 1554 cm^{-1}, 1021 cm^{-1}, and 647 cm^{-1} are related to EL. In addition, the bands at 3432 cm^{-1} (O–H stretching), 1413 cm^{-1} (C–H symmetrical scissoring of CH$_2$OH moiety), 804 cm^{-1} (C–O–C ring vibration), and 525 cm^{-1} (Abdullah *et al.*, 2018) belong to CS. Also, there are no new peaks observed for the interaction between CS. Finally, it was concluded from the FTIR results that the bands of EL and other additive polymer exist in the blend, which confirms the successful loading of polymer on the surface of EL.

89

SEM Analysis

Fig. 4 depicts the selected SEM images showing the top view for the EL/AG blend as well as the interface between the EL/AG mix and HDF wood or Al substrates. The homogenous dispersion of the AG within the EL throughout the polymers sample can be shown in **Fig. 4a**. **Fig. 4d** depicts a more enlarged SEM picture (5000×) of the EL/AG blends, demonstrating good dispersion and adhesion between the EL and the AG. The interfaces between the produced mixes and the coated materials, such as HDF wood and Al substrates are shown in **Figs. 4b-f**. The SEM images demonstrate that the EL/AG adheres well to both the HDF wood and the Al substrates.
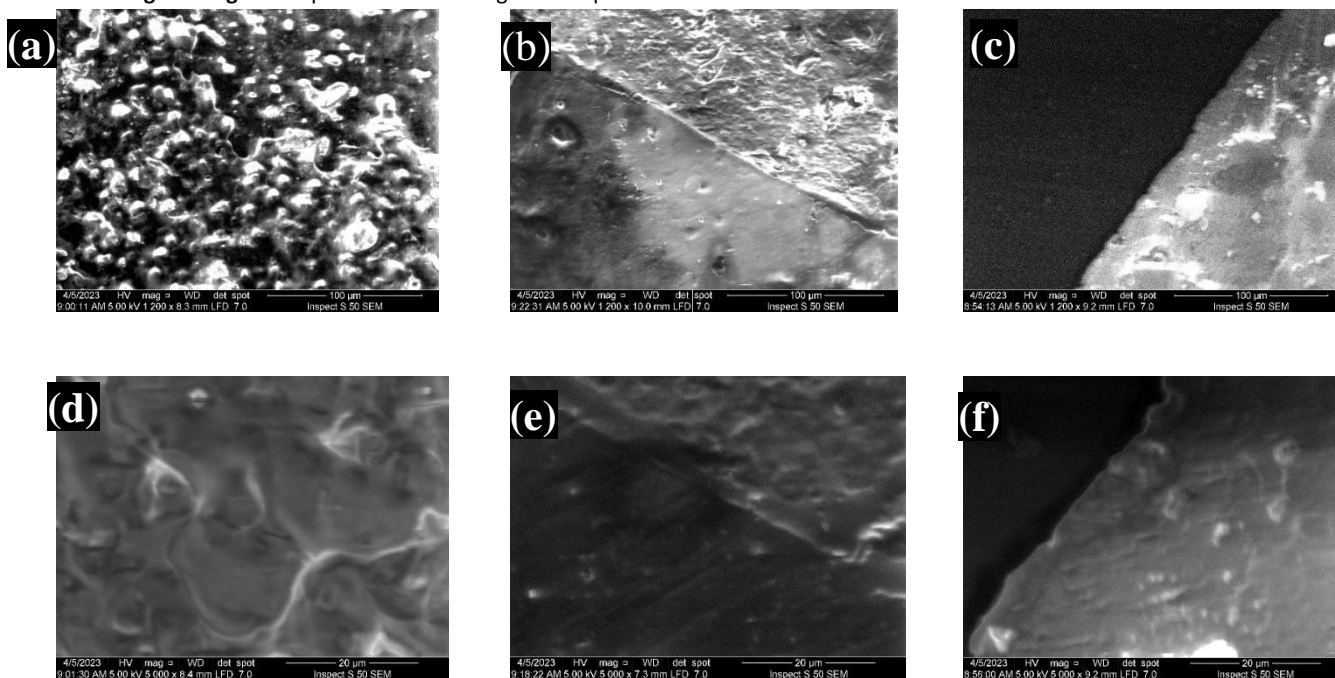

Figure 4. SEM images show the top view with lower (1200×) and higher (5000×) magnifications for **(a, d)** EL/AG blends, and the interface between EL/AG and **(b, e)** HDF wood, or **(c, f)** Al substrates.

Shear Strength

The average values of estimated shear strength, with the error bar, of HDF wood and Al bound with various adhesives are shown in **Fig. 5**. The shear strength of EL is increased by the mixing of various additives to the EL polymer. The maximum values for the shear strength are 771±11, and 52±3 N were observed for the EL/AG polymer at the HDF wood substrate and Al substrates, respectively. In addition, a considerable increase in the characteristics of the adhesive and an improvement in the mechanical performance of the adhesive result from the addition of polymers to the EL and the creation of a homogenous mixture. The best-formed polymer with high mechanical strength and adhesion is EL/AG, accordingly, AG could be the ideal mix. Such observations could be attributed to the characteristics of AG as compared to pure EL polymer. Besides, the strong binding and stabilizing qualities are seen in adhesives of high quality and strength (Baraya *et al.*, 2020). Due to its adhesive qualities and rapid drying time, dextrin follows good adhesion and strength after the AG (Azeez, 2005). Additionally, the combination produced a cross-linking between them that increased the shear strength of HDF wood joined with various adhesives. The shear strength data show a significant difference between Al and HDF wood, as their values are greater for HDF wood compared to Al substrates. The qualities of the wood are to blame for this variation in the outcomes. Its cells have openings that are large enough to provide a clear path for the liquid resin to travel through, and frequently enough, interconnected pits are adequate to encourage resin flow. Hardwood species have high porosity and include vessel and longitudinal fibers. The effectiveness of the bonding between HDF wood pieces depends significantly on how much adhesive reaches the porous network of interconnected cells. Since adhesive bonds move under stress from one component to another through the interphase area. The interphase geometry also affects the bonding performance. Cohesive force promotes chain contact and minimizes free volume, improving the bond strength with the surface of the HDF wood. As for Al, it has a smooth surface, and this makes the adhesion of the mixture to the surface weak (Vineeth *et al.*, 2020).
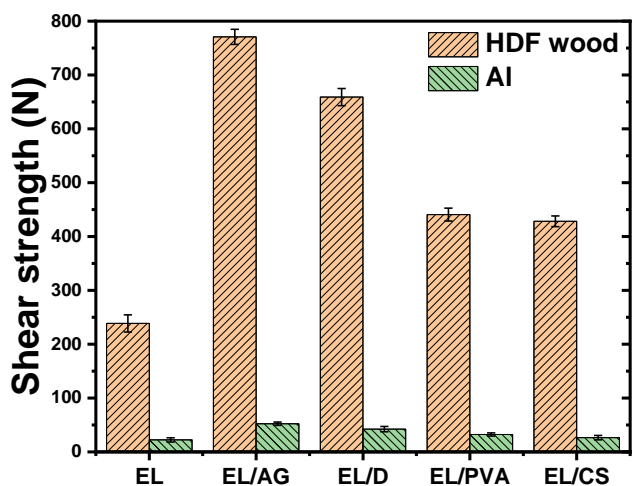
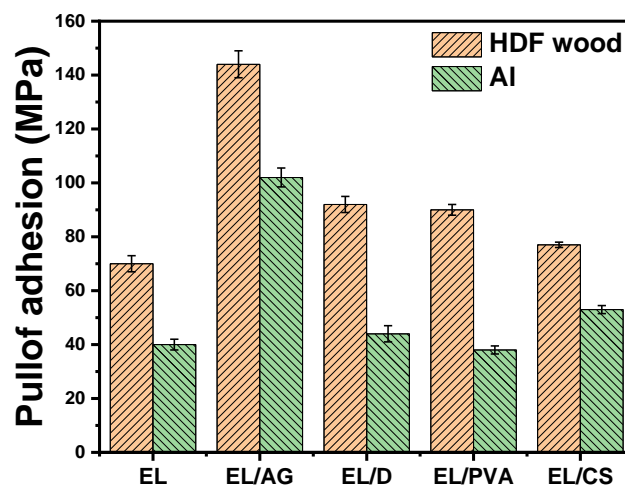Figure 5. Shear strength of EL, EL/AG, EL/D, EL/PVA, and EL/CS blends.

Figure 6. Pull-off adhesion for EL, EL/AG, EL/D, EL/PVA, and EL/CS blends.

Pull off Strength

The adhesive properties have been optimized for the adhesion of EL and EL/blends to the substrate using the pull-off test. **Fig. 6** illustrates the average values of estimated pull-off adhesion, with the error bar, of HDF wood and Al substrates, bonded with different adhesives. According to **Fig. 6**, the highest adhesion value of the material was obtained for EL/AG blend. The distinctive adhesion properties of EL/AG could be attributed to the high adhesive quality, high strength, strong binding, and stabilizing properties of AG (Baraya *et al.*, 2020). It is followed by EL/D and EL/PVA, respectively, with very close values because of the comparable properties of D and PVA. Dextrin has distinctive adhesion properties, in addition to that it dries quickly (Azeez, 2005). PVA is a polymer that is water-soluble and biodegradable and has exceptional adhesion properties. Consequently, PVA is considered one of the promising water-based adhesives and its combination with other polymers could enhance its adhesive capabilities (Azeez, 2005). It was noticed, a large discrepancy between Al and HDF wood in the Pull off results, as a significant and noticeable increase appeared in HDF wood, and these results decreased in Al. The discrepancy in results is due to the properties of the HDF wood. Hardwood species include extremely porous wood, longitudinal fibers, and vessels, cell cavities large enough to provide a favorable conduit for the flow of liquid resin, and connected pits that are frequently large enough to allow the resin to flow (Sultan *et al.*, 2022). The interphase geometry has an impact on the bond performance since the adhesive bonds under pressure migrate from one component to another component across the interphase area. Also, the effectiveness of the bonding between HDF wood components depends on how deeply the adhesive penetrates the porous network of interconnected cells. Cohesive force interacts with the chains and reduces the free volume to tighten the link between them and the wood's surface. As for Al, it is distinguished by its smooth surface, which makes the adhesion of the mixture to the surface weak as mentioned in the shear strength test which agrees with other work elsewhere (Bryaskova *et al.*, 2013).

Color Intensity

A colorimetry study was performed to evaluate and quantify the color deviation of the EL and EL blends. The mean deviation of the CIELab coordinates L^*, a^*, b^*, and ΔE (color difference) are summarized in **Table 1**. The value L^* of EL blends decreased compared with LE which indicates that the color adhesives have become darker. However, a^*, and b^* are the values of EL blends increased compared with EL, so the adhesives blend become more reddish and bluish. The technique of mixing increased the color's intensity as seen in **Table 1**. The formation of conjugated double bonds between the polymer and the modified substance is the fundamental cause of coloring. This yields instauration, which in turn induces electron excitation levels in the visible spectral range and gives discoloration.

Table 1: values of L^*, a^*, b^*, and ΔE for EL, EL/AG, EL/D, EL/PVA, and EL/CS blends

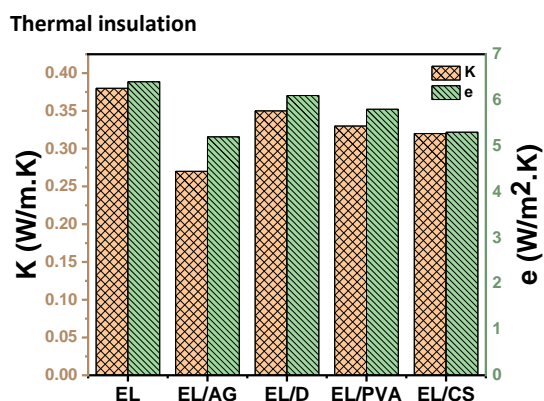| Sample	L^*	a^*	b^*	ΔE
EL	38.78	0.98	5.20	--
EL/AG	34.32	2.21	9.41	6.25
EL/D	29.73	1.86	6.13	9.139
EL/PVA	30.78	0.76	4.22	8.06
EL/CS	32.53	1.92	5.44	6.32

Thermal insulation

Figure 7. Thermal insulation (K) and passing thermal energy (e) of EL polymer and polymer blend.

Fig. 7 depicts the thermal insulation (K) and passing thermal energy (e) through EL and EL mixtures. In general, both K and e are lowered in EL/blends when compared to pure EL. EL/AG had the lowest observed values for K (0.27 W/m.K) and e (5.2 W/m^2.K), indicating good insulation when compared to other examined polymers. The enhanced thermal insulation of EL/AG could be due to the good bonding that occurs between the EL and AG. It is well known that the thermal conductivities of ceramic and metallic materials are orders of magnitude greater than those of polymeric materials (Vlassov *et al.*, 2022). Therefore, there is a need for agglomerations dispersed throughout the polymer blend to improve their thermal conductivity and hence allow for easy heat transmission via the densely packed matrix. Subsequently, when the overall material's solid content grew, decreasing porosity may be connected to higher thermal conductivity. Nonetheless, because of the lower porosity brought on by the denser packing after addition, the weight ratio of polymer to EL liquid improves their mechanical and thermal durability. Polymers combine a two-dimensional structure that vibrates to transfer heat, hence easing the transfer of heat across the material. Polymers are thermally insulators because polymers have a random chain structure and free space exists between chains. The rate of heat transfer in solids depends on whether the material is conductive or insulator (Wang *et al.*, 2022). Irregularity in the structure and the presence of voids between the strings lead to making the insulation process. Accordingly, the transfer of thermal energy from one end to the other through the polymer is difficult, considering the existence of Interfaces between the two phases of the polymeric mixture. The heat is transmitted in the form of elastic phonons within the structure and the presence of interfaces will obstruct the movement and passage of these waves, so the wave will lose part of its energy at the inter-mixture interface as shown in **Fig. 7**.

Anti-bacterial Activity

Investigation of the antibacterial properties of EL is very important because EL can degrade under working conditions due to environmental factors like mechanical stress, heating and cooling, chemicals, and hydrolysis, making the polymer susceptible to bacterial contaminations or infections that pose a serious threat to people (Suethao *et al.*, 2022). Antibacterial for EL mixed adhesives; decrease against initial bacterial loading for S. aureus and E. coli. By using the Agar diffusion technique, EL and mixes are evaluated for their antibacterial activity against the bacterial pathogens S. aureus (gram-positive) and E. coli (gram-negative). **Table 2** and **Fig. 8** both display the zone of inhibition values found for EL and mixed adhesives. Both bacteria were significantly inhibited from growing by the EL/D combination. Antibacterial pictures show more antibacterial efficacy against E. coli bacteria than S. aureus. AG had a bacterial-killing action (Jaafar, 2019). The substantial antibacterial efficacy of Sudanese and Omani AG against S. aureus, and E. coli was investigated (Al Alawi *et al.*, 2018). It was found that the high concentration of non-polar components is thought to be responsible for the antibacterial activity. Both AG and D have also long been used in the food industry and as adhesives, working as an antimicrobial towards gram-positive and gram-negative bacteria in commonly used products such as adhesives of HDF wood.

(a)   (b)
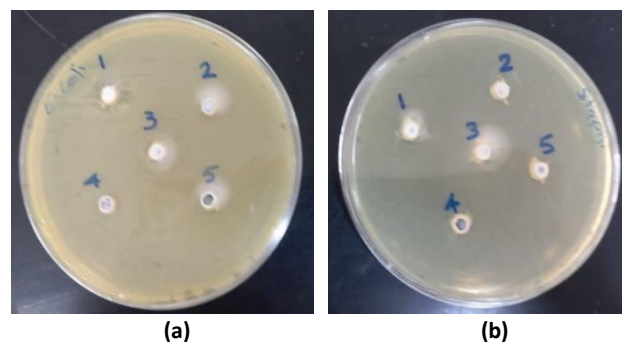
Figure 8. Anti-bacterial activity of EL and EL blends towards **(a)** *E. coli* and **(b)** *S. aureus* bacteria.

Table 2: Zone of inhibition values, in mm, for EL and EL blends towards the tested S. aureus and E. coli organism.

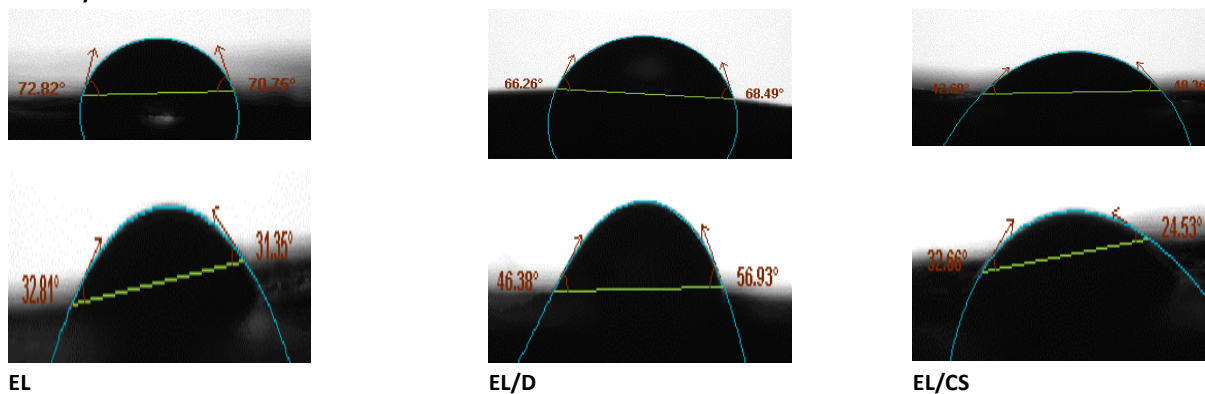| No.	Samples	Bacterial pathogens	
		E. coli	**S. aureus**
1	EL	13	12
2	EL/AG	14	11
3	EL/D	13	15
4	EL/PVA	11	11
5	EL/CS	13	11

Plasma Treatment for Surface Wettability

Figure 9. Selecected WCA for EL, EL/D, and EL/CS blends before (top images) and after (bottom images) plasma treatment.

The hydrophilic/hydrophobic character of the sample's surface was evaluated by estimating the WCA. **Fig. 9** displays the selected photos showing the WCA for various samples before and after plasma treatment. **Table 3** illustrates the average calculated WCA for various samples before and after the surface treatment using a plasma jet. The backbone of the AG had OH groups, which increased the WCA of the EL/AG combination. The AG polar groups were reduced by the EL, which made it transition from a hydrophilic to a hydrophobic substance. As a result of their combination with the EL groups, these groups decreased. The presence of AG content causes higher WCA values. This expected trend might be caused by the amphiphilic nature of the AG composition. The observed performance may be attributable to the amphiphilic moieties in the structure of AG, specifically an arabinogalactan-protein fraction that comprises both hydrophobic polypeptide chains and hydrophilic polysaccharide blocks, which provide the material's remarkable interfacial properties (do Nascimento *et al.*, 2021).

Table 3: left WCA (θ_1), right WCA and (θ_2), and average WCA ($\bar{\theta}$) of EL and EL blends before and after plasma treatment.

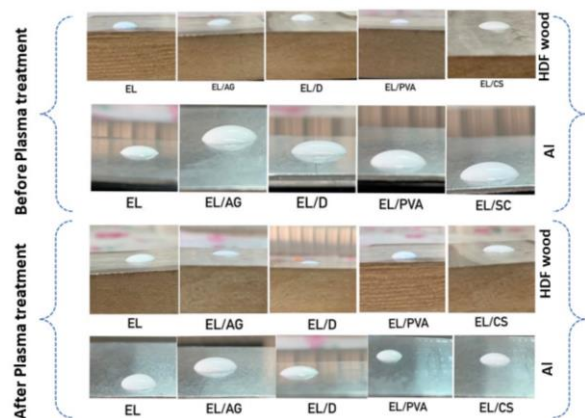| Plasma treatment	Before			After		
Samples	θ_1 (°)	θ_2 (°)	$\bar{\theta}$ (°)	θ_1 (°)	θ_2 (°)	$\bar{\theta}$ (°)
EL	72.7±0.3	70.6±0.4	71. 7±0.4	31.6±0.7	29.7±0.8	30.7±0.7
EL/AG	83.7±0.5	82.6±0.6	83.2±0.6	45.5±4.5	44.8±8.6	45.2±6.5
EL/D	65.2±1.5	67.6±1.8	66.4±1.6	49.0±2.8	60.6±3.2	54.8±3.0
EL/PVA	85.3±0.3	85.3±0.3	85.3±0.3	69.1±0.4	69.0±0.9	69.1±0.4
EL/CS	41.6±0.9	48.5±0.6	45.0±0.7	33.0±0.2	24.3±0.2	28.6±0.1

Figure 10. Optical images of droplets of adhesive on HDF wood and Al substrates for EL, EL/AG, EL/D, EL/PVA, and EL/CS blends.

The droplets of EL and EL blend adhesive before and after the plasma treatment over the HDF wood and Al substrates are shown in **Fig. 10**. **Table 4** summarises the estimated average values for contact angle (CA) of EL and EL blends adhesive with HDF wood and Al substrates before and after plasma jet treatment of respective surfaces. The CA for various adhesives is often higher for Al substrates than for HDF wood. Furthermore, plasma treatment reduced CA values for both HDF wood and Al substrates. Following the plasma treatment, the EL/D adhesive with HDF wood had the lowest CA of 38°. The polymer surface displayed perfect hydrophilicity with the adhesive fluids after plasma surface treatment, which decreased the CA starting to raise the surface-based plasma beam's energy. According to Fowkes' theory for calculating surface energy, the rate at which the dispersive and polar surface energies vary is connected to the change in CA. When the treatment impact on the phenomena degraded, the surface polar energy component declined and the dispersive component rose. Conversely, when the CA was low, the polar component of the interfacial energy of the treated sample increased dramatically. This may be explained by the fact that the surface's polar component is increased by a plasma treatment because the plastic's surface forms hydroxyl and carboxyl groups (Miklós & Zoltán, 2021).

Table 4: Average contact angle (CA) of EL and El blends adhesive with HDF wood and Al substrates before and after plasma treatment.

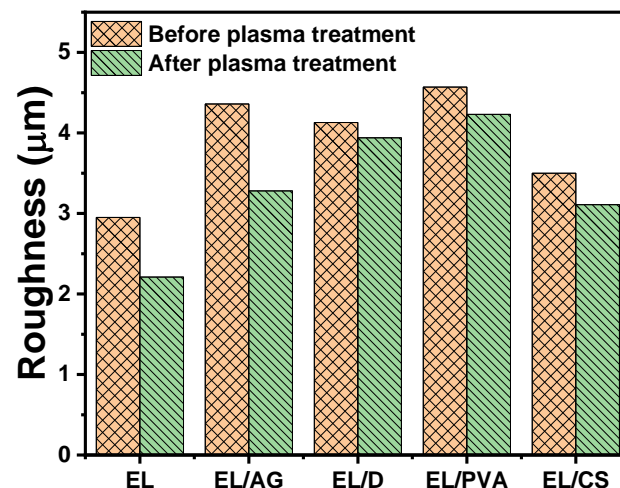| Plasma treatment	substrate	EL	EL/AG	EL/D	EL/PVA	EL/CS
Before	**HDF wood**	58°	54°	56°	49°	53°
	Al	72°	67°	64°	68°	58°
After	**HDF wood**	53°	46°	38°	47°	42°
	Al	65°	61°	62°	64°	53°

Surface Roughness

Figure 11. Surface roughness of EL and EL blends before and after plasma treatment.

The relationship between the surface roughness and WCA is that the surface roughness rises as the WCA rises. **Fig. 11** shows the surface roughness of EL and polymer blends before and after plasma treatment. We note that the highest value of roughness was for the non-plasma treated EL/PVA blend, where it was equal to 4.57 µm, and this conforms to the WCA test, where we obtained a high value for the same blend. The roughness ratio of pure PVA was low, and when blend with EL, its surface roughness increased, this means that the elastomer improved the properties of EL polymer which agrees with other work (Vacher & de Wijn, 2021). As well for AG, its properties have been improved and its surface roughness has become equal to 4.36 µm after blending it with EL. Where we obtained similar results in the WCA test for this blend. Accordingly, which agrees with (Sinkhonde, 2023). Also, the blend of EL/D showed a high roughness ratio equal to 4.13 µm, while EL/CS blend has a roughness ratio of 3.5 µm which agrees with other work (Sinkhonde, 2023). When plasma is applied to the surface, the surface becomes less rough, and this can be seen from the WCA values after the surface has been treated with plasma shown in **Fig. 11**.

The surface roughness of El and EL blends is dramatically changed by plasma jet treatment. Roughness values for EL/PVA, EL/D, EL/AG, EL/CS, and EL are 4.23, 3.94, 3.28, 3.11, and 2.21 µm, respectively. The largest drop in surface roughness ratio was obtained for EL (25.1%), while the least decrease (4.6%) was observed for EL/D. In comparison to a non-treated surface, plasma jet treatment of polymer surfaces resulted in a smooth surface. The surface can absorb the EL and EL blends adhesive with excellent efficiency and uniformity throughout its surface due to the reduced surface roughness modified by plasma treatment.

4. Conclusion

Various EL blends were prepared to be used for HDF wood and Al coating and adhesion. The filler dispersion and adhesion between the mixtures, coated HDF wood, and Al substrates were validated by SEM analysis. It was concluded from the FTIR results that the bands of EL and other additive polymer exist in the blend, which confirms the successful loading of polymer on the surface of EL. EL integrated with the adhesive's polymer (such as AG, D, PVA, and CS) to high pull-off strength was recorded to be 144 MPa and higher shear strength is 770.8 N for HDF wood as a substrate and 102 MPa, and 52.36 N, respectively, for Al substrates towards the EL/AG. The value L* of blends decreased compared with LE which indicates that the color adhesives have become darker. However, the values of a* and b* for the EL blends increased compared with pure EL, so the adhesives blend become reddish and bluish. The modified EL blend reveals a 0.27 W/m.K for thermal conductivity for EL/AG revealing better thermal insulation than other samples. Antibacterial activity for blended adhesives; decrease against initial bacterial loading for S. aureus and E. coli. Also, AG and D have long been used in the food industry and adhesives, working as an antimicrobial against gram-positive and gram-negative bacteria in commonly used products such as adhesives and coatings. The roughness and wettability of the surface of EL and EL blends were reduced by using a plasma jet, increasing the surface's hydrophilicity. As a result, the surface will be wetter for the adhesive and smoother overall. An alternate biopolymer material was chosen in this investigation because formaldehyde glue is one of the causes of cancer. The addition of EL to common adhesives such as PVA, CS, D, and AG was utilized to alleviate shortcomings such as low water resistance, resistance to conditions, and wet workability. The combination of EL and these natural adhesives improves its water resistance, resistance to conditions, and workability in wet environments. Furthermore, the physical, mechanical, and biological properties of the prepared EL/blends adhesive mixture were improved. It was found that the EL/blends adhesive has greater quality specifications with wood than with aluminum because the wood surface criteria are different from the Al specifications.

5. Acknowledgment

6. References

Abd-Elnaiem, A. M., Hussein, S. I., Ali, N. A., Hakamy, A., & Mebed, A. M. (2022). Ameliorating the Mechanical Parameters, Thermal Stability, and Wettability of Acrylic Polymer by Cement Filling for High-Efficiency Waterproofing. *Polymers*, 14(21), 4671.

Abdullah, A. Q. , Ali N. A. , Hussein , S. I., Hakamy, A., · Abd-Elnaiem, A. M. (2023) Improving the Dielectric, Thermal, and Electrical Properties of Poly (Methyl Methacrylate)/Hydroxyapatite Blends by Incorporating Graphene Nanoplatelets . Journal of Inorganic and Organometallic Polymers and Materials, published online 28 may 2023.

Al Alawi, S. M., Hossain, M. A., & Abusham, A. A. (2018). Antimicrobial and cytotoxic comparative study of different extracts of Omani and Sudanese Gum acacia. *Beni-Suef University Journal of Basic and Applied Sciences*, 7(1), 22-26.

Ali, A. M., Jaber, M. A., & Toama, N. A. (2021). Thermal Properties of Polyester/Epoxy Blend. *Iraqi Journal of Science*, 1128-1134.

Ali, A. N. M., Ali, N. A., Hussein, S. I., Hakamy, A., Raffah, B., Alofi, A. S., & Abd-Elnaiem, A. M. (2023). Nanoarchitectonics of silver/poly (methyl methacrylate) films: structure, optical characteristics, antibacterial activity, and wettability. *Journal of Inorganic and Organometallic Polymers and Materials*, 33(3), 694-706.

Ali, N. A., Abd-Elnaiem, A. M., Hussein, S. I., Khalil, A. S., Alamri, H. R., & Assaedi, H. S. (2021). Thermal and mechanical properties of epoxy resin functionalized copper and graphene hybrids using in-situ polymerization method. *Current Nanoscience*, 17(3), 494-502.

Al-Lhaibi, S. A., & Al-Shabander, B. M. (2022). Photocatalytic Activity and Wettability Properties of ZnO/Sawdust/Epoxy Composites. *Iraqi Journal of Physics*, 20(4), 54-65.

Almashhadani, N. J. H. (2021). UV-Exposure effect on the mechanical properties of PEO/PVA blends. *Iraqi Journal of Science*, 1879-1892.

Al-sharuee, I. F. (2019). Thermal conductivity performance of silica aerogel after exposition on different heating under ambient pressure. *Baghdad Science Journal*, 16(3 (Suppl.)), 0770-0770.

Awaja, F., Gilbert, M., Kelly, G., Fox, B., & Pigram, P. J. (2009). Adhesion of polymers. *Progress in Polymer Science*, 34(9), 948-968.

AZEEZ, O. (2005). Production of Dextrins from Cassava Starch. *Leonardo Journal of Sciences*, (7), 9-16.

Baraya, K. A., Boryo, D. E. A., Chindo, I. Y., & Hassan, U. F. (2020). Formulation and Characterization of Green Adhesive Using Agricultural and Plastic Waste Materials as Composites. *IOSR Journal of Applied Chemistry* (IOSR-JAC).

Berczeli, M., & Weltsch, Z. (2021). Enhanced wetting and adhesive properties by atmospheric pressure plasma surface treatment methods and investigation processes on the influencing parameters on HIPS polymer. *Polymers*, 13(6), 901.

Bryaskova, R., Georgieva, N., Andreeva, T., & Tzoneva, R. (2013). Cell adhesive behavior of PVA-based hybrid materials with silver nanoparticles. *Surface and Coatings Technology*, 235, 186-191.

Chen, X., Sun, C., Wang, Q., Tan, H., & Zhang, Y. (2022). Preparation of glycidyl methacrylate grafted starch adhesive to apply in high-performance and environment-friendly plywood. *International Journal of Biological Macromolecules*, 194, 954-961.

Christenson, E. M., Anderson, J. M., Hiltner, A., & Baer, E. (2005). Relationship between nanoscale deformation processes and elastic behavior of polyurethane elastomers. *Polymer*, 46(25), 11744-11754.

do Nascimento, F. C., de Aguiar, L. C. V., Costa, L. A. T., Fernandes, M. T., Marassi, R. J., Gomes, A. D. S., & de Castro, J. A. (2021). Formulation and characterization of crosslinked polyvinyl alcohol (PVA) membranes: effects of the crosslinking agents. *Polymer Bulletin*, 78(2), 917-929.

Ebewele, R. O. (2000). Polymer science and technology. *CRC press*.

Gharde, R. A., Mani, S. A., Lal, S., Khosla, S., & Tripathi, S. K. (2015). Synthesis and characterization of liquid crystal elastomer. *Materials Sciences and Applications*, 6(06), 527.

Hameed, N. J. (2016). Studying the effect of silica (SiO_2) addition on the adhesive properties of polyvinyl alcohol. *Iraqi Journal of Physics*, 14(29), 107-124.

Henke, M., Lis, B., & Krystofiak, T. (2022). Evaluation of Surface Roughness Parameters of HDF for Finishing under Industrial Conditions. *Materials*, 15(18), 6359.

Hussein, S. I., Ali, N. A., Saleh, G. M., & Jaffar, H. I. (2019). Effect of fiber (Glass, poly propylene) on hardness, water absorption and anti-bacterial activity of coating acrylic polymer. Iraqi Journal of Science, (Special Issue) *The Fourth Conference for Low Dimensional Materials and it's Applications-2018*.

Hussein, S., Abd-Elnaiem, A., Ali, N., & Mebed, A. (2020). Enhanced thermo-mechanical properties of poly (vinyl alcohol)/poly (vinyl pyrrolidone) polymer blended with nanographene. *Current Nanoscience*, 16(6), 994-1001.

Jaafar, N. S. (2019). Clinical effects of Arabic gum (Acacia): A mini review. Iraqi *Journal of Pharmaceutical Sciences* (P-ISSN 1683-3597 E-ISSN 2521-3512), 28(2), 9-16.

Kharazmi, A., Faraji, N., Hussin, R. M., Saion, E., Yunus, W. M. M., & Behzad, K. (2015). Structural, optical, opto-thermal and thermal properties of ZnS–PVA nanofluids synthesized through a radiolytic approach. *Beilstein Journal of Nanotechnology*, 6(1), 529-536.

Kubo, M. T. K., Augusto, P. E., & Cristianini, M. (2013). Effect of high pressure homogenization (HPH) on the physical stability of tomato juice. *Food Research International*, 51(1), 170-179.

Kun, D., & Pukánszky, B. (2017). Polymer/lignin blends: Interactions, properties, applications. *European Polymer Journal*, 93, 618-641.

Mohammed, M. A., Jaber, M. A., & Al-Maamouri, A. F. E. (2022). Study and Evaluation of Rock Wool Board by using PVA/PU as a Polymer Blend Binder. *Iraqi Journal of Science*, 4282-4291.

Parameswaranpillai, J., Thomas, S., & Grohens, Y. (2014). Polymer blends: state of the art, new challenges, and opportunities. *Characterization of Polymer Blends*, 1-6.

etrović, Ž., Ristić, M., Musić, S., & Fabián, M. (2017). The effect of gum arabic on the nano/microstructure and optical properties of precipitated ZnO. *Croatica Chemica Acta*, 90(2), 135-143.

Sinkhonde, D. (2023). Quantitative study on surface porosity and roughness parameters of mineral and organic admixtures based on multi-scale characterisation techniques. *Cleaner Materials*, 7, 100166.

Suethao, S., Prasopdee, T., Buaksuntear, K., Shah, D. U., & Smitthipong, W. (2022). Recent Developments in Shape Memory Elastomers for Biotechnology Applications. *Polymers*, 14(16), 3276.

Sultan, M., Elsayed, H., Abdelhakim, A. E. F., & Taha, G. (2022). Active packaging gelatin films based on chitosan/Arabic gum/coconut oil Pickering nano emulsions. *Journal of Applied Polymer Science*, 139(1), 51442.

Sunday, O. O. (2015). Strength of adhesive bonded joints: Comparative strength of adhesives. *International Journal of Engineering and Technical Research*, 3(8), 58-62.

Tohry, A., Dehghan, R., Hatefi, P., & Chelgani, S. C. (2022). A comparative study between the adsorption mechanisms of sodium co-silicate and conventional depressants for the reverse anionic hematite flotation. *Separation Science and Technology*, 57(1), 141-158.

Vacher, R., & de Wijn, A. S. (2021). Molecular-dynamics simulations of the emergence of surface roughness in a polymer under compression. *Materials*, 14(23), 7327.

Vineeth, S. K., Gadhave, R. V., & Gadekar, P. T. (2020). Glyoxal cross-linked polyvinyl alcohol-microcrystalline cellulose blend as a wood adhesive with enhanced mechanical, thermal and performance properties. *Mater Int*, 2, 0277-0285.

Vlassov, S., Oras, S., Timusk, M., Zadin, V., Tiirats, T., Sosnin, I. M., Lõhmus, R., Linarts, A., Kyritsakis, A. & Dorogin, L. M. (2022). Thermal, mechanical, and acoustic properties of polydimethylsiloxane filled with hollow glass microspheres. *Materials*, 15(5), 1652.

Wang, S., Chen, M., & Cao, K. (2022). Polymer composite with enhanced thermal conductivity and insulation properties through aligned Al_2O_3 fiber. *Polymers*, 14(12), 2374.

Zhang, Y., Ding, L., Gu, J., Tan, H., & Zhu, L. (2015). Preparation and properties of a starch-based wood adhesive with high bonding strength and water resistance. *Carbohydrate Polymers*, 115, 32-37.

AUTOMATED LEAK AND WATER QUALITY DETECTION SYSTEM FOR PIPED WATER SUPPLY

Eganoosi Esme Atojunere[1a]*, Godspower Elvis Amiegbe[2b]

Abstract: The volume of water loss because of leakage in the conveyance pipe has been alarming. Old and poorly constructed pipelines, inadequate corrosion protection, poorly maintained valves, and mechanical damage contribute to leakage. Water-carrying pipes were buried underground, so tracing leak points manually could be tasking, if not impossible. This work was to report on the effectiveness of a developed Automated Leak and Water Quality Detection (ALWQD) system. This device can detect leaks in the piped water system automatically and can also report any deterioration in the quality of water that flows through affected pipes. The ALWQD consisted of several drainpipe connections, pipe accessories, electronic components, and sensors to monitor water quality impairment. The control signal was the solenoid valves that interfaced with the ESP-32 microcontroller boards placed on the pipe manifold at intervals, along with water quality monitoring sensors of turbidity, Total Dissolved Solids (TDS), and pH. The fabrication and testing of the device followed standard procedures. Testing of ALWQD was done at 0, 5, and 10 minutes under load and no-load conditions, with average variation in reading recorded after three trials. The findings indicated that the efficiency of ALWQD was between 70% and 80%, which could be improved upon. The trend in the results of the monitored parameters was not different from that of similar previous work. Leaks caused pressure drops and disallowed the full flow of water found at pipe joints, which could be a pathway for the intrusion of contaminants into the water conveyance system.

Keywords: Automation, leakage detection, deterioration, water quality, impairment.

1. Introduction

Old and poorly constructed pipelines, inadequate corrosion protection, poorly maintained valves, and mechanical damage contribute to leakage (May, 2000). However, water leakage caused reduced pressure in conveyance systems and the loss of water resources in the supply system. The rise in such decline pressures by the water industry increases energy consumption. This rise in pressure could also make leaking worse and have adverse negative environmental impacts. Water supply through pipes gets contaminated when there is an opening along the pipe because of faulty pipe networks. This contamination renders water unfit for its intended purposes, especially for drinking. At loose joints in pipes, contaminants can intrude and cause dilution with flow water, deteriorating water quality. Leaks contribute to an economic loss to the water industry, thereby causing scarcity of water and raising the price of water per liter for water consumers. The challenges faced by the water industries in detecting water leakages are vast, as water pipes were laid underground with plastic PVC pipes that got broken when leak points were traced during excavation. Digging is done by hand without technology; it is costlier to dig a foot in dry soils than wet areas. Leak detection through analog pressure meter gauges has been used with inconsistent results based on the pressure that is readable on the gauge indicator because of the pressure drop in flow in conduit pipes. Intrusion in water pipes from surrounding agricultural soil occurred at the point of leakage and joint with a loose connection. The runoff water enabled emerging pollutants like over-agricultural chemicals, fertilizers, and pesticides to be dissolved and intruded into underground pipes at the leak point. Other leak-detecting methods, including pressure, acoustic, vibration, and sensors, have been deployed to detect water leakage (Al Qahtani et al., 2020). An effective way is a hybrid of processes that can autonomously detect leak points, measure deterioration in water pipes, and transfer information to a central processing unit for action. The two-way mechanism feeds the water supplier and the consumer with leak reports along with deterioration when the permissible level of set water quality parameter is exceeded. Water industries lack data on pipe leakages, and the quality of the distributed water is based on water quality data from the water at the waterworks because there has been no testing for deterioration along pipes to detect pollution. A hybrid leak detector provides data and monitors variations in water quality along the pipe in real-time with sensors and analog pressure combined to detect and record leaks and changes in water quality of water to detect intrusion from the surrounding soil (Fondriest, 2021). The built-in alarm system in the detector notifies both the water supplier and consumers of leak problems and deterioration in water quality for corrective actions.

Authors information:

[a]Department of Soil Science & Biosystems Engineering, College of Agriculture, Fisheries and Forestry, Fiji National University, Nasinu, FIJI ISLANDS. E-mail: atojunereeganoosi@yahoo.com[1]
[b]Department of Systems Engineering, University of Lagos, Lagos, NIGERIA. E-mail: elvydynasty1752@gmail.com[2]
*Corresponding Author: eganoosi.atojunere@fnu.ac.fj

Pollutant Intrusion in Water Distribution Pipes at Leak Points

Leaks happen at faulty or broken points in water distribution network pipes connecting water suppliers and consumers (Beat and Dorothee, 2020). Furthermore, Beat and Dorothee (2020) reported that leakage assessment indicated that millions of cubic water get lost annually. Leakage detection in water supply pipes is imperative to minimize loss by facilitating faulty pipe repairs and preventing water quality deterioration because of exposure to the surrounding soil (Eytan and Spuhler, 2021). There is a possibility of pollutant intrusion into water conveying pipes through leak points when in contact with soil surroundings (Oyedele, 2021). This finding is important because loose joints and openings at broken pipes not only leak water but also enter harmful pollutants that are residual from the use of fertilizers, pesticides, and herbicides that are non-biodegradable by farmers with farmland surrounding water pipe layout. The residual pollutant takes a longer time to denature and could cause damage to human and livestock animals that consume the contaminated water. When such pipes are broken or open, the water distribution becomes a receptacle for the migrating pollutants, thereby causing water quality impairment in the public water supply. These pollutants have no biological benefits. Intrusion of pollutants may occur because of the opening created at loose pipe connections, broken pipe points, damaged rubber seals at joints, and lost and faulty control valves. There is a need for regular monitoring of the quality of water in distribution systems to protect public health. Available technologies are expensive and unaffordable to some water industries. Water leakage detection methods such as hydrostatic testing and infrared and laser technology have been tested with advantages and disadvantages. One of the most used methods is the pressure/flow measurement method, which operates on the basis that a drop in flow pressure when open is detected, affecting the continuity of water flow in pipes as in Equation 1. Reduction in pipe pressure is readable through a pressure gauge placed at the interval to detect the drop in pressure or flow rate. Leak detection through pressure drops in fluid-flowing pipes has been used by the oil industry to detect leaks in hydrocarbon-conveying pipes such as petrol, kerosene, and diesel. Leak detection through infrared and laser technology works by scanning the entire length of the fluid-carrying pipes to detect irregularities or damages in the structure and recording weak spots in the pipe system as potential leak points.

$$P_1 v_1 = P_2 v_2 \qquad\qquad 1$$

$P_{1,} P_{2,} v_{1,} v_2$ are initial pressure, final pressure, initial velocity, and final velocity, respectively.

Review of Some Technologies for Leak Detection in Water Pipes

The Infrared Thermography

Thermography technology involves the use of a device that can determine a leak in a water distribution network in wet conditions. A leak is detected when there is a noticeable change in the thermal properties of the surrounding soil, leading to a change in temperature around the pipe (Mashhadani and Thompson, 2011). This section pinpoints leak points along the water distribution systems. However, thermography is not widely used in most countries because it is dependent on climate exchange. Leak develops in a buried piping system when fluid is lost to the surrounding earth, and the leak from a heated or cooled piping system is sufficiently large. A temperature change will occur at the surface of the ground in the vicinity of the pipe leak. Leaks from buried piping are generally characterized by amorphously shaped thermal anomalies that appear along the pathway of the subject piping system.

Leak Detection through the Excavation of Buried Water Pipes

Excavation is an old technology to find leaks in fluid-conveying pipes. It involves creating an opening through the earth with either hand or power tools. Excavation involves digging out soil particles to trace existing underground water pipes. This method, though considered effective, is tasking, time and labor-consuming, and a destructive testing method. Water Pipes often get damaged during excavation. Some public water suppliers still use excavation to trace leaks. It is challenging when physical structures are built on laid pipe networks (McEvoy and Wyatt, 2012). This method is a destructive leak detection method that could be replaced by a hybrid of a fast, real-time-based sensor and analog systems based on low pressure.

Leak Detection through the Wireless Method

The wireless method involved the use of wireless sensor networks to replace the analog leak detection method, which is often cumbersome. Wireless sensors are emerging technologies used to detect leaks, and they are portable, user-friendly, and reliable compared with other leak-detecting methods. The sensors were equipped with electrical and mechanical components that communicate using Bluetooth. Some of the sensors are equipped with their algorithm software for leak detection and the capacity to record deterioration of the inflow water quality. The sensors are placed at intervals on the water main pipe, transfer the pollution status of the flow of water and leakages in the pipe to the central system through Bluetooth technology (Sinha et al., 2007). These sensors are effective because of the automation, unlike thermography, which is based on the change in thermal properties of the surrounding soil because of leakage. Optimal detection of leak points is achievable with minimum noise interference, as noise from hooting from traffic vehicles affects the reliability of the result. This problem could be resolved by taking leak measurements at night when interference from noise is minimal. The detected leak points are exchanged among sensors through the Wireless/Bluetooth Technology to central control systems operated by the water industry.

Combined Leak Detection using Wireless and Analogue System.

A hybrid leak detector that detects leaks and reports deterioration in the quality of water in a pipe distribution network

because of pollutant intrusion. Data of the detected leak points were transferred through wireless technology to a central processing unit that coordinates networks of pipes for prompt action. Hybrid leak detectors are in sharp contrast to manual and excavation methods of detecting leaks in pipe water systems. It is fast and automated and allows flexibility in checking water quality at different points in the system and reporting water quality deterioration (Smith and Naud, 2013). The number of sensors is a function of the size of the pipe network, the length of the main pipes, and the bandwidth of the Wi-Fi of the microcontroller. This

leak and deterioration technique can be modeled and incorporated into Progressive Web App(PWA). This modified technique will allow the water industry and the consumer to monitor the quality of water that leaves the waterworks and deliver it into household piping systems. This work adopted the hybrid approach for developing leak-detecting and deterioration systems for water pipes. Some previous works and their viewpoints adopted in this work are presented in Table 1.

Table 1: Leak detection technologies in literature.

S/N	Title	Year	Reference
	Review and analysis of pipeline leak detection methods	2022	Naga Venkata Saidileep Korlapati et al. (2022)
	Leak detection in water distribution Networks	2019	El-Zahab and Zayed (2019)
	A review of different pipeline fault detection methods.	2016	Datta and Sarkar (2016)
	Statistical process control-based system for approximate location pipe bursts and leaks in water distribution systems	2017	Romano et al. (2017)
	Leak Detection, Size Estimation, and Localization in Pipe Flows	2016	Aamo (2016)
	Wireless Gas Leak Detection and Localization	2016	Chraim et al. (2016)
	An accelerometer-based real-time monitoring and leak detection system for pressurized water pipelines	2016	El-Zahab et al. (2016)
	Mobile sensor networks for optimal leak and backflow detection and localization in municipal water networks	2016	Gong et al. (2016)
	Non-destructive visual-statistical approach to detect leaks in water mains.	2015	Al Hawari et al. (2015)
	Locating leaks in water mains using noise loggers	2016	El-Abbasy et al. (2016)
	Acoustic Detection of Leaks in Water Pipelines Using Measurements Inside Pipe	2011	Khulief et al. (2011)
	Adaptive extended Kalman filter-based geolocation using TDOA/FDOA.	2011	Kim et al. (2011)

Sealant and adhesive substances pervade our environment and are used in almost every company and sector, as a result, significant efforts have been made to develop these compounds (Sunday, 2015; Ali *et al.*, 2021; Almashhadani, 2021; Kun & Pukánszky, 2017). Polar compounds with ionic groups, *i.e.,* hydrophilic molecules, readily absorb and dissolve in polar solvents such as water, where they generate hydrogen bonds. Thus, hydrophilic substances are polar (molecules) that easily establish hydrogen bonds and dissolve in water (Al-Lhaibi & Al-Shabander, 2022).

Natural polymers such as polyvinyl alcohol (PVA), corn starch(CS), and arabic gum (AG), have unique qualities that include non-toxicity, water solubility, and biodegradability, as well as physical traits such as high optical clarity (Hussein *et al.*, 2020; Abd-Elnaiem *et al.*, 2022). Surface coating and engineering boost polymer performance by applying synthesized film coatings, rendering itsuitable for use in energy harvesting, water treatment, and insulating barriers. The relevance of thin layers of polymeric substances on metal production is influenced by various factors such as lightweight and shock-resistant (Ali *et al.*,

2023). Homogeneous or heterogeneous blends of at least two polymers or co-polymers are known as polymer blends or as polymer mixtures. The polymers can interact chemically or physically, and their physical characteristics diverge from those of their parent components (Ali *et al.*, 2021). Polymer blends can be classified into five broad categories, each of which has received extensive research: Thermoplastic-thermoplastic, thermoplastic-rubber, thermoplastic-thermosetting, rubber-thermosetting, and polymer-filler blends (Parameswaranpillai *et al.*, 2014). Elastomers (EL) are polymers that, at typical ambient temperatures, are above their glass transition temperatures and are amorphous in their unstretched condition (Christenson *et al.*, 2005). The EL polymer was utilized in this investigation and had the following characteristics: strong, waterproof, flexible, chemically resistant, and temperature resistant up to 120 °C. They often have low glass transition temperatures, which fall between −50 and −70 °C. A network of cross-links holds the irregularly shaped chain molecules that make up EL together, preventing the chains as a whole from moving around but allowing individual chain segments to move locally. The network of cross-links may

result from physical connections between chain molecules or covalent bonding (Ebewele, 2000). The method used to synthesize polymer blends affected the structural and mechanical properties of polymer blends especially the adhesion strength (Awaja *et al.*, 2009).

Wood and Al have been used as natural building materials, furniture, tools, vehicles, and ornamental items since the dawn of time due to their distinctive properties and relative availability. Engineers, architects, and carpenters should have more accurate knowledge of wood variation to use it more effectively (Mohammed *et al.*, 2022). High-density fiberboard (HDF) wood is prepared when natural wood has a high density and a low amount of chemical additives. HDF wood is a scientific word that informally means the wood is of high quality and hence expensive (Henke *et al.*, 2022).

Certain polymers are more susceptible to bacterial attack due to the physical qualities of their surfaces or the chemical makeup of the polymer. The microbial population increases in polymers as it is usually used in humid conditions with large levels of organic materials (Hussein *et al.*, 2019). The use of hydrogen peroxide (H_2O_2), a silane coupling agent, and an olefin monomer as an oxidant, a cross-linking agent, and a comonomer, respectively, allowed for the creation of high-performance starch-based wood adhesives (Zhang *et al.*, 2015). It was demonstrated that starch-based wood adhesives' bonding strengths equal 7.88 MPa and 4.09 MPa in dry and wet conditions, respectively. The addition of silicon dioxide (SiO_2) as a filler affected the adhesive qualities of PVA (Hameed, 2016). Their findings revealed that the increases in SiO_2 content, increase the tensile strength and enable it to be used as an adhesive. High-performance, environmentally friendly starch-based glue was synthesized using cassava starch as the primary raw ingredient (Chen *et al.*, 2022). The plywood with modified starch adhesive demonstrated the maximum wet shear strength, 1 MPa, at a pH of 4.5 to 5.5, which was 163% greater than the nontreated starch adhesive.

The need for sustainable and alternative raw materials has increased as a result of the world's energy problems and reliance on petroleum resources. Unfortunately, the limitations include workability at low temperatures, poor water resistance, and limited heat resistance. It is generally known that D, AG, and CS are not moisture-resistant polymers, therefore can be used in damp settings significantly reducing their strength. Adhesive connections that withstand moisture may be created by blending EL and AG, D, PVA, or CS. Therefore, this study aims to improve the shear strength, pull-off adhesions, color intensity, thermal insulation, wearability, and antibacterial activity of EL mixed with naturally mentioned polymers so it may be used for HDF wood and Al coatings and adhesives. In addition, the effect of surface treatment by plasma jet on the wettability and roughness was investigated and compared.

2. Materials and Methods

The items used for developing the Automated Leak and Water Quality Detection (ALWQD) system and their functions are presented in Table 2. The development of ALWQD followed standard procedures.

Table 2: List of items used for developing the ALWQD and their purposes.

S/N	Items	Quantity	Purpose
	½ inch Polyvinylchloride (PVC) pipes	5 m long	Drainpipe/water flow
	Set of control valves	10	To close and open taps
	Samples of tap and polluted water	10 litres	For set up during loading condition
	Total Dissolved Solid module (Portable E-1 TDS)	2	To determine TDS in the setup
	pH meter (pH Tester PH-107)	2	To determine the pH value in the setup
	Turbidity meters module	2	To determine turbidity in the setup
	Flow meter	2	To determine the flow rate
	A laptop computer system	1	Control the setup
	Electrical power source	1	To power the electric components
	Solenoid valves	3	To shut off, release, dose, distribute, or mix fluids.
	ESP32 CH340 NodeMCU Wi-Fi Module	3	Interface with other systems; To provide Wireless Fidelity Wi-Fi and Bluetooth functions
	Relay Module with Optocoupler Relay Output	3	Input interface

Liquid pH 0-14	2	To determine the pH value in the setup
Male Thread Solenoid Valve 220V	2	To control the flow of water
Pipe Connectors	5	To Join pipes together
Electrical Casings	3	To house electrical components
Length of Wires and Jumper Cables	10 yards	To connect electrical components
Light Emitting Diodes (LEDs) and Light Dependent Resistors (LDRs)	2	To detect the light level
Liquid Crystal Display (LCD) display	2	Display parameter readings
Candle Gum	2	Joining items together as adhesive
Buck Converter and 12V Adapter	1	To step down voltage needed by Universal Serial Bus (USB)

The present study reviewed similar works by Atojunere and Ogundipe (2022), Daugirdas (2013), Nriagu et al. (1996), Atojunere et al. (2018), Howard et al. (1985), APHA (2022), and those in Table 1. The ALWQD setup involved two reservoirs: one holding 10 liters of water of known quality while the other was 10 liters of polluted water with known water quality parameters. Figure 1 shows the schematic diagram of the ALWQD system. Under loading and no loading conditions, the ALWQD system comprised sets of ½ inches of PVC pipes (2 meters long), the reservoirs, and the electrical components. The two reservoirs had on/off control and were also made to meet at a T-shaped junction before supply flow through a single 2-meter pipe where all sensors were located at different intervals. The ALWQD system included two identical systems, acting as senders/initiators, connected to an ESP32 NodeMCU microcontroller, a TDS meter turbidity meter, a pH level sensor with a water flow sensor to measure the pH values, turbidity, total dissolved solids, and flow rate along the pipe. System 3 acted as a responder that gathered measurements from sensors on the pipe and transferred them to the master unit, which controlled all other sensors. Systems 1 and 2 were not connected; they only sent measured readings to the master device connected to a computer. Arduino Integrated Development Environment (IDE)/Arduino Software was used to write the code to connect the ALWQD hardware's sensors: pH, turbidity, total dissolved solids, and the flow rates of the devices (systems 1 and 2) to interface with all the ALWQD components to the computer, to upload programs, and to allow interaction and communication. The master system/responder displayed Water Quality Indicator (WQI) readings received from devices 1 and 2 compared with the permissible level library data provided by WHO installed on the computer to call for action. This comparison prompted action by switching off the unpolluted water tap if pollution was recorded in the water pipes. The master system/responder turned off the tap control of the pipe that took supply from reservoir 2 through solenoid valve 2 and opened solenoid valve 1 once systems 1 and 2 deteriorated in water quality in the adjacent pipe. The ALWQD systems under loading and no loading conditions are shown in Figures 2 and 3. The ALWQD systems were run on three trials, and average results of WQI of pH, TDS, Turbidity, and flow rates on distilled, tap, and polluted water and points of leaks on the pipes were recorded at 0, 5, and 10 minutes. The efficiency of ALWQD was calculated, and data results were statistically analyzed. Visualization of ALWQD data (producing bar charts) was carried out using *Jupyter Notebooks (JN)* and Microsoft Excel 2016 software for comparison.
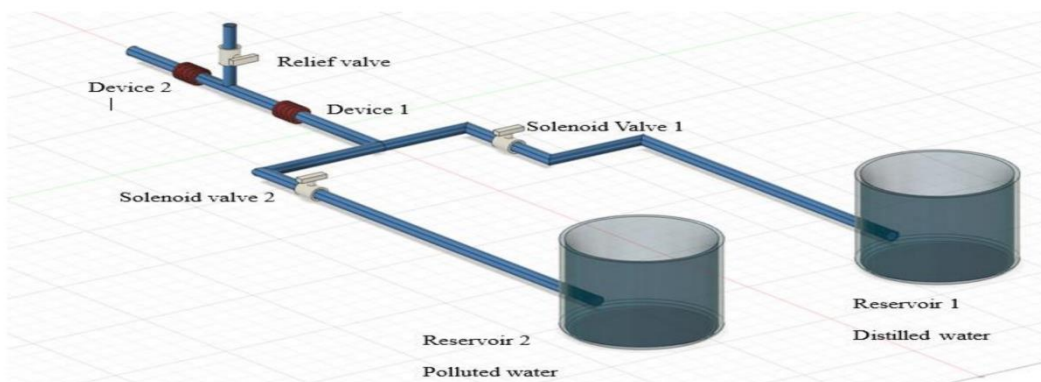

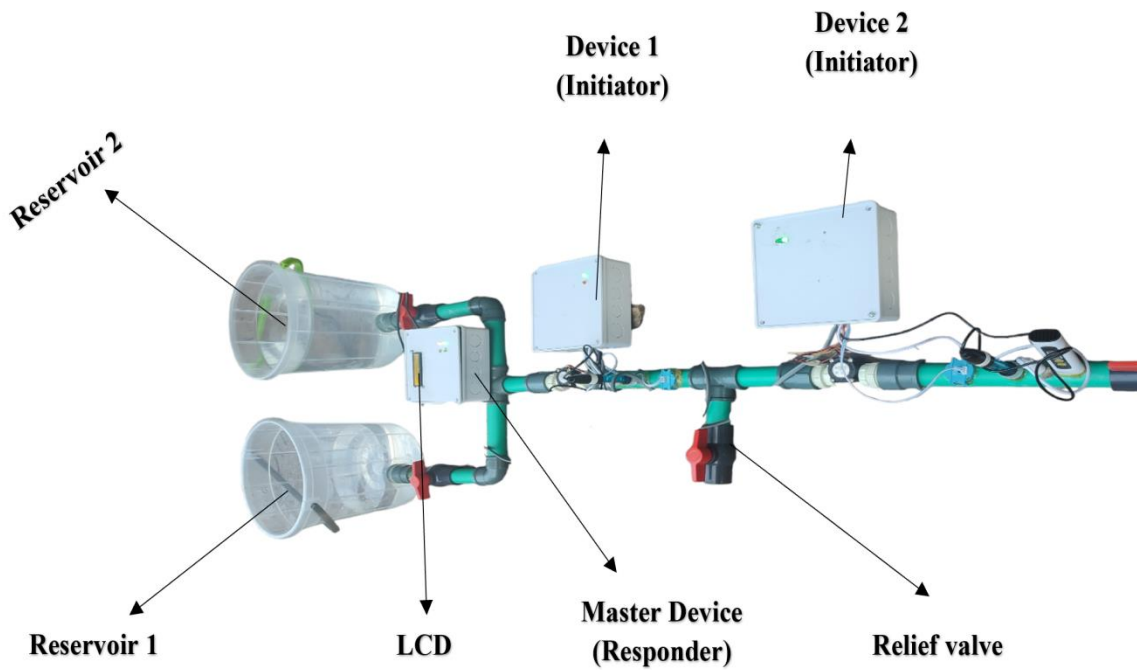**Figure 1.** Schematic diagram of the ALWQD system

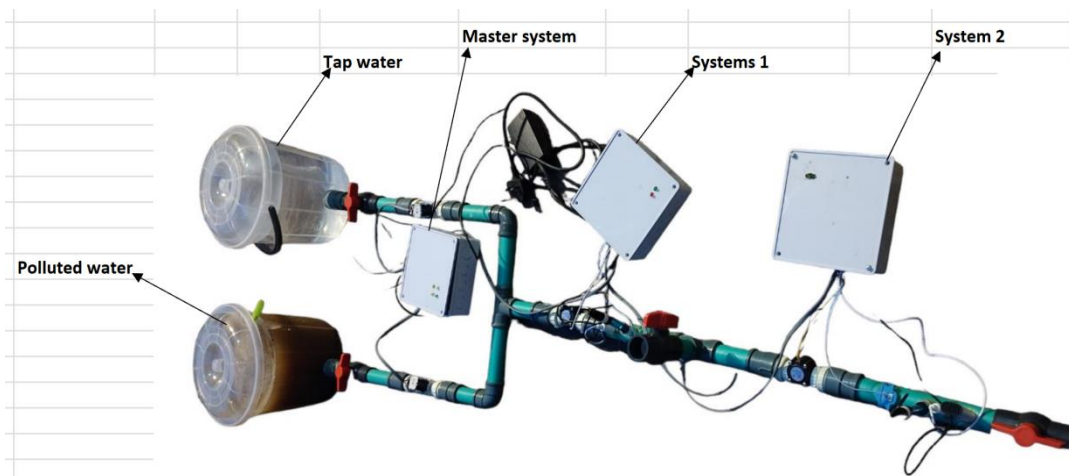**Figure 2:** Setup of the ALWQD systems under no load conditions.

Figure 3: Setup of the ALWQD systems during testing under load condition

3. Results and Discussion

The results of the water quality test for pH value, turbidity, and total dissolved solid test through the ALQWD for different samples are presented in Tables 3–6 for load and no-load conditions.

Table 3: Testing results of ALWQD under no load condition on distilled water.

Water Quality Indicator (WQI)	No load	
	System 1	System 2
Turbidity NTU*	0.00	0.00
pH value	6.99	6.98
Total dissolved solids (TDS) mg/L	0.00	0.00
Water Flow rates m³/s	1.04	1.07

Table 4: Testing results on the ALWQD system under load conditions.

Water Quality Indicator (WQI)	Tap water sample		Polluted water sample	
	System 1	System 2	System 1	System 2
Turbidity NTU	4.94	5.3	4.92	5.20
pH value	6.94	7.20	9.37	10.60
Total dissolved solids (TDS) mg/L	57.43	98.06	1088.21	1208.47
Water Flow rates m³/s	1.36	1.30	1.42	1.35

Table 5: Testing results of ALWQD under load conditions after 5 minutes

Water Quality Indicator (WQI)	Tap water sample		Polluted water sample	
	System 1	System 2	System 1	System 2
Turbidity NTU	4.90	5.2	4.95	5.30
pH value	6.52	6.92	8.65	8.82
Total dissolved solids (TDS) mg/L	59.10	101.86	1092.32	1143.05
Water Flow rates m³/s	1.52	1.36	1.42	1.33

NTU* Nephelometric Turbidity Unit

Table 6: Testing results of ALWQD under load conditions after 10 minutes.

Water Quality Indicator (WQI)	Tap water sample		Polluted water sample	
	System 1	System 2	System 1	System 2
Turbidity NTU	4.90	5.2	4.95	5.30
pH value	8.11	7.98	9.05	9.12
Total dissolved solids (TDS) mg/L	100.28	99.6	1219.83	1206.86
Water Flow rates m³/s	0.35	0.36	0.46	0.49

The determined water quality parameters align with those of previous works by Fashanu et al. (2019), Mala-Jetmarova (2015), Atojunere and Ogedengbe (2019), and water quality standards by Bartram and Balance (1996), WHO (2016), and WHO (2017). The ALQWD results demonstrated variations in the water quality indicators taken by systems 1 and 2 for distilled, tap, and polluted water, as shown in the graphs of Figures 5-11. The relative height differences recorded during testing were small and might be due to either instrument/component or human error. This finding indicates that ALQWD detected impairment in water quality along the water flow pipe and reported its leakages at loose joints. Leaks were detected by pressure drop and reduced flow rates in the pipes. The efficiency of ALQWD was from 70% to 80%. The TDS values in System 1 were greater than those of System 2, 59.10 mg/L > 101.86 mg/L; for tap water, System 2 > System 1: 1092.32 mg/L > 1143.05 mg/L for polluted water. A similar trend was recorded for pH and flow rates, except for turbidity values with a reverse trend. There was a significant difference among measured parameters in all the water tested. The turbidity values were above the 5 NTU recommended by WHO, suggesting that there could be other contaminants responsible for the higher turbid level. This result might not be unconnected to the possible intrusion of pollutants from surrounding soils or runoff from agricultural activities that migrated into the pipe through leak pipe and loose pipe joints.
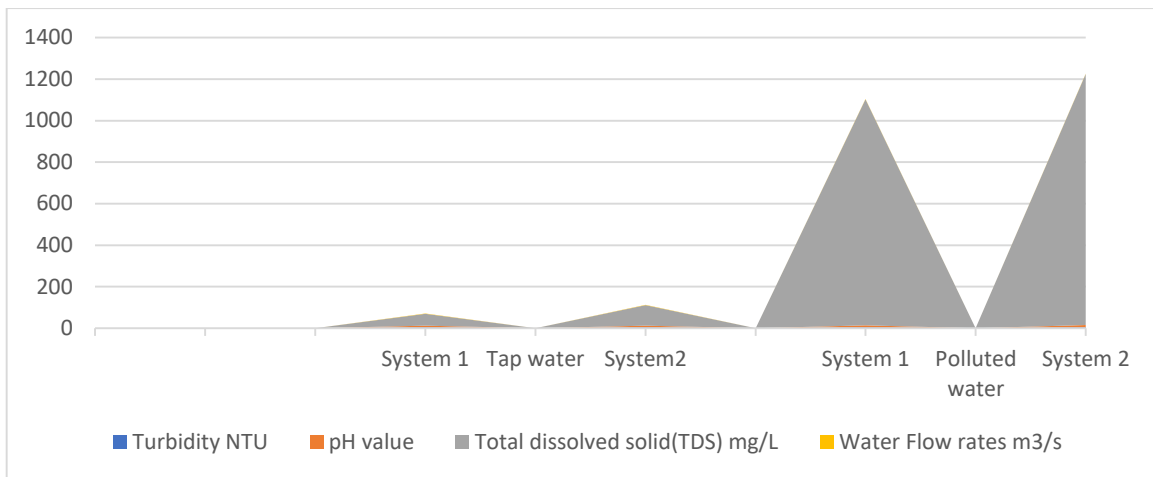
Figure 4: Plot of Turbidity value, TDS, and flow rates for tap and polluted water for 5 minutes.
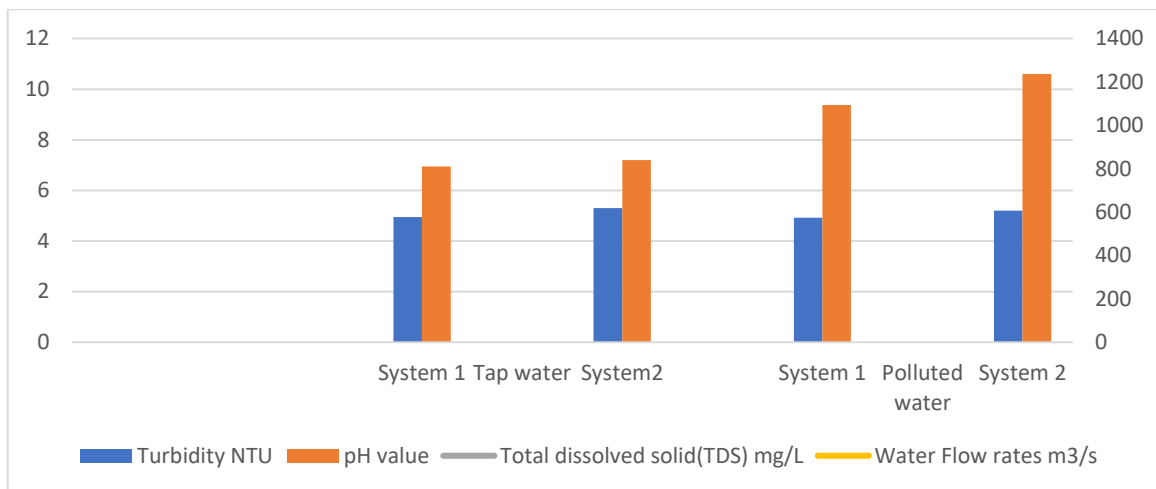

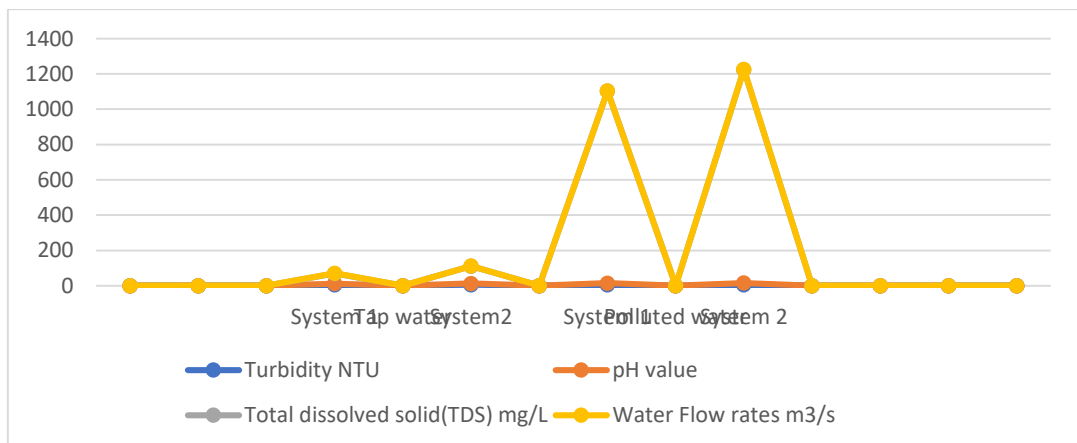**Figure 5:** Turbidity value, TDS, and flow rates for distilled, tap, and polluted water for 5 minutes.

Figure 6: Turbidity value, TDS, and flow rates for tap and polluted water for 10 minutes.
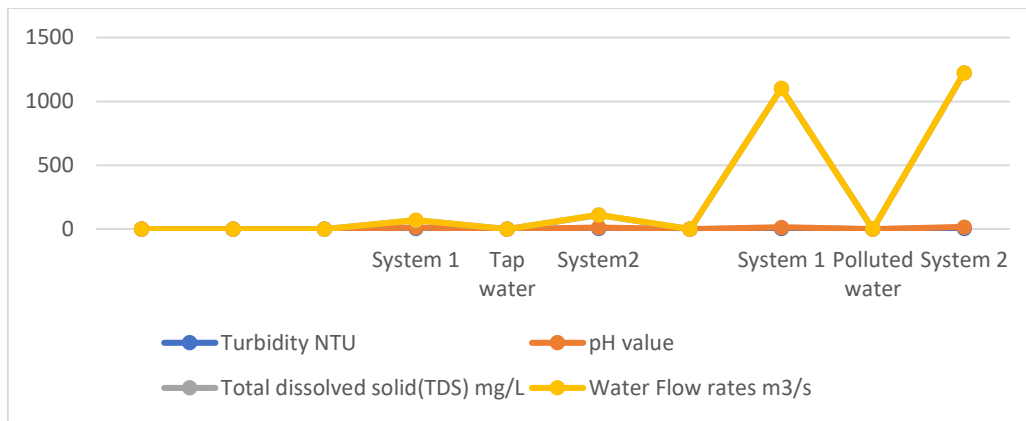
Figure 7: Turbidity value, TDS, and flow rates for tap and polluted water at 10 minutes
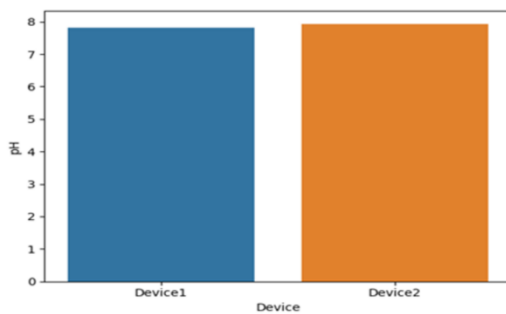

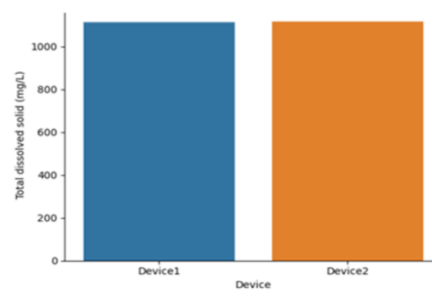**Figure 8** : Visual of turbidity of device 1 against 2 for tap water

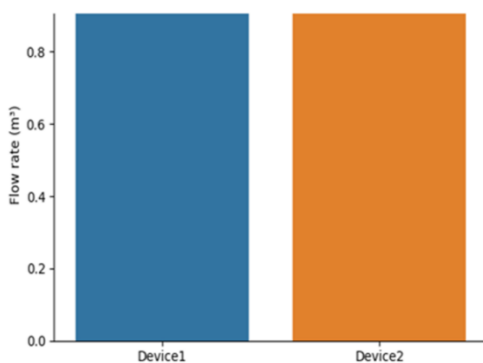**Figure 9**   Visual of TDS of device 1 against 2 for polluted water

Figure 10   Visual of flow rate of device 1 against 2 for polluted water
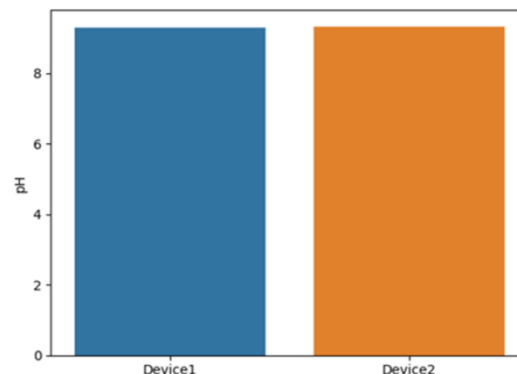
Figure 11   Visual of pH of device 1 against 2 for polluted water

4. Conclusion

The developed ALWQD system resolved the leakage problems associated with the water conveyance system. The development and testing of the ALWQD system followed standard procedures. The ALWQD system detected leaks in the simulated water pipes used for testing by indicating pressure drops at several points of leakage. The efficiency of ALWQD was 70%–80%. There were variations in some of the readings; however, they were considered insignificant. With modification, ALWOD will be a reliable water detection technology in the future as manual detection of leaks is becoming impracticable.

5. References

Aamo O.M (2016) Leak detection, size estimation and localization in pipe flows. IEEE Trans Autom Control 61(1):246–251 IEEE

Al Hawari A, Khader M, Zayed T, Moselhi O (2015) Non-destructive visual-statistical approach to detect leaks in water mains. World Acad Sci, Eng Technol, Int J Environ, Chem, Ecol, Geol Geophys Eng 9(3):230–234

Al Qahtani, T., Yaakob M. S, Yidris N., Sulaiman S., and Ahmad, K. A, (2020) "A Review on Water Leakage Detection Method in the Water Distribution Network". *Journal of Advanced Research in Fluid Mechanics and Thermal Sciences*, *68*(2), 152–163.

Al-Mashhadani, K.A, and D.J. Thompson (2011) "Leak Detection in Water Distribution Systems: A Review accessed date March 2023

APHA Public Health Association APHA(2022).Standard Methods for the Examination of Water and Wastewater (21st edition), American Public Health, Association, Washington DC.

Atef A, Zayed T, Hawari A, Khader M, Moselhi O (2016) Multi-tier method using infrared photography and GPR to detect and locate water leaks. Autom Constr 61:162–170 Elsevier

Atojunere,E.E, and O, Ogundipe(2022). Artificial Intelligence into Drip Irrigation of Roselle's *(Hibiscus Sabdariffa Linn)* Cultivation, *Agricultural Mechanization in Asia, Africa, and Latin, America)* *AMA* (ISSN: 00845841) 53(01) 6883-6895

Atojunere, E.E, and K.Ogedengbe (2019) Evaluating Water Quality Indicators of Some Water Sources in the Bitumen-Rich Areas of Ondo State, Nigeria, *International Journal of Environmental Pollution and Remediation*(IJPER) Avestia Publishing, Ontario, Canada,7(1) 9-22 https://ijepr.avestia.com/2019/002.html

Atojunere, E.E., K.Ogedengbe and E.B.Lucas (2018)The Development of Filtration and Bioremediation Technique for Decontaminating Bitumen-Polluted Water. *Proceedings of the 2nd International Conference of Recent Trends in Environmental Science and Engineering (RTESE'18)*, Academy of Science, Engineering and Technology, (ASET),NiagaraFall, Canada DOI:10.11159/rtese18.111

Bartram, J., and R. Balance(1996). Water quality monitoring–a practical guide to the designand implementation of freshwater quality and monitoring study UNEP/WHO, Chapman andHall. London. UNEP/WHO(1996)

Beat, S and S. Dorothee(2020) Water Distribution Pipes [Blog post]. Sustainable Sanitation and Water Management Toolbox https://sswm.info/sswm-university-course/module-centralised-and-decentralised-systems-water-and-sanitation-1/network-design- and- dimensioning accessed date May 2023

Chraim F, Erol YB, Pister K (2016) Wireless gas leak detection and localization. IEEE Trans Ind Inf 12(2):768–779 IEEE

Datta S, Sarkar S (2016) A review on different pipeline fault detection methods. J Loss Prev Process Ind 41:97–106 Elsevier

Daugirdas, J. T., (2013) "Handbook of water and wastewater treatment plant operations (3rd ed.)". BocaRaton, FL: CRC Press.

El-Zahab S, Mosleh F, Zayed T, El Zahab S, Mosleh F, Zayed T (2016) An accelerometer-based real-time monitoring and leak detection system for pressurized water pipelines. Pipelines:257–268

El-Zahab and Zayed (2019) Leak detection in water distribution networks: an introductory overview, https://doi.org/10.1186/s40713-019-0017-x

El-Abbasy MS, Mosleh F, Senouci A, Zayed T, Al-Derham H (2016) Locating leaks in water mainsusing noise loggers. Journal of Infrastructure Systems. 22(3):04016012

Eytan, G.and D, Spuhler(2021) Water Distribution Pipes accessed on https://sswm.info/sswm-University- course/module-2-centralized-and-decentralised systems-water- and-sanitation-1/water- distribution- pipes Accessed on February 2023

Fashanu, T.A. J.P.Eche, J.A Akanmu, O.J.Adeyeye and E.E. Atojunere(2019) . A Virtual Auto-desk-Simulink Reference Plant for Wastewater Treatment, Nigerian Journal of Technology (NIJOTECH), Faculty of Engineering, University of Nigeria, 38(1):267-267

Fondriest,F.J.(2021) .Conductivity, Salinity, and Total Dissolved Solids accessed on https://www.fondriest.com/Environmental-measurements/parameters/waterquality/conductivity salinity-TDS/ Accessed on December 2022.

Gong W, Suresh MA, Smith L, Ostfeld A, Stoleru R, Rasekh A, Banks MK (2016) Mobile sensor networks for optimal leak and backflow detection and localization in municipal water networks Environ Model Softw 80:306–321 Elsevier

Howard, S.P, D. R. Rowe and G.Tchobanoglous(1985). Environmental Engineering. McGraw-Hill, New York.

Khulief YA, Khalifa A, Mansour RB, Habib MA (2011) Acoustic detection of leaks in water pipelines using measurements inside the pipe. J Pipeline Syst Eng Pract 3(2):47–54 American Society of Civil Engineers

Kim D, Ha J, You K (2011) Adaptive extended Kalman filter based geolocation using TDOA/FDOA. Int J Control Autom 4(2):49–58

Nriagu, J.O, M.I. Blackson and K. Ocram(1996). Childhood Lead Poisoning in Africa, a GrowingPublic Health Problem. *Journal of Science Total Environment*. 181(2):93-101

Mala-Jetmarova, H .A.Barton A. A. Bagirov(2015) History of Water Distribution Systems andtheir Optimization. Water Science & Technology Water Supply https://www.researchgate.net/publication /274699540_accessed date June,2023

Mays, W. L(2000) Water Distribution Systems Handbook. American Water Works Association. New York: McGraw-Hill.

McEvoy, M.J. and S.J. Wyatt (2012) "Water Quality Monitoring: A Review" Accessed date January,2023

Naga Venkata Saidileep Korlapati, Faisal Khana, Quddus Noor, Saadat Mirzac,Sreeram Vaddirajua(2022) Review and analysis of pipeline leak detection methods, *Journal of Pipeline and Engineering, https://doi.org/10.1016/j.jpse.2022.100074.*

Oyedele, A.(2021) Water Distribution System Challenges and Solutionswww.wateronline.com/doc/water-distribution-system-challenges-and-solutions-0001 Accessed March,2023

Romano M, Woodward K, Kapelan Z (2017) Statistical process control-based system forapproximate location of pipe bursts and leaks in water distribution systems. Procedia Eng186:236–243 Elsevier.

Smith, T.F. and D.R. Naud (2013) "A Review of Water Quality Monitoring and Management inWater Supply Systems" Accessed date January 2023

Sinha, P.K. C.V. Madhava, and S.M. Shaikh (2007) "Leak Detection in Water Distribution Systems: A Review" Accessed date May 2023World Health Organization. Health Aspects of Plumbing (2016) Accessed date April,2023 https://www.who.int/water_sanitation_health/publications/plumbinghealthasp.pdf World Health Organization. (2017) Guidelines on drinking water quality 4th Edition Geneva, Switzerland, Accessed date January 2023

DETERMINATION RISK OF BREMSSTRAHLUNG RADIATION PRODUCED BY BETA-RAY

Naz T. Jarallah[1a]

Abstract: When interacting with absorption materials, beta rays, which are emitted by isotopes, are harmful because bremsstrahlung (braking) radiation is produced. Therefore, the efficiency of a shielding material can be improved by considering the bremsstrahlung radiation generated by the material's beta ray absorption. In this study, to determine the risk of bremsstrahlung radiation produced by beta rays, the fractions of beta energy transformed into bremsstrahlung radiation were calculated for beta emitters in the energy ranges of 0.0026–0.1734, 0.205–0.694, and 0.9345–2.640 MeV, using five different absorption materials ($_{13}$Al, $_{26}$Fe, $_{48}$Cd, $_{74}$W, and $_{82}$Pb). The relationship between the fractions of beta energy transformed into bremsstrahlung radiation by the five shielding materials and the maximum energies of some beta emitters was studied to determine the most suitable beta-ray shielding materials to effectively minimize bremsstrahlung radiation. The results showed that the fractions of beta energy transformed into bremsstrahlung radiation increased as the beta energy and the atomic number of the shielding material increased. The fraction of beta energy transformed into bremsstrahlung radiation in $_{13}$Al < $_{26}$Fe < $_{48}$Cd < $_{74}$W < $_{82}$Pb. Therefore, beta ray shields should be made with low atomic number materials to reduce the generation of bremsstrahlung radiation. Practically, beta shields made from materials with atomic numbers greater than 13 are rarely employed; notably, aluminum successfully decreased the production of bremsstrahlung radiation. However, it is also necessary to use materials with medium and high atomic numbers as secondary beta shields to reduce the effect of the bremsstrahlung radiation photons formed by the interaction between beta rays and shielding materials.

Keywords: beta emitters, beta particles, bremsstrahlung radiation, shielding materials.

1. Introduction

A beta (β) particle, which has moderate penetration power, is a high-velocity electron or sometimes a positron (the electron's antiparticle) (Duaa et al., 2019). Beta particles are electrons with a negative or positive charge (e⁻ and e⁺). The atomic number (Z) of an element increases by one unit in the case of β⁻ decay and decreases by one unit in the case of β⁺ decay. Some nuclei undergo radioactive change by taking an atomic electron, generally from the K shell, releasing a neutrino, and decreasing in atomic number (James, 2007; Murtadha et al., 2019). Beta particles react with absorber materials in four ways: direct ionization, delta rays from electrons generated by ionization, production of bremsstrahlung radiation, and Cerenkov radioactivity (Michael, 2003). Charged particles (e.g., beta particles) with enough energy can travel at speeds greater than the phase velocity of light through optically transparent media (e.g., water, organic solvents, plastic, glass). When this occurs, the charged particles produce Cherenkov photons at ultraviolet and visible wavelengths (Ahmed et al., 2022). The most significant reactions are bremsstrahlung radiation and direct ionization (Martin, 2006).

Shielding substances, when located between the source of radiation and the receptor, can affect the quantity of radiation that reaches the receptor. This implies that the reduction and absorption of produced radiation occurs in the source itself, in substances employed in the encapsulation of the source, or in a shielding block (Martin, 2006).

Radiation protection blocks people and the environment from the damaging results of ionizing radiation. One major concern in nuclear energy plant construction is radiation exposure. Using powerful (high-activity) radioisotopes in "spin-off" applications, such as medical X-ray diagnostic systems, food protection, particle acceleration, and cancer treatment, can be dangerous for workers involved in these radiation-based services (Thomas et al., 2016).

Many studies have focused on the absorption of beta rays into shielding substances and the resulting bremsstrahlung radiation. For example, Wesley et al. (2007) studied the production of bremsstrahlung photons from shielding materials, such as plastic and lead, in various arrangements to determine the absolute efficiency of plastic and lead alone and the optimal order and positions of plastic and lead together. Amato et al. (2009) established a Monte Carlo simulation in Geant4 to compare the bremsstrahlung radiation produced by various kinds of plastic substances used as shields for beta ray emitters and their attenuation properties. Serkan et al. (2016) estimated the radiation yields from electrons in several absorbing materials, such as water, carbon, aluminum, copper, lead, and uranium, in

Authors information:
Department of Physics, College of Education for Pure Science (Ibn Al-Haitham)/ University of Baghdad, Baghdad, IRAQ. E-mail: naz.t.ja@ihcoedu.uobaghdad.edu.iq
*Corresponding Author: naz.t.ja@ihcoedu.uobaghdad.edu.iq

the primary electron energy range from 10 keV to 1 GeV. Moreover, Manjunath (2020) measured the photon and bremsstrahlung yields from β^- particles in the energy range of 0.1668–2.274 MeV for intensive targets with atomic numbers of 13–83. This paper aims to determine the risk of bremsstrahlung radiation produced by beta rays. The fractions of beta energy transformed into bremsstrahlung radiation for some beta emitters in energy ranges of 0.0026–0.1734, 0.205–0.694, and 0.9345–2.640 MeV are calculated using five different absorption materials ($_{13}$Al, $_{26}$Fe, $_{48}$Cd, $_{74}$W, and $_{82}$Pb).

2. Theory

Bremsstrahlung radiation is produced when high-speed charged particles experience a fast transformation in velocity, specifically when they accelerate. Because velocity is a vector quantity that contains both direction and magnitude, a change in path—even if the speed value remains the same—results in a change in speed (Thomas, 2017).

As soon as an electron or beta particle passes near nuclei shielding material, beta particles deviate from their original path due to the influence of the nucleus's electric field. This transformation involves radial acceleration. According to Maxwell's classical theory, beta particles lose energy by emitting electromagnetic radiation that is proportional to the square of its acceleration (Thomas, 2017).

Bremsstrahlung radiation occurs when beta particles (high-speed electrons) pass near the nuclei of the absorbing material (Thomas et al., 2016; Mangiarotti et al., 2017), especially if the material has a high atomic number. Thus, when beta emitters or expedited monoenergetic electrons are used, the fraction of beta energy transformed into bremsstrahlung radiation must be considered to determine the type and design of shielding materials that can be used (Thomas et al., 2016).

It is significant for those who work with radionuclides to understand that bremsstrahlung radiation is not a feature of beta sources and thus cannot be seen in the spectrum of decay. X-rays are an outcome of the reaction of beta particles with neighboring materials, such as flasks or shields (Thomas, 2017).

To estimate the bremsstrahlung risk from beta radiation (Thomas, 2017), the fraction of beta energy transformed into bremsstrahlung rays can be calculated using the following equation (Wesley et al., 2007):

$$F = 3.5 \times 10^{-4}\, E_m\, Z \qquad (1)$$

where F is the fraction of beta energy (MeV) transformed into X-rays, E_m is the maximum energy (MeV) of the beta ray, and Z is the atomic number of the shielding material.

3. Methodology

This study focused on determining the risk of bremsstrahlung radiation, which can be achieved by calculating the fraction of beta energy transformed into bremsstrahlung radiation using Equation 1. These fractions have been calculated for 50 beta sources, which are classified into three energy ranges: low (0.0026–0.1734 MeV), medium (0.205–0.694 MeV), and high (0.9345–2.640 MeV), using five shielding materials ($_{13}$Al, $_{26}$Fe, $_{48}$Cd, $_{74}$W and $_{82}$Pb).

Aluminum is a multipurpose, cheap, and appealing metal substance for its wide scope of use. It can be processed as a smooth, highly flexible packaging foil and can be used in numerous engineering applications. Aluminum has a density of 2.7 g/cm^3, and its surface can be an efficient reflector. It efficiently reflects electromagnetic waves, radiant energy, visible light, and radiant heat (Davis, 2001).

Iron is a cheap but strong structural material that has a relatively high density. It is activated by neutrons. Thus, thicker and heavier shields are required to achieve equivalent attenuation in lead, bismuth, or tungsten. Significantly, the generation of bremsstrahlung radiation in iron is lower than in bismuth or lead (Daniel, 2018).

Cadmium (Cd) is a gray-white, soft, ductile metal (Honey et al., 2015). As a radiation shielding material, its photon-like mass attenuation factor (μ/ρ) and effective atomic number (Z_{eff}) gradually increase as CdO content increases (Alajerami et al., 2020).

Tungsten exhibits stability at high temperatures, with lower toxicity and attenuation factors than lead or bismuth, but its higher density means that a similar material thickness will achieve the same attenuation (Daniel, 2018). Tungsten also has a lower half-value layer compared to traditional shielding substances, such as lead (Nadin et al., 2020).

Metallic lead is frequently employed as a radiation shielding substance because it has a high atomic number, low cost, and easy processability; specifically, it offers good shielding against breakthrough gamma radiation. (Rajeshwari et al., 2017).

110

4. Results and Discussion

The fractions of the beta energy transformed into bremsstrahlung radiation in the five shielding materials, calculated using Equation 1, are shown in Tables 1, 2, and 3. The relationship between the beta energies and the calculated fractions of the beta energy transformed into bremsstrahlung radiation for each of the five shielding materials was visualized by plotting the fraction of beta energy as a function of total beta energy. A plot was created for each shielding material using the specific low, medium, and high ranges of beta energies (0.0026–0.1734, 0.205–0.694, and 0.9345–2.640) MeV, as shown in Figures 1, 2, and 3, respectively.

Table 1. Fractions of beta energy transformed into bremsstrahlung radiation by shielding material ($_{13}$Al, $_{26}$Fe, $_{48}$Cd, $_{74}$W, and $_{82}$Pb) for beta energies of 0.0026–0.1734 MeV.

| Beta sources	Maximum Beta Energy (MeV) (Wang et al., 2012)	Fraction (MeV)*10^{-3}				
		$_{13}$Al	$_{26}$Fe	$_{48}$Cd	$_{74}$W	$_{82}$Pb
Re-187	0.0026	0.0118	0.0236	0.0436	0.0673	0.0746
H-3	0.0186	0.0846	0.1692	0.3124	0.4817	0.5338
Pu-241	0.0208	0.0946	0.18928	0.3494	0.5387	0.5970
Tm-171	0.0297	0.1351	0.2703	0.4990	0.7692	0.8524
Pd-107	0.033	0.1502	0.3003	0.5544	0.8547	0.9471
Ru-106	0.0394	0.1793	0.3585	0.6619	1.0205	1.1308
Sm-151	0.0548	0.2493	0.4987	0.9206	1.4193	1.5728
W-188	0.058	0.2639	0.5278	0.9744	1.5022	1.6646
Ni-63	0.0669	0.3044	0.6088	1.1239	1.7327	1.9200
Sm-151	0.0763	0.3472	0.6943	1.2818	1.9762	2.1898
Tm-171	0.0964	0.4386	0.8772	1.6195	2.4968	2.7667
Bk-249	0.1257	0.5719	1.1439	2.1118	3.2556	3.6076
Se-79	0.1507	0.6857	1.3714	2.5318	3.9031	4.3251
C-14	0.1565	0.7121	1.4242	2.6292	4.0534	4.4916
S-35	0.1668	0.7589	1.5179	2.8022	4.3201	4.7872
Kr-85	0.1734	0.7890	1.5779	2.9131	4.4911	4.9766
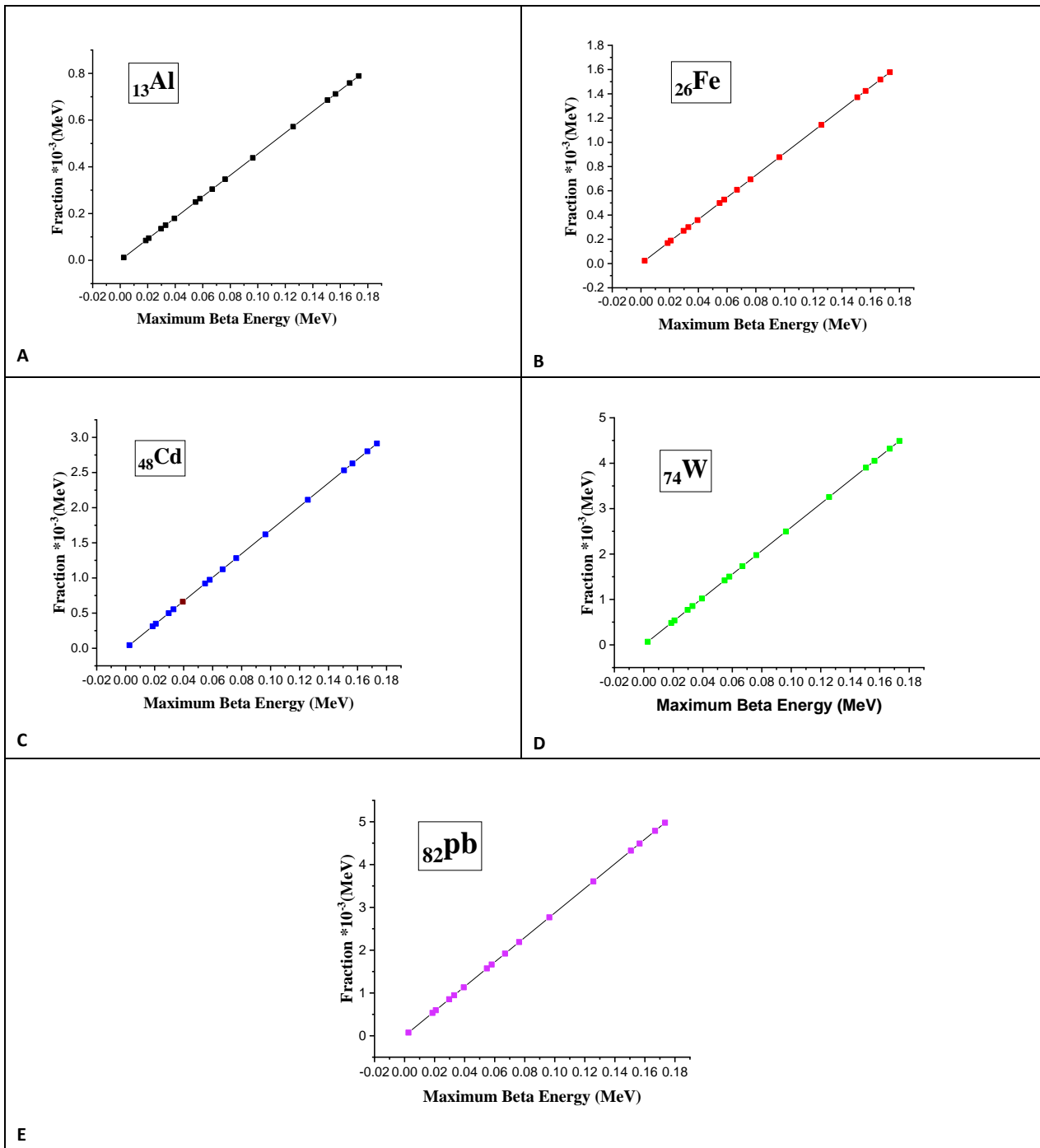
Figure 1. Fractions of beta energy transformed into bremsstrahlung radiation as a function of beta energy for a) $_{13}$Al, b) $_{26}$Fe, c) $_{48}$Cd, d) $_{74}$W, and e) $_{82}$Pb shielding materials for beta energies of 0.0026–0.1734 MeV.

Table 2. Fractions of beta energy transformed into bremsstrahlung radiation by shielding material ($_{13}$Al, $_{26}$Fe, $_{48}$Cd, $_{74}$W, and $_{82}$Pb) for beta energies of 0.205–0.694 MeV.

Beta sources	Maximum Energy (MeV) (Wang et al., 2012)	Fraction (MeV)*10^{-3}				
		$_{13}$Al	$_{26}$Fe	$_{48}$Cd	$_{74}$W	$_{82}$Pb
Cs-135	0.205	0.9328	1.8655	3.444	5.3095	5.8835
Pm-147	0.2246	1.0219	2.0439	3.7733	5.8171	6.4460
Si-32	0.225	1.0238	2.0475	3.7800	5.8275	6.4575
Ni-66	0.227	1.0329	2.0657	3.8136	5.8793	6.5149
P-33	0.2485	1.1307	2.2614	4.1748	6.4362	7.1320
Ca-45	0.2568	1.1684	2.3369	4.3142	6.6511	7.3702
Te-127	0.276	1.2558	2.5116	4.6368	7.1484	7.9212
W-188	0.285	1.2968	2.5935	4.7880	7.3815	8.1795
Tc-99	0.2935	1.3354	2.6709	4.9308	7.6017	8.4235
Sn-123	0.314	1.4287	2.8574	5.2752	8.1326	9.0118
Cd-113	0.316	1.4378	2.8756	5.3088	8.1844	9.0692
Y-91	0.3409	1.5511	3.1022	5.7271	8.8293	9.7838
Er-169	0.3425	1.5584	3.1168	5.7540	8.8708	9.8298
W-188	0.349	1.5880	3.1759	5.8632	9.0391	10.0163
Er-169	0.3509	1.5966	3.1932	5.8951	9.0883	10.0708
Sn-121	0.3889	1.7695	3.5390	6.5335	10.0725	11.1614
In-115	0.497	2.2614	4.5227	8.3496	12.8723	14.2639
Sr-90	0.5462	2.4852	4.9704	9.1762	14.1466	15.6759
Be-10	0.5562	2.5307	5.0614	9.3442	14.4056	15.9629
Ar-39	0.565	2.5708	5.1415	9.4920	14.6335	16.2155
Cd-113	0.580	2.6390	5.2780	9.7440	15.0220	16.6460
Ar- 42	0.600	2.7300	5.4600	10.0800	15.5400	17.2200
Pb-209	0.6444	2.9320	5.8640	10.8259	16.6900	18.4943
Kr-85	0.6874	3.12767	6.2553	11.5483	17.8037	19.7284
Te-127	0.694	3.1577	6.3154	11.6592	17.9746	19.9178

Figure 2. Fractions of beta energy transformed into bremsstrahlung radiation as a function of beta energy for a) $_{13}$Al, b) $_{26}$Fe, c) $_{48}$Cd, d) $_{74}$W, and e) $_{82}$Pb shielding materials for beta energies of 0.205–0.694 MeV.

Table 3. Fractions of beta energy transformed into bremsstrahlung radiation by shielding material ($_{13}$Al, $_{26}$Fe, $_{48}$Cd, $_{74}$W, and $_{82}$Pb) for beta energies of 0.9345–2.640 MeV

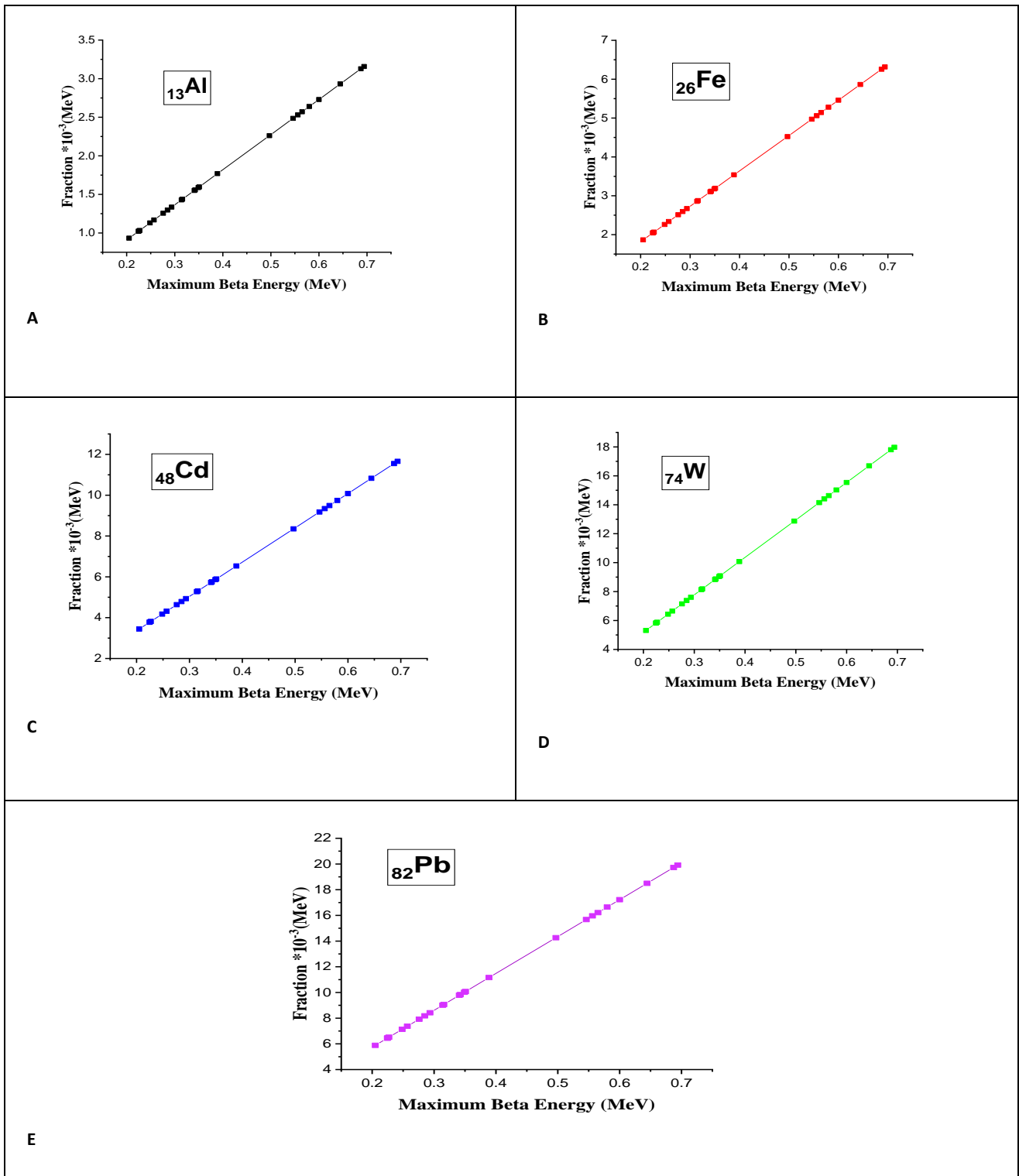| Beta sources	Maximum Energy (MeV) (Wang et al., 2012)	Fraction (MeV)*10^{-3}				
		$_{13}$Al	$_{26}$Fe	$_{48}$Cd	$_{74}$W	$_{82}$Pb
Pr-143	0.9345	4.2520	8.5040	15.6996	24.2036	26.8202
Bi-210	1.1615	5.2848	10.5697	19.5132	30.0829	33.3351
Sn-123	1.403	6.3837	12.7673	23.5704	36.3377	40.2661
Sr-89	1.492	6.7886	13.5772	25.0656	38.6428	42.8204
Y-91	1.5456	7.0325	14.0650	25.9660	40.0310	44.3587
P-32	1.7103	7.7819	15.5637	28.7330	44.2968	49.0856
Pr-145	1.805	8.2128	16.4255	30.3240	46.7495	51.8035
Y-90	2.2814	10.3804	20.7607	38.3275	59.0883	65.4762
Cu-66	2.640	12.0120	24.0240	44.3520	68.3760	75.7680
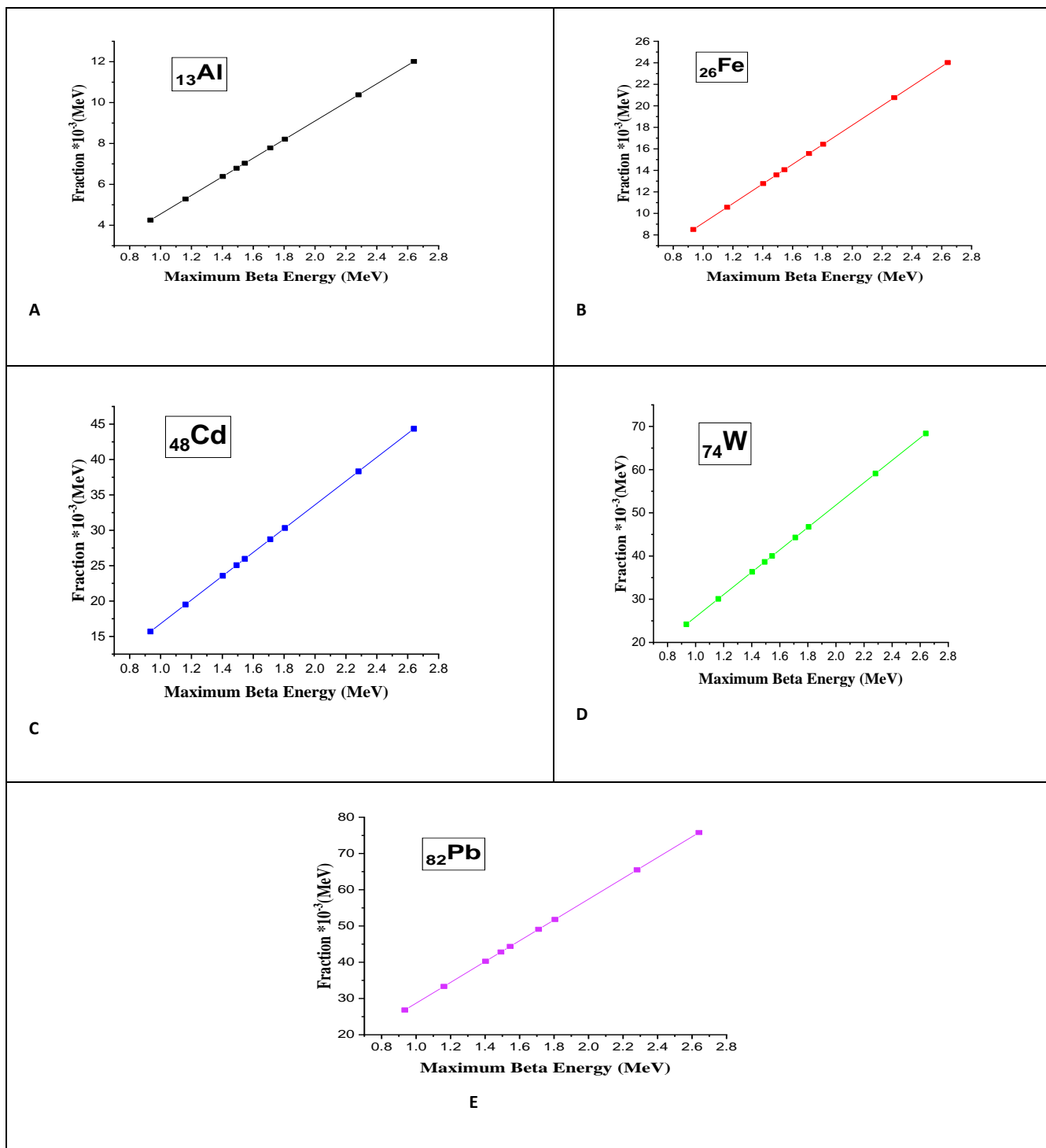
Figure 3. Fractions of beta energy transformed into bremsstrahlung radiation as a function of beta energy for a) $_{13}$Al, b) $_{26}$Fe, c) $_{48}$Cd, d) $_{74}$W, and e) $_{82}$Pb shielding material for beta energies of 0.9345–2.640 MeV.

For all five shielding materials ($_{13}$Al, $_{26}$Fe, $_{48}$Cd, $_{74}$W or $_{82}$Pb), the fractions of beta energy transformed into bremsstrahlung radiation related to the low beta energy range (0.0026–0.1734 MeV) [(0.01183–0.78897, 0.02366–1.57794, 0.04368–2.91312, 0.06734–4.49106, and 0.07462–4.97658) × 10^{-3} MeV] were significantly lower than the fractions resulting from the medium beta energy range (0.205–0.694 MeV) [(0.93275–3.1577, 1.8655–6.3154, 3.444–11.6592, 5.3095–17.9746, and 5.8835–19.9178) ×

10^{-3} MeV] and the high beta energy range (0.9345–2.640 MeV) [(4.251975–12.012, 8.50395–24.024, 15.6996–44.352, 24.20355–68.376, and 26.82015–75.768) × 10^{-3} MeV].

To compare the fractions of beta energy transformed into bremsstrahlung radiation for all shielding materials, the fraction values were plotted as a function of maximum beta energies for the three beta energy ranges, as shown in Figures 4, 5, and 6.
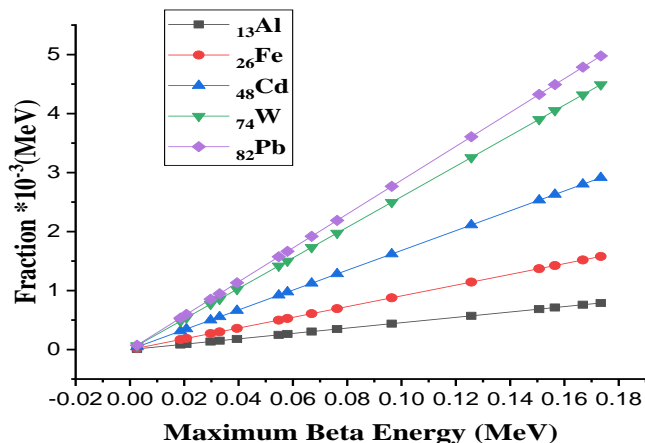
Figure 4. Comparison of the fractions of beta energy transformed into bremsstrahlung radiation for all shielding materials at beta energies of 0.0026–0.1734 MeV.
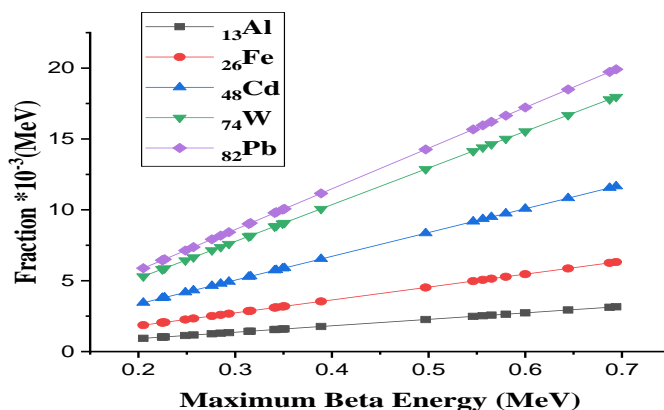

Figure 5. Comparison of the fractions of beta energy transformed into bremsstrahlung radiation for all shielding materials used in this work at beta energies of 0.205–0.694 MeV.
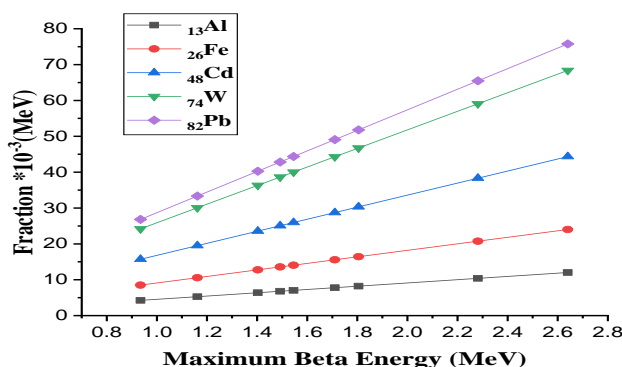
Figure 6. Comparison of the fractions of beta energy transformed into bremsstrahlung radiation for all shielding materials used in this work at beta energies of 0.9345–2.640 MeV.

Figures 4, 5, and 6 show that the fractions of $_{13}$Al (black line) are lower than the fractions of the other shielding materials. The fractions of bremsstrahlung production for the shielding materials, as well as the risk of beta sources, increase as the beta energy and atomic number of the shielding materials increase. This is due to the increased probability of interaction between beta rays and shield materials with increasing beta energies and atomic numbers.

5. Conclusion

This work demonstrated that the fractions of beta rays transformed into bremsstrahlung radiation increases as the beta

117

energy and atomic number of the shielding materials increase. Therefore, beta shields should be made from materials with lower atomic numbers to reduce the risk of bremsstrahlung radiation. Practically, beta shields with atomic numbers greater than 13 (e.g., aluminum) are rarely employed; however, shields made from substances of low mass number (e.g., aluminum) yield less bremsstrahlung radiation. It is also necessary to use materials with medium and high atomic numbers as secondary beta shields to reduce the effect of bremsstrahlung photons, which are formed in the interaction between beta rays and shielding material.

6. Acknowledgement

7. References

Ahmed Fadhil Mkhaiber and Naz T. Jarallah. (2022) Study the Relationship between Bremsstrahlung Dose Rate and The Energy of Beta Ray for different Types of Shiels", Malaysian Journal of Science, vol.41, no.2, pp. 47-54.

Alajerami, Y.S., Drabold, D., Mhareb, M.H.A., Cimatu, Katherine Leslee A., Chen, Gang and kurudirek M. (2020), Radiation Shielding Properties of Bismuth Borate Glasses Doped with Different Concentrations of Cadmium Oxides, Ceramics International, vol.46, pp.12718- 12727.

Amato, E. and Lizio, D. (2009), Plastic materials as a radiation shield for β – sources: a comparative study through Monte Carlo calculation, J. Radiol. Prot.,vol.29, no.2, pp.239–250.

A Mangiarotti and M N Martins. (2017), A review of electron–nucleus bremsstrahlung cross sections between 1 and 10 MeV, Radiation Physics and Chemistry,vol.141,pp.312-338.

Daniel R. McAlister. (2018), Gamma Ray Attenuation Properties of Common Shielding Materials, PG Research Foundation, Inc. University Lane Lisle, USA, June 18.

Davis, J.R. (2001), Alloying: Understanding the Basics", ASM International.

Duaa Abed Salim, and Sameera Ahmed Ebrahim. (2019) Measurement of Radon concentration in College of Education, Ibn Al- Haitham buildings using Rad-7 and CR-39 detector, Energy Procedia, vol.157, pp. 918–925.

H.C. Manjunatha. (2020), Empirical formula for beta-particle-induced bremsstrahlung yields, Pramana – J. Phys., vol. 94, no. 1.

James, E, Turner. (2007), Atoms, radiation and radiation protection", WILEY-VCH Verlag GmbH & Co.KGaA, Weinheim.

M. Wang ,G.Audi, A.H. Wapstra, F.G. Kondev, M. MacCormick, X.Xu and B. Pfeiffer. (2012), The Ame2012 atomic mass evaluation,Chinese Physics C,vol. 36, no.12, pp.1603–2014.

Martin J.E. (2006) Physics for Radiation Protection, WILEY-VCH Verlag GmbH & Co. KGaA, Weinheim, 3rd ed.

Michael F. (2003). Handbook of Radioactivity Analysis, (USA), Elsevier Science.

Mirji, Rajeshwari and Lobo, Blaise. (2017), Radiation shielding materials: A brief review on methods, scope and significance, In Proceedings of the National Conference on Advances in VLSI and Microelectronics, Huballi, India, pp.96-100.

Murtadha S Nayyef ., Naz T Jarallah. (2019) Study Mass Parabola and Most Stable Isobar from Some Isobaric Nuclides, AIP Conference Proceedings. 2190, 020007.

Nadin Jamal Abu Al Roos, Azman Mira Natasha, Amin Noor fatin Aida Baharul and Zainona, Rafidah. (2020), Tungsten-based material as promising new lead-free gamma radiation shielding material in nuclear medicine, Physica Medica, vol.78, pp.48-57.

Serkan Akkoyun, Tuncay Bayram, Nihat Yildiz. (2016), Estimations of Radiation Yields for Electrons in Various Absorbing Materials, Science Journal (CSJ), vol. 37, no.2, pp. 59-65.

Sharma, H.,Rawal, N. and Mathew, B. B. (2015), The Characteristics, Toxicity and Effects of Cadmium, International Journal of Nanotechnology and Nano science, vol. 3, pp.1-9.

Thomas E. Johnson. (2017) Introduction to Health Physics, Fifth Edition. McGraw-Hill Education.

Thomas, G. A. and Symonds, P. (2016) Radiation Exposure and Health Effects – is it Time to Reassess the Real Consequences, Clinical Oncology, vol. 28, no. 4, pp. 231–236.

R.Wesley, Pelt, Van and Drzyzga, Michael. (2007), Beta Radiation Shielding with Lead and Plastic Effect on Bremsstrahlung Radiation when Switching the Shielding Order, The Radiation Safety Journal, vol. 92, no.1, pp.13–17.

COMPUTATION OF RAIN-INDUCED ATTENUATION AT CENTIMETRIC WAVE BAND FOR SLANT PATH COMMUNICATION IN NORTH CENTRAL NIGERIA

K.C. Igwe[1a]*, O.D. Oyedum[2a], J.S. Ojo[3b], O.O. Obiyemi[4c], A.G. Ibrahim[5a]

Abstract: This paper examines five globally recognized rain attenuation models for slant path communication to compute the attenuation and identify the models required for optimal rain-induced attenuation prediction over Nigeria's North-Central region. The models considered are Garcia-Lopez, Svjatogor, Bryant, ITU-R P.618-9, and Simple Attenuation. These models have been evaluated for circularly polarized signals in the centimeter wave bands. The Lavergnat-Gole rain rate model was employed to transform the original 5-minute integration time rainfall data to a 1-minute integration time. Attenuation estimates for rain varied widely between 9 and 14 dB for the Ku-band and between 20 and 32 dB for the Ka-band at 0.01% of the time over a typical year. Furthermore, the calculations of the Garcia-Lopez, Bryant, and ITU-R P.618-9 models generally agreed, while the Simple Attenuation and Svjatogor models consistently underestimated the rain-induced attenuation across the selected region and all time percentages.

Keywords: Slant path, Ka, Ku-band, rain-induced attenuation, north-central Nigeria, rainfall rate

1. Introduction

Rain attenuation poses the most significant atmospheric threat to the reliability and efficiency of slant path communication systems operating at higher frequency bands (≥ 10 GHz). While degradation from other atmospheric elements such as fog, clouds, snow, and ice occurs, impairments caused by rain are more substantial (Shrestha et al., 2016; Hossain & Islam, 2017; Shrestha & Choi, 2017a; Pérez-García et al., 2023). Consequently, a thorough examination of the impacts of rain degradation on the efficiency of systems operating in high-frequency bands is essential (Shrestha & Choi, 2018).

Attenuation of radio waves propagating through rain occurs due to power absorption in the dielectric medium. Additionally, some losses occur in the directly transmitted wave because of energy scattering by the rain droplets. Scattering losses are typically smaller than those from absorption, depending on the frequency (Collin, 1985).

The inhomogeneity of rain causes complexity in computing rain attenuation. Rain varies greatly in shape, size, and density, leading to no distinct distribution of raindrop sizes for a particular rainfall rate, as it changes temporally and spatially (Tamosiunaite et al., 2010). Accurate analysis of rain attenuation requires precise evaluation of the corresponding rain rate (Oktaviani & Marzuki, 2019). This necessity has been confirmed by recent studies on rain rates (Ng et al., 2017; Shrestha & Choi, 2017b; Rafiqul et al., 2018; Singh & Acharya, 2019).

Due to higher rain intensity and larger raindrops in tropical regions, including Nigeria, signals propagating at centimetric and millimetric wave bands in the tropics are degraded by absorption and scattering during rainfall. Therefore, understanding the extent of rain attenuation in various localities in Nigeria is imperative for satellite system experts to provide quality network services. The Nigerian Communication Satellite (NIGCOMSAT-1R) also utilizes the Ku and Ka bands, and efforts are ongoing to solve the problem of signal outages during rainfall. This is being achieved through various rainfall measurement campaigns and rain attenuation predictions. The present study is part of these efforts.

This paper computes the extent of rain attenuation on slant path communication systems and evaluates the rain attenuation models for optimal predictions in North Central Nigeria. This was achieved using rain data collected at a 5-minute integration time instead of the daily rain data employed in Igwe et al. (2019). It continues the study documented in Igwe (2022) with additional computation of rain attenuation at the Ka-band. Furthermore, results from recent efforts in North Central Nigeria align with the present study (Alozie et al., 2022; Isabona et al., 2022a; Isabona et al., 2022b; Igwe, 2023).

Authors information:

[a]Department of Physics, Federal University of Technology, Minna, Niger State, NIGERIA. E-mail: k.igwe@futminna.edu.ng[1]; onyedidavid@futminna.edu.ng[2]; ibrahimaku@ futminna.edu.ng[5]

[b]Department of Physics, Federal University of Technology, Akure, Ondo State, NIGERIA. E-mail: ojojs_74@futa.edu.ng[3]

[c]Department of Electrical/Electronic Engineering, Osun State University, NIGERIA. E-mail: obiseye.obiyemi@uniosun.edu.ng[4]

*Corresponding Author: k.igwe@futminna.edu.ng

2. Background

Rain Rate Statistics and Conversion Model

The Lavergnat and Gole (L-G) rain rate conversion model has been widely employed since its development (Lavergnat & Gole, 1998). This model was used to analyze rainfall rates for this investigation because it has recently proven to be the most effective rainfall rate conversion tool for the zone under consideration (Igwe et al., 2021). The conversion of rainfall rate distribution from a given data acquisition time (integration time) t_1 to the required equivalent time of integration t_2 is facilitated by this model. This is accomplished using a conversion factor of the ratio t_2 to t_1 (Lavergnat & Gole, 1998):

$$Pr_2(R_2) = (CF)^a Pr_1(R_1) \qquad (1)$$

where

$$CF = \frac{t_2\,(\text{min})}{t_1\,(\text{min})} \qquad (2)$$

and

$$R_2(mm/h) = \frac{R_1(mm/h)}{(CF)^a} \qquad (3)$$

where Pr_1 and Pr_2 are the probabilities realised with rain gauges at t_1 and t_2 respectively, while the rain rates for Pr_1 and Pr_2 are represented by R_1 and R_2.

The region of interest relies on the parameter 'a', which has an estimate of 0.115 for the temperate region, with 0.143 being the equivalent estimate for the tropical climatic region, as quantified by Emiliani *et al.* (2009).

The Selected Models for Rain-Induced Attenuation

Five widely recognized models for estimating rain attenuation were employed in this study. These are the Bryant model, the Garcia-Lopez (G-L) model, the internationally recognized ITU-R P.618-9 model (ITU-R model), the Simple Attenuation Model (SAM), and the Svjatogor model. Detailed explanations can be found in Igwe et al. (2019); however, the models are briefly defined below.

The ITU-R model: This model uses the rainfall rate that exceeded 0.01% to predict rain attenuation. For other percentage exceedances, an adjustment factor is applied. The computational steps are detailed in ITU-R (2007).

The Bryant Model: Derived by Bryant et al. (1999), this model calculates rain attenuation distribution based on the concept of an effective rain cell and variable rain height.

The Garcia-Lopez Model: Developed to predict rain attenuation on slant-path links, this model uses coefficients specific to tropical regions (Garcia-Lopez et al., 1988).

The Simple Attenuation Model: Stutzman and Dishman derived this model in 1984. It is based on an exponentially shaped rain rate profile and incorporates characteristics of both convective and stratiform rain types.

The Svjatogor Model: This model, derived by Svjatogor (1985), is unique in that its effective rain height depends on the measured rain intensity.

The parameters inputted into the attenuation models used are listed in Table 1.

Table 1. Parameters used in the attenuation models

Attenuation model	H_S	θ	λ	f	k, α	$R_{0.01}$	$R_P(p)$
ITU-R	√	√	√	√	√	√	
G-L	√	√	√		√		√
Bryant	√	√			√		√
Svjatogor	√	√			√		√
SAM	√	√	√		√		√

where H_S: Station's altitude (km), θ: elevation angle (°), λ: Station's latitude (°), f: frequency (in GHz), k and α: Coefficients dependent on frequency and polarisation (ITU-R, 2005), $R_{0.01}$ (mm/h): Point rain rate at 0.01%, p: Percentage time of the year (%), $R_p(p)$: Point rain rate (mm/h).

3. Methodology

Part of the rainfall data used in this study was collected at 5-minute integration intervals from the Tropospheric Data Acquisition Network (TRODAN) situated at the Federal University of Technology, Minna, Nigeria. Additional rainfall data were obtained from the Centre for Atmospheric Research (CAR), Anyigba, Nigeria. The CAR stores rainfall data collected from other locations with TRODAN stations, such as Benue State University, Makurdi; University of Abuja; University of Jos; and Kogi State University, Anyigba. The North Central region of Nigeria comprises six states and the Federal Capital Territory (FCT), Abuja. However, rainfall data were obtained from only four states, including Abuja, as TRODAN weather stations have not been installed in the remaining two states, Kwara and Nasarawa. The rainfall data obtained from the five locations ranged between 2 and 4 years.

The data were collected using a tipping bucket rain gauge and a Campbell CR-1000 data logger. The rain gauge measures rainfall at 5-minute integration intervals, necessitating the conversion of the measured data to 1-minute integration intervals. The data logger can measure almost any sensor with an electrical response, recording the signals and converting the measurements to engineering units. The CR-1000 data logger and tipping bucket rain gauge in the TRODAN station are shown in Figure 1.

Figure 1. (a) The outdoor TRODAN measuring console equipped with a CR-1000 data acquisition system (b) The TRODAN in-situ measuring rain gauge

The 5-minute rain rate (mm/h) statistics were converted to a 1-minute rainfall rate (mm/h) equivalent using the L-G model discussed in section 2. The attenuation models outlined in section 2 were employed to compute the rain attenuation values. Circular polarisation was used to examine the downlink centre frequencies of 12.68 GHz and 19.45 GHz for the Ku- and Ka-bands, respectively. This followed the interpolation of the horizontal and vertical polarisation values of k and α at both frequencies (Ajewole, 1997). Elevation angles of 55 degrees and 42.5 degrees were used. Satellite receivers in Nigeria employ these two angles: 55 degrees for the Atlantic Ocean Region (AOR) and 42.5 degrees for NIGCOMSAT-1R reception across the AOR. Figure 2 provides the flow diagram of the methodology.
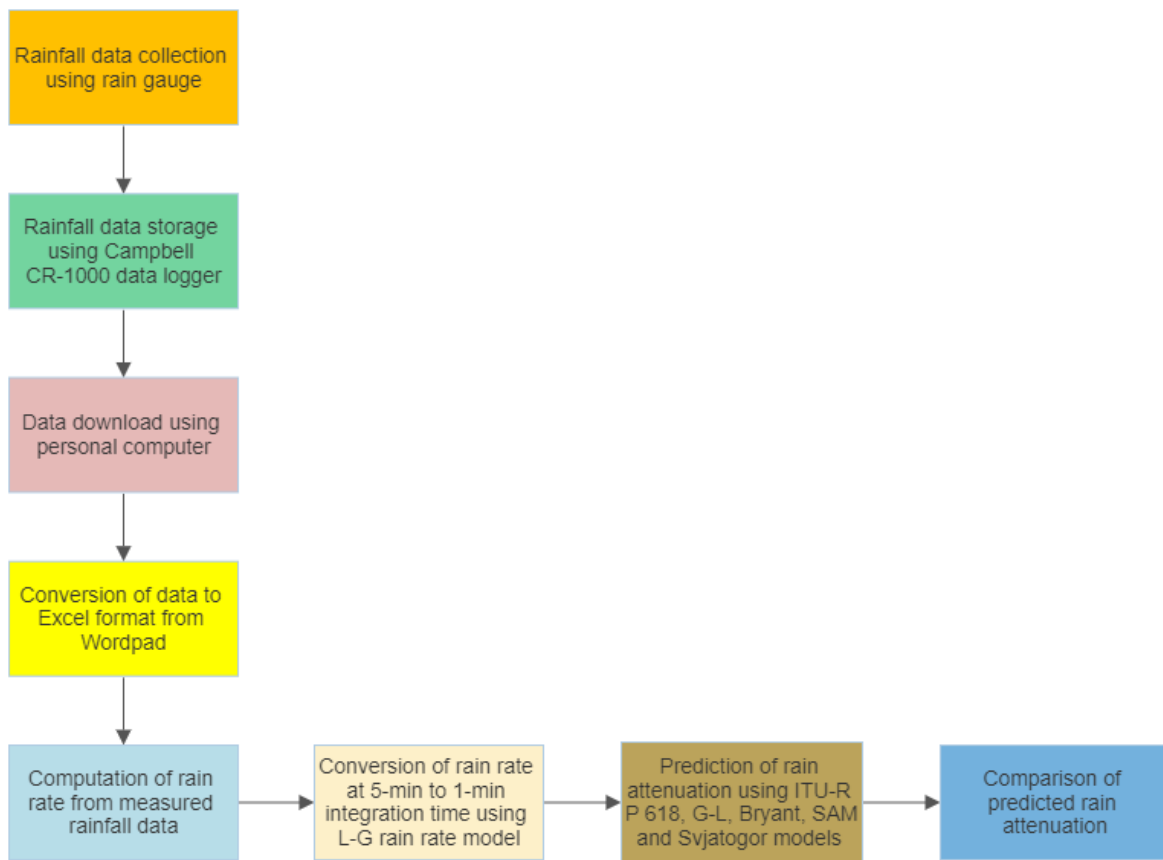

Figure 2. Flow diagram of methodology

4. Results and Discussion

Rainfall Rate Computation

Table 2 presents the preliminary requirements for rain attenuation that must be satisfied.

Table 2. Station parameters and converted rain rate

Location	Lat (°N)	Long (°E)	Alt (m)	$R_{0.01}$ (mm/h)
Abuja	9.00	7.28	334	44.00
Anyigba	7.25	7.18	420	37.80
Jos	9.58	8.57	1110	75.50
Makurdi	7.70	8.50	142	75.50
Minna	9.54	6.54	249	75.50

According to Table 2, the maximum $R_{0.01}$ is 75.50 mm/h, which is recorded in three stations, Jos, Makurdi and Minna. Meanwhile, the minimum $R_{0.01}$ is 37.80 recorded in Anyigba.

Rain Attenuation Computation

The computed attenuation using the aforementioned models was compared against the ITU-R model, which serves as the standard due to its global acceptance for accuracy. It is common practice to compare estimated rain attenuation values from various models to the ITU-R model in the absence of direct observations (Abayomi & Khamis, 2012). Research findings confirm that ITU-R model computations align with direct measured values (Mandeep & Allnut, 2007; Ojo et al., 2008; Panchal & Joshi, 2016; Hossain & Islam, 2017).

Rain attenuation computation depends on numerous parameters, some of which are shown in Table 1. Other crucial parameters include rain height (Hr), slant path length (Ls), effective path length (Le), and horizontal projection (Lg). Accurate computation of these parameters ensures precise calculation of the corresponding rain attenuation. Therefore, these relevant input parameters were determined as a prerequisite for rain attenuation prediction. Tables 3 and 4 present the values of these parameters at the two super-high frequency bands (Ku and Ka).

Table 3. Parameters for computation at 55°

Location	H_r (km)	L_s (km)	L_g (km)	L_e_Ku (km)	L_e_Ka (km)
Abuja	4.76	5.40	3.10	4.72	5.18
Anyigba	4.75	5.28	3.03	5.04	5.46
Jos	4.76	4.45	2.55	3.22	3.65
Makurdi	4.76	5.64	3.23	3.68	4.19
Minna	4.79	5.54	3.18	3.61	4.13

Table 4. Parameters for computation at 42.5°

Location	H_r (km)	L_s (km)	L_g (km)	L_e_Ku (km)	L_e_Ka (km)
Abuja	4.76	6.55	4.83	4.89	5.30
Anyigba	4.75	6.41	4.72	5.25	5.62
Jos	4.76	5.40	3.98	3.30	3.70
Makurdi	4.76	6.84	5.04	3.75	4.23
Minna	4.79	6.72	4.95	3.67	4.15

It is observed from Tables 3 and 4 that the computed values of H_r, L_s, L_g and L_e increase as the elevation angles decrease from 55° to 42.5° in all locations, and at both frequency bands considered. It is also noticed that computed values are higher at Ka than at Ku.

Table 5 shows the computed rain attenuation at Ku, 55° elevation angle.

Table 5. Computed rain attenuation at Ku, 55° elevation angle

% time Exceedance	Station	ITU-R P.618-9 (dB)	Bryant (dB)	Garcia-Lopez (dB)	SAM (dB)	Svjatogor (dB)
0.001	Abuja	16.0	13.0	11.0	2.3	8.2
	Anyigba	15.0	12.0	9.0	1.7	7.7
	Jos	19.5	16.0	17.0	4.1	6.9
	Makurdi	21.5	19.5	18.0	2.5	12.7
	Minna	21.5	19.5	18.0	2.7	12.3
0.01	Abuja	10.0	8.0	6.5	1.1	4.6
	Anyigba	9.0	7.0	5.6	0.8	4.4
	Jos	12.0	9.7	10.6	2.1	3.8
	Makurdi	13.8	12.0	11.0	1.2	7.6
	Minna	13.5	12.0	11.0	1.4	7.2
0.1	Abuja	3.3	3.2	2.6	0.4	1.8
	Anyigba	3.0	3.0	2.3	0.3	1.7
	Jos	4.0	4.0	4.5	0.7	1.4
	Makurdi	5.0	5.0	5.0	0.4	3.2
	Minna	6.0	5.0	5.0	0.5	3.0
1	Abuja	0.8	0.6	0.5	0.1	0.3
	Anyigba	0.7	0.5	0.4	0.0	0.3
	Jos	1.0	0.8	0.8	0.1	0.2
	Makurdi	1.2	1.0	0.9	0.1	0.6
	Minna	1.1	1.0	0.9	0.1	0.5

Table 5 shows that locations with similar rain rate values at 0.01% (as recorded in Table 2) also exhibit similar attenuation values. This trend is particularly noticeable in Makurdi and Minna, both of which recorded the highest rainfall rate of 75.5 mm/h at 0.01%. Consequently, the maximum attenuation values at 0.01% of the year are 13.8 dB for Makurdi and 13.5 dB for Minna, as computed by the ITU-R model. A relatively close attenuation value was also recorded at the Jos station, which has a similar rain rate. Conversely, a minimum attenuation value of 9 dB is predicted for Anyigba, corresponding to its lower rainfall rate.

It is further observed that the Bryant and G-L model computations closely align with the ITU-R model, especially at higher percentage exceedances of 0.1% and 1%. The deviation here ranges from 0.1 to 1 dB, whereas the differences at lower percentage exceedances of 0.001% and 0.01% are about 2-5 dB. Predictions by the Svjatogor model and SAM deviate significantly from the others.

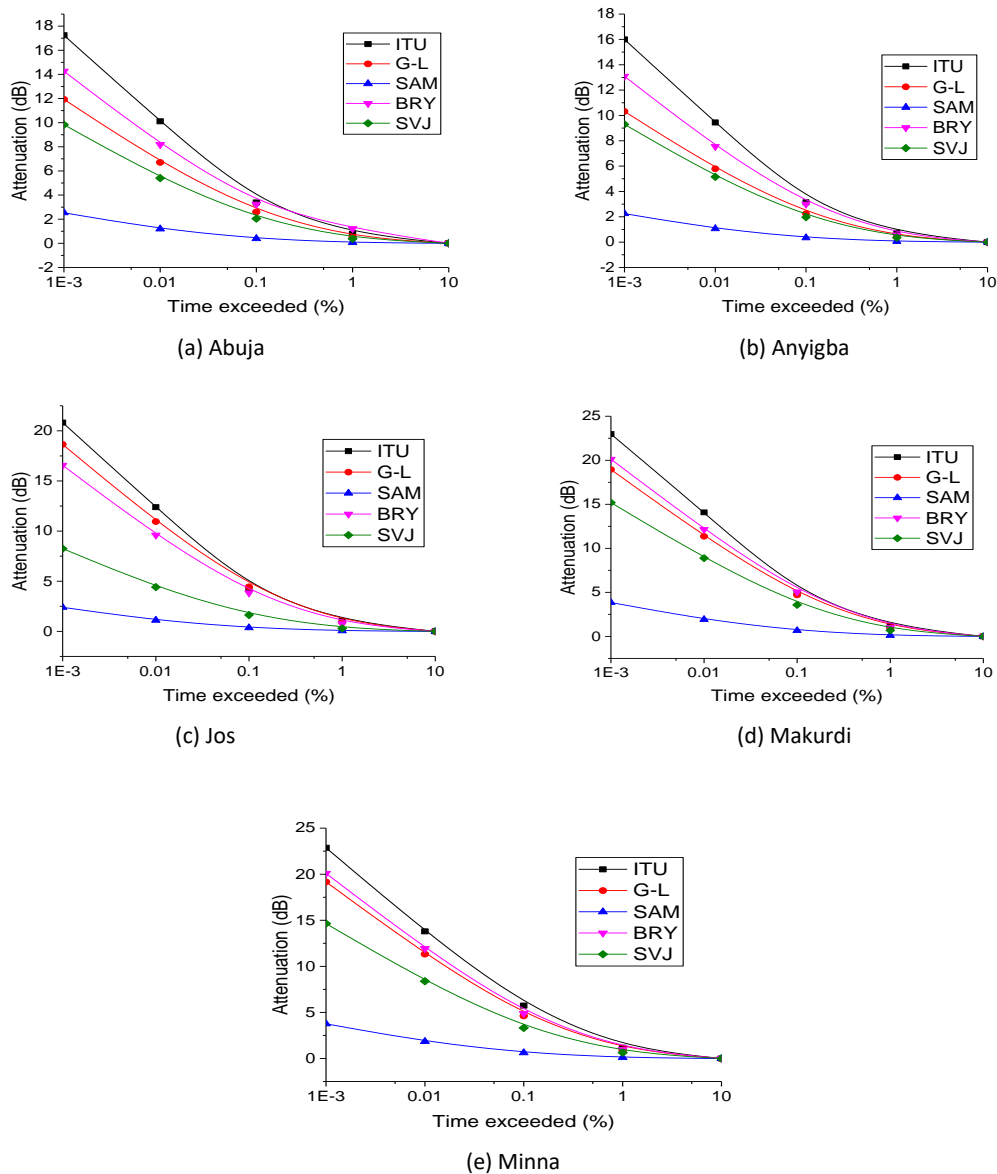The predicted attenuation at Ku, 42.5° is presented in Figures 3(a)-(e).

(a) Abuja

(b) Anyigba

(c) Jos

(d) Makurdi

(e) Minna

Figure 3. Computed attenuation at Ku, 42.5° look angle

As depicted in Figure 3, the computed attenuation values at 42.5° are slightly higher than those computed at 55°, with a 2-5 dB deviation across the entire distribution. Furthermore, the estimations by the Bryant and G-L models align closely with the

ITU-R model, particularly at higher time percentage exceedances. In contrast, the predicted values from the SAM and Svjatogor models consistently underestimate the computed attenuation at every percentage of time.

Table 6 shows the computed attenuation at Ka-band, 55° elevation angle.

Table 6. Computed attenuation at Ka, 55° look angle

% time Exceedance	Stations	ITU-R P.618-9 (dB)	Bryant (dB)	Garcia-Lopez (dB)	SAM (dB)	Svjatogor (dB)
0.001	Abuja	33.3	25.3	21.3	3.0	15.6
	Anyigba	30.1	23.0	18.6	2.7	14.8
	Jos	40.5	29.8	32.3	9.5	12.8
	Makurdi	45.0	36.1	32.9	10.5	23.6
	Minna	45.1	36.2	33.3	10.5	22.8
0.01	Abuja	22.1	16.3	13.5	1.5	9.5
	Anyigba	20.4	15.0	11.7	1.4	9.2
	Jos	27.3	19.4	21.2	5.4	7.6
	Makurdi	31. 4	24.6	22.1	6.2	15.3
	Minna	31.0	24.1	22.0	6.1	14.4
0.1	Abuja	8.0	7.2	5.9	0.5	4.0
	Anyigba	7.4	6.6	5.1	0.5	3.9
	Jos	10.1	8.7	9.6	2.1	3.1
	Makurdi	11.8	11.5	10.2	2.5	6.8
	Minna	14.5	11.1	10.0	2.4	6.3
1	Abuja	2.1	1.4	1.1	0.1	0.7
	Anyigba	1.9	1.3	1.0	0.1	0.7
	Jos	2.7	1.8	2.0	0.4	0.6
	Makurdi	3.1	2.3	2.1	0.4	1.3
	Minna	3.1	2.3	2.0	0.4	1.2

Table 6 shows that attenuation computed at the Ka-band is substantially higher than at the Ku-band. The maximum attenuation value exceeded at 0.01% of the year is 31 dB, as computed by the ITU-R model for Makurdi and Minna, while the minimum value of 20.4 dB is predicted for Anyigba. The computed values by the G-L and Bryant models are close to those computed by the ITU-R model, albeit with higher deviations. At higher percentage exceedances of 0.1% and 1%, the deviations in computed attenuation range between 1 and 3 dB, whereas at lower percentage exceedances of 0.001-0.01%, the deviations are in the 5-11 dB range. The SAM and Svjatogor models again underestimate the computed values at every percentage of time. Predictions by these two models deviate significantly from the others, with differences at higher percentage exceedances of 0.1% and 1% ranging from 2 to 12 dB, while computed attenuation at lower percentage exceedances of 0.001-0.01% ranges from 11 to 22 dB.

124

Figures 4(a)-(e) show the computed attenuation at Ka, 42.5° elevation angle.

(a) Abuja

(b) Anyigba

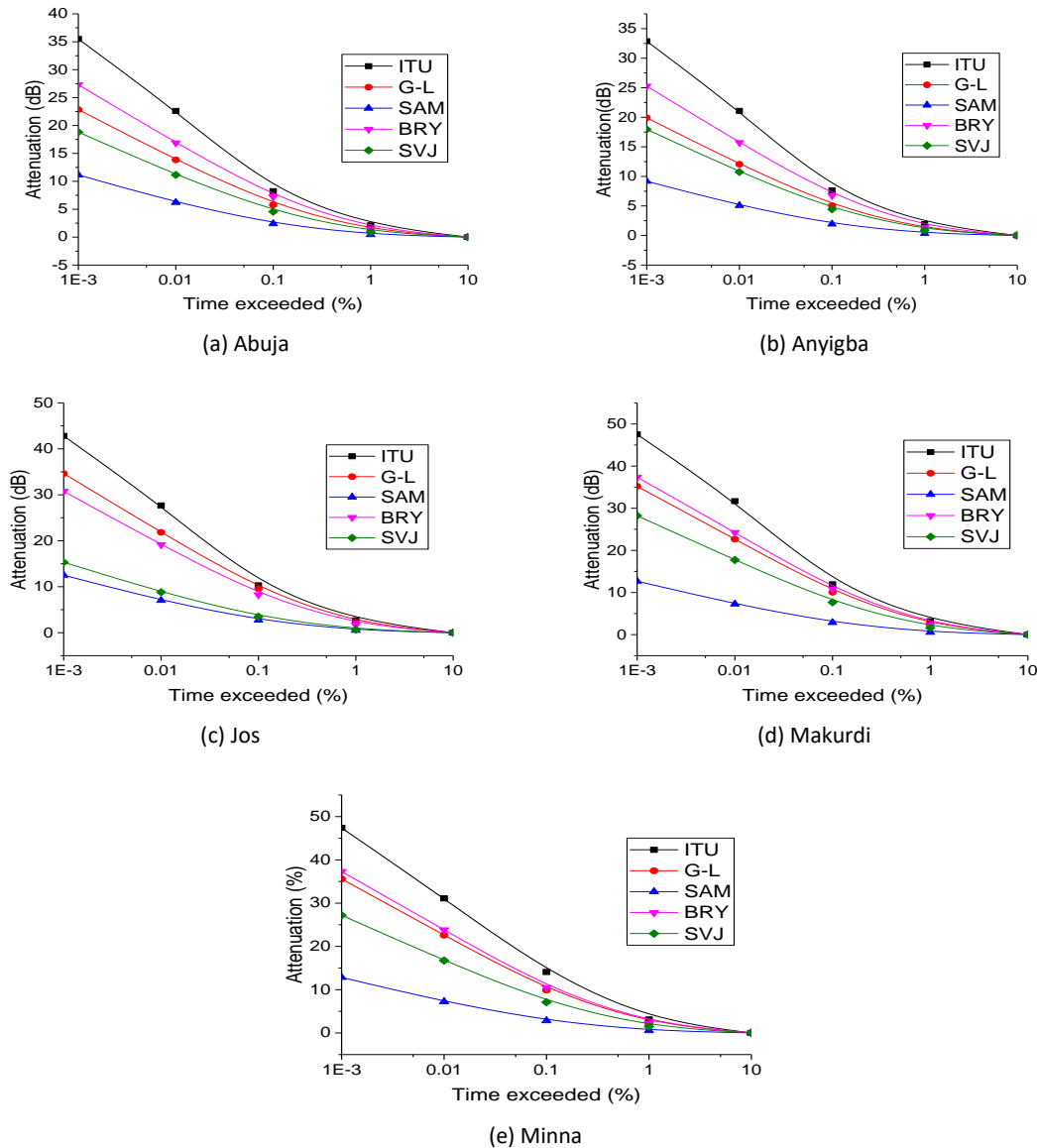(c) Jos

(d) Makurdi

(e) Minna

Figure 4. Computed attenuation at Ka-band, 42.5° elevation angle

As seen in Figure 4, the computed values of rain attenuation at 42.5° are slightly higher compared to those obtained at 55°. At 0.01%, attenuation varies between a minimum value of 21.1 dB, predicted for Anyigba, and a maximum value of 31.7 dB, predicted for Makurdi, as computed by the ITU-R model. At the Ka-band, predictions by the Bryant and G-L models closely match the ITU-R model only at higher percentage exceedances of 0.1% and 1%. All four models underestimate the computed attenuation at lower percentage time exceedances of 0.001% and 0.01%.

5. Conclusion

Computations of rain attenuation on slant path links at super high frequency (SHF) bands (Ku and Ka) were conducted using five commonly employed models for rain attenuation prediction: Bryant, Garcia-Lopez, ITU-R P.618-9, Simple Attenuation, and Svjatogor. These computations were performed at elevation angles of 55° and 42.5°. The findings revealed that higher rainfall rates resulted in greater rain attenuation, and higher attenuation was observed at lower percentage time exceedances. At the examined elevation angles, lower attenuation values were obtained at 55°, while higher values were noted at 42.5°, indicating that higher elevation angles are generally associated with lower attenuation. Additionally, the results indicated that rain attenuation values were significantly higher at the Ka-band than at the Ku-band, suggesting that attenuation increases with frequency. At the Ku-band, attenuation ranged from 9 to 14 dB at both 55° and 42.5° at 0.01% time exceedance. At the Ka-band, attenuation ranged from 20 to 31 dB at 55° and 21 to 32 dB at 42.5° at 0.01% time exceedance.

Furthermore, the Bryant, Garcia-Lopez, and ITU-R P.618-9 models showed good agreement, especially at the Ku frequency band. However, at the Ka frequency band, deviations among these three models were lower at higher percentage exceedances

(0.1% and 1%) than at lower exceedances (0.001% and 0.01%) for the entire distribution. The SAM and Svjatogor models consistently underestimated the computed rain attenuation values for every percentage of time. Therefore, the Bryant, Garcia-Lopez, and ITU-R P.618-9 models could be effectively used to compute rain attenuation at the Ku-band and at higher percentage exceedances of the Ka-band in the North Central region of Nigeria.

A limitation of this study is the inability to corroborate the predicted rain attenuation with actual signal attenuation measurements. However, the values computed using the ITU-R P.618 model, which served as the standard, were consistent with the model's validation examples for prediction methods.

6.Acknowledgement

7. References

Abayomi Y.I.O., Khamis N.H.H. (2012). Rain attenuation modelling and mitigation in the tropics: Brief review. *Int. J. of Elect. and Comp. Eng*., 2(6), 748-757.

Ajewole, M. O. (1997). Scattering and attenuation of centimeter and millimetre radio signals by tropical rainfall. *Ph.D thesis, Federal University of Technology, Akure, Nigeria.*

Alozie, E., Abdulkarim, A., Abdullahi, I., Usman, A.D., Faruk, N., Olayinka, I.-F.Y., Adewole, K.S., Oloyede, A.A., Chiroma, H., Sowande, O.A., *et al* (2022). A review on rain signal attenuation modeling, analysis and validation techniques: Advances, challenges and future direction. *Sustainability,* 14, 11744, 1-65.

Bryant G.H., Adimula I., Riva C., Brussard G. (1999). Rain attenuation statistics from rain column, diameters and heights. *Int. J. of Sat. Commun*., 19, 263-283.

Collin R. E. (1985). *Antennas and radiowave propagation*. McGraw-Hill international editions, electrical engineering series, Singapore, 339-409.

Emiliani L. D., Luini L. & Capsoni C. (2009). Analysis and parameterization of methodologies for the conversion of rain-rate cumulative distributions from various integration times to one minute. *IEEE Antennas and Propagation Magazine*, 51(3), 70–80.

Garcia-Lopez J.A., Hernando J.M., Selga J. (1988). Simple rain attenuation method for satellite radio links. Year-to-year variability of rainfall for microwave applications in the USA. *IEEE Trans. on Ant. and Propag*., 36(3), 444-448.

Hossain M.S., Islam M.A. (2017). Estimation of rain attenuation at EHF bands for earth-to-satellite links in Bangladesh. *Int. Conf. on Elect., Comp. and Commun. Eng. (ECCE)*, Cox's Bazar, Bangladesh, 589-593.

Igwe K. C., Oyedum O. D., Ajewole M. O., Aibinu A. M. (2019). Evaluation of some rain attenuation prediction models for satellite communication at Ku and Ka bands. *Journal of Atmospheric and Solar-Terrestrial Physics*, 188, 52–61.

Igwe K.C., Oyedum O.D, Ajewole M.O, Aibinu A.M, Ezenwora J.A. (2021) Performance evaluation of some rain rate conversion models for microwave propagation studies. *Adv Space Res* 67:3098-3105.

Igwe K. C. (2022). Optimal rain attenuation prediction models for earth-space communication at Ku-band in North Central Nigeria. Proceedings of the 7th International Conference on the Applications of Science and Mathematics. *Springer Proceedings in Physics,* 273, 415-428.

Igwe K. C. (2023). Derivation of regression coefficients and conversion factors for 1-minute rain rate statistics in a tropical environment. *Journal of Advanced Industrial Technology and Application,* 4 (1), 29-37.

ITU-R (2005). Specific attenuation model for rain for use in prediction methods. *Rec. P.838-3, ITU-R P Sers., Int. Telecomm, Union*, Geneva.

ITU-R 2007. Propagation data and prediction methods required for the design of earth–space telecommunication systems. *Rec. P.618-9, ITU-R P Sers., Int. Telecomm, Union,* Geneva.

Isabona, J., Imoize, A.L., Rawat, P., Jamal, S.S., Pant, B., Ojo, S., Hinga, S.K. (2022). Realistic prognostic modeling of specific attenuation due to rain at microwave frequency for tropical climate region. *Wireless Communications and Mobile Computing (Wiley-Hindawi)*, 1-10.

Isabona, J., Imoize, A.L., Ojo, S., Lee, C.-C., Li, C.-T. (2022). Atmospheric propagation modelling for terrestrial radio frequency communication links in a tropical wet and dry savanna climate. *Information*, 13 (141), 1-16.

Lavergnat J., & Golé P. (1998). A stochastic raindrop time distribution model. *Journal of Applied Meteorology*, *37*(8), 805–818.

Mandeep J. S., Allnut J. E. (2007). Rain attenuation predictions at Ku-band in south east Asia Countries. *Progress in Electromagnetics, PIERS,* 76, 65-74.

Ng Y., Singh M., Singh J., Thiruchelvam V. (2017). Performance analysis of 60-min to 1-min integration time rain rate conversion models in Malaysia. *Journal of Atmospheric and Solar-Terrestrial Physics*, 167, 13–22.

Ojo J. S., Ajewole M.O., Sarkar S.K. (2008). Rain rate and rain attenuation prediction for satellite communication in Ku and Ka bands over Nigeria. *Progress in Electromagnetics,* Res. B, 5, 207-223.

Oktaviani, R., Marzuki. (2019). Estimation of rainfall rate cumulative distribution in Indonesia using global satellite mapping of precipitation data. *International Conference on Basic Sciences and Its Applications*, 2019, 259–265.

Panchal P., Joshi R. (2016). Performance analysis and simulation of rain attenuation models at 12-40 GHz band for an earth space path over Indian cities. 7th Int. Conf. on Commun., Comput. and Virtualiz., *ScienceDirect*, 79, 801-808.

Pérez-García, N., Pinto, A.D., Torres, J.M., Rivera, Y.E., Mello, L.A.R. S, Garcia, R., Ramírez, E.J., Guevara-Salgado, P. (2023). Preliminary rain rate statistics with one-minute integration time for radio propagation uses in Venezuela. *Electronics Letters,* 59(6), 1-3*.*

Rafiqul I., Alam M., Lwas A. K., Mohamad S. Y. (2018). Rain rate distributions for microwave link design based on long term measurement in Malaysia. *Indonesian Journal of Electrical Engineering and Computer Science*, 10(3), 1023–1029.

Shrestha S., Park J., Choi, D. (2016). Rain rate modeling of 1-min from various integration times in South Korea. *SpringerPlus*, 5:433, 1-34.

Shrestha S., Choi D. (2017a). Characterization of rain specific attenuation and frequency scaling method for satellite communication in South Korea. *Int. J. of Antenn. and Propag*., 1-16.

Shrestha S., Choi D. (2017b). Study of 1-min rain rate integration statistics in South Korea. *J. of Atm. and Solar-Terr. Phys*., 155, 1–11.

Shrestha S., Choi D. (2018). Diurnal and monthly variations of rain rate and rain attenuation on Ka-band satellite communication in South Korea. *Prog. In Electromagn. Res. B*, 80, 151-171.

Singh R., Acharya R. (2019). Development of a new global model for estimating one-minute rainfall rate. *IEEE Transactions on Geoscience and Remote Sensing*, 56(11), 6462–6468.

Stutzman W.L., Dishman W.K. (1984). Correction to a simple model for the estimation of rain-induced attenuation along earth-space paths at millimeter wavelengths. *Rad. Sci*., 19, 946.

Svjatogor L. (1985). Prostranstvennaia korelacia vypadenjija dozdjej vdol zemnoj poverchnostji (in Russian), Symposium expertov stran uchastnic programmy *INTERKOSMOS* (Interkosmos symposium, theme 5 of the established telecommunication working group, Dresden, GDR).

Tamosiunaite M., Tamosiuniene M., Gruodis A., Tamosiunas S., 2010. Prediction of electromagnetic wave attenuation due to water in the atmosphere. 1. Attenuation due to rain. *Innov. Infotech. for Sci, Business and Edu*., ISSN 2029-1035, 2(9), 3-10.